Arene Ruthenium(II) Thiosemicarbazone Complexes as Anticancer Agents

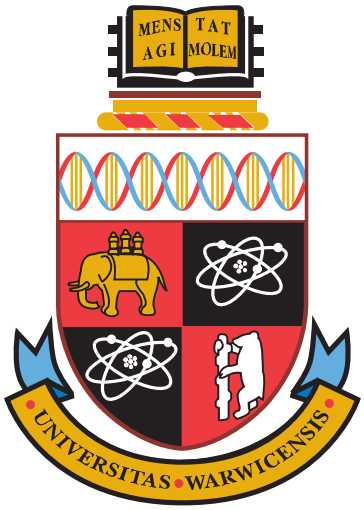

A Thesis Submitted for the Degree of Doctor of Philosophy

***Dipl. Chem.* Anna Louisa Noffke**

Supervisor: Prof. Peter J. Sadler, FRS

Department of Chemistry,

University of Warwick

Thursday 15th January, 2015

Contents

Acknowledgements **iv**

Declaration **v**

Abstract **vi**

Abbreviations **vii**

1 Introduction **1**
1.1 Motivation for the Research 2
1.1.1 Cancer Incidence and Mortality 2012 3
1.1.2 The Need for Novel Cancer Treatments 3
1.2 Metal-based Anticancer Agents 5
1.2.1 Inorganic Ru(III) Anticancer Complexes 7
1.2.2 Arene Ruthenium and Osmium Anticancer Complexes 8
1.3 Thiosemicarbazones 15
1.3.1 Properties of Thiosemicarbazone Metal-Complexes . 17
1.3.2 Organometallic Ruthenium Thiosemicarbazone Complexes 22
1.4 Synchrotron Radiation for X-ray Spectroscopy 24
1.4.1 Synchrotron Radiation 24
1.4.2 The Production of Synchrotron Light 25
1.4.3 X-ray Absorption Spectroscopy 26
1.5 Aims 29
References 30

2 Synthesis, Structure and NMR Spectroscopy of Thiosemicarbazone Arene Ruthenium Complexes **37**
2.1 Introduction 38
2.2 Experimental Section 39
2.2.1 Materials 39
2.2.2 Thiosemicarbazone Synthesis 40
2.2.3 Synthesis of Ruthenium Complexes 47
2.2.4 Elemental Analysis 60
2.2.5 Mass Spectrometry 60

2.2.6 X-ray Crystallography 61
2.2.7 Nuclear Magnetic Resonance Spectroscopy 61
2.2.8 $^{1}H^{15}N$-Heteronuclear Multiple-bond Coherence Spectroscopy 63
2.3 Results 65
2.3.1 Synthesis of Thiosemicarbazones 65
2.3.2 Synthesis of Arene Ruthenium TSC Complexes . . . 67
2.3.3 Mass Spectrometry 69
2.3.4 X-ray Crystal Structures 72
2.3.5 NMR Spectroscopy of Thiosemicarbazones 79
2.3.6 Natural-Abundance ^{1}H,^{15}N NMR Spectroscopy . . . 82
2.3.7 NMR Spectroscopy of Ruthenium TSC Complexes . 88
2.4 Discussion 99
2.4.1 Synthesis 99
2.4.2 Mass Spectrometry 101
2.4.3 X-ray Crystal Structures 102
2.4.4 Natural-Abundance ^{1}H,^{15}N NMR Spectroscopy . . . 105
2.4.5 NMR Spectroscopy with Ruthenium TSC Complexes 108
2.5 Summary 113
References 115

3 Synchrotron X-ray Absorption Spectroscopy of Arene Ruthenium TSC Complexes 119
3.1 Introduction 120
3.2 Experimental Section 121
3.2.1 Materials 121
3.2.2 Solid-State X-ray Absorption Spectroscopy 123
3.2.3 Solution-State X-ray Absorption Spectroscopy 125
3.2.4 Solid-State XAS Data Collection 127
3.2.5 XAS Data Processing 128
3.2.6 UV-visible Spectroscopy 130
3.3 Results 131
3.3.1 X-ray Absorption Near-Edge Spectroscopy 131
3.3.2 EXAFS Fitting 133
3.3.3 Solution-state Ru K-edge XAFS 140
3.3.4 UV-vis Spectroscopy 142
3.4 Discussion 146
3.4.1 X-ray Absorption Near-Edge Structure 147
3.4.2 Extended X-ray Absorption Fine Structure 147
3.4.3 Structural Models for EXAFS of Ruthenium Arene Complexes 149
3.4.4 EXAFS Fitting 151
3.4.5 The Dimerisation of an Arene Ruthenium TSC Complex 154
3.5 Summary 157

References . . . 158

4 Biological Investigations and Iodine Tracing 160
4.1 Introduction . . . 161
4.2 Experimental Section . . . 162
4.2.1 Materials . . . 162
4.2.2 Inductively Coupled Plasma Mass Spectrometry . . . 163
4.2.3 High Performance Liquid Chromatography . . . 165
4.2.4 Cell-Culture Experiments . . . 165
4.2.5 Significance Tests . . . 172
4.3 Results . . . 173
4.3.1 Antiproliferative Activity . . . 174
4.3.2 Total Cellular Ru/I Accumulation . . . 176
4.3.3 Sub-cellular Ru/I Distribution . . . 178
4.3.4 HPLC of iodido and chlorido complexes . . . 181
4.3.5 Cell-Cycle Analysis by Flow Cytometry . . . 183
4.3.6 Detection of Apoptotic Cell-Populations . . . 187
4.4 Discussion . . . 191
4.4.1 Antiproliferative Activity . . . 192
4.4.2 Accumulation and Distribution of Ruthenium and Iodine in Cancer Cells . . . 193
4.4.3 HPLC of Iodido and Chlorido Complexes . . . 198
4.4.4 Structure-Activity Relations . . . 200
4.4.5 Cell-Cycle Analysis . . . 202
4.4.6 Apoptosis Detection . . . 205
4.5 Summary . . . 208
References . . . 210

5 Conclusions and Future Work 215
5.1 Structure and Spectroscopy of Arene Ruthenium TSC Complexes . . . 216
5.2 Anticancer Activity and Mode of Action of Arene Ruthenium TSC complexes . . . 218
5.2.1 Iodine Labelling . . . 219
References . . . 221

Appendix 222

Conferences and Courses attended 225

Acknowledgements

First and foremost I would like to thank my supervisor Prof. Peter J. Sadler for accepting my research proposal and for all his support, advice, and the many opportunities he has given me throughout the course of my project.

Thanks to my advisors Prof. Peter Scott and Prof. Claudia Blindauer for their helpful feedback, and to the Warwick Postgraduate Research Scholarship (WPRS) scheme for financial support.

All members of the PJS group, both past and present, who have supported me during my time in the lab. Thanks for the enthusiastic scientific and not-so-scientific discussions. In particular, thanks to Nicolas Barry for his invaluable help during the night shifts at the synchrotron - it was both an honour and a great pleasure to work with you!

My dearest thanks go to you, Iso, not only for all the boxes we made, but even more for all the ones we ticked together. I am grateful for your guidance and friendship, and for wearing the black hat at times when I least wanted but most needed you to. To Ruth, who completes the fabulous O.T., thanks for your help and advice, and for your patience with me and the HPLC. Thank you, girls, *for coffee*, spain (TYL!) and a truly memorable time.

Sincere thanks to all the people and institutions that supported this work by providing resources, help with equipment, expertise and advice: Silvia Ramos, Steve Parry, Giannantonio Cibin and The Diamond Light Source, for the experiment time at B18; Ivan Prokes, Edward Tunnah (NMR); Prof. David Scanlen (Flow Cytometer); Lijiang Song, Phil Aston (MS); Guy Clarkson (X-ray structures); Prof. Alison Rogers for guidance; and Susanna Graham-Jones for a place to write.

Last, but by no means least, special thanks to extraordinary people in my life: Rajiv, thank you, thank you, thank you, for your unconditional and unprecedented **100 %**. I owe this one to you: I could not have done it without you! A million thanks to my family, for their endless support, encouragement, love, and understanding. To Tom & Ellen for their love and incredible patience. To the Bee's, for everything they have shown me and been for me. And to Felix, who always said "Mach immer was dein Herz dir sagt."

Thank you. Louisa

Declaration

I hereby declare that except where specific reference is made to other sources, the work described herein was conducted solely by myself, the undersigned author.
This thesis is submitted to the University of Warwick in support of my application for the degree of Doctor of Philosophy. It has been composed by myself and has not been submitted, in whole or in part, in any previous application for any degree diploma or other qualification within higher education.

Anna Louisa Noffke
Thursday 15th January, 2015

Arene Ruthenium(II) Thiosemicarbazone Complexes
as Anticancer Agents

Abstract

This thesis presents the synthesis and characterisation of thiosemicarbazones (TSCs) and their arene ruthenium complexes for the use as anticancer agents. Based on substituted benzaldehyde derivatives, 12 different TSCs were used as N,S-chelating ligands in 24 different ruthenium half-sandwich complexes. The variations in their general structure [(*p*-cymene)Ru(R-TSC)Z]$^{+}$[A^{-}] include the use of both chloride and iodide as monodentate Z ligand. Iodine substituents in the TSC (R = I) were used to introduce a possible tracer moiety.

Structure and reactivity elucidations by NMR, ESI-MS and X-ray absorption spectroscopy in Chapters 2 and 3 include the ^{15}N-NMR chemical shift determination for the 12 TSCs by ^{1}H^{15}N-HMBC NMR in solution. The TSC imino (N^{1}) and the hydrazinic (N^{2}) nitrogen atoms exhibit significant ^{15}N-NMR chemical coordination shifts of -60 ppm and +122 ppm, respectively. The latter indicates deprotonation of the NH in solution.

X-ray crystal structures of two complexes are presented, for [(*p*-cymene)Ru(PTSC*NMe*$_2$)][PF$_6$] **[10]** and for the dinuclear complex [(*p*-cymene)Ru(DTSC*IPh*)]$_2$[PF$_6$]$_2$ **[30]**. The crystallographic data were used as models for theoretical fitting of Ru K-edge EXAFS data. The EXAFS fits to data obtained for the presented complexes strongly match the first coordination sphere found in the crystal structure of complex **[10]**. Solution-state XAS on freeze-quenched aliquots of a solution of [(*p*-cymene)Ru(DTSC*NMe*$_2$)Cl]Cl confirm its conversion into **[30]**.

[(*p*-cymene)Ru(PTSC*NMe*$_2$)I]PF$_6$ **[12]** and [(*p*-cymene)Ru(ITSC*NMe*$_2$)I]PF$_6$ **[29]** with an iodine substituent are investigated in Chapter 4. Both have antiproliferative activity (IC$_{50}$ = 2 μM) against human ovarian cancer cells (A2780) , causing cell-cycle arrest in G1-phase and induction of apoptotic pathways. The strategic positional variations of iodine labels within this series combined with the simultaneous detection of ^{101}Ru and ^{127}I by ICP-MS showed that the monodentate ligand Z does not enter the cancer cells. In contrast to this, the aromatic iodine substituent in the TSC ligand of [(*p*-cymene)Ru(R-TSC)I]$^{+}$ enhances cellular accumulation of both ruthenium and TSC-bound iodine, but not the cytotoxicity of the complex.

Abbreviations

BTSC Benzaldehydethiosemicarbazone

CCDC Cambridge crystallographic database

CDDP *cis*-Diammino-dichlorido-platinum(II), Cisplatin

DAD Diode array detector

DMEM Dulbecco's Modified Eagle Medium

DNA Deoxyribonucleic acid

DpT di-pyridyl-2-thiosemicarbazone

DTSC 4-(N,N-Dimethylamino)benzaldehydethiosemicarbazone

ESI Electrospray Ionisation

EXASF Extended X-ray Absorption Fine Structure

FID Free induction decay

FLY Total Fluorescence Yield

FT Fourier Transform

HMBC Heteronuclear Multiple Bond Correlation

HPLC High Performance Liquid Chromatography

HSA Human serum albumin

HSQC Heteronuclear Single Quantum Correlation

ICP Inductively coupled plasma

ITSC 3-iodobenzaldehydethiosemicarbazone

LCF Linear Combination Fitting

NCI National Cancer Institute

PBS Phosphate buffered saline

PCD Programmed cell death

PI Propidium iodide

ppb parts per billion

ppm parts per million

PS Phosphatidyl serin

RDC Residual dipolar coupling

RNAse Ribonuclease

RPMI Roswell Park Memorial Institute

SRB Sulforhodamine B

SVM Support vector machine

SW Spectral width

TCA Trichloroacetic acid

TEA Triethylamine

TEY Total Electron Yield

TFA Trifluoroacetic acid

THF Tetrahydrofuran

TSC Thiosemicarbazone

VWD Variable Wavelength Detector

WHO World Health Organisation

XANES X-ray Absorption Near Edge Spectroscopy

XAS X-ray Absorption Spectroscopy

Chapter 1

Introduction

Cancer is one of the most frequent causes of death in the developed world today. In the field of bio-organometallic chemistry, the research of organometallic co-ordination compounds with anticancer properties contributes to the search for new cancer chemotherapeutics. Within this field of research, arene ruthenium anticancer complexes are an area that has grown and established itself in recent years. The work presented in this thesis contributes to this field with the synthesis of new ruthenium(II) arene complexes and the investigation of their cytotoxicity towards cancer cells.

Thiosemicarbazones (TSCs) are a class of organic molecules that has shown vast therapeutic potential in the past. Furthermore, their use as chelating ligands for ruthenium-based anticancer research has recently gained substantial interest in the field. For these reasons, the presented work combines TSCs with the ruthenium-arene fragment, with the aim to derive novel TSC ruthenium half-sandwich complexes that have added potential to become new anticancer compounds.

1.1 Motivation for the Research

In its recent report on trends in cancer incidence[i] and mortality[ii] worldwide, the World Health Organisation (WHO) highlights how fast the cancer burden grows: In 2012, 14.1 million people died of cancer, but the latest estimates suggest that the mortality is likely to rise to 19.3 million by 2025, an increase of 5 million cancer deaths per year.[1]

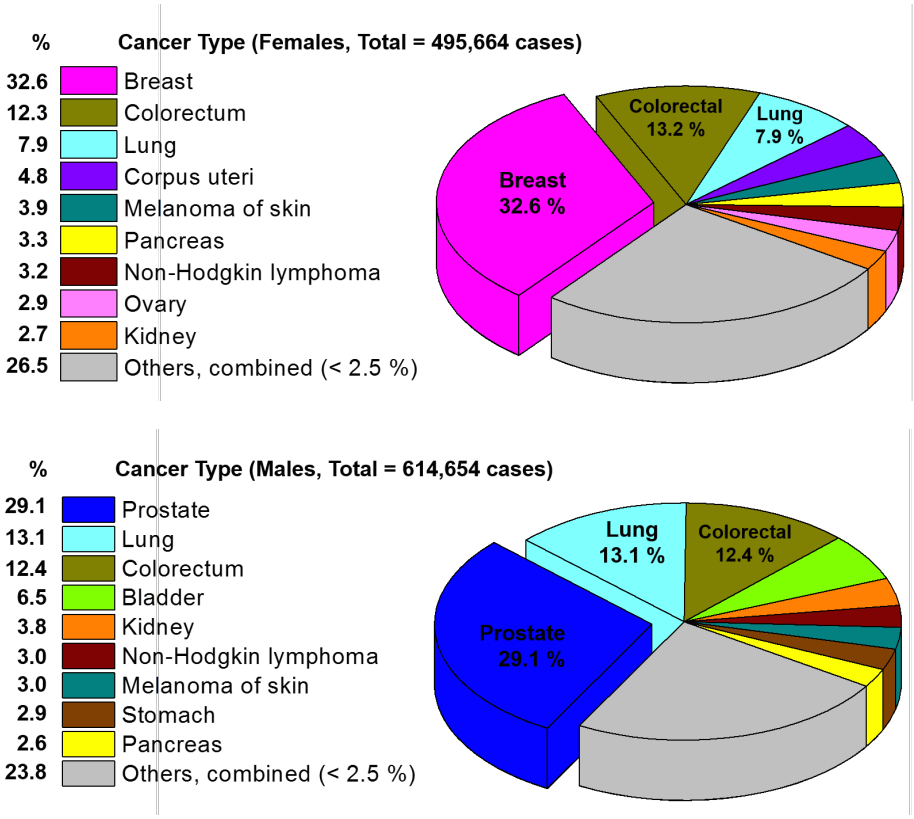

Figure 1.1: The two charts visualise the gender-specific abundance of common cancer types: breast/prostate, colorectal and lung cancer were the most frequent in Western Europe in 2012. [Data reproduced from: GLOBOCAN 2012: *Estimated Cancer Incidence, Mortality and Prevalence Worldwide* (published by the WHO in February 2014)[2, 3]]

[i] Cancer *Incidence* is the number of new cases arising in a given period in a specified population. This information is collected routinely by cancer registries.

[ii] Cancer *Mortality* is the number of deaths occurring in a given period in a specified population. It can be expressed as an absolute number of deaths per year or as a rate per 100,000 persons per year.

1.1.1 Cancer Incidence and Mortality 2012

Two pie charts in Figure 1.1 illustrate the most frequent types of cancers diagnosed in male and female patients in Western Europe[iii] in 2012. The graphic shows that the most abundant cancers in the Western European population are the gender specific ones. Prostate cancer alone made up 29.1% of cancer diagnoses in men, while breast (32.6%), uteral (4.8%), and ovarian cancer (2.9%) accounted for almost half (42.6%) of all incidences in female patients. Breast cancer also remains the most lethal form of the disease in women. Noticeably, lung cancer appears to be twice as frequent in men than in women, while both genders are equally affected by colorectal cancer (ca 12%).

The report by the WHO emphasises the need for urgent implementation of efficient prevention strategies in order to counteract climbing cancer incidence rates. However, it is also apparent from the presented statistics that improved ways of treatment and novel chemotherapeutics are paramount in coping with the increasing number of cancer cases.

1.1.2 The Need for Novel Cancer Treatments

There are several options of treatment available when a tumour is detected. The most effective of those treatments is the surgical removal of a solid tumour mass, followed by radiation therapy to reduce the risk of a recurrence due to cancerous cells which might have remained in the tissue. Where surgery is not possible, radiation therapy alone, chemotherapy, or a combination of the two is the next most favourable option.

[iii] Details about the exact region this data represent can be found in the online resource www.globocan.iarc.fr

Drug Resistance Limits the Scope of Current Chemotherapeutics

Patients in clinical chemotherapy have been treated with Cisplatin, *cis*-$[PtCl_2(NH_3)_2]$, for more than 30 years, and two close variants, Carboplatin and Oxaliplatin (Figure 1.2), have also been approved for the treatment of cancers. A drawback, however, is that side-effects such as nausea, neuro-, nephro-, and myelotoxicity impair the success of platinum-based chemotherapeutics.[4]

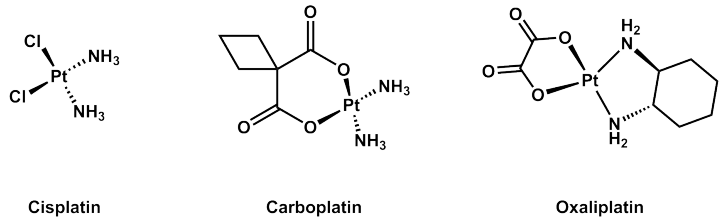

Figure 1.2: Platinum drugs in clinical use: Cisplatin *cis*-$[(NH_3)_2PtCl_2)]$, Carboplatin (Paraplatin®), and Oxaliplatin (Eloxatin®)

In addition to the severe side-effects, the scope of platinum drugs is more and more limited by cellular drug resistance.[5] This phenomenon, when a chemotherapeutic agent looses its effect and over the course of the treatment becomes inactive, occurs on the cellular level.[6] Chemotherapeutics aim to stop tumour growth by inhibiting cell proliferation, and also to reduce the number of cancer cells, i.e. decrease tumour mass.[7] However, cancer cells can develop mechanisms by which they detect and subsequently excrete the drug molecules.[6] When this process happens faster than the original drug-action, the net result is complete activity loss, or, in other words, the cells have become resistant. This 'acquired drug resistance' has rendered some cancer types untreatable with todays most commonly used chemotherapeutics, which is one of the reasons for many cancer related fatalities.[8]

As a result of drug resistance, the highest demand for new anticancer

drugs resides with the types of cancers that show both high numbers of incidence and drug resistance. Ovarian cancer is the most frequent type diagnosed in women in Western Europe, and it is most commonly treated with Cisplatin, *cis*-$[PtCl_2(NH_3)_2]$,[9] but most strains are already resistant against this platinum based drug.[9, 10] Therefore, advanced ovarian cancer is one for which new treatments are urgently required.

The following sections introduce and explore the use of ruthenium complexes in anticancer drug research and give an overview over recent research with ruthenium arene complexes, which provides the background of the work presented in thesis.

1.2 Metal-based Anticancer Agents

Researchers in metal-based medicinal chemistry aim to develop new cancer treatments that can overcome the resistance and side-effects connected with cisplatin.[11, 12] A vast number of transition metals other than platinum are under investigation in the development of new coordination compounds with better bioavailability, selectivity and fewer side-effects.[11–17]

Coordination complexes offer versatile reactivities, and because of this they can be subject to modification during their uptake and transport inside the human body. Hence they are almost always pro-dugs. Therefore, the ligands must be chosen carefully, as they may possess different functions. Not only can they influence the reactivity of the metal or be involved in redox reactions, but also greatly affect the absorption and delivery of the complex, and sometimes even the specificity of target recognition.

Organometallic Iron Complexes against Breast Cancer

An example of an organometallic compound that achieves the difficult task of target recognition is the Tamoxifen analogue Ferrocifen. The similarities between the structures of Ferrocifen and Hydroxytamoxifen, the active metabolite of Tamoxifen, are illustrated in Figure 1.3.

The growth of several types of breast and prostate cancer cells is dependent on the natural hormones estradiol and testosterone, respectively. These cancer cells over-express hormone receptors, and treatment usually relies on drugs that modulate the receptors in order to lower overall hormone levels. An example is the selective endocrine receptor-modulator (SERM) Tamoxifen, which is widely used for anti-oestrogen treatment of hormone dependent breast cancer.[18]

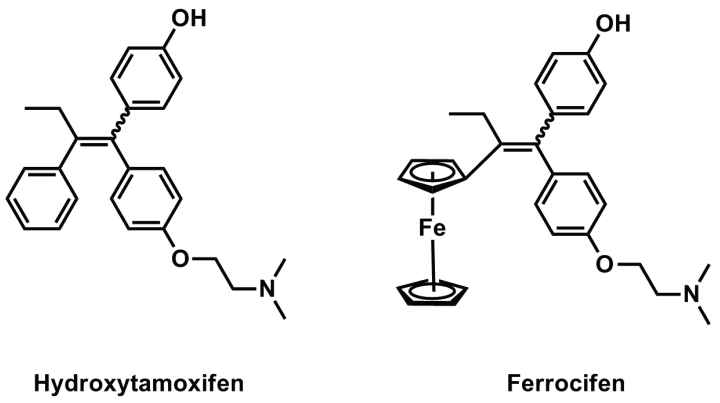

Figure 1.3: Molecular structures of the Tamoxifen metabolite Hydroxitamoxifen and its iron-containing analogue Ferrocifen.

Iron-incorporating derivatives of Tamoxifen exhibit improved anticancer activity.[19] Ferrocifen (Figure 1.3), in which one phenyl ring is replaced with a ferrocenyl unit, is used as a vector to recognise the oestrogen receptor, and to carry the redox active fragment into cancer cells. Ferrocifen is an example for the scope that lies in metal-based anticancer compounds.

1.2.1 Inorganic Ru(III) Anticancer Complexes

Two ruthenium(III) complexes are currently undergoing clinical trials. Figure 1.4 shows the structures of the imidazolyl-complex NAMI-A and of its indazolyl congener KP1019. Both molecules are monoanionic octahedral Ru(III) complexes with two axial heterocyclic N-donor ligands and four equatorial chlorido ligands.

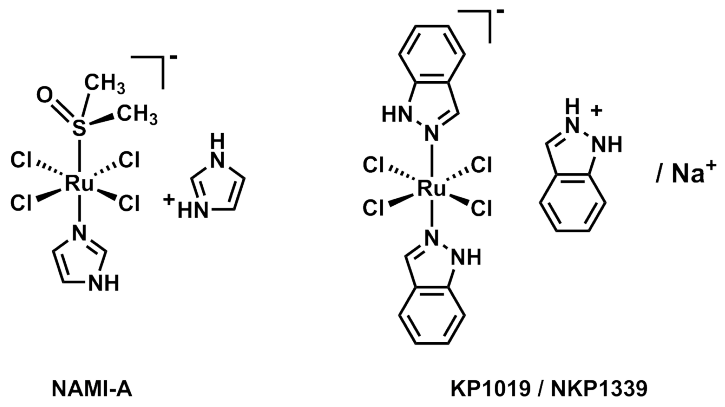

Figure 1.4: Structures of NAMI-A and KP1019, two Ru(III) complexes undergoing clinical trials as anticancer agents.

NAMI-A, invented by Sava and co-workers, is an antimetastatic agent.[20] Its activity is likely related to integrin dependent inhibition of cancer cell motility and invasiveness.[20, 21]

KP1019 has a very similar general structure, but its activity profile is different from NAMI-A. The indazolyl-ruthenium complex is cytotoxic towards solid cancer and has been evaluated in a phase–I clinical trial in 2004; but the study had to be stopped early due to the insolubility of the compound.[22, 23] Compared to KP1019, its sodium salt NKP1339 (Figure 1.4) is more water soluble, and therefore more suitable for clinical development.[24] NKP1339 is currently being developed by NikkiPharm as a 'first-in-class' ruthenium-based anti-tumour drug,[25] and the first clinical trial has been

completed.[26]

These examples show that ruthenium complexes are promising anticancer drug candidates that might potentially overcome cellular drug-resistance mechanisms, although further studies are required.

1.2.2 Arene Ruthenium and Osmium Anticancer Complexes

Half-sandwich anticancer complexes are of the general structure depicted in Figure 1.5. The corresponding formula that describes this 'piano-stool' geometry is $[(\eta^6\text{-arene})\text{Ru(XY)Z}]^+$, where XY is a bidentate chelating ligand and Z^- is a monodentate halido ligand.

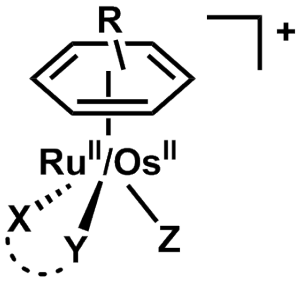

Figure 1.5: General structure of arene ruthenium/osmium half-sandwich complexes: The 'piano-stool' geometry around the metal centre is given by the facially co-ordinated arene, and the three legs opposite which are the donor atoms X, Y, and Z. Chelating ligands connect X and Y to form a mostly five membered ring including the metal.

Different ligand sets can give rise to relatively labile or rather inert complexes, depending on the nature of M, X-Y, Z, and the arene ligand, and the possible variations of each of these four building blocks are countless. It is therefore even more important to systematically investigate the way in which particular structural groups affect the anticancer activity of the resulting complexes.

Progress within the field has been reviewed frequently in recent years.[27–32] The next sections will briefly summarise the current state of structure-activity relations for ruthenium and osmium arene anticancer complexes.

Structure - Activity Relations

Figure 1.6 depicts three important examples of arene anticancer complexes. It highlights the fact that these three compounds have very different ligand sets, while all belong to the same class of molecules. The ruthenium arene PTA complex RAPTA-C (PTA = 1,3,5-triaza-7-phosphaadamantane, C = *p*-cymene) has three monodentate ligands instead of an XY chelating ligand + monodentate Z ligand. The complex is selective for acidic tumour tissue by virtue of the PTA ligand. The biphenyl complex **RM175** is an early example from the Sadler lab,[33] with an ethylenediamine chelating ligand and Z = Cl. Development of the early structure has yielded iodido-Os(II) complexes such as **FY26**, with azopyridine chelators and Z = I.[34]

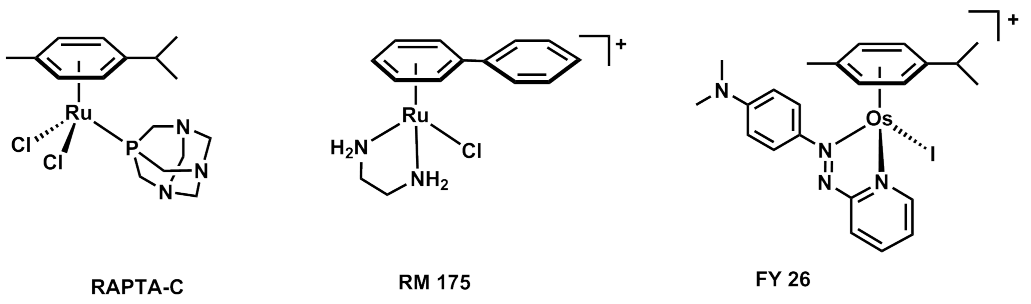

Figure 1.6: Examples of half-sandwich anticancer complexes: RAPTA-C,[35] RM 175[33] and Os(II) complex FY26[34]

The research of the last decade has revealed a number of promisingly active structures, and systematic studies have led to first structure-activity relations for osmium anticancer complexes.[30, 36] Figure 1.7 highlights a set of four structures, two containing Ru and two with Os. Two of the structures

contain a chlorido ligand ([Ru-Cl] & [Os-Cl]) and two contain I ([Ru-I] & [Os-I]).

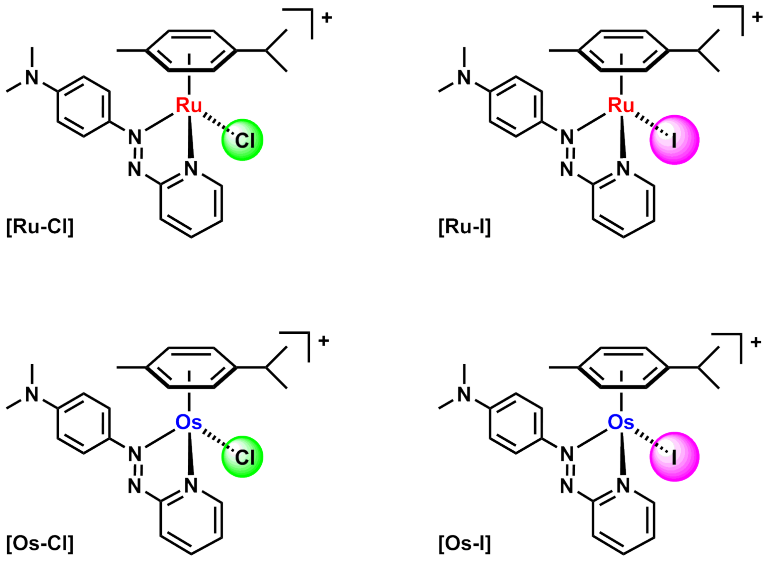

Figure 1.7: Only one atom is different between [**Ru-Cl**] & [**Ru-I**] (top), between [**Os-Cl**] & [**Os-I**] (bottom), between [**Ru-Cl**] & [**Os-Cl**] (left), and between [**Ru-I**] & [**Os-I**] (right).

Between the four complexes in Figure 1.7, either the metal centre changes from Ru to Os, while the ligands remain the same, or the monodentate ligand Z changes from Cl to I while keeping the metal centre constant. Recent research showed that such one-atom changes within the structure of two otherwise identical complexes can have a significant effect on the biological properties of piano-stool anticancer complexes.

For example, the nature of the monodentate ligand Z influences the way in which ruthenium half-sandwich complexes [**Ru-Cl**] and [**Ru-I**] of Figure 1.7 are internalised by human ovarian cancer cells (A2780), and change the antiproliferative activity of the compounds as a result.[37]

These findings are not as surprising when one takes into account that a change in biological activity of a metal complex can also be caused by ligand substitution reactions such as hydrolysis of the Z-ligand. Those reactions

may occur, for example, in the bloodstream or inside a cancer cell, which makes it implicit that it is important to elucidate speciation(-changes) of anticancer metal complexes. The next section outlines the structural properties that can control the exchange of the monodentate Z–ligand in aqueous solutions.

Structural Switches: Activation by Hydrolysis

Activation of a metal-based drug by hydrolysis of the M-Z bond can play an important role in their mode of action, as is precedent for cisplatin. Most arene anticancer complexes also undergo hydrolysis of the monodentate ligand Z (Figure 1.8), and for some this is an activation mechanism of their anticancer activity.[29]

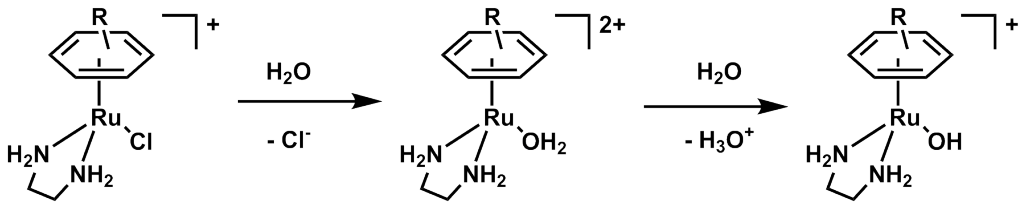

Figure 1.8: Scheme shows the steps involved in the hydrolysis of ruthenium half-sandwich complex $[(\text{arene})\text{Ru(en)Cl}]^+$ (where en = ethylenediamine).

The rate with which the Z-ligand is replaced by water depends on the nature of the metal centre, the Z-ligand, and on the chelating ligand (XY). While dissociation of the M-Z bond appears to be the rate-determining step, density functional theory (DFT) calculations suggest that aquation occurs in a concerted ligand exchange mechanism which is associative in character.[38] As such, sterically demanding XY ligands can affect the rate of aquation by hindering access to the metal, and this consequently slows down the formation of a possible transition state.

In general, ruthenium arene complexes that hydrolyse readily are more

likely to exhibit cancer cell cytotoxicity, whereas those which do not undergo aquation exhibit little or no activity. The concentration gradient between blood and cytoplasm can be used as a switch for anticancer activity after a complex has entered the cell.[39] High concentrations of chloride ions suppress the hydrolysis of $[(\eta^6\text{-arene})\text{Ru(en)Cl}]^+$ in the bloodstream (103 mM Cl),[39] but chloride concentrations are much lower in the cytoplasm (23 mM) and in the nucleus (4 mM).[40] At these concentrations, it is more likely that a ruthenium complex hydrolyses.

Osmium(II) arene complexes can also be activated by hydrolysis of the OsZ bond. However, two parameters differ markedly between osmium complexes and their ruthenium parent compounds. Firstly, aquation reactions can be up to 100x slower for Os,[29] and secondly, the resulting aqua adducts are ca. 1.5 pKa units more acidic than [Ru]-OH_2 species.

Fine-tuning with the Chelating Ligand

The cytotoxic effects of piano-stool complexes towards cancer cells can be tuned by appropriate choice of the other building blocks.[38]

For both Ru and Os complexes, changing the donor atoms in the chelating ligand from N to O increases the hydrolysis rates and decreases the acidity of the aqua adducts.[27, 41] Hydrolysis rates increase with a change in chelating ligand donors in the order N,N to N,O to O,O.

N,O-chelated Os(II) arene complexes exhibit intermediate behaviour compared to N,N- and O,O-chelates.[42, 43] Within the N,O-series, the reactivity is highly dependent on the balance of the σ-donor vs. π-acceptor power of the ligand. For example, complexes with N,O-chelating amino acids hydrolyse rapidly, whereas complexes with π-acceptor pyridine as N-donor and carboxylate as O-donor hydrolyse much more slowly.

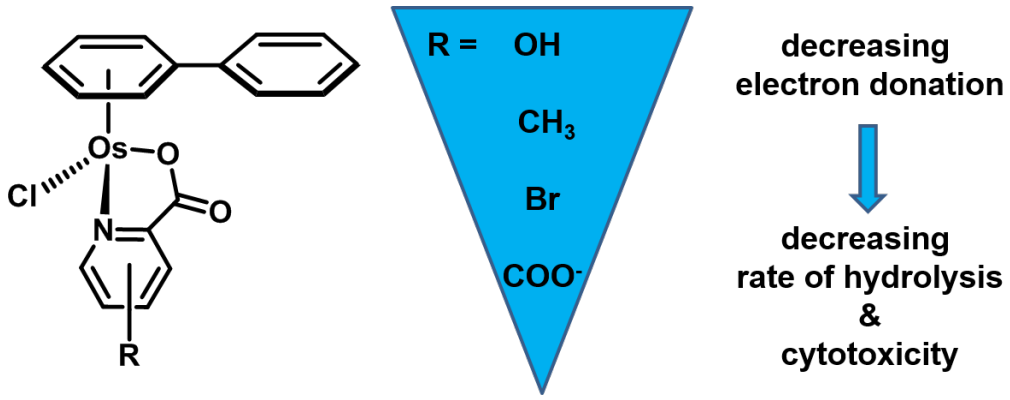

Figure 1.9: Effect of substituents on the rate of hydrolysis and cytotoxicity of Os(II) picolinato complexes.

The rates of hydrolysis of Os picolinato complexes [(η^6-biphenyl)Os(R-pico)Cl] that differ only in their pico-substituent (R-pico, Figure 1.9) decrease with a decrease in electron donating ability of the substituent OH $\leq$ Me $\leq$ Br $\leq$ COO^-. In this series, a *para*–carboxylate proves to be the most deactivating substituent – it slows the hydrolysis down the most. This complex was also the least active against human ovarian cancer cells.

Hydrogen-bonding Interactions

A change in XY from ethylenediamine (en) to acetylacetone (acac) can not only significantly increase the pKa of the aqua-complex,[44] but can also influence recognition patterns in biological targets. For example, the selectivity towards the nucleobase Guanine (G) over Adenine (A) changes with the choice of the donor atoms X and Y.[44] Primary and secondary amine N,N-ligands such as *en* can act as H–bond donors and enhance the selectivity for G-binding by H–bond formation to C6O of the nucleobase. O,O-ligands, in contrast, are H-bond acceptors and can H-bond with the C(6)NH_2 of adenine.[39] Therefore, H-bonding properties can be used to direct a metal complex towards specific target molecules. Selective recognition might be

particularly crucial for the activity of drugs that target DNA.

In summary, the systematic structural investigations of the last years conclusively point out that the activity of osmium(II) and ruthenium(II) anticancer complexes can be modulated by chelate-ligand variations. One aim of this thesis is therefore the design of new XY-chelating ligands and the investigation of their ruthenium(II) half-sandwich complexes under biologically relevant conditions.

Advancing the Selection of Chelating Ligands

Because ruthenium arene complexes of both N,N– and N,O–chelating ligands have been studied extensively in the past, this thesis focusses on thiosemicarbazones as a new class of N,S-chelators. These are structurally related to picolinamide ligands that were investigated previously by Van Rijt and McGowan.[45] The structures and properties of thiosemicarbazones will be introduced in the next sections which constitute the second part of this chapter. The aim of this choice for the chelating ligand is to contribute to the search for new active anticancer compounds on the one hand, and to the pool of information that relates their structure to anticancer activity on the other.

1.3 Thiosemicarbazones

Thiosemicarbazones (TSCs) were chosen for this research project due to their biological and structural properties. The general structure of these small organic molecules is shown in Figure 1.10.

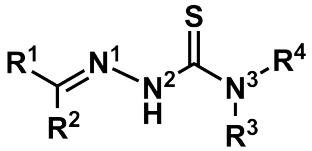

Figure 1.10: General molecular structure of thiosemicarbazones.

One of the reasons why TSCs are interesting for drug development is their ratio of hydrogen-bond donors and acceptors in the structure compared to a generally low molecular weight. These properties fit well into Lipinski´s 'Rule of 5' [iv]– the rule of thumb by which medicinal chemists have estimated 'drug-likeness' of organic molecules since 1997.[46, 47]

But TSCs have been investigated in medicinal chemistry for several decades longer than Lipinski's 'Rule' has been used. The earliest reference to a TSC with antiviral activity was published in the British Medical Journal in 1964.[48] The one-page report briefly describes the success of *N*-methylisatin-β-thiosemicarbazone (Marborane, Figure 1.11) in the prevention of smallpox infections. More reports on Methisazone followed this early study and supported the antiviral activity of the TSC that was subsequently marketed under the tradename Marborane®.[49, 50]

The first detailed assessment of the anticancer activity of thiosemicar-

[iv] In his first publication of these estimations, Lipinski suggests that an organic molecule is easier absorbed, or better permeating, in a physiological environment when it containes ≤ 5 H-bond donors, ≤ 10 H-bond acceptors, a molecular weight below 500 Da, and a $log\ P$ value ≤ 5.[46]
When Lipinski reviewed these guidelines in 2004,[47] they had been cited more than 1000 times - in less than 10 years. Today, his approximations of the relationship between the structural properties of a molecule and its physiological availability are still popular amongst medicinal chemists

bazones was discussed in 1966.[51] Studies by French et al. showed that a nitrogen heterocycle in *alpha* position to the imine bond improved the results for many TSC compounds.

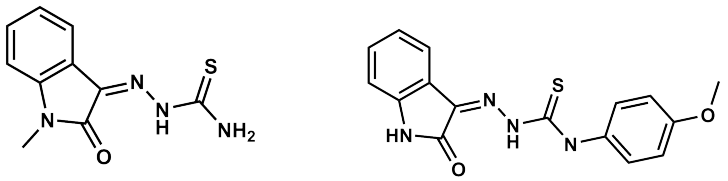

(a) (b)

Figure 1.11: Structures of the smallpox drug Marborane® (Methiazone) and the P-gp-inhibitor NSC73306.

Thiosemicarbazones are still under investigation for their biological properties today,[52] and the α -N-heterocycle appears to have been a consistent structural feature. For example, NSC73306 (Figure 1.12) showed that the incorporation of an isatin site in the molecule is essential for the thiosemicarbazone to be active against cell-lines that over-express P-glycoprotein.[53] By targeting this (drug-)efflux pathway, NSC73306 might overcome multi-drug resistance.[53, 54]

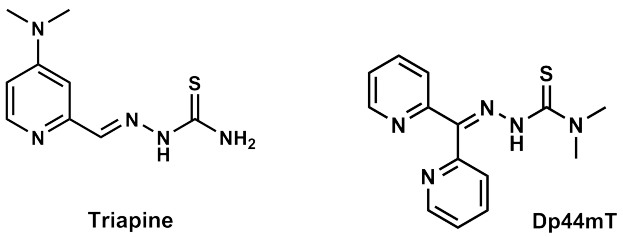

(a) (b)

Figure 1.12: Structures of the iron-chelators Triapine® and Dp44mT.

The iron-chelators 3-aminobenzaldehydethiosemicarbazone and di-pyridylketone-4,4-dimethylthiosemicarbazone ((Triapine® and Dp44mT, Figure 1.12) both have *N*-heterocyclic moieties that are discussed to be closely linked to their

activity as anticancer agents. Triapine is currently under clinical development for the treatment of cervical cancer,[55] and for iron-chelators of the di-2-pyridylketone thiosemicarbazone (DpT) class, progress is steady.[56–58] DpTs show excellent antiproliferative activity against neuroepithelioma cells (SK-N-MC) with IC_{50} values in the low nano molar (nM) range and have the ability to overcome cellular resistance to other cancer therapeutics.[59]

In summary, these examples show that TSCs are promising new drug candidates, and the hypothesis that their potential for anticancer activity may be transferable into new ruthenium based therapeutics is not without reason. The following sections will give an overview of the general coordination chemistry of TSCs towards transition metal ions, and describe possible relations to their biological activity.

1.3.1 Properties of Thiosemicarbazone Metal-Complexes

Many of the biological activities of TSCs seem to involve interactions with metal ions inside the body. In fact, one of the first anticancer metal complexes that included a TSC was a thiosemicarbazone-copper complex.[60] During the last ten years, most of the related literature has described research of TSCs as chelators for biologically important transition metals such as iron(II/III)[58, 59] or copper(I/II),.[61–63] Tri- and tetradentate TSCs form particularly stable complexes with copper[64] or gallium ions, and those find their application in radioimaging.[65]

As this thesis is focussed on the investigation of TSC ruthenium half-sandwich complexes, the following sections will give an overview of the general coordination chemistry of TSCs towards transition metal ions, and the relation to biological activity.

Tautomerisation of TSCs in Solution

TSC molecules in solution exist in one or more tautomeric forms. Figure 1.13 depicts the two tautomers; the thione form with a C=S double bonded sulfur on the left, and the thiolate form with a N=C double and C-SH single bond. Depending on the nature of the solvent and the pH, the equilibrium between these forms can shift to either side. In the thiolate form, the TSC can be deprotonated at the sulfur atom, which leads to the negatively charged thiolato structure that is shown in Figure 1.13 on the right. The different tautomeric forms need to be taken into account when metal coordination of a TSC is discussed.

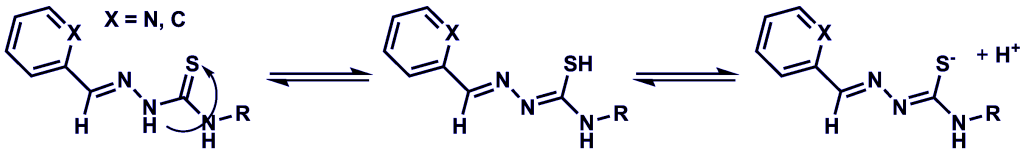

Figure 1.13: Tatomerism in TSCs.

Figure 1.14 summarises possible structures of thiosemicarbazone coordination modes towards metal ions. The central metal ion is shown in pink, and the structures that arise from the different binding modes are arranged in two rows, one for the thione form (top), and one for the thiolate (bottom). From left to right, the denticity of the TSC towards the metal increases, from monodentate to bi- and tridentate.

When the TSC sulfur atom is deprotonated, the coordination to a metal ion leads to reduction of one positive charge at the metal centre. Coordination in the neutral thione form, however, yields a complex that bears the original charge of the metal ion.

Most thiosemicarbazones that are discussed in the literature concerned with biologically active TSC metal complexes contain a pyridine moiety in

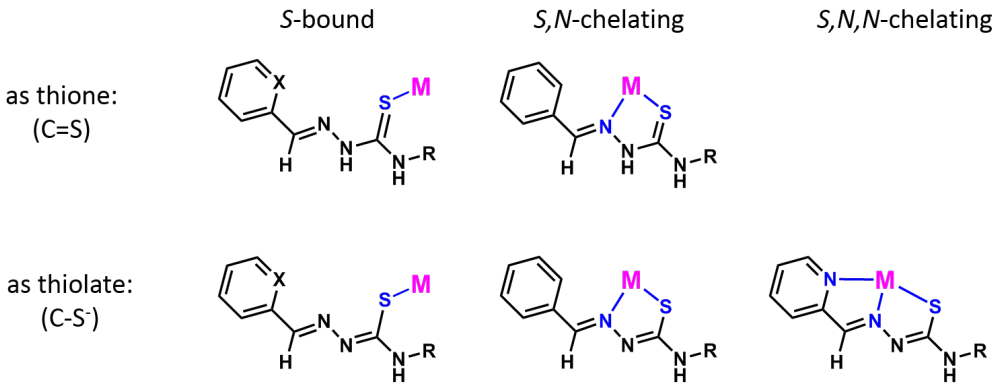

Figure 1.14: TSC - metal binding modes.

their structure. As the structure in the bottom right corner of Figure 1.14 suggests, the pyridine nitrogen can also act as a donor atom towards metal ions, and thus most TSCs of current interest appear to be tridentate ligands.

For example, pyridyl-*N,N*-dimethylthiosemicarbazones, with a structure similar to Dp44mT (Figure 1.12), form octahedral bis-ligand complexes with Ga^{III}, Fe^{III} and Ru^{III} in which the N,N,S-ligands are deprotonated.[66, 67] This is understandable, as the coordination of two tridentate TSCs, bound in the deprotonated thiolate form, is both sterically and entropically more favoured than the coordination of three bidentate ligands.[68] The steric component in this explanation is important, because the strict planarity of α N-heterocyclic TSCs aids deprotonation and tridentate meridional coordination to metals with d^6 electron configuration. Those metals, such as Fe^{3+} in its low-spin form, prefer octahedral coordination, and the tridentate planar TSC ligands offer good overlap between their donor atoms and three meridional d-orbitals of the metal.

Metal Coordination Can Enhance Biological activity

Coordination to metal ions can enhance the biological activity of TSCs compared to their unbound state. For example, benzoylpyridine thiosemi-

carbazones show activity against leukaemia cells (HL60) with IC_{50} values in the micromolar (μM) range, but become significantly more active (from μM to nM) when bound to Sb^{3+}.[69]

The antimicrobial activity of *N*-alkyl-substituted TSCs (alkyl = H, Me, Et)was found to increase when they are incorporated into organometallic tin compounds.[70] Furthermore, the activity of these TSCs against brain tumour cells increased not only with longer alkyl chains, but their Ga^{3+} complexes showed much higher activity than the free ligands. Overall, the Ga-methyl analogue proved to be best.[71]

Interestingly, the main increase in activity upon coordination to the metal is attributed to a conformation change of the ligand from *E* to *Z* with regard to the (S=)CN(-N) bond. It can therefore be concluded that coordination to a metal ion is a means to activate thiosemicarbazone cytotoxicity.

Thiosemicarbazone Complexes with Precious Metals

Many recent studies focus on complexes of thiosemicarbazones with precious metals. Moving systematically from group nine to group ten metals, this section summarises the main findings with respect to structural as well as biological data. In the platinum group, most examples are of Pd(II) and Pt(II) along with some Ni(II) complexes. The group ten examples are mostly of Cu(I/II) amongst a few Au(I) and Au(III) complexes.

The TSC ligands bind differently in square planar d^8-complexes of Pd(II) and Ni(II).[72, 73] In the former, the TSC is coordinated to Pd(II) in the thiolate form, while it binds in the neutral thione form to Ni(II). The nickel complexes are more active than the palladium derivatives against A549 cancer cells.

The ligand substituents seem to tune this activity further. In particular, derivatisation of O,N,S-ligands by systematically substituting one of the thioamide NH_2 protons showed a dependency of the biological activity on the electron donating ability of the substituent (Et > Me > H > Ph).[74, 75] Furthermore, H and Ph substituted compounds showed intercalative binding towards ct-DNA, while Me and Et derivatives exhibited weaker interactions due to the increased steric bulk. This result shows that the amide substituents, the charge of the TSC and the metal itself all have an effect on structure and activity of the complex.

The strong effect of the d^8-configuration in Pd(II) and Pt(II) complexes forcing their square-planar coordination environment is demonstrated by examples reported by Quiroga et al. who found examples of bidentate TSCs, i.e. without a pyridine moiety, that acted as planar tridentate (C,N,S)-ligands *via* a cyclometallated phenyl ring. The tetranuclear complexes exhibit cytotoxic activity comparable to cisplatin and are also active in cell lines with resistance to the clinical Pt drug.[76, 77]

Moving to group ten of the d-block elements, the structures of TSC complexes depend on the charge of the metal centre. In Cu(I) complexes the d^{10} configuration forces octahedral geometries, while Au(I) prefers linear S-coordination. Au(III), in contrast, pushes towards square-planar coordination due to its d^8-configuration, comparable to Pt(II) and Pd(II).

Similarly, Au(I)-TSC complexes are formed by linear monodentate S-coordination. Examples presented by Beraldo et al. exhibit anticancer activity and inhibit thioredoxin reductase better than the free ligands.[78] Organometallic square-planar Au(III) complexes are formed both with bidentate and tridentate TSCs,[79] and the low affinity of the Au^{3+} cation for oxygen ligands (according to the HSAB concept) could explain bidentate coordina-

tion of a potentially tridentate ligand, as found for a salicylaldehyde-derived thiosemicarbazone.

The main conclusion that results from this overview is that the structures of organometallic TSC complexes with precious metals are highly governed by the d-electron configuration of the metal. In particular, most complexes of the d^8 metal ions Pd^{2+}, Pt^{2+} and Au^{3+} appear to be of the expected square planar geometry.

For the work presented herein, this finding implies that the coordination of a TSC to the ruthenium arene fragment might be affected more by the electronic structure of the metal than steric factors introduced by the *p*-cymene ligand. Most certainly, α-N-heterocyclic TSCs that lend themselves easily to planar meridional coordination should be avoided in the search for a chelating ligand for a piano-stool complex. The facially bound arene only leaves room for another facial ligand, or for mono- / bidentate coordination.

1.3.2 Organometallic Ruthenium Thiosemicarbazone Complexes

The facile availability of thiosemicarbazones can lead to a great structural diversity of this class of chelators. Because small variations to their substituents can influence the biological properties of the TSC as well as their metal complexes, they appear to be ideal ligands for anticancer metal complexes. Although TSCs have been widely studied as ligands for metals such as palladium, platinum, copper and gold, not many examples can be found for organometallic ruthenium or osmium complexes.

Only few arene-ruthenium complexes of thiosemicarbazone ligands have been reported. In those, it has been found that the TSC either binds as

N,S-chelator towards a Ru^{2+} centre, or coordinates in a monodentate, S-bound fashion.[80, 81] Examples of both anticancer and antimicrobial activity of Ru TSC complexes exist,[82–84] and those early reports encourage the work presented in this thesis as they indicate that the combination of thiosemicarbazones with the ruthenium-arene fragment could potentially yield novel active complexes. One example shows how target selectivity for acidic tumour tissue might be introduced by coordination of a TSC to a ruthenium(III) centre.[85]

It can be concluded that TSC metal complexes offer a broad variety of structural switches, not only because the ligands are easily available, but also because they have potential anticancer activity of their own. Coordination to metals further increases this potential, and also allows for the properties of the resulting compounds to be tuned more precisely. In summary, it is worth to investigate all properties of both thiosemicarbazones and their various metal complexes in order to understand how these can be utilised for particular biological applications. For this reason, combining thiosemicarbazones with the ruthenium-arene fragment to TSC ruthenium half-sandwich complexes bears the potential for new anticancer chemotherapeutics.

1.4 Synchrotron Radiation for X-ray Spectroscopy

Synchrotron radiation (SR) contains a broad spectrum of high-energy X-rays, and the brilliance and focus that dedicated synchrotron light sources can achieve is much greater than what is attainable with laboratory X-ray sources. The high flux and brightness allow good quality XAS data to be obtained on a much shorter timescale than with bench-top X-ray spectrometers. Beamlines of third-generation synchrotrons that host XAS experiments, such as B18 at the Diamond Light Source, use high-precision optical equipment to provide a tuneable monochromatic X-ray beam of excellent focus and energy resolution. Hence, X-ray absorption spectroscopy benefits greatly from the use of synchrotron light.

As an introduction to the synchrotron XAS experiments that are presented in Chapter 3 of this thesis, the following sections will briefly describe the basic theory of XAS and the production of synchrotron radiation.

1.4.1 Synchrotron Radiation

Synchrotron radiation (SR) was discovered as a by-product that occurred in particle accelerators. Purpose-built 3^{rd}-generation synchrotrons such as Diamond Light Source generate synchrotron light of a broad energy spectrum that ranges from infrared (IR), visible (vis), and ultraviolet (UV) light up to the energy of X-rays.

When charged particles (e.g. electrons) travel at almost the speed of light, their energy increases as a function of their velocity. Upon entering a magnetic field which forces the travelling high-energy electrons to alter their flight path, this change in direction slows the electrons down, they

loose kinetic energy. This energy is emitted in the form of photons, and these constitute synchrotron radiation. The phenomenon is well described (quite literally) by the German word "Bremsstrahlung".

Photons are non-charged particles, and as such they are unaffected by the magnetic field that bends the electron path. As a result, the photon beam propagates along the original trajectory of the parent electrons at the point their path was bent.

1.4.2 The Production of Synchrotron Light

A synchrotron light source (Figure 1.15) accelerates a beam of electrons by directing it around a ring of bending magnets, known as the storage ring. Figure 1.15 summarises the constituents of a typical synchrotron, navigating through the path of the beam by starting from the electron gun (**a**) and ending in the experimental hutch of a beamline (**e**), where it can be used for X-ray spectroscopy.

The path of the beam starts at the heart of the synchrotron, at the electron gun (**a**) which emits thermionic high-energy electrons. Those are linearly accelerated (**b**) directly into the booster synchrotron (**c**). Here, acceleration to near speed of light increases the beam energy to 3.0 GeV. The main synchrotron (**d**), i.e. the storage ring, receives regular injections of electrons to maintain the beam energy as well as a stable current and flux. Each bending magnet represents a corner of the ring at which insertion devices such as wigglers or undulators produce additional "Bremsstrahlung" that exits the storage ring into a beamline (**e**). The optics set-up inside each beamline uses collimating and focussing mirrors to immediately refocus (and filter) the synchrotron radiation for its respective experimental use.

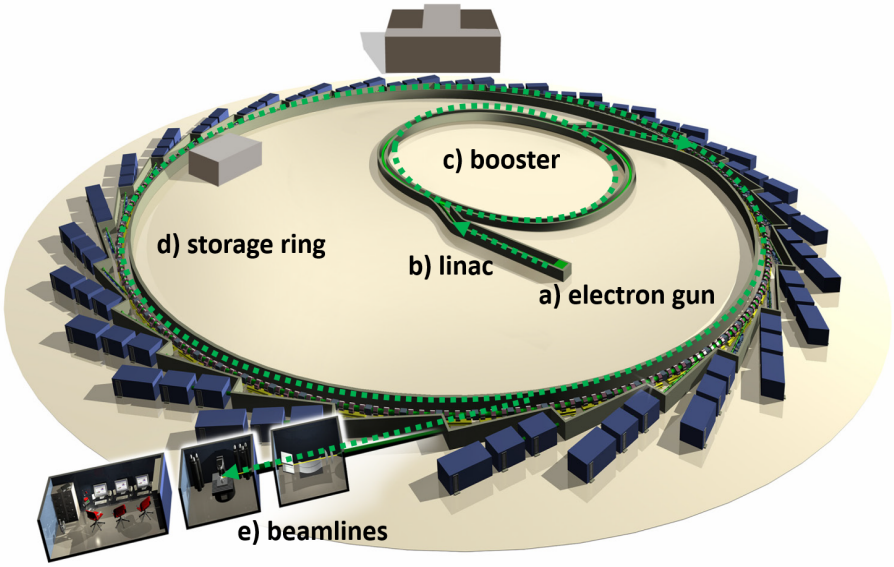

Figure 1.15: Operating scheme of a Synchrotron Light Source: (**a**) **electron gun** produces high-energy electrons, (**b**) the linear accelerator and (**c**) **booster synchrotron** accelerate electrons to approx. speed of light, (**d**) the **storage ring** maintains the electron beam. Insertion devices produce synchrotron radiation that exits the storage ring, (**e**) **beamlines** re-focuss and filter the SR for experimental use.
[v].

1.4.3 X-ray Absorption Spectroscopy

The Beer − Lambert law (Equation 1.1) describes the attenuation of light that has the energy E and intensity I_0 by a sample of the length d. Equation 1.1 states that the intensity of transmitted light I_t depends on the molar absorption coefficient μ(E) of the material as well as the sample thickness.[86, 87]

$$I_t = I_0 \cdot \ e^{-\mu(E) \cdot \ d} \tag{1.1}$$

X-ray absorption spectroscopy measures the element specific absorption coefficient of a material whose core-electrons are excited by light in the energy range of X-rays (2-35 keV). Figure 1.16 depicts a Ru K-edge XAS

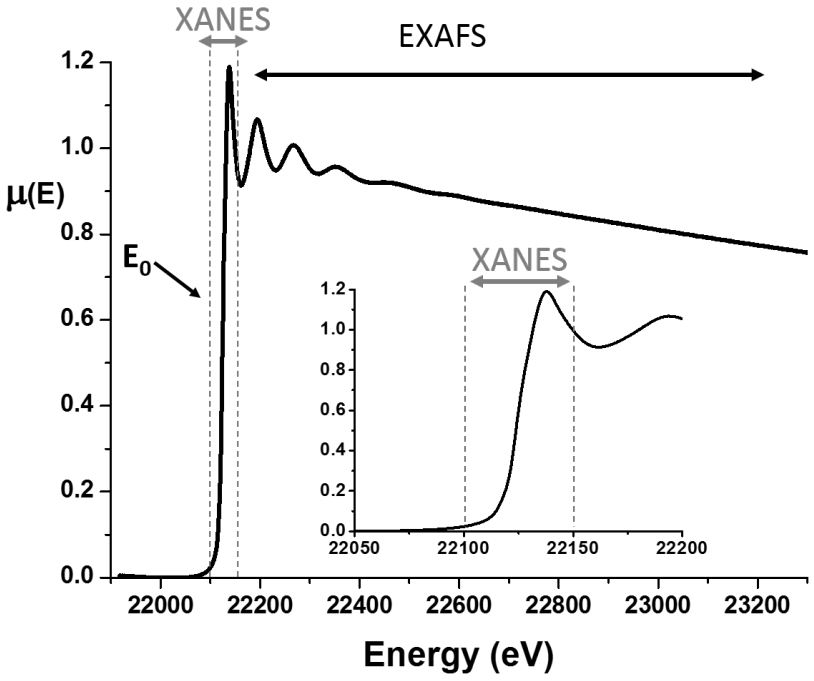

Figure 1.16: A Ru K-edge X-ray absorption spectrum, showing the edge position E_0 and the two main spectral regions of interest: X-ray absorption near-edge structure (**XANES**) around ± 30 eV of E_0 and the extended X-ray absorption fine-structure (**EXAFS**), consisting of the higher-energy oscillations beyond E_0 + 50 eV. Inset shows expansion of XANES region.

spectrum.

During the experiment, the energy of the incident X-ray beam sweeps from lower to higher values within the range of a few hundred eV around the ionisation energy of a core-electron level of the respective element. When the incident monochromatic X-ray beam has sufficient energy to eject a core electron from the K-shell, this electron is being excited to a higher orbital.

At this energy, an abrupt increase in the absorption coefficient $\mu(E)$ is visible in the spectrum. This dominant feature is known as absorption edge or rising edge. The inflection point of the absorption edge is used to determine the edge energy E_0.[88, 89] Spectral features within E_0 ± 50 eV are referred to as near-edge structure, and are analysed in X-ray absorption near-edge

spectroscopy (XANES).[90] This region can contain useful information about the electronic structure of metal-ligand interactions.[91] In particular, ligand K-edge XANES is an increasingly popular tool, for example in the study of proteins that contain spectroscopically silent metals,[92] but can also be used for the study of ligand binding in organometallic anticancer complexes.[93]

The extended X-ray absorption fine-structure (EXAFS) comprise of the high-energy oscillations in the XAS spectrum beyond E_0 + 50 eV. These are visible modulations to an otherwise linearly decaying absorptivity, and are caused by electron-scattering within the coordination sphere of the central absorber whose core-electron has been ejected. The EXAFS oscillations therefore hold specific information about the atomic structure of a material that can be extracted by careful theoretical modelling of the experimental data.

Chapter 3 presents XAS studies of novel arene ruthenium TSC complexes. It describes the procedure and results of EXAFS fitting of their first coordination sphere, which elucidates Ru-TSC coordination in both solid state and solution.

1.5 Aims

The hypothesis that combining the properties of TSCs with the ruthenium arene motif can lead to new anticancer piano-stool complexes give rise to the following aims for this thesis.

- Synthesise and characterise thiosemicarbazones and incorporate iodine as a substituent in some of the TSCs to introduce a possible reporter label.
- Synthesise and characterise novel *p*-cymene Ru(II) complexes with these TSCs as chelating XY ligands and both chloride and iodide as the respective monodentate Z ligand.
- To elucidate the structures of the TSC ligands in solution and the nature of their coordination to Ru(II) using ^{1}H and ^{15}N NMR spectroscopy.
- Characterise the complexes in the solid state by X-ray crystallography and by X-ray absorption spectroscopy. Use EXAFS to determine the first co-ordination sphere of complexes that do not crystallise, and extend this to solution studies.
- Determine the antiproliferative activities of selected new complexes in human ovarian cancer cells (A2780) and investigate their mode of action.
- Investigate the use of ICP-MS for the detection of iodine and ruthenium and study the accumulation of both elements from the complexes in A2780 cells to determine whether Ru(II) and its ligands, both the TSC and iodide as Z ligand are accumulated inside cancer cells.

References

[1] B. Stewart and C. Wild, *World Cancer Report 2014*, WHO press, 2014.

[2] J. Ferlay, I. Soerjomataram, M. Ervik, R. Dikshit, S. Eser, C. Mathers, M. Rebelo, D. Parkin, D. Forman, and F. Bray, *GLOBOCAN 2012 v1.0 - Cancer Incidence and Mortality Worldwide*, International Agency for Research on Cancer, Lyon, France, 2013.

[3] F. Bray, J.-S. Ren, E. Masuyer, and J. Ferlay, *Int. J. Cancer*, 2013, **132**(5), 1133–1145.

[4] L. Kelland, *Nat. Rev. Cancer*, 2007, **7**(8), 573–584.

[5] Y. Luqmani, *Med. Princ. Pract.*, 2005, **14**(1), 35–48.

[6] M. M. Gottesman, T. Fojo, and S. E. Bates, *Nat. Rev. Cancer*, 2002, **2**(1), 48–58.

[7] R. C. Bast, D. W. Kufe, R. E. Pollock, R. R. Weichselbaum, J. F. Holland, E. F. III, and T. S. Gansler (Eds.), *Cell Proliferation, Differentiation, and Apoptosis*, chap. 2, 5 ed., BC Decker Inc., Ontario, 2000.

[8] Z. H. Siddik, *Oncogene*, 2003, **22**(47), 7265–7279.

[9] B. Li, H. Chen, N. Wu, W.-J. Zhang, and L.-X. Shang, *Int. J. Gynecol. Cancer*, 2014, **24**(8), 1381–1388.

[10] G. Hamilton and B. Rath, *Wien. Med. Wochenschr.*, 2014.

[11] L. Ronconi and P. J. Sadler, *Coord. Chem. Rev.*, 2007, **251**(1314), 1633–1648.

[12] N. J. Wheate, S. Walker, G. E. Craig, and R. Oun, *Dalton Trans.*, 2010, **39**, 8113–8127.

[13] P. C. Bruijnincx and P. J. Sadler, *Curr. Opin. Chem. Biol.*, 2008, **12**(2), 197–206.

[14] S. H. van Rijt and P. J. Sadler, *Drug Disc. Today*, 2009, **14**(2324), 1089–1097.

[15] G. Jaouen and N. Metzler-Nolte (Eds.) *Medicinal Organometallic Chemistry*, vol. 32, Springer, Berlin Heidelberg, 2010.

[16] G. Gasser, I. Ott, and N. Metzler-Nolte, *J. Med. Chem.*, 2011, **54**(1), 325.

[17] I. Romero-Canelón and P. J. Sadler, *Inorg. Chem.*, 2013, **52**(21), 12276–12291.

[18] U. Administration, 1998.

[19] E. A. Hillard, A. Vessières, and G. Jaouen, *Ferrocene Functionalized Endocrine Modulators as Anticancer Agents*, *Top. Organomet. Chem.*, vol. 32, chap. 4, Springer, Berlin Heidelberg, 2010, 81–117.

[20] G. Sava, F. Frausin, M. Cocchietto, F. Vita, E. Podda, P. Spessotto, A. Furlani, V. Scarcia, and G. Zabucchi, *European Journal of Cancer*, 2004, **40**(9), 1383–1396.

[21] G. Sava, G. Jaouen, E. A. Hillard, and A. Bergamo, *Dalton Trans.*, 2012, **41**(27), 8226.

[22] J. M. Rademaker-Lakhai, *Clin. Cancer Res.*, 2004, **10**(11), 3717–3727.

[23] C. G. Hartinger, M. A. Jakupec, S. Zorbas-Seifried, M. Groessl, A. Egger, W. Berger, H. Zorbas, P. J. Dyson, and B. K. Keppler, *Chem. & Biodivers.*, 2008, **5**(10), 2140–2155.

[24] R. Trondl, P. Heffeter, M. A. Jakupec, W. Berger, and B. K. Keppler, *BMC Pharmacol. Toxicol.*, 2012.

[25] R. Trondl, P. Heffeter, C. R. Kowol, M. A. Jakupec, W. Berger, and B. K. Keppler, *Chem. Sci.*, 2014, **5**, 2925–2932.

[26] D. S. Thompson, G. J. Weiss, S. F. Jones, H. A. Burris, R. K. Ramanathan, J. R. Infante, J. C. Bendell, A. Ogden, and D. D. V. Hoff, *J. Clin. Oncol.*, 2012, **30**, ASCO Meeting Supplement, Abstract 3033.

[27] A. Habtemariam, M. Melchart, R. Fernandez, S. Parsons, I. Oswald, A. Parkin, F. Fabbiani, J. Davidson, A. Dawson, R. Aird, D. Jodrell, and P. Sadler, *J. Med. Chem.*, 2006, **49**(23), 6858–6868.

[28] G. Suess-Fink, *Dalton Trans.*, 2010, **38**, 16731688.

[29] A. M. Pizarro, A. Habtemariam, and P. J. Sadler, *Activation Mechanisms for Organometallic Anticancer Complexes*, *Top. Organomet. Chem.*, vol. 32, chap. 2, Springer, Berlin Heidelberg, 2010, 21–56.

[30] Y. Fu, A. Habtemariam, A. Basri, D. Braddick, G. Clarkson, and P. Sadler, *Dalton Trans.*, 2011, **40**, 10553–10562.

[31] A. L. Noffke, A. Habtemariam, A. M. Pizarro, and P. J. Sadler, *Chem. Commun.*, 2012, **48**, 5219–5246.

[32] G. Suess-Fink, *J. Organomet. Chem.*, 2014, **751**, 2–19.

[33] R. E. Aird, J. Cummings, A. A. Ritchie, M. Muir, R. E. Morris, H. Chen, P. J. Sadler, and D. I. Jodrell, *Br. J. Cancer*, 2002, **86**, 16521657.

[34] Y. Fu, A. Habtemariam, A. M. Pizarro, S. H. van Rijt, D. J. Healey, P. A. Cooper, S. D. Shnyder, G. J. Clarkson, and P. J. Sadler, *J. Med. Chem.*, 2010, **53**(22), 8192–8196.

[35] C. Scolaro, A. Bergamo, L. Brescacin, R. Delfino, M. Cocchietto, G. Laurenczy, T. J. Geldbach, G. Sava, and P. J. Dyson, *J.Med. Chem.*, 2005, **48**(12), 4161–4171.

[36] Y. Fu, M. J. Romero, A. Habtemariam, M. E. Snowden, L. Song, G. J. Clarkson, B. Qamar, A. M. Pizarro, P. R. Unwin, and P. J. Sadler, *Chem. Sci.*, 2012, **3**, 2485–2494.

[37] I. Romero-Canelón, A. Pizarro, A. Habtemariam, and P. Sadler, *Metallomics*, 2012, **4**, 1271–1279.

[38] F. Wang, A. Habtemariam, E. P. L. van der Geer, R. Fernandez, M. Melchart, R. J. Deeth, R. Aird, S. Guichard, F. P. A. Fabbiani, P. Lozano-Casal, I. D. H. Oswald, D. I. Jodrell, S. Parsons, and P. J. Sadler, *Proc. Nat. Sci. USA*, 2005, **102**, 18269–18274.

[39] M. Melchart, A. Habtemariam, S. Parsons, S. A. Moggach, and P. J. Sadler, *Inorg. Chim. Acta*, 2006, **359**, 3020–3028.

[40] M. Jennerwein and P. A. Andrews, *Drug Metab. Dispos.*, 1995, **23**, 178–184.

[41] A. F. A. Peacock, A. Habtemariam, R. Fernández, V. Walland, F. P. A. Fabbiani, S. Parsons, R. E. Aird, D. I. Jodrell, and P. J. Sadler, *J. Am. Chem. Soc.*, 2006, **128**, 17391748.

[42] A. F. Peacock, A. Habtemariam, S. A. Moggach, A. Prescimone, S. Parsons, and P. J. Sadler, *Inorg. Chem.*, 2007, **46**, 40494059.

[43] A. F. A. Peacock, S. Parsons, and P. J. Sadler, *J. Am. Chem. Soc.*, 2007, **129**, 3348.

[44] R. Fernandez, M. Melchart, A. Habtemariam, S. Parsons, and P. J. Sadler, *Chem. Eur. J.*, 2004, **10**, 5173–5179.

[45] K. D. Camm, A. El-Sokkary, A. L. Gott, P. G. Stockley, T. Belyaeva, and P. C. McGowan, *Dalton Trans.*, 2009, **48**, 10914–10925.

[46] C. A. Lipinski, F. Lombardo, B. W. Dominy, and P. J. Feeney, *Adv. Drug Deliv. Rev.*, 1997, **23**(13), 3–25.

[47] C. A. Lipinski, *Drug Disc. Today: Technologies*, 2004, **1**(4), 337–341.

[48] G. Kune, *Brit. Med. J.*, 1964, **2**, 621.

[49] B. Jaroszyska-Weinberger, *Arch. Dis. Child.*, 1970, **45**(242), 573580.

[50] W. Levinson, V. Coleman, B. Woodson, A. Rabson, J. Lanier, J. Whitcher, and C. Dawson, *Antimicrob. Agents Chemother.*, 1974, **5**(4), 398–402.

[51] F. A. French and E. J. Blanz, *J. Med. Chem.*, 1966, **9**(4).

[52] I. Dilović, M. Rubčić, V. Vrdoljak, S. K. Pavelić, M. Kralj, I. Piantanida, and M. Cindrić, *Bioorg. Med. Chem.*, 2008, **16**(9), 5189–5198.

[53] M. D. Hall, N. K. Salam, J. L. Hellawell, H. M. Fales, C. B. Kensler, J. A. Ludwig, G. Szaka, D. E. Hibbs, and M. M. Gottesman, *J. Med. Chem.*, 2009, **52**(10), 3191–3204.

[54] M. D. Hall, K. R. Brimacombe, M. S. Varonka, K. M. Pluchino, J. K. Monda, J. Li, M. J. Walsh, M. B. Boxer, T. H. Warren, H. M. Fales, and M. M. Gottesman, *J. Med. Chem.*, 2011, **54**(16), 5878–5889.

[55] A. M. Traynor, J.-W. Lee, G. K. Bayer, J. M. Tate, S. P. Thomas, M. Mazurczak, D. L. Graham, J. M. Kolesar, and J. H. Schiller, *Invest. New Drugs*, 2010, **28**(1), 91–97.

[56] D. R. Richardson, P. C. Sharpe, D. B. Lovejoy, D. Senaratne, D. S. Kalinowski, M. Islam, and P. V. Bernhardt, *J. Med. Chem.*, 2006, **49**(22), 6510–6521.

[57] D. Kalinowski, P. Quach, and D. Richardson, *Fut. Med. Chem.*, 2009, **1**(6), 1143–1151.

[58] D. R. Richardson, D. S. Kalinowski, S. Lau, P. J. Jansson, and D. B. Lovejoy, *Biochim. Biophys. Acta*, 2009, **1790**, 702–717.

[59] A. Gaál, G. Orgován, Z. Polgári, A. Réti, V. G. Mihucz, S. Bősze, N. Szoboszlai, and C. Streli, *J. Inorg. Biochem.*, 2014, **130**(0), 52–58.

[60] S. A. C. and B. A. Booth, *Cancer Research*, 1967, **27**(9), 1614–1619.

[61] M. B. Ferrari, G. G. Fava, and P. Tarasconi, *J. Chem. Soc. Dalton Trans.*, 1989, (2), 361–366.

[62] T. S. Lobana, Rekha, R. J. Butcher, A. Castineiras, E. Bermejo, and P. V. Bharatam, *Inorg. Chem.*, 2006, **45**(4), 1535–1542.

[63] R. Agarwal, L. Singh, and D. Sharma, *Bioinorg. Chem. Appl.*, 2006, 59509.

[64] J. L. Hickey, S. Lim, D. J. Hayne, B. M. Paterson, J. M. White, V. L. Villemagne, P. Roselt, D. Binns, C. Cullinane, C. M. Jeffery, R. I. Price, K. J. Barnham, and P. S. Donnelly, *J. Am. Chem. Soc.*, 2013, **135**(43), 16120–16132.

[65] J. R. Dilworth and R. Hueting, *Inorg. Chim. Acta*, 2012, **389**, 3–15.

[66] C. R. Kowol, R. Eichinger, M. A. Jakupec, M. Galanski, V. B. Arion, and B. K. Keppler, *J. Inorg. Biochem.*, 2007, **101**(11-12), 1946–1957.

[67] C. R. Kowol, R. Berger, R. Eichinger, A. Roller, M. A. Jakupec, P. P. Schmidt, V. B. Arion, and B. K. Keppler, *J. Med. Chem.*, 2007, **50**(6), 1254–1265.

[68] D. F. Shriver, P. W. Atkins, T. L. Overton, J. P. Rourke, M. T. Weller, and F. A. Armstrong, *Inorganic Chemistry*, 4th ed., Oxford University Press, Oxford, UK, 2006.

[69] D. C. Reis, M. C. Pinto, E. M. Souza-Fagundes, S. M. Wardell, J. L. Wardell, and H. Beraldo, *Eur. J. Med. Chem.*, 2010, **45**(9), 3904–3910.

[70] I. C. Mendes, J. P. Moreira, J. . D. Ardisson, R. G. dos Santos, P. R. O. da Silva, I. Garcia, A. Castineiras, and H. Beraldo, *Eur. J. Med. Chem.*, 2008, **43**(7), 1454–1461.

[71] I. C. Mendes, M. A. Soares, R. G. dos Santos, C. Pinheiro, and H. Beraldo, *Eur. J. Med. Chem.*, 2009, **44**(5), 1870–1877.

[72] E. Ramachandran, P. Kalaivani, R. Prabhakaran, N. P. Rath, S. Brinda, P. Poornima, V. V. Padma, and K. Natarajan, *Metallomics*, 2012, **4**, 218–227.

[73] E. Ramachandran, D. S. Raja, J. L. Mike, T. R. Wagner, M. Zeller, and K. Natarajan, *RSC Adv.*, 2012, **2**, 8515–8525.

[74] P. Kalaivani, R. Prabhakaran, E. Ramachandran, F. Dallemer, G. Paramaguru, R. Renganathan, P. Poornima, V. V. Padma, and K. Natarajan, *Dalton Trans.*, 2012, **41**(8), 2486.

[75] P. Kalaivani, R. Prabhakaran, P. Poornima, F. Dallemer, K. Vijayalakshmi, V. V. Padma, and K. Natarajan, *Organometallics*, 2012, **31**(23), 8323–8332.

[76] A. G. Quiroga, J. M. Prez, I. Lpez-Solera, J. R. Masaguer, A. Luque, P. Romn, A. Edwards, C. Alonso, and C. Navarro-Ranninger, *J. Med. Chem.*, 1998, **41**(9), 1399–1408.

[77] A. G. Quiroga and C. Navarro-Ranninger, *Coord. Chem. Rev.*, 2004, **248**(12), 119–133.

[78] J. a. Lessa, *J. Inorg. Biochem.*, 2011, **105**(12), 1729–1739.

[79] U. Abram, K. Ortner, R. Gust, and K. Sommer, *J. Chem. Soc. Dalton Trans.*, 2000, 735–744.

[80] G. Garcia, I. Solano, G. Sánchez, M. D. Santana, G. Lòpez, J. Casabó, E. Molins, and C. Miravitlles, *J. Organomet. Chem.*, 1994, **1**, 119–126.

[81] S. Grguric-Sipka, *J. Serb. Chem. Soc.*, 2008, **73**(6), 619–630.

[82] F. A. Beckford, G. Leblanc, J. Thessing, M. S. Jr., B. J. Frost, L. Li, and N. P. Seeram, *Dalton Trans.*, 2009, **48**, 10757–10764.

[83] F. A. Beckford, G. Leblanc, J. Thessing, M. S. Jr., B. J. Frost, L. Li, and N. P. Seeram, *Inorg. Chem. Commun.*, 2009, **12**, 1094–1098.

[84] F. Beckford, D. Dourth, M. S. Jr., J. Didion, J. Thessing, J. Woods, V. Crowell, N. Gerasimchuk, A. Gonzalez-Sarras, and N. P. Seeram, *J. Inorg. Biochem.*, 2011, **105**(8), 1019–1029.

[85] S. Grguric-Sipka, *Eur. J. Inorg. Chem.*, 2007, **18**, 2870–2878.

[86] P. W. Atkins and J. de Paula (Eds.) *Physical Chemistry*, 9 ed., W. H. Freeman and Company, New York, 2010.

[87] M. Newville, *Fundamentals of XAFS*, revision 1.7 ed., Consortium for Advanced Radiation Sources, 2004.

[88] G. Bunker, *Introduction to XAFS: A Practical Guide to X-ray Absorption Fine Structure Spectroscopy*, Cambridge University Press, 2010.

[89] S. Calvin, *XAFS for Everyone*, 1 ed., CRC Press, Florida, US, 2013.

[90] J. E. Penner-Hahn, *Encyclopedia of Life Sciences - www.els.net*, 2004, 1–4.

[91] S. E. Shadle, B. Hedman, K. O. Hodgson, and E. I. Solomon, *J. Am. Chem. Soc.*, 1995, **117**(8), 2259–2272.

[92] J. Penner-Hahn, *Coord. Chem. Rev.*, 2005, **249**, 161177.

[93] T. Sriskandakumar, H. Petzold, P. C. A. Bruijnincx, A. Habtemariam, P. J. Sadler, and P. Kennepohl, *J. Am. Chem. Soc.*, 2009, **131**(37), 13355–13361.

Chapter 2

Synthesis, Structure and NMR Spectroscopy of Thiosemicarbazone Arene Ruthenium Complexes

Thiosemicarbazones have been investigated as therapeutic agents for over 50 years. The structures of current interest contain a nitrogen heterocycle in *alpha* position to the imine bond, which is the result of historic anticancer studies which concluded that α-N-heterocyclic TSC showed stronger activities.[1, 2] NSC73306 is one current example with potential to overcome multi-drug resistance.[3, 4] Moreover, coordination to metal ions often enhances the biological activity of cytotoxic or antibacterial TSCs.[5]

Because of the promising anticancer activity of some TSCs, this work sets out to shed light on the activity of thiosemicarbazone ruthenium arene complexes against human ovarian cancer cells.

2.1 Introduction

Ruthenium arene complexes are promising candidates in the research for novel anticancer treatments. One of their intrinsic properties is their structural versatility, which can yield labile structures or rather inert ones, depending on the ligand set. Labile structures have the potential to be fine-tuned in a way that allows the controlled release of ligands inside cells. For this purpose, it is important to develop a method of tracking the ligands inside cells or other biological matrices.

This chapter presents the synthesis and characterisation of twelve thiosemicarbazones, including six structures that incorporate iodine substituents in order to use their complexes in iodine tracing experiments. Subsequently, the synthesis and characterisation of *p*-cymene ruthenium complexes of the general formula $[(\eta^6\text{-arene})\text{Ru(XY)Z}]^+\text{A}^-$ will be presented, which includes the chlorido ($\text{Z} = \text{Cl}^-$) and iodido ($\text{Z} = \text{I}^-$) analogue for each TSC ligand. Single crystal structures for two examples will be discussed.

In-depth characterisation by NMR-spectroscopic methods is an objective to elucidate as many potential reporter atoms within the structure of a ruthenium arene TSC complex as possible. Therefore, $^{1}\text{H}^{15}\text{N}$-HMBC-NMR studies will be used to characterise the ^{15}N-NMR chemical shifts for the TSCs and their corresponding complexes.

2.2 Experimental Section

2.2.1 Materials

Chemicals for the synthesis and characterisation of thiosemicarbazone ligands and arene ruthenium TSC complexes are listed in Table 2.1 below. The table lists the quality and sources of the purchased materials. Chemicals were used as received, without further purification.

Table 2.1: Materials which were used to carry out the work presented in this chapter, listing their source and the quality/purity as stated by the vendor.

Material (**Quality**)	**Source**
Chemicals:	
Benzaldehyde	Fischer Scientific
3-Iodobenzaldehyde	Apollo Scientific
4-*N,N*-Dimethylaminobenzaldehyde	Sigma Aldrich
Thiosemicarbazide (99 %)	Sigma Aldrich
4-Methyl-3-thiosemicarbazide (97 %)	Sigma Aldrich
4-Dimethyl-3-thiosemicarbazide (98 %)	Sigma Aldrich
4-Iodophenylisothiocyanate (97 %)	Sigma Aldrich
$RuCl_3 \cdot n^{a)}$ H_2O (min. 42-44 % Ru)	Precious Metals Online, PMO Pty Ltd.
Deuterated solvents:	
Chloroform-*d* ($CDCl_3$, $\geq$ 99 % D)	Cambridge Isotopes Laboratories, Inc.
DMSO-d_6 (CD_3SOCD_3)	
Methanol-d_4 (CD_3OD)	

[a)] For stoichiometric calculations, an average Ru content of 43% was assumed, equal to n = 1.5.

2.2.2 Thiosemicarbazone Synthesis

Thiosemicarbazone ligands were synthesised using adapted literature procedures.[6, 7] The basic reaction is the condensation of an aldehyde component with a free NH_2 moeity of a thiosemicarbazide (Figure 2.1).

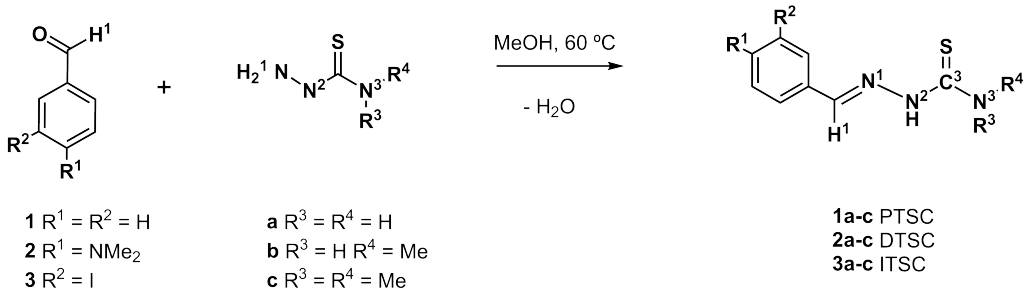

Figure 2.1: Reaction scheme of *Schiff*-base formation between aldehydes (**1-3**) and thiosemicarbazides (**a-c**) in methanol to form thiosemicarbazones **1-3a-c**.

The following section contains the experimental details and also summarises the spectroscopic data which were obtained for each ligand. To aid clarity, the TSCs are systematically referred to by their aldehyde component, combined with the respective substitution of the parent thiosemicarbazide and the suffix 'thiosemicarbazone'.

Benzaldehydethiosemicarbazones

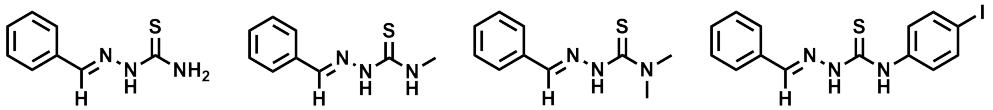

1a **1b** **1c** **1d**

Figure 2.2: TSC ligands of benzaldehyde.

(1a) Benzaldeydethiosemicarbazone

Thiosemicarbazide (0.91 g, 10 mmol) was dissolved in ethanol (10 mL) by stirring at ambient temperature for 10 min. A solution of benzaldehyde

(1.1 mL, 1.06 g, 10 mmol) in ethanol (15 mL) was added and the reaction mixture was heated to reflux and stirred for 16 h while refluxing. Cooling to room temperature yielded a white precipitate which was isolated by filtration and dried in air (551 mg, 30%). **^{1}H NMR** (400 MHz, dmso-d_6) 7.50-7.32 (m, 3H), 7.86-7.70 (m, 2H), 7.99 (s, 1H, NH), 8.05 (s, 1H, NH), 8.20 (s, 1H, N=C*H*), 11.43 (s, 1H, N-N*H*) **^{13}C NMR** (100 MHz, dmso-d_6) 127.2 (*C*H), 128.5 (*C*H), 129.7 (*C*H), 134.1 (*C*H), 142.1 (*C*=N), 177.9 (*C*=S), **ESI-MS** (MeOH) m/z (rel. int.) 360 (100) $[2M+H]^+$, 202 (30) $[M+Na]^+$, **CHN** (calc. for $C_8H_9N_3S$, FW = 179.25) 53.50 (53.61) %C, 5.07 (5.06) %H, 23.45 (23.44) %N, 17.94 (17.89) %S.

(1b) Benzaldeyde-4-methyl-3-thiosemicarbazone

Procedure as for **1a**, except solvent change to methanol for solubility reasons. Benzaldehyde was added without prior dilution. Reaction of 4-methyl-3-thiosemicarbazide (213 mg, 2 mmol) with benzaldehyde (200 μL, 2 mmol) in methanol. Yield: 339 mg (88%) white powder. **^{1}H NMR** (400 MHz, dmso-d_6) 3.02 (3H, d, J=4.6 Hz), 7.40 (2H, m), 7.80 (3H, m), 8.04 (1H, s, N=C*H*), 8.50 (1H, q, J=4.3 Hz, N*H*Me), 11.47 (1H, s, N*H*-N) **^{13}C NMR** (100 MHz, dmso-d_6) 30.9 (N*C*H$_3$), 127.2 (2 *C*H), 128.6 (2 *C*H), 129.7 (*C*H), 134.3 (C_q), 141.7 (*C*=N), 177.8 (*C*=S) **ESI-MS** (H_2O) m/z (rel. int.) 194 (10) $[M+H]^+$, 409 (10) $[2M+Na]^+$, 425 (100) $[2(M-H)+Na+H_2O]^+$ **UV/Vis** (H_2O) 307 nm (5199 L·mol^{-1}·cm^{-1}) **CHN** (calc. for $C_9H_{11}N_3S$, FW = 193.27) 55.41 (55.93) %C, 5.74 (5.74) %H, 22.08 (21.74) %N.

(1c) Benzaldeyde-4-dimethyl-3-thiosemicarbazone[8]

Procedure as for **1b**. Reaction of 4-dimethyl-3-thiosemicarbazide (238 mg, 2 mmol) with benzaldehyde (200 μL, 2 mmol) in methanol. Yield: 213 mg,

(51%) white crystalline powder. **^{1}H NMR** (400 MHz, dmso-d_6) 3.33 (s, 6H), 7.41 (m, 3H), 7.64 (m, 2H), 8.19 (s, 1H, N=C*H*), 10.94 (s, 1H, N*H*) **^{13}C NMR** (100 MHz, dmso-d_6) 42.2 (N*C*H$_3$), 126.7 (2 *C*H), 128.9 (2 *C*H), 129.6 (*C*H), 134.6 (C_q), 143.8 (*C*=N), 180.5 (*C*=S) **ESI-MS** (H_2O) m/z (rel. int.) 208 (5) $[M+H]^+$, 230 (100) $[M+Na]^+$. UV/Vis (H_2O) 302 nm (9811 L·mol^{-1}·cm^{-1}) **CHN** (calc. for $C_{10}H_{13}N_3S$, FW = 207.30) 57.62 (57.94) %C, 6.21 (6.32) %H, 20.13 (20.27) %N.

(1d) Benzaldehyde-4-(4-iodophenyl)-3-thiosemicarbazone

4-Iodo-phenylisothiocyanate (4.0 mmol, 1.04 g) was dissolved in methanol (25 mL). With stirring, hydrazine monohydrate (4 mmol, 200 μL) and benzaldehyde (4 mmol, 400 μL) were added. The mixture was heated to reflux and a white solid precipitated subsequently. The mixture was stirred under reflux for 2 hours. After cooling to room temperature, the white solid was isolated by filtration and dried in air (1.09 g, 71%). **^{1}H NMR** (400 MHz, dmso-d_6) 7.42 (d, 2H, J=2.5 Hz), 7.45 (d, 2H, J=8.6 Hz), 7.71 (d, 2H, J=8.6 Hz), 7.83-7.98 (m, 2H), 8.17 (s, 1H), 10.11 (s, 1H, N*H*), 11.91 (s, 1H, N-N*H*) dmso-d_6 (100 MHz, dmso-d_6) 89.9 (C_q), 127.7 (2*C*H$_{arom}$), 127.9 (2*C*H$_{arom}$), 128.6 (2*C*H$_{arom}$), 130.1 (*C*H$_{arom}$), 133.9 (C_q), 136.7 (2*C*H$_{arom}$), 139.0 (C_q), 143.2 (*C*=N), 175.8 (*C*=S) **ESI-MS** (MeOH) m/z (rel. int.) 404 (100) $[M+Na]^+$ **CHN** (calc. for $C_{14}H_{12}N_3ISNa$, FW = 404.23) 41.50 (41.60) %C, 2.98 (2.99) %H, 10.72 (10.40) %N.

N,N-Dimethylaminobenzaldehydethiosemicarbazones

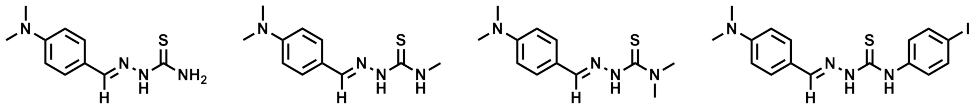

2a **2b** **2c** **2d**

Figure 2.3: TSC ligands prepared from *N,N*-dimethylaminobenzaldehyde (**2**).

(2a) *N,N*-Dimethylaminobenzaldehydethiosemicarbazone[9, 10]

Procedure as for **1b**. Thiosemicarbazide (467 mg, 5 mmol) was reacted with 4-*N,N*-dimethlaminobenzaldehyde (748 mg, 5 mmol) in methanol. Yield: 740 mg, 67%. ^{1}**H NMR** (400 MHz, dmso-d_6) 2.94 (s, 6H, NMe_2), 6.69 (d, 2H, J = 9.3 Hz CH_{arom}), 7.58 (d, 2H, J = 8.7 Hz, CH_{arom}), 7.77 (s, 1H, NH_2), 7.93 (s, 1H, N=CH), 8.01 (s, 1H, NH_2), 11.19 (s, 1H, NH) ^{13}**C NMR** (100 MHz, dmso-d_6) 39.9 (NCH_3), 111.7 (CH_{arom}), 121.5 (C_q), 128.7 (CH_{arom}), 141.4 (C_q), 143.4 (C=N), 177.1 (C=S) **ESI-MS** (MeOH) m/z (rel. int.) 507 (90) $[(2M+Na)+OH^-]^+$, 245 (95) $[M+Na]^+$, 223 (100) $[M+H]^+$ **CHN** (calc. for $C_{10}H_{14}N_4S$, FW = 222.31) 53.93 (54.03) %C, 6.27 (6.35) %H, 25.23 (25.20) %N, 14.41 (14.42) %S.

(2b) *N,N*-Dimethylaminobenzaldehyde-4-methyl-3-thiosemicarbazone[11]

Procedure as for **1b**. 4-Methyl-3-thiosemicarbazide (210 mg, 2 mmol) was reacted with 4-(*N,N*-dimethylaminobenzaldehyde (298 mg, 2 mmol) in methanol. Yield: 100 mg, 21 %. Suitable single-crystals of DTSC*NMe* **2b** for structure determination by X-ray diffraction grew by slow evaporation of solvent from a saturated solution of the ligand in dmso-d_6. ^{1}**H NMR** (400 MHz, dmso-d_6) 2.96 (s, 6H, NMe_2), 3.00 (d, 3H, J=4.6 Hz, $NHCH_3$), 6.71 (d, 2H, J=9.3 Hz), 7.58 (d, 2H, J=8.7 Hz), 7.92 (s, 1H, N=CH),

8.28 (q, 1H, J=4.4 Hz, NHMe), 11.19 (s, 1H, NH-N) ^{13}**C NMR** (100 MHz, dmso-d_6) 30.7 (NHCH$_3$), 39.8 (NMe$_2$), 111.7 (2 CH), 121.5 (C_q), 128.5 (2 CH), 142.8 (C=N), 151.3 (C_qN), 177.1 (C=S) **ESI-MS** (H$_2$O) m/z (rel int.) 235 (70) [M-H]$^+$, 259 (100) [M+Na]$^+$ **CHN** (calc. for C$_{11}$H$_{16}$N$_4$S, FW = 236.64) 55.58 (55.90) %C, 6.77 (6.82) %H, 23.29 (23.71) %N.

(2c) *N,N*-Dimethylaminobenzaldehyde-4-dimethyl-3-thiosemicarbazone

Procedure as for **1b**. 4-Dimethyl-3-thiosemicarbazide (240 mg, 2 mmol) reacted with 4-*N,N*-dimethylaminobenzaldehyde (298 mg, 2 mmol) in methanol. Yield: 73 mg, 14%. ^{1}**H NMR** (dmso-d_6) 2.95 (s, 6H, NMe$_2$), 3.26 (s, 6H, NMe$_2$), 6.74 (d, 2H, J=8.8 Hz), 7.45 (d, 2H, J=8.9 Hz), 8.03 (s, 1H, NCH), 10.65 (s, 1H, NNH) ^{13}**C NMR** (dmso-d_6) 39.8 (NCH$_3$), 42.1 (NCH$_3$), 111.9 (2CH$_{arom}$), 122.0 (C_q), 128.0 (2CH$_{arom}$), 144.9 (C=N), 151.3 (C_q), 170.5 (C=S) **ESI-MS** (H$_2$O) m/z (rel. int.) 249 (20) [M-H]$^+$, 273 (100) [M+Na]$^+$ **UV/Vis** (H$_2$O) 352 nm (20693 L·mol^{-1}·cm^{-1}) **CHN** (calc. for C$_{12}$H$_{18}$N$_4$S·H$_2$O, FW = 268.38) 53.75 (53.70) %C, 7.47 (7.51) %H, 20.36 (20.88) %N.

(2d) *N,N*-Dimethylaminobenzaldehyde-4-(4-iodophenyl)-3-thiosemicarbazone

Procedure as for **1d**. 4-Iodophenyl-isothiocyanate (840 mg, 3.1 mmol) reacted with 4-*N,N*-dimethylaminobenzaldehyde (465 mg, 3.1 mmol) and hydrazine monohydrate (200 μL, 4 mmol). Yield: 1.13 g, 76%. ^{1}**H NMR** (300 MHz, dmso-d_6) 2.97 (s, 6H, NMe$_2$), 6.72 (d, 2H, J=9.2 Hz), 7.47 (d, 2H, J=13.9 Hz), 7.47 (d, 2H, J=4.7 Hz), 7.47 (d, 2H, J=8.7 Hz), 7.70 (d, 2H, J=1.5 Hz), 8.04 (s, 1H, N=CH), 9.94 (s, 1H, NH), 11.67 (s, 1H, NH)

^{1}H NMR (400 MHz, $CDCl_3$) 3.05 (s, 6H, NMe_2), 6.88 (d, 2H, J=7.2 Hz), 7.46 (d, 2H, J=8.6 Hz), 7.58 (d, 2H, J=8.9 Hz), 7.68 (d, 2H, J=8.4 Hz), 7.77 (s, 1H, N=CH), 9.13 (s, 1H, NH), 9.47 (s, 1H, NH) **^{13}C NMR** (75 MHz, dmso-d_6) 174.8 (C=S), 151.6 (C_q), 144.3 (C=N), 139.1 (C_q), 136.9 (2CH$_{arom}$), 129.3 (2CH$_{arom}$), 127.6 (2CH$_{arom}$), 121.0 (C_q), 111.6 (2CH$_{arom}$), 89.6 (C_q), 30.4 (NCH$_3$) **ESI-MS** (MeOH/H_2O) m/z (rel. int.) 447 (100) [M+Na]$^+$ **CHN** (calc. for $C_{16}H_{17}IN_4S$, FW = 424.30) 45.22 (45.29)%C, 3.95 (4.04)%H, 13.13 (13.20)%N.

3-Iodobenzaldehydethiosemicarbazones

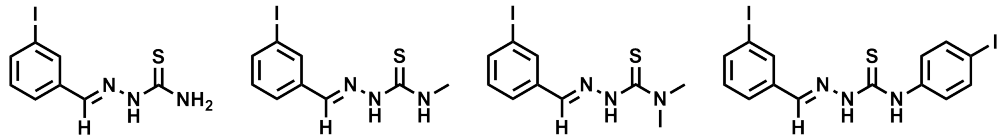

3a **3b** **3c** **3d**

Figure 2.4: TSC ligands of 3-iodobenzaldehyde (**3**).

(3a) 3-Iodobenzaldehydethiosemicarbazone

Procedure as for **1b**. 3-Iodobenzaldehyde (5 mmol, 1.17 g) was reacted with thiosemicarbazide (5 mmol, 459 mg) in methanol. Yield: 1.15 g, 77%. **^{1}H NMR** (400 MHz, dmso-d_6) 7.18 (t, 1H, J=7.8 Hz), 7.71 (t, 2H, J=7.0 Hz), 7.96 (s, 1H), 8.16 (s, 1H), 8.23 (s, 1H), 8.29 (s, 1H), 1.47 (s, 1H, NH) **^{13}C NMR** (100 MHz, dmso-d_6) 178.2 (C=S), 140.6 (C=N), 138.2 (CH), 136.5 (C_q), 138.8 (CH), 130.8, 127.3, 95.5 (C_q) **ESI-MS** (MeOH) m/z (rel. int.) 328 (100) [M+Na]$^+$ **CHN** (calc. for $C_8H_8IN_3S$, FW = 305.14) 31.44 (31.49) %C, 2.57 (2.64) %H, 13.77 (13.77) %N, 10.40 (10.51) %S.

(3b) 3-Iodobenzaldehyde-4-methyl-3-thiosemicarbazone

Procedure as for **1b**. Reaction of 4-methyl-3-thiosemicarbazide (210 mg, 2 mmol) with 3-iodobenzaldehyde (467 mg, 2 mmol). Yield: 573 mg, 90%. ^{1}**H NMR** (dmso-d_6) 3.02 (d, 3H, J=4.5 Hz), 7.20 (t, 1H, J=7.8 Hz), 7.72 (dt, 2H, J=12.40, 7.7 Hz), 7.96 (s, 1H, N=CH), 8.26 (d, 1H, J=3.0 Hz), 8.60 (q, 1H, J=4.5 Hz, NHMe), 11.53 (s, 1H, NH-N) ^{13}**C NMR** (dmso-d_6) 30.9 (NCH_3), 95.4 (C_q), 127.2 (CH), 130.7 (CH), 134.6 (CH), 136.6 (C_q), 138.1 (CH), 140.1 (C=N), 177.8 (C=S) **CHN** (calc. for $C_9H_{10}IN_3S$, FW = 319.17): 33.85 (33.87) %C, 3.07 (3.16) %H, 13.33 (13.17) %N.

(3c) 3-Iodobenzaldehyde-4-dimethyl-3-thiosemicarbazone

Procedure as for **1b**. 4-Dimethyl-3-thiosemicarbazide (240 mg, 2 mmol) was reacted with 3-iodobenzaldehyde (464 mg, 2 mmol) in methanol. Yield: 532 mg, 80%. ^{1}**H NMR** (dmso-d_6) 3.28 (s, 6H, NMe_2), 7.22 (t, 1H, J=7.8 Hz), 7.64 (dt, 1H, J=7.8, 1.1 Hz), 7.74 (dt, 1H, J=7.88, 1.4 Hz), 8.00 (t, 1H, J=1.6 Hz), 8.12 (s, 1H, N=CH), 11.01 (s, 1H, NH). ^{13}**C NMR** (dmso-d_6) 42.1 (CH_3), 95.3 (C_q), 126.4 (CH), 131.0 (CH), 134.6 (CH), 137.0 (C_q), 138.0 (CH), 142.2 (C=N), 180.5 (C=S) **ESI-MS**-pos (H_2O) m/z (rel. int.) 356 (100) $[M+Na]^+$ **ESI-MS**-neg (H_2O) m/z (rel. int.) 332 (100) $[M-H]^-$ **CHN** (calc. for $C_{10}H_{12}N_3ISNa$ (356.19)) 34.08 (33.72) %C, 3.55 (3.40) %H, 12.08 (11.80) %N.

(3d) 3-Iodobenzaldehyde-4-(4-iodophenyl)-3-thiosemi-carbazone

Procedure as for **1d**. Reaction of 4-iodophenylisothiocyanate (840 mg, 3.1 mmol), 3-iodobenzaldehyde (718 mg, 3.1 mmol), and hydrazine monohydrate (200 μL, 4 mmol) in methanol. Yield: 1.41 g, 89 %. ^{1}**H NMR** (300 MHz, dmso-d_6 7.22 (1H), 7.39 (2H), 7.71 (2H), 7.82 (1H) 8.08 (1H),

8.35 (1H), 10.20 (1H, NH), 11.95 (1H, NH) **^{13}C NMR** (75 MHz, dmso-d_6) 176.2 (C=S), 141.7 (N=CH), 139.0 (C_q), 138.6 (CH), 136.9 (2CH arom.), 136.3 (C_q), 135.1 (CH), 130.7 (CH), 128.5 (CH), 127.6 (CH), 95.4 (C_q), 90.3 (C_q) **ESI-MS** m/z (rel. int.) 530 (100) $[M+Na]^+$, 508 (20) $[M+H]^+$ **CHN** (calc. for $C_{14}H_{11}I_2N_3S$) 32.92 (33.16) %C, 2.13 (2.19) %H, 8.56 (8.29)% N.

2.2.3 Synthesis of Ruthenium Complexes

Arene Ruthenium Starting Materials

Ethanol used during the preparation of *p*-cymene-ruthenium starting materials was freshly distilled over Mg prior to the synthesis.

For the preparation of ruthenium TSC complexes, $[(p\text{-cymene})RuCl_2]_2$ ([**4**]) and $[(p\text{-cymene})RuI_2]_2$ ([**5**]) were used as precursors, which were synthesised according to literature procedures.[12, 13] The reaction of α-phellandrene (Figure 2.5) with ruthenium(III) chloride ($RuCl_3 \cdot 1.5\ H_2O$) yields the ruthenium chlorido dimer [**4**].

Reacting [**4**] with excess KI (Figure 2.6) substitutes all four chlorido ligands in the molecular structure with iodide, resulting in the iodido dimer [**5**]. The purity of the two precursor compounds was assessed by comparison of their individual ^{1}H NMR spectra with reported values.

[**4**] **$[(p\text{-cymene})RuCl_2]_2$** A 1L three-necked round-bottom flask was equipped with a reflux condenser and evacuated four times prior to addition of $RuCl_3 \cdot 1.5\ H_2O$ (5.27 g, 22.5 mmol Ru). Freshly distilled ethanol was added (350 mL) to give a dark brown solution. With stirring, α-phellandrene (34 mL, 29 g, 209 mmol, 9.5 mol. eq.) were added to the mixture which was stirred un-

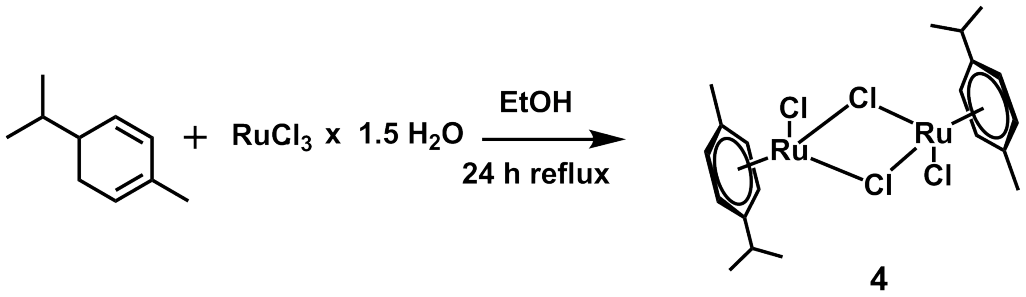

Figure 2.5: Synthesis of [(*p*-cymene)$RuCl_2$]$_2$

der reflux for 36 h. A black solid was separated from the hot, dark red solution by suction filtration while hot, washed with hot ethanol (15 mL) and the filtrate was left to cool overnight. Bright red crystals precipitated from the solution. These were isolated by filtration and dried in air (3.1 g, 50 %).^{1}**H NMR** (300 MHz, $CDCl_3$) 1.25 (*d*, *J*=6.8 Hz, 6H), 2.13 (s, 3H), 2.9 (m, 1H), 5.31 (d, *J*=5.8 Hz, 2H), 5.44 (d, *J*=5.8 Hz, 2H).

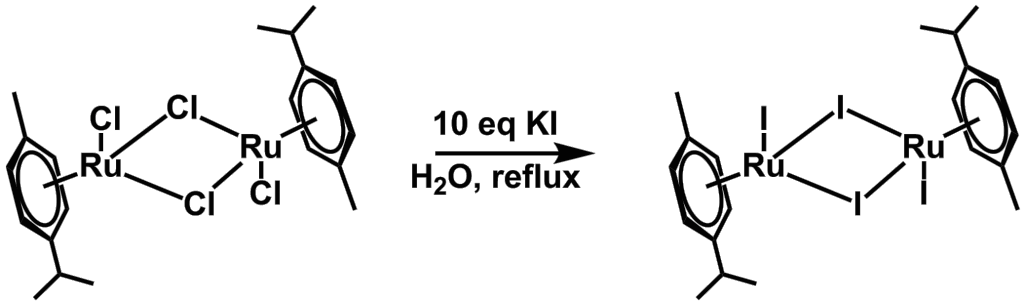

Figure 2.6: Synthesis of [(*p*-cymene)RuI_2]$_2$

[5] **[(*p*-cymene)RuI_2]$_2$** ([**4**], 1.22 g, 2 mmol) was suspended in water (250 mL) and heated to reflux. The red solution was stirred for one hour and then filtered while hot. To the filtrate, a solution of potassium iodide (4.0 g, 24 mmol) in water (15 mL) was added drop wise. The colour of the reaction mixture changed immediately from orange to purple as a solid

precipitated with further addition of KI. After cooling to room temperature, the dark purple suspension was filtered, the purple solid was washed with cold water (30 mL) and subsequently dried with suction and in vacuum (1.8 g, 100 %). **^{1}H NMR** (400 MHz, $CDCl_3$) 1.23 (d, J=6.9 Hz, 6H), 3.00 (m, J=7.4 Hz, 1H), 5.41 (d, J=5.4 Hz, 2H), 5.51 (d, J=5.9 Hz, 2H).

Arene Ruthenium TSC Complexes

This section summarises the experimental details for the synthesis of arene Ru(II) complexes, using the TSCs prepared above as chelating ligands. The complexes were synthesised by an adapted literature method.[14–16] Figure 2.7 presents the reaction scheme. Briefly, the precursors [(*p*-cymene)$RuCl_2$]$_2$ or

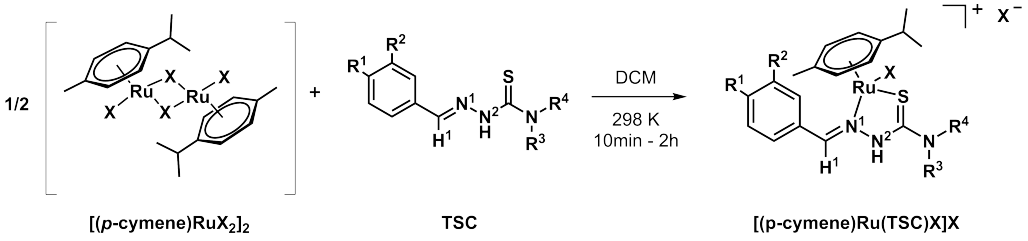

Figure 2.7: Reaction scheme showing the synthesis of arene Ru^{II} TSC complexes.

[(*p*-cymene)RuI_2]$_2$ were reacted with 2 mol equivalents of a thiosemicarbazone in dichloromethane at room temperature. After a reaction period of 30 min - 18 h (detailed for individual complexes below), the mixtures were added to a ten-fold excess volume of diethyl ether, in which the products precipitated as yellow to red solids. This procedure yields complexes of the general formula [(*p*-cymene)Ru(TSC)X]X (Figure 2.7).

[7] [(*p*-cymene)Ru(1a)I]I [(*p*-cymene)$RuCl_2$]$_2$ (194 mg, 0.20 mmol) and benzaldehydethiosemicarbazone (**1a**, 82 mg, 0.46 mmol) were mixed in dichloromethane (10 mL). The dark red mixture was stirred at room temperature for 16 h. The solution was reduced in volume to 4 mL and subsequently poured into diethylether (40 mL). A red solid precipitated which was separated by filtration. The red filtrate was evaporated to dryness, the residue taken up in dichloromethane (2 mL) and immediately poured into diethylether (50 mL). The orange precipitate was isolated by filtration and the combined solids were dried under vacuum (127 mg, 48%). **ESI-MS** (MeOH) m/z (rel. int.) = 414 (100) [M-I-HI]+ **CHN** (calc. for $C_{18}H_{23}N_3SRuI_2$, FW = 668.34) 33.28 (32.35) %C, 3.59 (3.47) %H, 7.06 (6.29) %N.

[10] [(*p*-cymene)Ru(1c)Cl]PF_6 [(*p*-cymene)$RuCl_2$]$_2$ (82 mg, 0.14 mmol) and benzaldehyde-4-dimethyl-3-thiosemicarbazone (**1c**, 57 mg, 0.28 mmol) were mixed in dichloromethane (8 mL) and the resulting red solution stirred for 14 h. A solution of NH_4PF_6 (218 mg, 1.35 mmol) in methanol (10 mL) was added and the red solution was stirred for 2 h and then kept at 278 K for several days. Orange block shaped crystals, suitable for X-ray diffraction, were isolated by filtration, washed with methanol and dried in air (70 mg, 40 %). ^{1}**H NMR** (400 MHz, $CDCl_3$) 1.13 (3H, d, J=6.6 Hz), 1.17 (3H, d, J=6.9 Hz), 2.06 (3H, s), 2.71 (1H, m, J=6.9 Hz), 4.76 (1H, d, J=5.7 Hz), 4.80 (1H, d, J=6.0 Hz), 5.03 (1H, d, J=5.7 Hz), 5.34 (1H, d, J=6.0 Hz), 7.58 (3H, m), 8.30 (2H, d, J=5.9 Hz), 9.13 (1H, s, N=CH), 10.89 (1H, s, NH). ^{13}**C NMR** (100 MHz, $CDCl_3$) 18.6 (CH_3), 21.5 (CH_3), 23.3 (CH_3), 30.7

(CH), 43.0 (NMe_2), 82.8 (CH), 83.3 (CH), 88.5 (CH), 88.7 (CH), 129.2 (CH), 131.0 (CH) 165.9 (N=CH) **ESI-MS** (MeOH) m/z (rel. int.) 442 (100) [M-PF_6-HCl]$^+$ **CHN** (calc. for $C_{20}H_{27}N_3SRuClPF_6$): 38.44 (38.56) %C, 4.36 (4.37) %H, 6.69 (6.74) %N.

[11] [(*p*-cymene)Ru(1c)I]I [(*p*-cymene)RuI_2]2 (55 mg, 0.06 mmol) and benzaldehyde-4-dimethyl-3-thiosemicarbazone (**1c**, 23.5 mg, 0.11 mmol) were mixed in dichloromethane (2.5 mL). The red solution was stirred for 10 min before it was poured into diethylether (25 mL) to precipitate a red solid. The resulting suspension was stirred for 30 min before filtering and isolating the red solid and drying under vacuum (66 mg, 83 %). ^{1}**H NMR** (400 MHz, $CDCl_3$) 1.14 (3H, d, J=6.9 Hz), 1.19 (3H, d, J=7.3 Hz), 1.54 (H_2O), 2.29 (3H, s), 2.88 (1H, m), 4.65 (1H, d, J=6.5 Hz), 4.70 (1H, d, J=6.9 Hz), 4.99 (1H, d, J=5.6 Hz), 5.34 (1H, d, J=5.6 Hz), 7.57 (3H, m), 8.33 (2H, m), 9.83 (1H, s), 12.22 (1H, s, NH). ^{13}**C NMR** (100 MHz, $CDCl_3$) 20.5 (CH_3), 21.5 (CH_3), 31.2 (NMe_2), 82.9 (CH), 83.5 (CH), 87.6 (CH), 88.9 (CH), 103.6 (C_q), 106.7 (C_q), 128.6 (CH), 130.6 (CH), 131.6 (CH), 133.1 (CH), 167.0 (C=N), 175.6 (C=S). **ESI-MS** (MeOH) m/z (rel. int.) 442.50 (100) [M-I-HI]$^+$, **CHN** (calc. for $C_{20}H_{27}N_3SRuI_2$): 34.39 (34.49) %C, 3.84 (3.91) %H, 5.91 (6.03) %N.

[12] [(*p*-cymene)Ru(1c)I]PF_6 [(*p*-cymene)RuI_2]$_2$ (70 mg, 0.075 mmol) and benzaldehyde-4-dimethyl-3-thiosemicarbazone (**1c**) (31 mg, 0.15 mmol) were mixed in dichloromethane (8 mL) and the resulting clear red solution was stirred for 60 min before a solution of NH_4PF_6 (130 mg, 0.67 mmol)

in methanol (5 mL) was added. The red solution was kept at 278 K for 5 days. Dark red crystals were isolated by filtration, washed with methanol and diethylether and dried with suction (81 mg, 76 %). **^{1}H NMR** (400 MHz, $CDCl_3$) 1.12 (3H, d, J=7.0 Hz), 1.18 (3H, d, J=7.0 Hz), 2.30 (3H, s), 2.85 (1H, m), 4.66 (1H, d, J=6.0 Hz), 4.70 (1H, d, J=6.0 Hz), 4.96 (1H, d, J=6.6 Hz), 5.30 (1H, d, J=6.2 Hz), 7.62 (3H, m), 8.28 (2H, m), 8.86 (1H, s), 9.90 (1H, s) **^{13}C NMR** (100 MHz, $CDCl_3$) 19.1 (CH_3), 19.7 (CH_3), 22.0 (CH_3), 41.1 (NMe_2), 82.0 (CH), 83.4 (CH), 87.6 (CH), 90.0 (CH), 128.7 (2 CH), 129.8 (2CH), 131.1 (CH), 163.5 (HC=N), 175.8 (C=S) **ESI-MS** (MeOH) m/z (rel. int.) 442.50 (100) $[M\text{-}PF_6\text{-}HI]^+$, **CHN** found (calc. for $C_{20}H_{27}N_3SRuIPF_6CH_3OH$) 33.69 (33.79) %C, 4.18 (4.19) %H, 5.60 (5.63) %N.

[13] [(*p*-cymene)Ru(1d)Cl]Cl [(*p*-cymene)$RuCl_2$]$_2$ (53 mg, 0.09 mmol) and benzaldehyde-4-(4-iodophenyl)-3-thiosemicarbazone (**1d**, 63 mg, 0.17 mmol) were placed in a Schlenk tube and dissolved in dichloromethane (10 mL). The red mixture was stirred at room temperature for 18 hours. A yellow solid precipitated which was isolated from a red solution by suction filtration and dried in air (75 mg, 63 %). **^{1}H NMR** (400 MHz, methanol-d_4) 1.10 (3H, d, J=6.9 Hz), 1.16 (3H, d, J=6.5 Hz), 2.06 (3H, s), 2.61 (1H, m, J=6.9 Hz), 4.80 (1H, d, J=5.8 Hz), 5.00 (1H, d, J=6.3 Hz), 5.05 (1H, d, J=6.8 Hz), 5.63 (1H, d, J=6.0 Hz), 7.29 (2H, d, J=8.3 Hz), 7.67 (3H, d, J=5.0 Hz), 7.73 (2H, d, J=8.9 Hz), 8.25 (2H, q, J=3.0 Hz), 9.00 (1H, s) ^{13}C NMR (100 MHz, MeOD) **ESI-MS** (MeOH) m/z (rel. Int.) = 615.9 (100) $[M\text{-}Cl\text{-}HCl]^+$ IR (solid) 697, 766 (C=S), 1004, 1103, 1480, 1544, 1576 (C=N), 2959 **CHN** (calc. for $C_{24}H_{26}N_3SIRuCl_2CH_2Cl_2$ (772.37)): 38.96

(38.88) %C, 3.47 (3.65) %H, 5.80 (5.44) %N.

[14] [(*p*-cymene)Ru(1d)I]I [(*p*-cymene)RuI_2]$_2$ (192 mg, 0.19 mmol) and benzaldehyde-4-(4-iodophenyl)-3-thiosemicarbazone (**3d**, 167 mg, 2.3 eq, 0.44 mmol) were mixed in dichloromethane (10 mL). The deep violet-red mixture was stirred at room temperature over night. Leftover solid particles were separated by filtration and the dark red filtrate poured into diethyl-ether (50 mL). A red precipitate was isolated with suction filtration and dried under vacuum (143 mg, 42%). **^{1}H NMR** ($CDCl_3$) 1.10 (3H, d, J=6.9 Hz), 1.17 (3H, d, J=6.9 Hz), 1.29 (1H, d, J=7.3 Hz), 2.35 (3H, s), 2.78 (1H, m, J=6.9 Hz), 4.57 (1H, d, J=5.9 Hz), 4.73 (1H, d, J=5.9 Hz), 4.86 (1H, d, J=5.6 Hz), 5.31 (1H, d, J=5.9 Hz), 7.36 (2H, d, J=8.4 Hz), 7.62 (3H, d, J=2.8 Hz), 7.71 (2H, d, J=8.7 Hz), 8.15 (2H, d, J=3.1 Hz), 8.17 (1H, d, J=2.1 Hz), 9.05 (1H, s), 10.36 (1H, s), 13.86 (1H, s) ^{13}C-NMR (100 MHz, $CDCl_3$) 175.2 (C=S), 161.2 (C=N), 138.5, 138.2, 136.1 (C_q), 132.8 (C_q), 130.5 (CH), 129.0 (CH), 128.1 (CH), 127.6 (CH), 125.8 (CH), 107.5 (C_q), 104.2 (C_q), 89.4 (CH), 86.9 (CH), 84.2 (CH), 83.0 (CH), 82.4 (CH), 31.4 (CH_3), 23.5 (CH_3), 21.3 (CH_3), 20.7 (CH_3) **ESI-MS** (MeOH) m/z (rel. int.) = 616 (100) [M-H-HCl]$^+$ **CHN** (calc. for $C_{24}H_{26}N_3SRuI_3$, (870.34) 33.83 (33.12) %C, 2.93 (3.01) %H, 4.75 (4.83) %N.

[15] [(*p*-cymene)Ru(2a)Cl]Cl [(*p*-cymene)$RuCl_2$]$_2$ (62 mg, 0.1 mmol) and *N,N*-dimethylamino-benzaldehydethiosemicarbazone (**2a**, 50 mg, 0.22 mmol) were mixed with dichloromethane (5 mL). The red mixture was stirred at room temperature for 20 hours, filtered through a syringe filter

and evaporated to dryness (123 mg, 58%). ^{1}**H NMR** (400 MHz, $CDCl_3$) 1.12 (d, J=6.9 Hz, 3H, cym-iPr), 1.19 (d, 3J=6.9 Hz, 3H, cym-iPr), 2.14 (s, 3H cym-iPr), 2.67 (sept, 1H, cym-iPr), 3.12 (s, 6H, NMe), 5.03 (d, J=6.1 Hz, 1H, cym-CH), 5.08 (d, J=6.1 Hz, 1H, cym-CH), 5.14 (d, J=6.1 Hz, 1H, cym-CH), 5.53 (d, J=6.1 Hz, 1H, cym-CH), 6.77 (d, J=9.1 Hz, 2H, arom. CH), 8.18 (d, J=9.1 Hz, 2H, arom. CH), 8.76 (s, 1H, N=CH) $_{13}$**C NMR** (100 MHz, CDCl3): 31.1 (cym-iPrCH), 40.4 (NCH3), 82.6 (cym-CH), 83.7 (cym CH), 88.0 (cym CH), 88.8 (cym CH), 111.6 (Ph CH), 133.9 (Ph CH), 162.6 (N=CH) **ESI-MS** (MeOH) m/z = 457 $[M\text{-}Cl\text{-}HCl]^+$ **UV-vis** (MeOH/H_2O = 10/90 v/v) λ_{max} = 362 nm **CHN** (calc. for $C_{20}H_{28}N_4SRuCl_2$, FW = 528.51) 45.11 (45.45) %C, 5.37 (5.34) %H, 11.53 (10.60) %N.

[19] [(*p*-cymene)Ru(2c)Cl]PF_6 [(*p*-cymene)$RuCl_2$]$_2$ (21 mg, 0.04 mmol) and *N,N*-dimethylaminobenzaldehyde-4-dimethyl-3-thiosemicarbazone (**2c**, 17 mg, 0.08 mmol) were mixed in dichloromethane (4 mL) and the clear, red solution was stirred at room temperature for 1 h before NH_4PF_6 (55 mg in 5 mL methanol) was added. The red solution was stored at 278 K for two days. Red crystals were isolated by filtration and dried in air (26 mg, 0.04 mmol, 57 %). ^{1}**H NMR** (600 MHz, dmso-d_6) 0.91 (3H, d, J=7.1 Hz), 0.97 (3H, d, J=7.0 Hz), 2.39 (3H, s) 3.07 (6H, s), 5.95 (1H, d, J=6.7 Hz), 6.12 (1H, d, J=6.2 Hz), 6.25 (1H, d, J=6.4 Hz), 6.32 (1H, d, J=6.4 Hz), 6.71 (2H, d, J=9.3 Hz), 8.04 (2H, d, J=9.1 Hz), 8.17 (1H, s). **ESI-MS** (MeOH) m/z (rel. int.) = 485 $[M\text{-}PF_6\text{-}HCl]^+$ (100) **CHN** (calc. for $C_{22}H_{32}N_4SRuClPF_6$, FW = 666.07) 40.07 (39.67) %C, 4.69 (4.84) %H, 8.68 (8.41) %N.

[20] [(*p*-cymene)Ru(2c)I]I [(*p*-cymene)RuI_2]$_2$ (15.0 mg, 0.015 mmol) and *N,N*-dimethylaminobenzaldehyde-4-dimethyl-3-thiosemicarbazone (**2c**, 7.9 mg, 2.1 eq, 0.032 mmol) were placed in a small glass vial. The solids were mixed in chloroform-*d* (0.6 mL, final concentration ca. 50 mM). The red solution was transferred into a 5mm NMR tube and a proton spectrum was recorded approx. 2 hours after mixing the reactants. **^{1}H NMR** (400 MHz, $CDCl_3$) 1.14 (3H, d, *J*=6.9 Hz), 1.21 (3H, d, *J*=7.1 Hz) 2.26 (3H, s), 2.94 (1H, m7, *J*=7.1 Hz), 3.09 (6H, s), 3.46 (6H, s, br), 4.96 (1H, d, *J*=6.2 Hz), 5.17 (2H, s), 5.61 (1H, d, *J*=6.0 Hz), 6.73 (2H, d, *J*=9.0 Hz), 8.37 (2H, d, *J*=8.6 Hz), 9.61 (1H, s), 11.45 (1H, s, br) **^{13}C NMR** (100 MHz, $CDCl_3$) 19.9 (CH3, p-cym-Me), 21.2 (CH3, p-cym-iPr), 23.9 (CH3, p-cym-iPr), 31.1 (CH, p-cym-iPr), 40.0 (Ph-NMe2), 43.9 (SCNMe2), 83.8 (p-cym-CH), 85.3 (p-cym-CH), 87.6 (p-cym-CH), 88.3 (p-cym-CH), 102.7 (Cq, p-cym-Me), 105.2 (Cq, p-cym-iPr), 110.5 (Ph-CH), 117.1 (Cq, Ph-CN), 134.0 (Ph-CH), 152.6 (Cq, Ph-NMe2), 167.0 (N=CH) **ESI-MS** (MeOH) m/z (rel. int.) = 485 (100) $[M\text{-}I\text{-}HI]^+$.

[21] [(*p*-cymene)Ru(2d)Cl]Cl [(*p*-cymene)$RuCl_2$]$_2$ (64 mg, 0.1 mmol) and *N,N*-dimethylaminobenzaldehyde-4-(4-iodophenyl)-3-thiosemicarbazone (**2d**, 91 mg, 0.21 mmol) were placed in a Schlenk-tube and mixed with 10 mL dichloromethane. The clear red solution was stirred at room temperature for 19 hours. The solution was reduced to 2 mL and subsequently poured into diethylether (40 mL). A red solid precipitated which was stirred in the suspension for 15 min before suction filtration. It was washed with diethylether and dried with suction to yield a red powder (131 mg, 86 %). **^{1}H NMR**

(400 MHz, $CDCl_3$) 1.12 (3H, d, J=6.9 Hz), 1.17 (3H, d, J=7.0 Hz), 2.12 (3H, s), 2.67 (1H, m7, J=6.8 Hz), 3.11 (6H, s), 4.99 (1H, d, J=5.7 Hz), 5.11 (2H, dd, J=13.96, 5.7 Hz), 5.49 (1H, d, J=5.9 Hz), 6.77 (2H, d, J=9.0 Hz), 7.35 (2H, d, J=8.8 Hz), 7.67 (2H, d, J=8.7 Hz), 8.19 (2H, d, J=9.0 Hz) **ESI-MS** (MeOH) m/z (rel. int.) = 659 (100) $[M\text{-}Cl\text{-}HCl]^+$ **CHN** (calc. for $C_{26}H_{31}N_4SIRuCl_2$ FW = 730.50): 42.59 (42.75) %C, 4.23 (4.28) %H, 7.61 (7.67) %N.

[22] [(*p*-cymene)Ru(2d)I]I [(*p*-cymene)$RuI_2]_2$ (185 mg) and *N,N*-dimethyl-aminobenzaldehyde-4-(4-iodophenyl)-3-thiosemicarbazone (**2d**, 160 mg) were mixed in 10 mL anhydrous dichloromethane and stirred at room temperature for 3 hours. The volume was reduced to 3 ml and the solution was poured into 50 mL diethylether. A solid precipitated which was filtered and dried under vacuum. **^{1}H NMR** ($CDCl_3$) 1.12 (3H, d, J=7.0 Hz), 1.19 (3H, d, J=7.0 Hz), 2.34 (3H, s), 2.82 (1H, m, J=7.0 Hz), 3.12 (6H, s), 4.93 (1H, d, J=6.1 Hz), 5.05 (1H, d, J=6.0 Hz), 5.16 (1H, d, J=5.8 Hz), 5.53 (1H, d, J=5.8 Hz), 6.78 (2H, d, J=9.2 Hz), 7.37 (2H, d, J=8.6 Hz), 7.68 (2H, d, J=8.8 Hz), 8.20 (2H, d, J=9.2 Hz), 8.73 (1H, s), 10.30 (1H, s), 13.44 (1H, s). **ESI-MS** (MeOH) m/z (rel. int.) = 659 (100) $[M\text{-}I\text{-}HI]^+$, **CHN** (calc. for $C_{26}H_{31}N_4SRuI_3$, FW = 913.41): 33.85 (34.19) %C, 3.33 (3.42) %H, 6.00 (6.13)%N.

[23] [(*p*-cymene)Ru(3a)Cl]Cl [(*p*-cymene)$RuCl_2]_2$ (54 mg, 0.09 mmol) and 3-iodobenzaldehyde-3-thiosemicarbazone (**3a**, 50 mg, 0.16 mmol) were stirred in dichloromethane (10 mL) for 16 h. After 4 h a yellow precipitate

had formed. It was filtered off with suction and washed with small amounts of petroleum ether and dried in air. (69 mg, 71 %) **1H-NMR** (400 MHz, methanol-d_4) 1.17 (6H, dd, J=7.2, 24.5 Hz), 2.13 (3.0H, s), 2.65 (1H, m7, J=6.8 Hz), 4.95 (1H, d, J=6.6 Hz), 5.05 (1H, d, J=5.8 Hz), 5.10 (1H, d, J=6.6 Hz), 5.69 (1H, d, J=5.8 Hz), 7.44 (1H, t, J=7.8 Hz), 8.05 (2H, dd, J=1.6, 7.8 Hz), 8.79 (1H, s), 8.90 (1H, s) **ESI-MS** (MeOH) m/z (rel. int.) = 540 (100) $[M\text{-}Cl\text{-}HCl]^+$ **CHN** (calc. for $C_{18}H_{22}N_3SIRuCl_2$, FW = 611.34) 34.87 (35.36) %C, 3.53 (3.63) %H, 6.48 (6.87) %N.

[24] [(*p*-cymene)Ru(3a)I]I [(*p*-cymene)$RuI_2]_2$ (203 mg, 0.21 mmol) and 3-iodobenzaldehyde-3-thiosemicarbazone (**3a**, 115 mg, 2.5 eq, 0.52 mmol) were mixed in dichloromethane (10 mL). The violet-red mixture was stirred at room temperature for 16 h. The resulting dark solution was reduced in volume to 3 mL and subsequently poured into diethylether (75 mL). A red-orange precipitate was separated by filtration and dried under vacuum (130 mg, 41 %). **ESI-MS** (MeOH) (rel. int.) m/z = 668 (5) [M-I]+, 540 (100) $[M\text{-}I\text{-}HI]^+$ **CHN** (calc. for $C_{18}H_{22}N_3SRuI_3$ FW = 794.24) 27.09 (27.22) %C, 2.78 (2.79) %H, 5.13 (5.29) %N.

[27] [(*p*-cymene)Ru(3c)Cl]Cl [(*p*-cymene)$RuCl_2]_2$ (50 mg, 0.08 mmol) and 3-iodobenzaldehyde-4-dimethyl-3-thiosemicarbazone (**3c**) (51 mg, 0.15 mmol) were mixed in dichloromethane (5 mL) and the resulting clear red solution stirred for 2 h before it was poured into excess diethylether to precipitate a yellow solid. The suspension was stirred for 30 min before the solid was isolated by filtration and dried in air (55 mg, 60%). **^{1}H NMR**

(400 MHz, $CDCl_3$) 1.14 (3H, d, J=7.2 Hz), 1.21 (3H, d, J=7.2 Hz), 2.35 (3H, s), 2.89 (1H, m), 3.47 (6H, s, br), 4.77 (1H, d, J=6.0 Hz), 4.84 (1H, d, J=5.9 Hz), 5.02 (1H, d, J=5.9 Hz), 5.45 (1H, d, J=6.0 Hz), 7.34 (1H, t, J=7.8 Hz), 7.90 (1H, d, J=8.0 Hz), 8.15 (1H, d, J=8.0 Hz), 9.00 (1H, s), 9.66 (1H, s), 12.02 (1H, s). **^{13}C NMR** (100 MHz, $CDCl_3$) 20.8 (CH_3), 21.7 (CH_3), 23.8 (CH_3), 31.3 (CH), 44.2 (NMe_2), 83.3 (CH), 83.4 (CH), 88.1 (CH), 88.7 (CH), 93.8 (C_q), 111.2 (C_q), 130.1 (CH), 130.3 (CH), 134.8 (C_q), 138.5 (CH), 140.6 (2 CH), 165.1 (N=CH).**ESI-MS** (MeOH) m/z (rel. int.) 568 (100) $[M\text{-}Cl\text{-}HCl]^+$, **CHN** (calc. for $C_{20}H_{25}N_3SIRuCl_2$) (37.63) %C, (3.95) %H, (6.58) %N.

[28] [(*p*-cymene)Ru(3c)I]I [(*p*-cymene)$RuI_2]_2$ (36.4 mg, 0.037 mmol) and 3-iodobenzaldehyde-4-dimethyl-3-thiosemicarbazone (**3c**) (25 mg, 0.08 mmol) were mixed in dichloromethane (5 mL) to give a clear, dark red solution which was left to stand for 24 hours. Red crystals formed which were isolated by filtration and dried in air (32 mg, 52 %). **^{1}H NMR** (400 MHz, $CDCl_3$) 1.16 (3H, d, J=6.8 Hz), 1.21 (3H, d, J=7.0 Hz), 1.55 (3H, s, H_2O), 2.33 (3H, s), 2.91 (1H, m), 3.52 (6H, s), 4.76 (1H, d, J=6.0 Hz), 4.85 (1H, d, J=5.8 Hz), 5.03 (1H, d, J=6.0 Hz), 5.28 (2H, s, CH_2Cl_2), 5.47 (1H, d, J=6.8 Hz), 7.31 (1H, t, J=7.9 Hz), 7.90 (1H, d, J=8.1 Hz), 8.14 (1H, d, J=8.1 Hz), 9.02 (1H, s), 9.77 (1H, s), 12.22 (1H, s). **^{13}C NMR** (100 MHz, $CDCl_3$) 20.6 (CH_3), 21.6 (CH_3), 23.7 (CH_3), 27.7 (CH), 46.7 (NMe_2), 82.8 (CH), 87.9 (CH), 88.0 (CH), 129.8 (CH), 130.1 (CH), 138.0 (CH), 140.5 (CH), 164.8 (N=CH), 174.4 (C=S). **ESI-MS** (MeOH) m/z (rel. int.) 568 (100) $[M\text{-}I\text{-}HI]^+$. **CHN** (calc. for $C_{20}H_{25}N_3SRuI_3$) 27.90 (29.25) %C, 3.05 (3.07) %N, 4.62 (5.12) %H.

[29] [(*p*-cymene)Ru(3c)I]PF_6 [(*p*-cymene)RuI_2]$_2$ (41.6 mg, 0.043 mmol) and 3-iodobenzaldehyde-4-dimethyl-3-thiosemicarbazone (**3c**) (28 mg, 0.084 mmol) were mixed in dichloromethane (5 mL) and diluted with a solution of NH_4PF_6 (71 mg, 0.43 mmol) in methanol (5 mL) to give a clear red solution. This was kept at 278 K for 4 days to precipitate a red crystalline solid which isolated by filtration, washed with diethylether and dried in air (33.5 mg, 53 %). **^{1}H NMR** (400 MHz, $CDCl_3$) 1.15 (3H, d, J=6.4 Hz), 1.21 (3H, d, J=7.2 Hz), 2.34 (3H, s), 2.88 (1H, m), 3.53 (6H, s, br), 4.76 (1H, d, J=6.1 Hz), 4.85 (1H, d, J=5.8 Hz), 5.02 (1H, d, J=5.8 Hz), 5.46 (1H, d, J=6.1 Hz), 7.31 (1H, t, J=7.9 Hz), 7.90 (1H, d, J=7.8 Hz), 8.14 (1H, d, J=7.8 Hz), 9.03 (1H, s), 9.71 (1H, s), 12.00 (1H, s, NH). **^{13}C NMR** (100 MHz, $CDCl_3$) 20.8 (CH_3), 21.7 (CH_3), 23.8 (CH_3), 31.3 (CH), 44.2 (NMe_2), 83.3 (CH), 83.4 (CH), 88.1 (CH), 88.7 (CH), 93.8 (C_q), 111.2 (C_q), 130.1 (CH), 130.3 (CH), 134.8 (C_q), 138.5 (CH), 140.6 (2 CH), 165.1 (N=CH). **ESI-MS** (MeOH) m/z (rel. int.) 568 (100) [M-I-HI]$^+$, **CHN** found (calc. for $C_{20}H_{25}N_3SRuI_2PF_6$) 29.18 (28.62) %C, 3.11 (3.00) %H, 5.07 (5.01) %N.

Synthesis for *in-situ* ^{1}H NMR Reaction Monitoring

The ruthenium TSC complexes listed below were synthesised only on an NMR scale (approx. 20 mg). While NMR and ESI-MS data were collected on the sample solutions, the reaction products were not isolated as solids.

The following procedure describes the preparation of complexes [**6**], **8**, [**9**], **16 - 18**, [**20**], [**25**], and [**26**].

NMR scale synthesis: Dinuclear ruthenium precursors [(*p*-cymene)$RuCl_2$]$_2$ (10 mg, 16 μmol) or [(*p*-cymene)RuI_2]$_2$ (15 mg, 15 μmol) were weighed into

small glass vials, followed by addition of 2 mol eq. of thiosemicarbazone ligand. Mixing the starting materials in deuterated chloroform resulted in red solutions of the corresponding complexes which were immediately transferred into NMR tubes. Filtration over celite assured that the samples were free from any remaining undissolved solid. ^{1}H NMR spectra were recorded within 30 min after mixing the reactants. Approx. 20 μL of the reaction mixture were diluted with methanol (1 mL) to prepare a sample for ESI-MS measurements of the reaction mixtures.

The NMR and MS data are summarised and described in Section 2.3, where Table 2.13 (Section 2.3.7, page 90) presents the corresponding ^{1}H NMR data and Table 2.5 (Section 2.3.3, page 69) contains the corresponding ESI-MS results for the complexes specified here.

2.2.4 Elemental Analysis

Elemental analysis (CHN) was carried out on a CE440 CHN/O/S Elemental Analyser by Warwick Analytical Services of Exeter Analytical (UK) Ltd., University of Warwick Science Park, Coventry, CV4 7EZ.

2.2.5 Mass Spectrometry

Electrospray mass-spectra were collected on a Bruker Esquire 2000 Ion Trap spectrometer in positive acquisition mode. Sample introduction was achieved by flow injection, using an Agilent 1100 LC system and methanol/TFA as the carrier solvent.

High-resolution accurate mass data for confirmation of molecular formulae were acquired by Dr. Lijiang Song or Phil Aston on a Bruker MaXis Ultra-

High Resolution Quadrupole Time-Of-Flight Mass Spectrometer (UHR-Q-TOF-MS) in the Mass Spectrometry Facility at the University of Warwick. Samples of ruthenium complexes were prepared at 1 mg/mL in methanol for further dilution by the MS operators as appropriate. Data were acquired in the mass range of 50 - 2500 m/z in positive ion mode, using an ESI source with a capillary voltage of 3000 V and a nebulizer pressure of 0.4 bar (gas flow 4.0 L/min). Bruker Compass DataAnalysis 4.0 was used for the calculation of molecular formulae from the experimental m/z results.

2.2.6 X-ray Crystallography

Crystallographic data and refinement were provided by Dr. G. Clarkson in the Department of Chemistry. Data were collected using an Oxford Diffraction Gemini four-circle system with Ruby CCD area detector which was cooled to 100 ± 2 K or 150 ± 2 K by an Oxford Cryosystem Cryostream Cobra. With the SHELXS[17] software suite, successful structure refinement confirmed the respective space groups as indicated by the refined data, placing additional light atoms by Fourier methods with refinement of calculated hydrogen atom positions by a riding model; NHs were located in a difference map. The H-atoms were given isotropic displacement parameters equal to 1.2 times the equivalent isotropic displacement parameter of the atom to which they are attached (1.5 times for methyl and NH protons).

2.2.7 Nuclear Magnetic Resonance Spectroscopy

Samples were dissolved in deuterated solvents and the solutions were filtered into 5 mm Wildmann "economy" NMR tubes. Basic one-dimensional (1D) ^{1}H and ^{13}C NMR experiments for purity control were carried out on Bruker

drx spectrometers with either 400 MHz or 300 MHz proton resonance frequency. Two dimensional (2D) correlation experiments such as ^{1}H,^{1}H-COSY, ^{1}H,^{13}C-HSQC and ^{1}H,^{13}C-HMBC, were performed on the same instruments to obtain additional data for structure confirmation.

^{1}H NMR Studies with [(*p*-cymene)Ru(2a)Cl]Cl [15]

Complex [**15**] was dissolved in dmso-d_6 and diluted into D_2O to achieve a final concentration of approx. 1 mM with a maximum dmso content of 5% (v/v). Two samples were prepared, one was inserted into the magnet immediately and the 1H NMR spectrum was recorded, while the other one was equilibrated at room temperature for 48 h. Spectra were also recorded after 12 h.

Observation of Dimerisation by ^{1}H NMR

Complex [**21**] (3.7 mg) was dissolved in $CDCl_3$ (50 μL) and diluted into a solution of NH_4PF_6 (5 mg in 500 μL). The resulting clear red solution was transferred into a Wildman precision 5 mm NMR tube, and a ^{1}H NMR spectrum was recorded 30 min after sample preparation. The sample was kept at 293 K for 14 h before a second ^{1}H NMR spectrum was recorded. Red crystals were found at the bottom of the tube. These were isolated by filtration and analysed by single crystal X-ray diffraction (see Section 2.3.4, page 76).

2.2.8 $^{1}H^{15}N$-Heteronuclear Multiple-bond Coherence Spectroscopy

Samples of thiosemicarbazones for $^{1}H^{15}N$ HMBC NMR experiments were dissolved in dmso-d_6 at a concentration of 100 mM and subsequently filtered into 5 mm Wildman 507 precision NMR tubes.

A Bruker Avance III 600 MHz spectrometer was used for the $^{1}H^{15}N$-HMBC NMR experiments. This was equipped with one of the two following probes: an auto-tunable multinuclear ($^{31}P-^{109}Ag$) Broad Band Observe (BBO) probe, or a Triple Resonance Inverse (TXI) probe (^{1}H, ^{13}C (inner coil), ^{15}N (outer coil)). Both probes also use gradient coils.

Experiment Parameters:

The NMR probe was tuned automatically (using the Bruker automatic tunig and matching device (ATM)) closest to the ^{1}H resonance frequency of 600.13 MHz and the corresponding ^{15}N frequency of 60.83 MHz. Automated shimming in three dimensions was achieved by the *topshim* programme.

Table 2.2 lists parameters which were used in the Bruker pulse programme *hmbcgpndqf* (Avance version, 07/04/04) for the ^{1}H,^{15}N-HMBC experiment. The parameters and abbreviations are consistent with Bruker naming conventions.

Spectral widths (SW) were optimised to 10 ppm for ^{1}H and 400 ppm for ^{15}N to achieve a measurement time of 60 min. Individual offsets were set according to the shift range of the 1D ^{1}H NMR spectrum (O1P) which was recorded beforehand for each compound. 16 scans in f2 (TD = 1024) were acquired per transient in f2 (TD = 256), with zero-filling to 2048 (^{1}H) and 1024 (^{15}N) points during data processing. As a result, the processed spectra

Table 2.2: Selected parameters for the acquisition of $^{1}H^{15}N$ HMBC NMR spectra with the Bruker pulse program *hmbcgpndqf*.

Parameter	Channel f1[a)]	Channel f2
Nucleus	^{1}H	^{15}N
Frequency (SFO)	600.13 MHz	60.81 MHz
Spectral Width (SW)	10 ppm	400 ppm
Off-set (OP)	7.5 ppm	200 ppm
Data points (TD)	2048	256
No. of Scans (NS)	16	-
No. of Dummy Scans (DS)	16	-
Dwell Time (DW)	83.3 μ	-
Pre-scan Delay (DE)	6.55 μs	-
Pulse Width (P1)	13.75 s	-
J coupling (CNST13)	8.000 Hz	-
Relaxation Delay (D1)	1.5 s	-
Delay for coupling (D6)	62.5 μs	-
FID resolution	2.93 Hz	95.03 Hz
Zero Filling (SI)	2048	1024
Spectral Resolution	2.93 Hz/pt	23.45 Hz/pt
Temperature (TE)	298 K	

[a)] Note: Channel f1 translates to the direct dimension of the spectrum, represented by F2.

had a resolution of 2.93 Hz per data point in the F2 (^{1}H) dimension and 23.45 Hz/pt in the F1 (^{15}N) dimension. Sine-bell window-functions were applied in both spectral dimensions prior to Fourier transformation.

2.3 Results

2.3.1 Synthesis of Thiosemicarbazones

Three series of thiosemicarbazones were prepared by imine condensation between aldehydes and thiosemicarbazides in refluxing methanol. White crystalline powders where obtained in yields of 50 - 95 %. The combination of benzaldehyde (**1**), *N,N*-dimethylamino-benzaldehyde (**2**), and 3-iodobenzaldehyde (**3**) with each thiosemicarbazide (TSC, **a**), 4-methyl-3-thiosemicarbazide (TSC*NMe*, **b**) 4-dimethyl-3-thiosemicarbazide (TSCNMe_2, **c**), and 4-iodophenylthiosemicarbazide (TSC*IPh*, **d**) yielded 12 different TSCs. Table 2.3 provides an overview over the substitution pattern in the ligands **1a-d**, **2a-d** and **3a-d**.

Table 2.3: Overview of substitution pattern in TSC ligands.

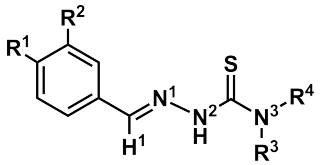

No.	Name	$\mathbf{R}^1$	$\mathbf{R}^2$	$\mathbf{R}^3$	$\mathbf{R}^4$
1a	PTSC	H	H	H	H
1b	PTSC*NMe*	H	H	H	CH_3
1c	PTSCNMe_2	H	H	CH_3	CH_3
1d	PTSC*IPh*	H	H	H	(p-C_6H_4-I)
2a	DTSC	$N^4(CH_3)_2$	H	H	H
2b	DTSC*NMe*	$N^4(CH_3)_2$	H	H	CH_3
2c	DTSCNMe_2	$N^4(CH_3)_2$	H	CH_3	CH_3
2d	DTSC*IPh*	$N^4(CH_3)_2$	H	H	(p-C_6H_4-I)
3a	ITSC	H	I	H	H
3b	ITSC*NMe*	H	I	H	CH_3
3c	ITSCNMe_2	H	I	CH_3	CH_3
3d	ITSC*IPh*	H	I	H	(p-C_6H_4-I)

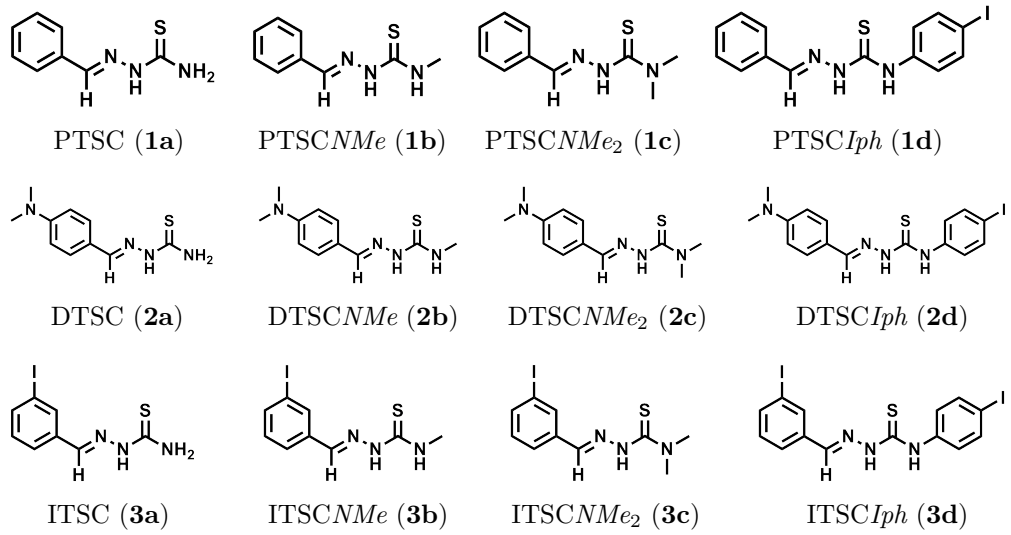

Figure 2.8: Combination of aldehydes **1-3** with four different thiosemicarbazides **a-d** resulted in a library of 12 TSCs: **1a-d**, **2a-d**, and **3a-d** discussed in this chapter.

Each row in Figure 2.8 presents one series of TSCs according to substituents R^1 and R^2 on the phenyl ring. From **1** to **3** these substituents are: phenyl (**P**) in **PTSC** ligands **1a-d** ($R^1 = R^2 = H$), 4-*N,N*-**d**imethylaminophenyl (**D**) in **DTSC** ligands **2a-d**, and 3-iodophenyl (I) in **ITSC** ligands **3a-d**. The columns in Figure 2.8 arrange the TSCs by substituents R^3 and R^4, located on the thioamide side of the structure. For example, the first column **(a)** represents the NH_2 group in the three TSCs **1-3a**, in which $R^3 = R^4 = H$. Conversely, these columns **a - d** allow for data comparison that highlights the influence of phenyl substituents R^1 and R^2, while comparison within a row studies the influence of amide substituents R^3 and R^4.

2.3.2 Synthesis of Arene Ruthenium TSC Complexes

Arene ruthenium complexes of the TSC ligands were synthesised according to literature procedures.[14, 15, 18] The reaction of the dinuclear Ru(II) precursors $[(p\text{-cymene})RuX_2]_2$ with X = Cl ([**4**]) or X = I ([**4**]) with two equivalents of a TSC ligand **HL** yielded 23 different ruthenium complexes of the general formula $[(p\text{-cymene})Ru(HL)X]^+X^-$ (Table 2.4). The complexes formed within 30 min to 18 hours and were obtained as powders of orange to red colour.

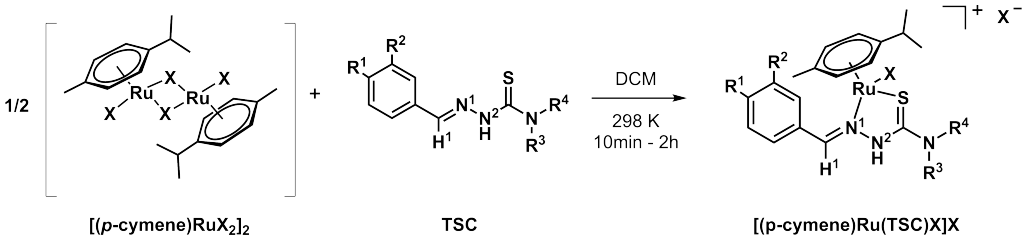

Figure 2.9: Reaction scheme showing the synthesis of arene Ru^{II} TSC complexes.

In addition to NMR and ESI-MS analyses, the composition of those powders was assessed by CHN elemental analysis, and the results were in agreement with the proposed formulae. For complex [**10**] and [**29**] the counter ion X^- was exchanged to PF_6^- by mixing a solution of the halido complex in dichloromethane (DCM) with a saturated solution of NH_4PF_6 in methanol. Crystals of complex [**10**] grew upon evaporation of DCM from the mixture. The single crystal structure was determined by X-ray crystallography and will be presented in Section 2.3.4.

Table 2.4: Overview of arene ruthenium TSC complexes prepared from [(*p*-cymene)$RuCl_2$]$_2$ or [(*p*-cymene)RuI_2]$_2$.

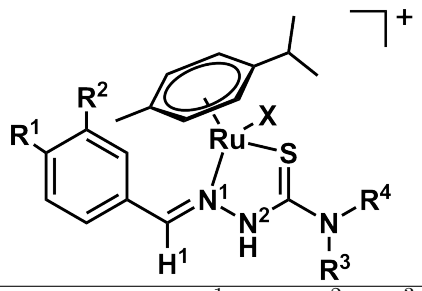

Complex	Ligand	R^1	R^2	R^3	R^4	X	Z
[**6**] *	PTSC	H	H	H	H	Cl	Cl
[**7**]	PTSC	H	H	H	H	I	I
[**8**] *	PTSC*NMe*	H	H	H	Me	Cl	Cl
[**9**] *	PTSC*NMe*	H	H	H	Me	I	I
[**10**]	PTSC*NMe*$_2$	H	H	Me	Me	Cl	PF_6
[**11**]	PTSC*NMe*$_2$	H	H	Me	Me	I	I
[**12**]	PTSC*NMe*$_2$	H	H	Me	Me	I	PF_6
[**13**]	PTSC*IPh*	H	H	H	IPh	Cl	
[**14**]	PTSC*IPh*	H	H	H	IPh	I	
[**15**]	DTSC	$N^4(CH_3)_2$	H	H	H	Cl	Cl
[**16**] *	DTSC	$N^4(CH_3)_2$	H	H	H	I	I
[**17**] *	DTSC*NMe*	$N^4(CH_3)_2$	H	H	Me	Cl	PF_6
[**18**] *	DTSC*NMe*	$N^4(CH_3)_2$	H	H	Me	I	I
[**19**]	DTSC*NMe*$_2$	$N^4(CH_3)_2$	H	Me	Me	Cl	PF_6
[**20**]	DTSC*NMe*$_2$	$N^4(CH_3)_2$	H	Me	Me	I	I
[**21**]	DTSC*IPh*	$N^4(CH_3)_2$	H	H	IPh	Cl	Cl
[**22**]	DTSC*IPh*	$N^4(CH_3)_2$	H	H	IPh	I	I
[**23**]	ITSC	H	I	H	H	Cl	
[**24**]	ITSC	H	I	H	H	I	
[**25**] *	ITSC*NMe*	H	I	H	Me	Cl	
[**26**] *	ITSC*NMe*	H	I	H	Me	I	
[**27**]	ITSC*NMe*$_2$	H	I	Me	Me	Cl	PF_6
[**28**]	ITSC*NMe*$_2$	H	I	Me	Me	I	I
[**29**]	ITSC*NMe*$_2$	H	I	Me	Me	I	PF_6

Complexes labelled with * were only prepared for NMR and ESI-MS experiments detailed in this Section, but the products were not isolated.

2.3.3 Mass Spectrometry

Ruthenium TSC complexes were analysed by Electrospray Mass Spectrometry (ESI-MS) as part of the initial characterisation. The results are summarised in Table 2.5. The spectra of all complexes showed the typical isotopic pattern for mononuclear ruthenium species.

Each row in Table 2.5 lists data for the two complexes of one TSC ligand **HL** and compares the theoretical and experimental mass-to-charge ratios ($\mathbf{m/z}_{theor.}$ and $\mathbf{m/z}_{exp.}$) for the chlorido complex, $[(p\text{-cymene})\mathrm{Ru}(\mathbf{HL})Cl]^+$ to the values for their corresponding iodido congeners $[(p\text{-cymene})\mathrm{Ru}(\mathbf{HL})I]^+$.

Table 2.5: ESI-MS data for ruthenium complexes of selected TSC ligands **HL**. **m/z (theor.)** $\equiv [(p\text{-cymene})\mathrm{Ru(HL)}X]^+$, with X = Cl, I

HL	$[(p\text{-cymene})\mathrm{Ru(HL)Cl}]^+$				$[(p\text{-cymene})\mathrm{Ru(HL)I}]^+$			
	[C]	**m/z (theor.)**	**m/z (exp.)**	**Δm/z**	**[C]**	**m/z (theor.)**	**m/z (exp.)**	**Δm/z**
1a	[6]	449.98	414.0	35.98	[7]	541.43	414.0	127.43
1b	[8]	464.01	428.0	36.01	[9]	555.46	428.0	127.46
1c	[10]	478.04	442.0	36.04	[11]	569.44	442.0	127.44
1d	[13]	651.97	615.9	36.07	[14]	743.43	616.0	127.43
2a	[15]	493.06	457.0	36.06	[16]	612.48	485.0	127.48
2c	[19]	521.11	485.0	36.11	[20]	612.48	485.0	127.48
2d	[21]	695.04	659.0	36.04	[22]	786.49	659.0	127.49
3a	[23]	575.88	540.0	35.88	[24]	667.33	540.0	127.33
3b	[25]	589.89	554.0	35.89	[26]	681.34	553.8	127.54
3c	[27]	603.93	568.0	35.93	[28]	695.38	568.0	127.38

The two columns in Table 2.5 that are labelled **Δm/z** present the mass-difference between the $\mathbf{m/z}_{theor.}$ for the cationic complexes $[(p\text{-cymene})\mathrm{Ru(HL)}X]^+$ and the experimentally determined result. There is a consistent loss of 36 mass units (mu) for all chlorido complexes, and of 127.5 mu for the iodido analogues. Furthermore, in every row, the detected m/z is identical for the two complexes of the same TSC ligand **HL**. These values clearly highlight

the loss of either HCl or HI from the structure, resulting in a complex that has the formula [(*p*-cymene)Ru(**L**)]$^+$.

High-resolution accurate mass data were acquired for the four arene ruthenium TSC complexes [**11**], [**13**], [**21**], and [**28**], which were selected as representatives of the three TSC ligand series **1-3**. Complexes [**13**] and [**21**] have a chlorido monodentate ligand, while [**11**] and [**28**] have an iodido monodentate ligand.

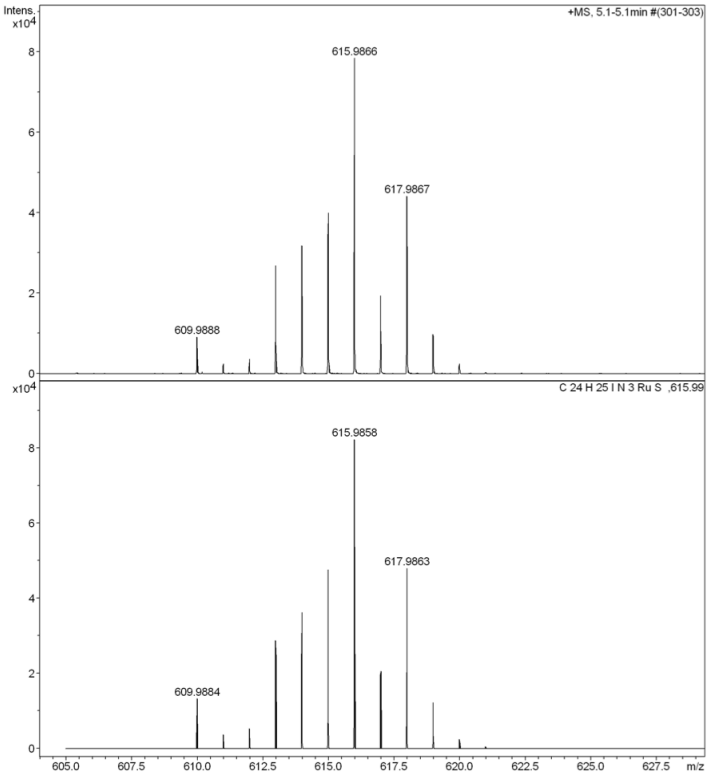

Figure 2.10: Comparison between measured and calculated isotopic pattern of the mass spectrum of complex [(*p*-cymene)Ru(**1d**)Cl]$^+$ shows that the experimental data fits with the molecular formula for the deprotonated species [(*p*-cymene)Ru(**1d**-H)]$^+$.

Figure 2.10 shows that the isotopic pattern detected in the HR-MS spectrum of the chlorido complex [**13**] is in excellent agreement with a mononuclear ruthenium complex of the formula $C_{24}\mathbf{H}_{25}N_3SIRu$, which does not include any chloride atoms.

Table 2.6: High-resolution ESI-MS data for complexes **[C]** ([(*p*-cymene)Ru(**HL**)X]X) of selected TSC ligands **HL**.

[(*p*-cymene)Ru(HL)X]$^+$ - [HX] →					**[(*p*-cymene)Ru(L)]$^+$**	
[C]	**HL**	**FW**	**m/z (theor.)**	**Δm/z**	**m/z (exp.)**	**m/z (calc.)**
[11]	**1c**	696.39	569.44	**127.35**	442.0890	442.0890
[13]	**1d**	687.42	651.97	**35.983**	615.9870	615.9858
[21]	**2d**	730.49	695.04	**36.011**	659.0291	659.0279
[28]	**3c**	822.28	695.38	**127.39**	567.9858	567.9856

m/z theor. ≡ [(*p*-cymene)Ru(**HL**)X]$^+$, **m/z calc.** ≡ [(*p*-cymene)Ru(L)]$^+$.

Data summarised in Table 2.6 are the detected m/z for each complex, compared to its formula weight (FW) and to the calculated m/z for a monocationic ruthenium complex of the formula $[(C_{10}H_{14})Ru(L)]^+$. The molecular formulae that were used for the calculation represent the most likely solution for the detected arene ruthenium TSC species, as the experimental values match this calculated m/z to the second last digit.

For example, the molecular formula of complex **[13]** is $C_{24}\mathbf{H}_{26}N_3SIRuCl_2$, with a formula weight of 772.37 Da. The m/z of the same complex determined by HR-MS is 615.9866 Da, and the formula which best represents this result is $C_{24}\mathbf{H}_{25}N_3SIRu$ (calc. m/z 615.9857). This formula has changed by two Cl atoms and one H atom, and its calc. m/z matches the low-resolution ESI-MS results presented in Table 2.5. Because this formula does not contain the halido ligand or counter ion, it is consistent with a molecule that can form as a fragment of the chlorido complexes as well as from the iodido analogues.

2.3.4 X-ray Crystal Structures

For three compounds presented in this thesis, crystal structures were obtained. The first one is for colourless needle-shaped crystals of *N,N*-dimethylaminobenzaldehyde-4-methyl-3-thiosemicarbazone, ligand **2b**. The other two structures are of two different ruthenium TSC complexes: one for orange block crystals of [(*p*-cymene)Ru(PTSC*NMe*$_2$)Cl]PF_6, complex **[10]**, and the other is for red crystals obtained from the reaction of [(*p*-cymene)Ru(DTSC*NMe*$_2$)Cl]Cl (**[21]**) with NH_4PF_6.

N,N-Dimethylaminobenzaldehyde-4-methyl-3-thiosemicarbazone (2b)

The ligand DTSC*NMe* (**2b**) crystallises with space group P2(1)/1, with an asymmetric unit that contains one of four molecules in the unit cell. Table 2.7 depicts the structure and lists a collection of significant interatomic distances and torsion angles for the structure. These data show that the TSC molecule is almost completely planar in the solid state. None of the torsion angles that describe the TSC unit (C1 through C6), is larger than 5°. In fact, the largest dihedral angle between non-hydrogen atoms is 11.2(2)° between the aromatic ring and C14/15 of the two N-methyl groups.

Table 2.7: Bond distances, torsion angles, and intra- and inter molecular (hydrogen)-bond geometry (Å, °) in DTSC*NMe* (**2b**).

Bond Distance (Å)		
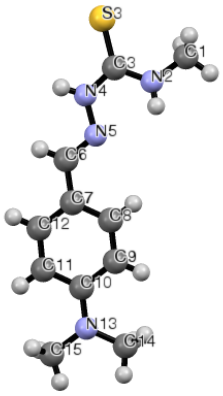	C1—N2	1.463(1)
	N2—C3	1.347(1)
	S3—C3	1.716(1)
	C3—N4	1.366(1)
	N4—N5	1.400(1)
	N5—C6	1.304(1)
	C6—H6	0.950
	C6—C7	1.471(1)
	C10—N13	1.389(1)
	N13—C14	1.466(2)
	N13—C15	1.468(1)

A1 — A2 — A3 — A4	**Torsion (°)**
C1 — N2 — C3 — S3	-4.7(2)
C1 — N2 — C3 — N4	174.6(1)
N2 — C3 — N4 — N5	-0.9(2)
S3 — C3 — N4 — N5	178.36(8)
C3 — N4 — N5 — C6	-177.2(1)

D-H...A	**D–H (Å)**	**H...A (Å)**	**D...A (Å)**	**< D-H...A (°)**
N2-H2...S3 $1	0.856(17)	2.932(17)	3.5076(11)	126.3(13)
N4-H4...S3 $2	0.874(18)	2.553(18)	3.4093(10)	166.4(14)
N2-H2...N5	0.856(17)	2.279(17)	2.6566(13)	106.9(13)

$1) Symmetry operators: x, -y+1/2, z+1/2 $2) -x, -y, -z

The graphic in Figure 2.11 captures the planarity of the structure. It can be contributed to two factors: the conjugated π-system which runs through the length of the molecule on the one hand, and intramolecular hydrogen bond interactions on the other. The dashed lines in Figure 2.11 highlight the short contacts that are attributed to H-bonds, for example the contact between N2-H2 and N5 (N2-H2...N5 = 0.856(17)).

There are also intermolecular H-bonds, between a sulfur atom S(3) and the corresponding N4-H4 of a second TSC molecule (Figure 2.11). Be-

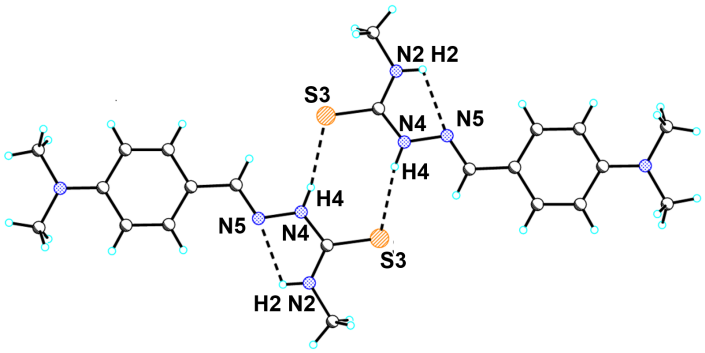

Figure 2.11: Illustration of the X-ray crystal structure of *N,N*-dimethylaminobenzaldehyde-4-methyl-3-thiosemicarbazone (DTSC*NMe*, **2b**) with atom numbering. Thermal ellipsoids are shown at 50% probability. Dashed lines represent H-bond interactions which lead to the formation of dimeric pairs in the solid state.

cause of this pairing, S(3) is located *trans* with respect to the imino group (N(5)=CH), which is referred to as imine-*E*-configuration of the TSC.

[(*p*-cymene)Ru(PTSC*NMe*$_2$)Cl]PF$_6$ [10]

Figure 2.12 depicts the structure that was determined for the orange crystals of ruthenium(II) TSC complex [**10**]. The unit cell contains four cationic ruthenium complexes that have the formula [(*p*-cymene)Ru(PTSC*NMe*$_2$)Cl]PF$_6$.

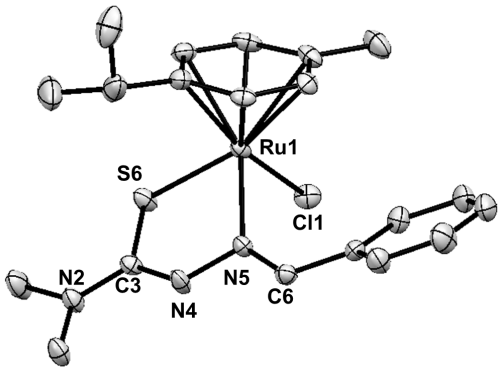

Figure 2.12: ORTEP representation of the X-ray crystal structure of complex [**10**] with atom labelling. Thermal ellipsoids are shown at 50% probability. PF$_6$ counter ion and H-atoms omitted for clarity.

The structure is that of a half-sandwich 'piano-stool' complex in which the Ru(II) central atom bears an aromatic *p*-cymene ligand as 'seat', and the TSC donor atoms N(5), S(6) and the Cl(1) are in the position of the 'legs'. The asymmetric unit consists of one such molecule plus a PF_6 counter ion.

Table 2.8: Selected bond distances (Å) and angles (°), and H-bond geometry for complex ([**10**]).

Bond Distances (Å)			
Ru(1)—N(5)	2.1364(14)	N(2)—C(3)	1.329(2)
Ru(1)—S(3)	2.3589(4)	C(3)—N(4)	1.343(2)
Ru(1)—Cl(1)	2.4319(4)	N(4)—N(5)	1.3995(19)
C(3)—S(3)	1.7065(17)	N(5)—C(6)	1.292(2)
D-H...A	**D—H (Å)**	**H...A (Å)**	**D...A (Å)**
N4-H4...F11	0.855(16)	2.385(19)	3.0752(19)
N4-H4...Cl1 $^{\$1}$	0.855(16)	2.82(2)	3.4142(16)
C6-H6...Cl1 $^{\$1}$	0.95	2.88	3.6014(17)
Bond Angles	(°)	**< D—H...A**	(°)
S(3)—Ru(1)—Cl(1)	85.943(16)	N(4)-H...F(11)	138.2(19)
N(5)—Ru(1)—Cl(1)	89.72(4)	N(4)-H...Cl(1) $^{\$1}$	128.3(18)
N(5)—Ru(1)—S(3)	81.13(4)	C(6)-H...Cl(1) $^{\$1}$	133.2

$1) Symmetry operators: 1-X,-Y,1-Z

Table 2.8 provides selected interatomic distances and angles as well as short contacts (H-bonds). Those short contacts were located between the TSC NH group (N(4)H) and a chloride (Cl(1)) of a neighbouring complex (N(4)-H...Cl(1) = 0.855(16) Å) and also between the imino CH proton C(6)-H and the same neighbouring Cl(1) (C6-H...Cl(1) = 0.95 Å).

[(*p*-cymene)Ru(DTSC*NMe*$_2$)]$_2$[PF$_6$]$_2$ [30]

Red crystals of [**30**] formed in a mixture of complex [**21**] with 10 mol eq. NH_4PF_6 in DCM/methanol by slow evaporation of DCM from the solution.

Complex [**30**] crystallises in space group P2/n. The asymmetric unit contains a dinuclear di-cationic ruthenium complex, displayed in Figure 2.13, of the formula [(*p*-cymene)Ru(DTSC*NMe*$_2$)]$_2$[PF$_6$]$_2$.

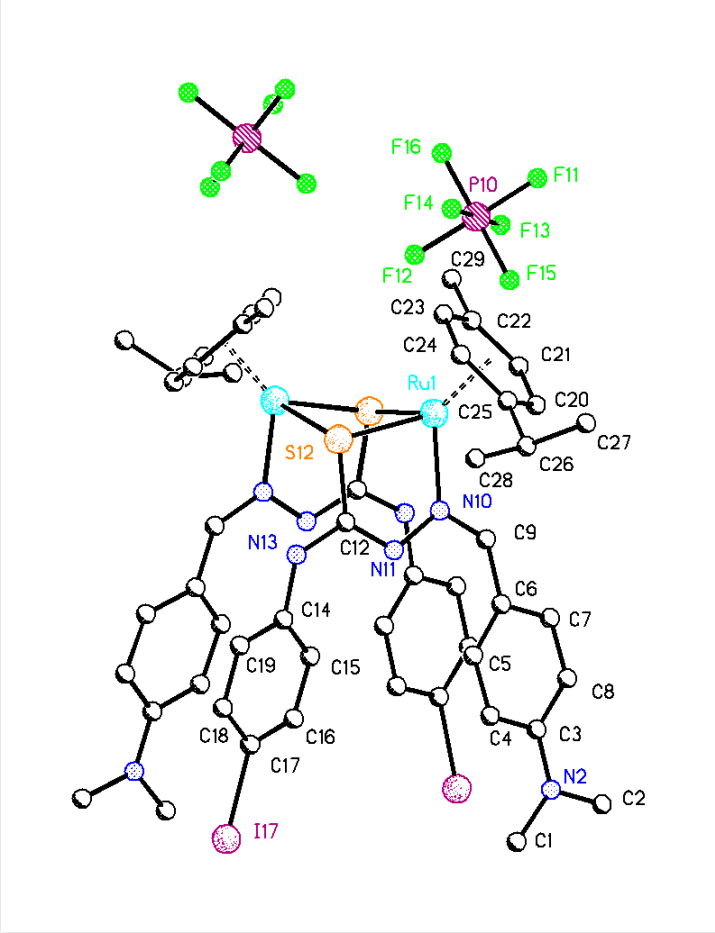

Figure 2.13: X-ray crystal structure and atom labels of dinuclear Ru TSC complex [(*p*-cymene)Ru(DTSC*NMe*$_2$)]$_2$[PF$_6$]$_2$ [**30**]. Each molecule of [**30**] has two PF_6^- couterions.

Table 2.9: Selected interatomic distances (Å) in the crystal structure of complex ([**30**]). † the Ru–Ru distance does not qualify as a chemical bond but is included for future reference.

Bond Distance (Å)	
Ru(1)—Ru(2) †	3.04
Ru(1)—N10	2.0835(16)
Ru(1)—S12	2.3511(5)
Ru(1)—S12(2)	2.4249(5)
S12—C(3)	1.7891(19)
C3—N(2)	1.365(2)
C3—N(4)	1.291(2)
N(4)—N(10)	1.400(2)

The structure consists of two identical Ru(II) piano-stool subunits, each with a *p*-cymene and a chelating TSC ligand (DTSC*IPh*, **2d**).

The two TSC molecules are arranged such that each sulfur atom bridges the two ruthenium atoms, which results in the formation of a distorted Ru_2S_2 rectangle with distances of dRu(1)–S(12) = 2.3511(5) Å and dRu(2)–S(12) = 2.4249(5) Å. The bond angles in this rectangle are 82.5 ° at Ru (< S—Ru—S) and 94.4 ° at sulfur (< Ru—S—Ru), respectively. The imino nitrogen N(5) of TSC ligand **2d** completes the piano-stool sub-structure of each ruthenium centre (dRu-N = 2.0835(16) Å). Two molecules of this dimeric structure are located in the unit cell.

In the dinuclear structure presented in Figure 2.13, the planar TSC ligand DTSC*IPh* (**2d**) exhibits overall (*Z*)-configuration of the imine double-bond. This way, the two substituted aromatic rings at either end of the TSC ligand overlap with their respective opposite (Figure 2.13): the *p*-iodophenyl ring faces the dimethylamino end of its counterpart and vice versa. This arrangement causes two-fold rotational symmetry in the dinuclear complex.

Characteristic for the structures of both [**10**] and [**30**] is the C-S bond of the coordinated thiosemiarbazone ligand, which is a measure of its binding

Table 2.10: Comparison of bond lengths(Å) in the TSC **2b**, the mononuclear complex [(*p*-cymene)Ru(1c)Cl]PF_6 **[10]** and the dinuclear complex [(*p*-cymene)Ru(2d)]$_2$[PF_6]$_2$ **[30]**.

Bond	**2b**	**[10]**	**[30]**
C(3)-N(2)	1.3475(14)	1.329(2)	1.365(2)
S(12)-C(3)	1.7164(11)	1.7065(17)	1.7891(19)
C(3)-N(4)	1.3660(14)	1.343(2)	1.291(2)
N(4)-N(5)	1.4002(13)	1.3995(19)	1.400(2)

mode as either neutral thione or negatively charged thiolate. In the former, the C-S bond has double bond character and is therefore shorter, while the C-S distance in the latter is longer due to the sigma-bond character of the thiolate.

Table 2.10 compares significant bond lengths of the ligand with the monomeric and the dimeric complex. The data show that the distance between carbon and sulfur increases in the dimer (1.7891(19) Å) compared to the monomer (1.7065(17)), while there is no difference between the C=S bond length in the monomer and the free ligand (1.7164(11)). At the same time, the corresponding amide C-N bond is short in the dimer, but does not change much between free TSC and the mononuclear complex. This difference in the bond distances is an effect of deprotonation of the TSC ligand at the hydrazinic NH and subsequent tautomerisation to the thiolate. When the C-S^- binds to the ruthenium centre, the negative charge replaces the chlorido ligand.Conclusively, the TSC ligand **1c** is coordinated as thione in complex **[10]**, while ligand **2d** binds as thiolate in dimer **[30]**.

2.3.5 NMR Spectroscopy of Thiosemicarbazones

This section presents solution state ^{1}H and ^{13}C NMR data for the TSC ligands. ^{1}H and ^{13}C NMR chemical shifts for the characteristic moieties such as the imino group HC^{1}=N and the thione carbon (C=S) are listed in Table 2.11 on the next page. The data are organised in four groups, **a**, **b**, **c**, and **d**, according to the amide substitution pattern which is highlighted by the structures in the first column. In each of those four blocks, three different ligands are grouped together; **1a - 3a** in the first, **1b - 3b** in the second, **1c - 3c** in the third, and **1d - 3d** in the final block.

Results of the ^{13}C NMR experiments are summarised first. The $C = S$ column in Table 2.11 reveals that the chemical shifts for the thione carbon are almost identical within each block. In groups **a** and **b**, $\delta_{C=S}$ is 178 ppm, while in group **c** for the dimethylated TSCNMe_2 ligands, the C=S carbon signal shifts to 180 ppm. Compared to this, the ^{13}C NMR signal for the thione in TSCIPh ligands **1d - 3d** is found 5 ppm higher at 175 ppm.

The chemical shifts for the imino carbon resonance $\delta_{C=N}$ is also shifted downfield, to $140 - 145$ ppm. Here, the results are similar between the four blocks of the the table. However, comparing the third row in each block with the other two rows above shows that the ligands of 3-iodobenzaldehyde, i.e. of series **3**, have lower shifts for this carbon signal (140-142 ppm) than the ligands derived from benzaldehyde (**1a-d**) and dimethylaminobenzaldehyde (**2a-c**) with 144-145 ppm.

Next, significant ^{1}H NMR signals are listed for the structural analysis of TSCs and their metal complexes. These are for the imino proton H^{1}, the hydrazinic proton $N^{2}H^{2}$, and the proton(s) of the thioamide group ($N^{3}H_2$ for **1-3a)**. N=CH^{1} is one residue which all TSCs in this thesis have in common. Its NMR signal is a sharp singlet at a chemical shift close to

Table 2.11: ^{13}C and ^{1}H chemical shifts for selected atoms: δ_C of the thione (C=S) and imine (C=N) carbon and δ_H for the imine proton H^1C=N, the hydrazinic proton H^2N and the thioamide protons N$^3H^{3\dagger}$, recorded in dmso-d_6 at 298 K.

Ligand		δ_C [ppm]		δ_H [ppm]		
		C=S	C=N	H^1	H^2	H$^{3'\dagger}$ / H^3
R^1 = 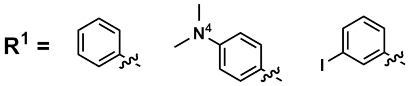 1a-d 2a-d 3a-d	**1a**	177.9	142.1	8.07	11.45	8.00 / 8.22
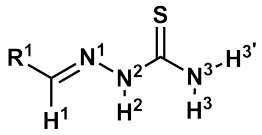	**2a**	177.1	143.4	7.93	11.19	7.77 / 8.01
	3a	178.1	140.5	8.00	11.49	8.16 / 8.24
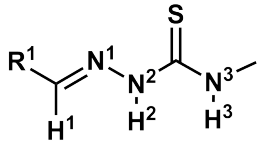	**1b**	177.8	141.7	8.04	11.47	8.50
	2b	177.1	142.8	7.92	11.19	8.28
	3b	177.8	140.1	7.96	11.53	8.60
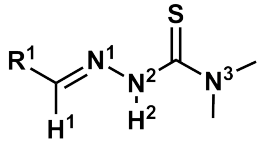	**1c**	180.5	143.8	8.19	10.94	–
	2c	n.o.	144.9	8.04	10.65	–
	3c	180.5	142.2	8.12	11.01	–
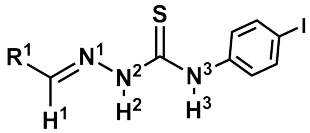	**1d**	174.8	144.3	8.17	11.91	10.12
	2d	174.8	144.3	8.04	11.67	9.94
	3d	176.2	141.7	8.07	11.95	10.20

† The signal for the thioamide protons NH^3 and NH$^{3'}$ of ligands **1-3a** is split into two broad singlets at 298 K.
*n.o. not observed

8.0 ppm. With a range from 7.93 - 8.19 ppm, the results for δ_{H^1} are similar between all TSCs listed in Table 2.11. Only series **1** ligands have slightly higher shifts for H^1 than their two direct analogues in each block.

A second group which all of the presented TSCs have in common is the hydrazinic proton N^2H. This NH signal presents itself as a sharp singlet furthest downfield in the spectrum, with chemical shifts as high as 11.95 ppm (**3d**). The variation in the shift for N^2H are approx. 1 ppm within the range of TSCs presented here, with group **c** ligands showing significantly lower shift values than the TSCs in the other three blocks.

The TSCs of series **a** (Table 2.11, top) have a thioamide NH_2 group. The two protons showed two separate signals, both as broad singlets with chemical shifts in the region of 7.77 - 8.24 ppm. While the ^{1}H NMR signal for the thioamide NH in group **b** had a shift comparable to the group **a** results, the respective NH proton of group **d** ligands **1d - 3d**, is remarkably shifted further downfield, to 10 ppm.

2.3.6 Natural-Abundance $^{1}H,^{15}N$ NMR Spectroscopy

All TSCs contain at least three nitrogen atoms. Each has a different chemical environment, as highlighted by the structure depicted in Figure 2.14: the imino nitrogen N^1, its hydrazinic neighbour N^2, and the thioamide nitrogen N^3.

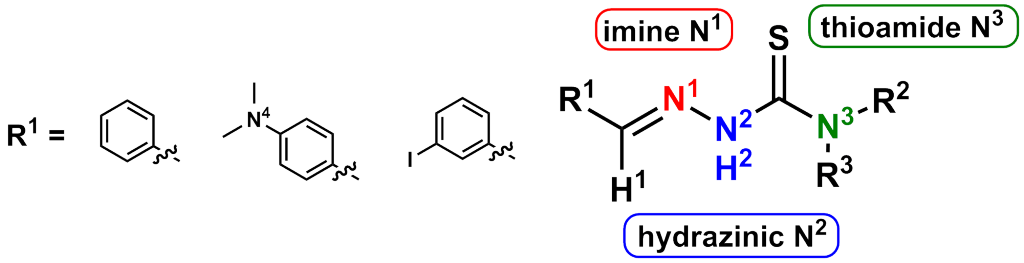

Figure 2.14: General structure of TSCs with numbering scheme for ^{15}N chemical shift assignment by $^{1}H^{15}N$-HMBC NMR: In series **1-3a** $R^2 = R^3 = H$; for **1-3b** $R^2 = Me$, $R^3 = H$; for **1-3c** $R^2 = R^3 = Me$; and in **1-3d** $R^2 = 4$-iodophenyl (PhI), $R^3 = H$.

This NMR study determined the ^{15}N NMR chemical shifts for those nitrogen atoms, and the results are summarised in Table 2.12 below.

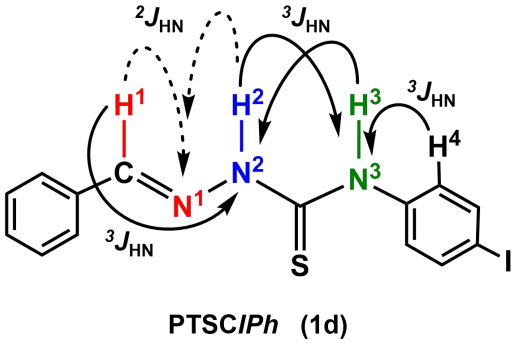

Figure 2.15: Schematic representation of long-range $^{1}H^{15}N$-couplings in TSC ligands.

As a representative example of the spectra that were obtained in this study, the $^{1}H^{15}N$-HMBC NMR spectrum of DTSC*Iph* (**1d**) is presented in Figure 2.16. It shows seven significant cross-peaks for the $^{1}H^{15}N$ correlations

in the molecule, illustrated by the schematic in Figure 2.15.

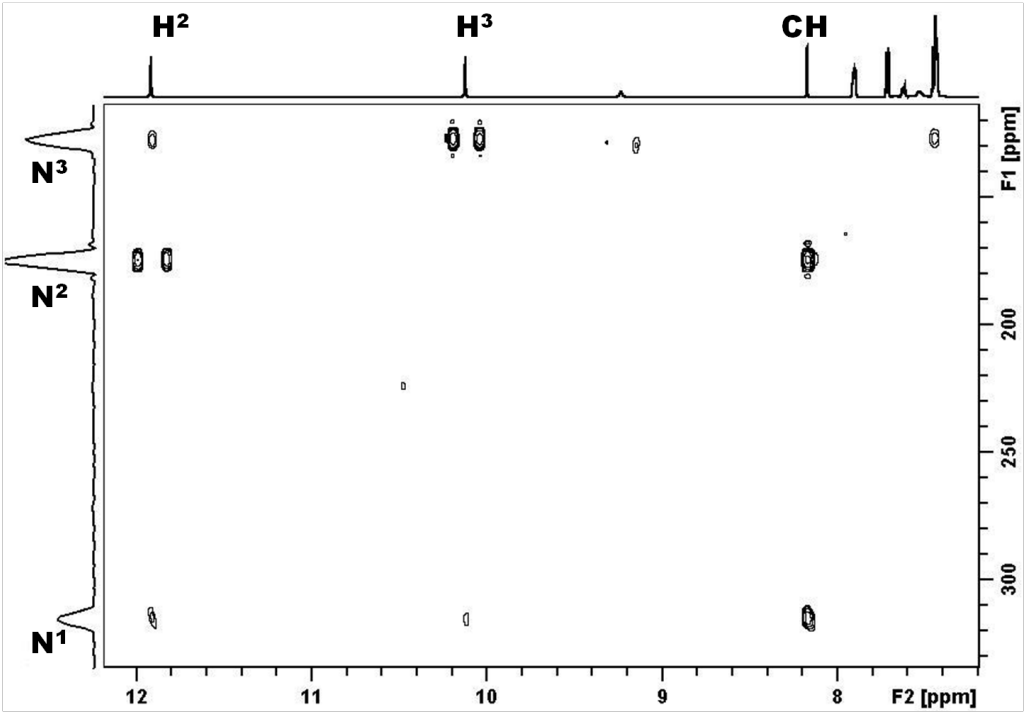

Figure 2.16: $^{1}H^{15}N$-HMBC NMR spectrum of PTSC*IPh* (**1d**) and **2d** (R = $N^{4}Me_2$).

The ^{15}N NMR chemical shifts are listed in Table 2.12. They are distributed over a range of almost 300 ppm, from 334 ppm (low field) to 53 ppm (high field). With the information from the corresponding ^{1}H NMR spectra (data summarised in Table 2.11 on page 80), assignment of the shift values $\delta_{^{15}N}$ to the corresponding nitrogen atoms in the TSC structure was achieved.

The starting point for ^{15}N signal assignment was the proton signal of the imine group, $\delta_H(H^1C{=}N)$, the sharp singlet at 8 ppm. This proton (H^1) is coupled to two nitrogen atoms in the TSC molecule (Figure 2.15): through two bonds to the imine nitrogen N^1 at δ_N = 300 ppm, and through three bonds to N^2. N^2 has a direct $^{1}J_{H,N}$ coupling, visible as a double cross-peak that is easily identified in the spectrum. The signal which matches those

two conditions, i.e. the coupling to H^1C=N and the $^1J_{H,N}$ coupling, is the double cross-peak at $\delta_N = 174$ ppm. H^2 exhibits two further ^2J correlations, to N^1 and N^3.

Completing the assignment, the thioamide protons of S=C-N^3H^3 group are represented by the second double cross-peak at $\delta_H = 10$ ppm and $\delta_N = 110$ ppm for ligand **1d**. N^3 receives two further couplings, one from H^2 (as mentioned above), and the other from the aromatic *ortho*-protons of the *p*-iodophenyl substituent (Figure 2.15). Both are found in the 2D spectrum and confirm the correct assignment to the respective nitrogen atoms in the TSC structure.

Table 2.12: ^{15}N NMR chemical shifts δ_N and ^{1}H^{15}N coupling constants $^{1}J_{H,N}$ for TSC ligands dissolved in dmso-d_6 (298 K).

Ligand R^1 = 1a-d, 2a-d, 3a-d		δ_{N^1} [ppm]	δ_{N^2} [ppm]	$^{1}J_{H,N^2}$ [Hz]	δ_{N^3} [ppm]	$^{1}J_{H,N^3}$ [Hz]
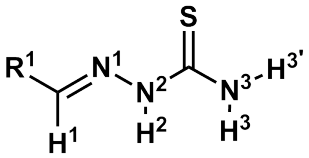	**1a**	319	171	97.7	110	93.5 / 89.0
	2a	306	170	98.5	107	95.1 / 88.7
	3a	322	172	98.9	110	93.5 / 89.5
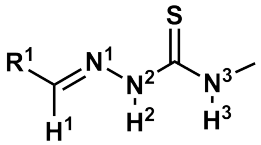	**1b**	316	170	99.0	104	n.o.*
	2b	304	169	97.8	101	n.o.
	3b	319	171	99.0	104	n.o.
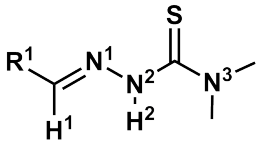	**1c**	331	171	n.o.	103	–
	2c	318	170	92.3	100	–
	3c	334	171	n.o.	104	–
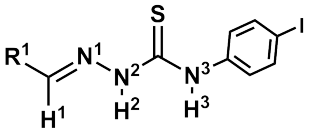	**1d**	315	174	98.8	127	91.7
	2d	302	174	97.7	125	90.8
	3d	319	175	99.1	128	91.5

*n.o. not observed, – not applicable because atom or bond not present in respective ligand.

The imino nitrogen resonance δ_{N^1} is found at around 300 ppm. This represents the largest chemical shift for the TSC nitrogen atoms. This signal also shows the largest variation between different ligands. ITSCNMe_2 **3c** has the lowest shift of 334 ppm of all TSCs presented here.

The hydrazinic nitrogen N^2 shows a double cross peak around 170 ppm with a coupling constant of 98 Hz. N^2 is less downfield-shifted than N^1, and N^3 resonates even further towards higher field, between 101 ppm and 128 ppm.

Ligands **2a-d** also have a fourth nitrogen atom in their structure, the dimethylamino substituent N^4Me_2 (Figure 2.14). Its chemical shift is found at 53 ppm for all four TSCs of series **2**. N^4 is the most high-field ^{15}N signal.

Table 2.12 lists the values of the scalar $^1J_{NH}$ coupling constants. The one-bond correlation between a proton and a nitrogen atom it is directly attached to are in the range of 90 to 100 Hz,[19] measured as the shift difference (in Hz) between the two cross-peaks that constitute the signal.[20]

The two amide protons in ligands **1-3a** exhibit two different coupling constants for the N^3H_2 group, one of 87.5-89.0 Hz that is smaller, and one of 93-95 Hz that is slightly larger. For series **b** ligands, which bear one proton and one methyl group at the amide position N^3, the N^3H coupling was not observed. In contrast, for the hydrazinic N^2H^2 the coupling constant is between 92.3 Hz and 99.1 Hz and it is the largest observed in this study.

In summary, all ^1H and ^{13}C NMR signals of thiosemicarbazones were assigned to the structure and the most characteristic resonances were compared within the series of TSCs presented here. The knowledge of the chemical shifts of ligand signals will be crucial for the characterisation of their ruthenium complexes. Section 2.4.5 will discuss the influence of the structural variations between the TSCs on their NMR chemical shifts in

more detail.

2.3.7 NMR Spectroscopy of Ruthenium TSC Complexes

NMR spectra of TSC ruthenium complexes were recorded in three different solvent systems. Therefore, this section is split into three parts. The first one presents the initial NMR characterisation of the complexes, which was carried out in deuterated chloroform ($CDCl_3$). Selected ruthenium complexes were synthesised in $CDCl_3$ directly, with the aim to gather chemical shift data for comparison purposes. The second part of this section describes ^{1}H NMR spectra recorded of DMSO solutions of selected complexes. Finally, spectra of D_2O solutions of complex [**15**] provide an insight into the stability of these TSC ruthenium complexes in aqueous systems.

Structure Confirmation and Chemical Shifts in $CDCl_3$

Figure 2.17 shows the ^{1}H NMR spectrum of complex [**15**], [(*p*-cymene)Ru(**2a**)Cl]Cl, recorded in $CDCl_3$, including the complete signal assignment of ^{1}H NMR resonances to the structure. From left to right, signals **a,b,c** and **f** are assigned to the TSC ligand **2a**. The sharp singlet **a** at 8.75 ppm belongs to the imino proton N=C*H*, and the two doublets **b** and **c** are the resonances of the aromatic ring protons. In the aliphatic region of the spectrum, the intense singlet **f** (δ_H = 3.5 ppm) represents the dimethylamino group of the TSC. The remaining signals in Figure 2.17 (**d**, **e**, **g-j**) are of the *p*-cymene protons. Of those, the two pairs of doublets around 4.8 ppm - 5.5 ppm (**d**/**e** either side of the DCM peak), belong to the four aromatic protons. Those signals were assigned by 2D NMR methods, using ^{1}H/^{13}C correlations which will be discussed in detail in Section 2.4.5. With this assignment in place, spectra of other *p*-cymene ruthenium complexes with TSC ligands

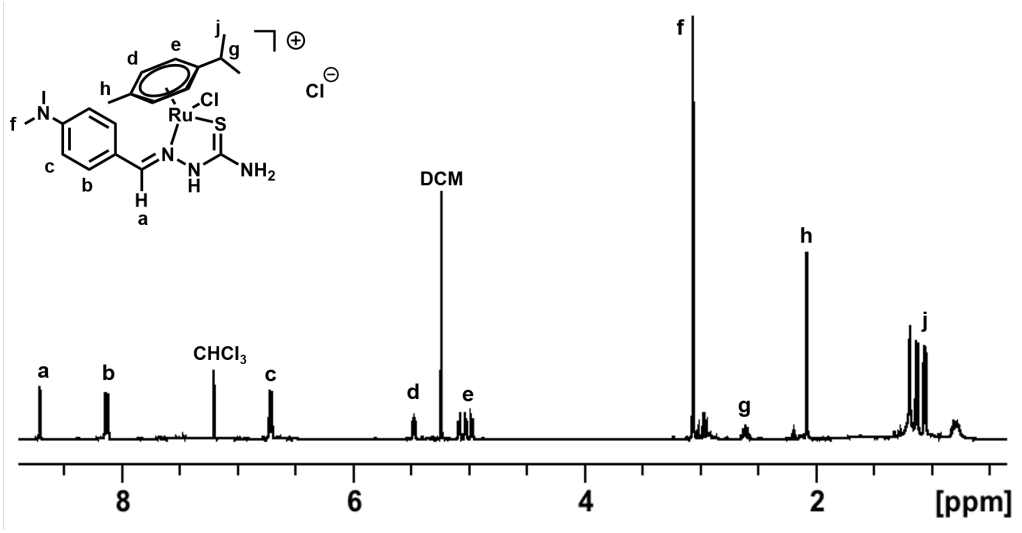

Figure 2.17: ^{1}H NMR spectrum and signal assignment for [(*p*-cymene)Ru(2a)Cl]Cl ([**15**]), recorded in $CDCl_3$, at 400 MHz and 298 K.

were analysed by comparison.

Table 2.13 contains ^{1}H NMR data for 21 ruthenium TSC complexes, aggregated in three groups: Complexes [**6**]-[**14**] have a PTSC ligand, complexes [**15**] - [**22**] are of dimethylamino TSCs **2 a-d**, and complexes [**23**] - [**28**] have a iodophenyl TSC of series **3**.

Within each group, the table directly compares characteristic ^{1}H NMR chemical shifts between the chlorido and the iodido complex of each individual TSC ligand. The following results stand out.

- The largest shift difference ($\Delta\delta_H$) between chlorido complexes and iodido complexes is for the hydrazinic N^{2}H. This NH signal is observed as far downfield as 13.1 ppm for chlorido complexes ([**19**]) or 15.2 ppm ([**13**]), for the corresponding iodido complexes this shift is ca. 2 ppm lower and is found between 11.45 ppm ([**20**]) and 13.97 ppm ([**22**]), respectively.

- Iodophenyl *IPh* substituted ligands **1d** and **2d** cause larger shifts for

Table 2.13: Characteristic ^{1}H NMR chemical shifts for Ru-TSC complexes: Comparison between chlorido and iodido analogues of [(*p*-cymene)Ru(*TSC*)X]$^+$ (X = Cl, I) for TSCs **1a** - **3c**.

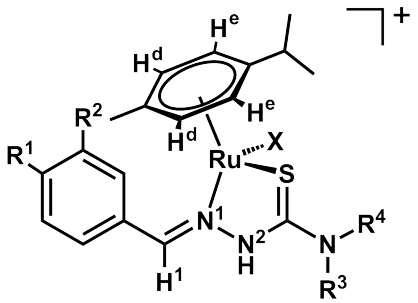

No	[(***p*-cymene**)**Ru**(***TSC***)**X**]$^+$			**N**^{2}H	**N**^{1}**=C**H^1	**H**^{d}	**H**$^{d'}$	**H**$^{e'}$	**H**^{e}
6*	PTSC	(**1a**)	**Cl**	14.66	9.07	5.43	4.88	4.82	4.66
8*	PTSC*NMe*	(**1b**)	**Cl**	14.84	8.90	5.38	4.86	4.79	4.62
9*			**I**	13.48	8.96	5.31	4.85	4.75	4.50
10	PTSCNMe_2	(**1c**)	**Cl**	14.03	10.12	5.34	4.96	4.73	4.66
12			**I**	11.76	9.88	5.33	4.95	4.76	4.66
13	PTSC*IPh*	(**1d**)	**Cl**	15.24	8.94	5.33	4.84	4.74	4.65
14			**I**	13.97	9.08	5.36	4.92	4.78	4.63
15	DTSC	(**2a**)	**Cl**	n.o.	8.75	5.51	5.12	5.06	5.01
16*			**I**	n.o.	8.78	5.53	5.14	5.03	4.94
17*	DTSC*NMe*	(**2b**)	**Cl**	13.39	8.76	5.46	5.06	5.04	4.94
18*			**I**	12.92	8.69	5.53	5.12	5.02	4.92
19	DTSCNMe_2	(**2c**)	**Cl**	13.14	9.71	5.17	5.17	5.05	4.96
20*			**I**	11.45	9.61	5.60	5.18	5.18	4.96
21	DTSC*IPh*	(**2d**)	**Cl**	n.o.	9.00	5.49	5.11	5.11	4.99
22			**I**	13.44	8.73	5.53	5.16	5.05	4.93
23	ITSC	(**3a**)	**Cl**	15.08	8.95	5.54	4.92	4.92	4.88
24			**I**	n.o.	9.02	5.43	4.89	4.80	4.73
25*	ITSC*NMe*	(**3b**)	**Cl**	14.94	8.83	5.48	4.91	4.86	4.84
26*			**I**	13.20	9.01	5.43	4.88	4.76	4.75
27	ITSCNMe_2	(**3c**)	**Cl**	14.12	10.03	5.45	5.00	4.84	4.80
28			**I**	11.89	9.84	5.45	4.99	4.83	4.76

† recorded in dmso-d_6.

the NH resonance than ligands of the other series **a-c**. This result compares well with the findings for the free TSC ligands (Section 2.3.5). The NH proton signal showed the same trend compared between the three seies **1 -3**.

- Complexes [**10**], [**12**], [**19**], [**20**], [**11**] and [**28**] of amide-NMe_2 substituted TSCs **1-3c** show the largest chemical shift for the imino proton N=CH^1. Their H^1 signal is shifted approx. 1 ppm further downfield (than for complexes of the other TSC ligands in their respective group.

- For all complexes, the four doublets for the aromatic *p*-cymene protons H^d - H^e are found in the range of 4.50 ppm - 5.60 ppm, with group **1** showing the lowest and group **3** the highest shifts.

^{1}H NMR of [(*p*-cymene)Ru(2a)Cl]Cl [15] in Aqueous Solution

The ^{1}H NMR spectra of [(*p*-cymene)Ru(**2a**)Cl]Cl ([**15**]) in D_2O solutions (5% DMSO) were recorded at 600 MHz and 298 K.

Figure 2.18 shows the spectral region of the aromatic *p*-cymene protons **d/d'** and **e/e'**. Only two of the three spectra show clearly resolved signals. The spectrum which was recorded 10 min after complex [**15**] was dissolved does not show the same sharp peaks as the one that was recorded of the same solution 12 hours later (Figure 2.18, middle), in which the sample was equilibrated at room temperature. In contrast, the spectrum of the sample of [**15**] which was equilibrated in NaCl solution (154 mM in D_2O) for the same period shows signals of the same chemical shifts and comparable intensity.

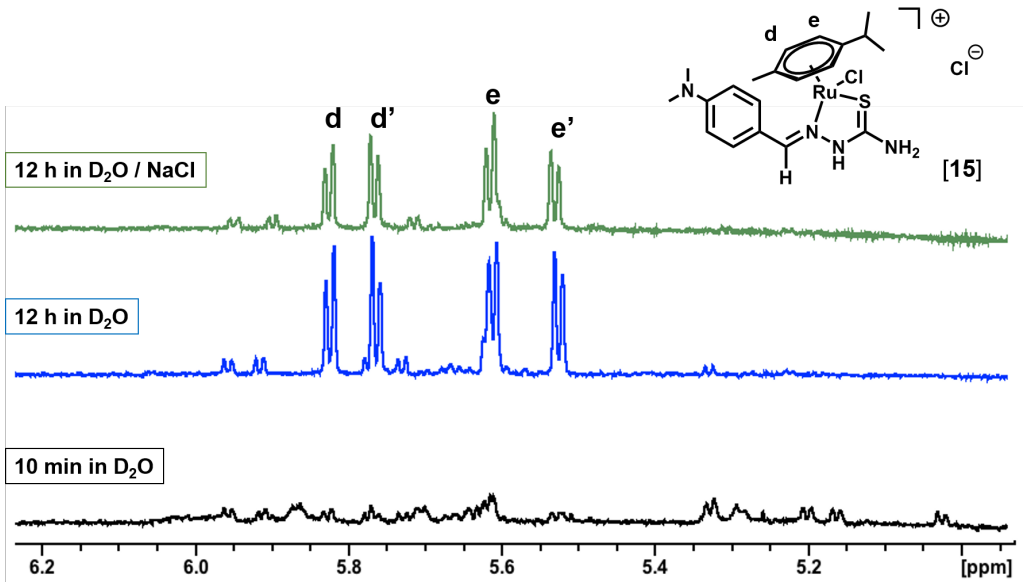

Figure 2.18: Comparison of ^{1}**H NMR** signals of the aromatic *p*-cymene protons **d/d'** and **e/e'** of [(*p*-cymene)Ru(**2a**)Cl]Cl (**[15]**) in D_2O solutions (5% DMSO), recorded at 600 MHz and 298 K after 10 min and after 12 h of equilibration at room temperature, and after 12 h in NaCl solution (154 mM in D_2O).

^{1}H NMR in dmso-d_6

The ^{1}H NMR spectra of DMSO solutions of several ruthenium TSC complexes showed varied results. Figure 2.19 compares the spectra of the chlorido complex of ligand **1d**, [(*p*-cymene)Ru(PTSC*IPh*)Cl]Cl, that were recorded prior to and after the acquisition of 2D NMR data on the same sample. The first spectrum was recorded within 10 min of dissolving the sample, while the second was acquired 2 h later. The two spectra both show six intense doublets in the region expected for the *p*-cymene proton resonances. The roofing and intensity suggest that the two doublets at 5.8 ppm belong to one species, and the four doublets further up-field belong to a second species.

Figure 2.20 shows ^{1}H NMR spectra of three complexes, each dissolved

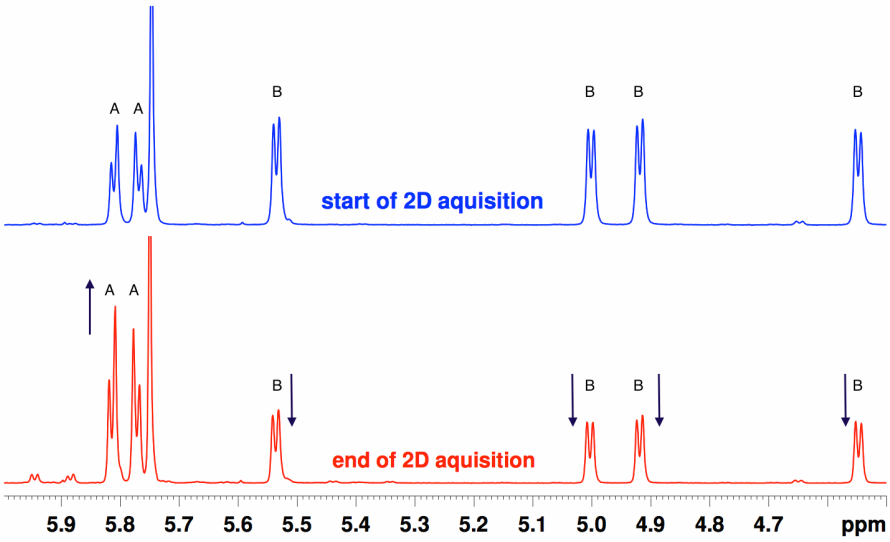

Figure 2.19: Comparison of ^{1}H NMR spectra of complex [**13**] recorded before and after acquisition of a ^{1}H^{15}N-HMBC spectrum in dmso-d_6 at 298 K shows the presence of two sets of signals for the *p*-cymene protons, indicating two species A and B are present in solution and that the ratio of A to B changes in the period of 2 h in which 2D NMR data was acquired.

in dmso-d_6. The spectral region which is enlarged in the box below the full spectra highlights the differences in the chemical shifts of the aromatic *p*-cymene protons between complexes [**19**] (top), [**12**] (middle), and [**29**] (bottom). For the latter two there is a second set of four doublets (marked with $*$). The presence of this second species indicates that the complexes undergo a structural change or substitution reaction in the solution. It is to be investigated what the nature of the second species is, and whether, in equilibrium, one structure is favoured.

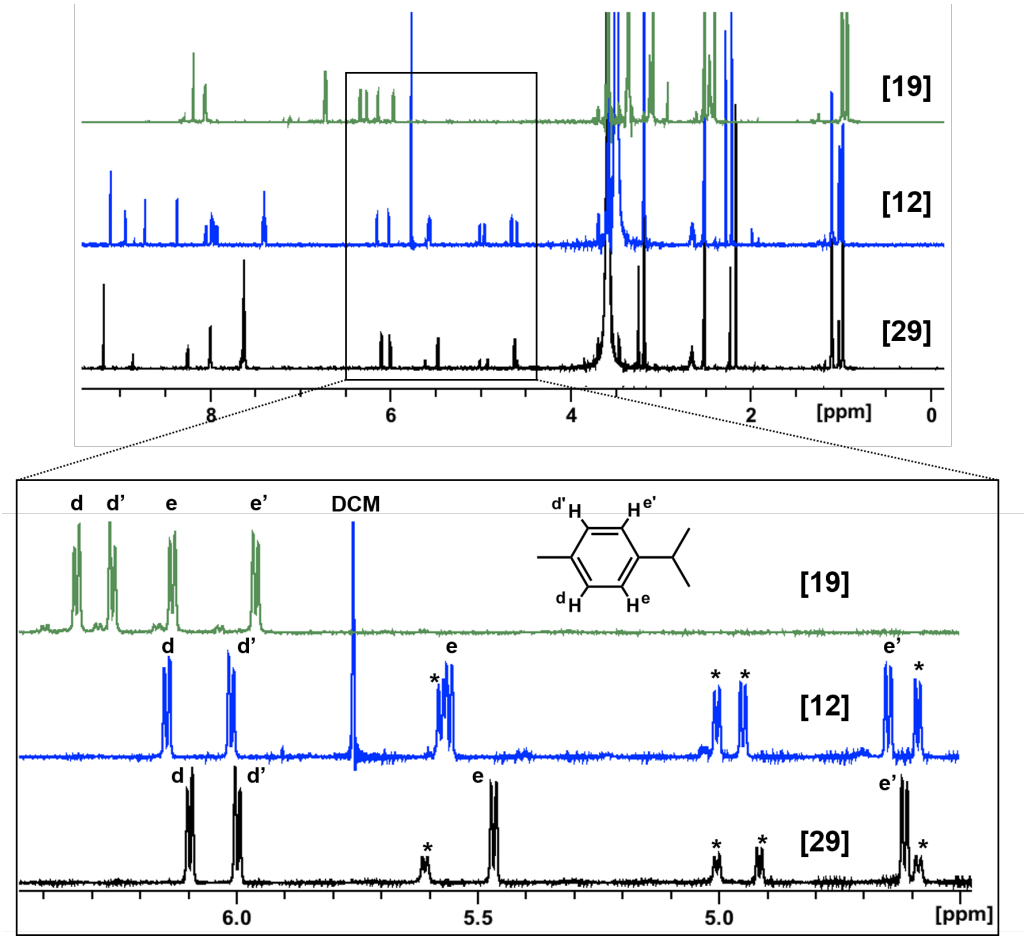

Figure 2.20: Comparison of ^{1}H NMR spectra of complexes [**19**], [**12**], and [**29**]. Spectra were recoded in solution (dmso-d_6, 600MHz, 298K). The figure shows the signals of the *p*-cymene protons **d,e**. Spectra of complexes [**12**] and [**29**] show a second set of those signals (∗).

Dimerisation of [(*p*-cymene)Ru(DTSC*IPh*)Cl]Cl ([21])

The reaction of complex [**21**] to [**30**] was first observed by NMR. Figure 2.21 shows the two spectra of the solution containing [**21**] and NH_4PF_6 in methanol, 2 and 12 h after mixing.

The first spectrum already shows two sets of signals, with 8 doublets in the region between 5 and 6.5 ppm, which correspond to two chiral *p*-cymene complexes. The two sets exhibit a significant shift difference between each other, with the first one ranging from 5.2 - 5.8 ppm and the second from

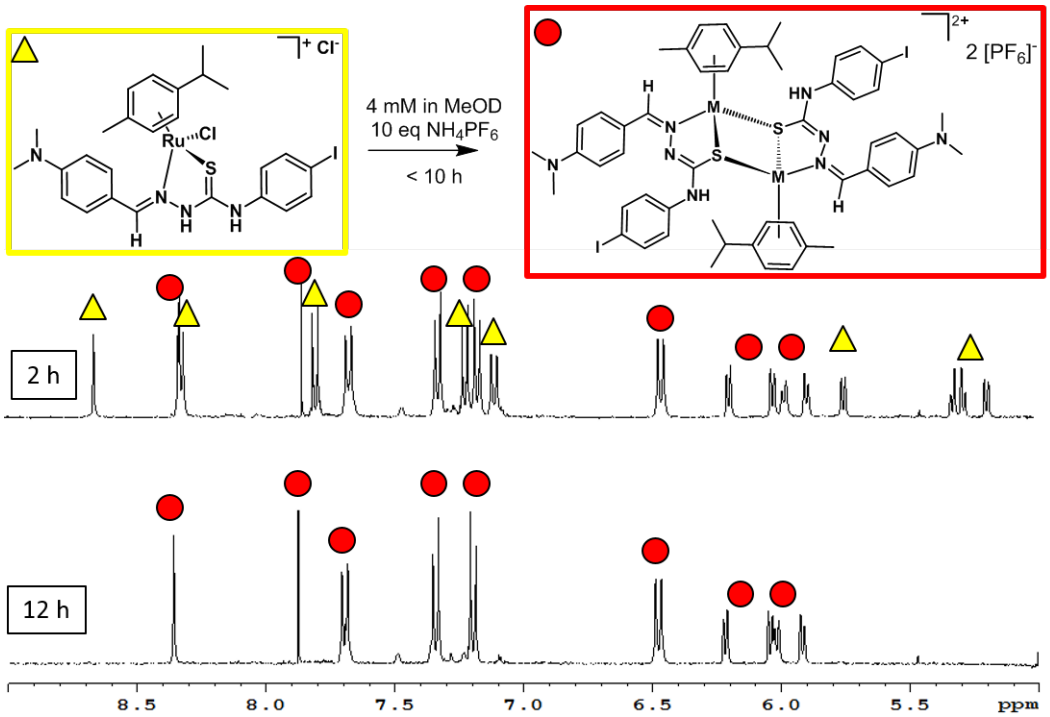

Figure 2.21: ^{1}H NMR spectra of a solution of [**21**] in methanol-d_4 show two species after 2 h and only one after 12 h. The dimer [**30**] crystallised in the NMR tube.

5.9-6.2 ppm.

Figure 2.22 shows the ^{1}H NMR spectrum of the dimer, recorded within 30 min after dissolving the red crystals in dmso-d_6. The *p*-cymene signals are shifted as far downfield as in the spectrum of the reaction mixture after 12 h (Figure 2.21). Only one set of signals is present, and the integrals of the signals are consistent with the expected values. The signal is observed for the hydrazinic NH proton, which is consistent with the expected structure of the dimeric complex.

Complex [**30**] is stable in solution for several hours. The observation of only one NH proton is in accordance with the crystal structure, and comparison to the spectrum of the free ligand in the same solvent reveals that the signal for the hydrazinic NH is lost while the thioamide proton

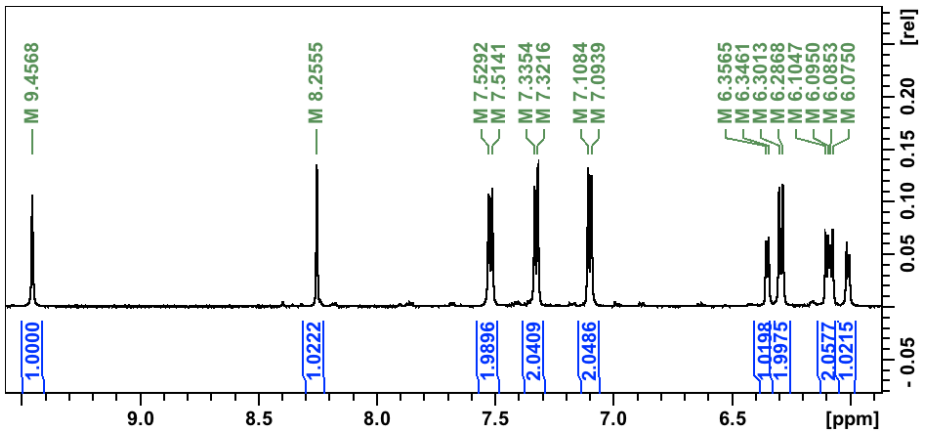

Figure 2.22: Plot showing the aromatic region of the ^{1}H NMR spectrum of dinuclear ruthenium complex [**30**] in DMSO solution with peak labels and integral values. Integrals highlight the up-field shift of

remains part of the structure after complex formation.

Due to the rotational (C_2) symmetry of the molecule, the dimeric nature is not obvious from a standard ^{1}H NMR spectrum. Both the imine proton and carbon signal shift to lower field, δ_H = 0.2 ppm, δ_C = 19 ppm.The aromatic protons of the *p*-cymene ring shift differently in the two structures. The arene protons are more de-shielded in the dimer, in which the ligand is deprotonated. They are found at 5.5 - 6.3 ppm), while for the monomeric, chloride containing complexes they are shifted closer to 5ppm (5.5-4.5 ppm).

The difference between the chemical shifts is remarkable, compared to the data presented in Table 2.13. It is assumed that the electronic structure of the deprotonated TSC influences the electronics at the metal and that this effect is transferred to the arene, leading to this de-shielding that is observed in the ^{1}H NMR spectrum.

These shifts are solvent independent. Shift variations in polar solvents are as small as 0.1 ppm between the spectrum in methanol-d_4 (Figure 2.21 and dmso-d_6 (Figure 2.22), respectively.

^{15}N NMR coordination shift in Ru-bound TSCs

After the nitrogen atoms of the TSCs were characterised by their ^{15}N-chemical shift, the ^{1}H^{15}N-HMBC NMR experiment was repeated with solutions of selected arene-ruthenium TSC complexes.

Figure 2.23 presents the correlation spectrum of the dinuclear complex [(*p*-cymene)Ru(DTSC*NMe*$_2$)]$_2$[PF$_6$]$_2$ (**[30]**, Figure 2.23 **A**). There are five signals visible in the spectrum, which are caused by the couplings denoted in the Table included in Figure 2.23 B.

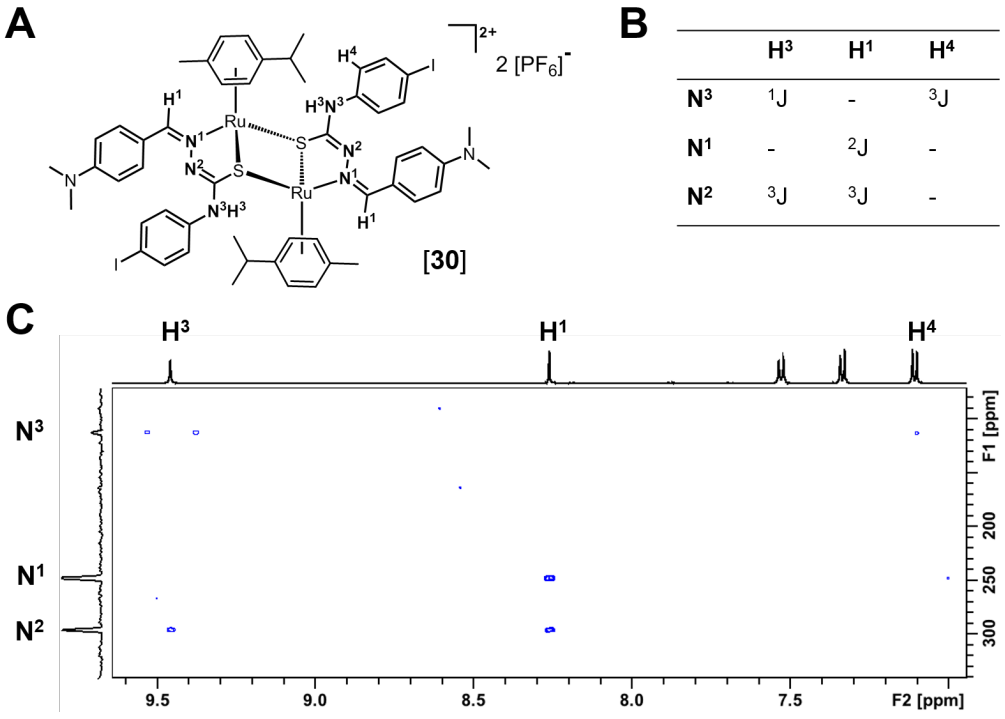

Figure 2.23: ^{1}H^{15}N-HMBC NMR spectrum of [(*p*-cymene)Ru(DTSC*NMe*$_2$)]$_2$[PF$_6$]$_2$ **[30]**

Compared to the results for mononuclear TSC complexes, the ^{15}N NMR signal of N^2 is shifted downfield to 297 ppm, while N^1 experienced an up-

field shift to 250 ppm.

The results of the ^{15}N NMR chemical shift determination for three further ruthenium complexes are listed in Table 2.14. The ^{1}H^{15}N HMBC NMR spectrum of complex [**19**] showed two cross-peaks, both correlations of the same proton signal (δ_H = 8.18 ppm); the first at δ_N = 247.4 ppm, and the other at δ_N = 292.3 ppm. Similarly, the spectrum of complex [**12**] also shows two cross signals for one proton (δ_H = 9.17 ppm); one at δ_N = 271 and one at 292 ppm. Both the ^{1}H and the ^{15}N chemical shifts for complex [**29**] were similar to those of complex [**12**].

Table 2.14: ^{15}N chemical shifts for Ru-TSC complexes, recorded in solution (50 μM in dmso-d_6), at 61.8 MHz and 298 K.

Complex	**Peak**	δ_H **[ppm]**	δ_{N^1} **[ppm]**	δ_{N^2} **[ppm]**
[**19**]	H^{1}C=N	8.18	247	292
[**12**]	H^{1}C=N	9.17	271	292
[**29**]	H^{1}C=N	9.10	272	293
[**30**]	NH^3(*IPh*)	8.70	187 (N^3)	296
	H^{1}C=N	8.36	250	296

No coupling was observed from the NH proton in the three mononuclear complexes [**12**], [**19**], and [**29**]. Compared to the data for the free ligands **1c**, **2c**, and **3c**,

2.4 Discussion

Three different series of TSC ligands were prepared and their structures were fully characterised by NMR spectroscopic methods.

2.4.1 Synthesis

Thiosemicarbazones form by imine condensation between thiosemicarbazides and carbonyl compounds. Using this common reaction has the benefit that a broad range of starting materials is available, most of which are inexpensive. Additionally, the yields are high and the reaction is comparably 'green'; except for one equivalent of water, all atoms from the starting materials are also incorporated in the product molecule. The efficiency and diversity that are provided by imine formation are attractive reasons for its use in the design of TSC ligands for arene ruthenium anticancer complexes.

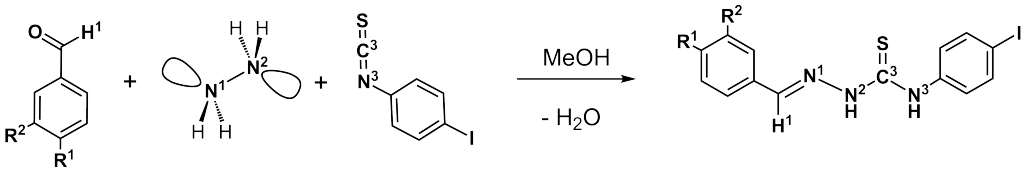

1 $R_1 = R_2 = H$
2 $R_1 = NMe_2$
3 $R_2 = I$

d

1-3d

Figure 2.24: Scheme showing the multi-component reaction of aldehydes **1-3** with hydrazine (H_2N-NH_2) and thiosemicarbazide (**d**) in a one-pot reaction to form TSC ligands **1-3d**.[7]

A multi-component reaction,[7] illustrated in Figure 2.24, was used for the introduction of a 4-iodophenyl substituent (-C_6H_4-I, *IPh*) at the thioamide nitrogen N^3. Mechanistically, hydrazine first reacts with 4-iodophenylisothiocyanate to form 4-iodophenylthiosemicarbazide, and this intermediate subsequently reacts with the respective aldehydes to the (4-iodophenyl)-thiosemicarbazones **1d-3d**. With this protocol, first published by Cunha

and da Silva,[7] the isolation and purification of the thiosemicarbazide intermediate can be avoided by mixing all three starting materials at the same time. However, to limit side-reactions, hydrazine monohydrate needs to be added to the reaction vessel last, as it is the component which reacts first. The products that were obtained under these conditions, the three iodinated ligands **1d-3d**, are novel compounds according to a search of the Cambridge Crystallographic Data Centre database (CCDC), and their structures have not been reported in the literature.

Preparation of Ruthenium Complexes

Arene ruthenium complexes were prepared in $CDCl_3$ and the proton spectra recorded within 30 min of mixing. The reactions had reached completion during this time in all cases, which can be seen from the splitting of the *p*-cymene aromatic proton resonances. In the precursors **4** and **5**, these protons resonate as two doublets, because their structures are symmetrical and therefore non-chiral. Upon coordination of the TSC, this symmetry is lost and the asymmetry of the metal centre renders the four aromatic *p*-cymene protons magnetically inequivalent. As a result, they appear as four signals in the NMR spectrum, each split into a doublet by a coupling of 6 Hz, consistent with the expected three-bond coupling to its neighbour proton.

The speed with which the reaction proceeded to completion is particularly surprising with respect to the structural change the TSCs have to undergo in order to coordinate the metal in the N^1,S-bidentate fashion that results in a five-membered chelate ring.

2.4.2 Mass Spectrometry

Mass spectrometric results can help to identify the molecular formula of stable fragments of metal complexes.[21] Furthermore, the isotopic pattern is a useful indicator for identity between mass-spectrometric data and the mathematically predicted mass-distribution.[22, 23]

ESI-mass spectra show the same mass/charge signal for the chlorido as for the iodido complex, and the isotopic pattern is in agreement with a mononuclear Ru(II) species in which not only the respective counter ion is lost, but in addition to this the halido monodentate ligand is lost as well. Ruthenium exhibits a wide isotopic distribution with a characteristic fingerprint, which is easily detectable from mass spectra, even at lower mass-accuracy.[23]

As concluded in Section 2.3.3, this formula is consistent with a species that has lost the counter ion, which is the easiest ionisation pathway, but has also lost the monodentate ligand and a proton to match the single positive charge.

The results are coherent between all complexes that were studied here, and research by others in the field confirms the presented findings: Su et al. report the structure and spectroscopic data for complex [(*p*-cymene)Ru(BzTSC)Cl]Cl, with BzTSC = benzaldehydethiosemicarbazone which is named PTSC (or ligand **1a**) in this thesis.[24] They found a m/z of 414.0587 (calc. 428.0739) for the species [(*p*-cymene)Ru(BzTSC)Cl]-**HCl**$^+$. This value matches the m/z of 414.0 that was determined for the two complexes [**6**] and [**6**] of ligand **1a** (Table 2.5 on page 69).

In Chapter 1, the possibility of the TSC to tautomerise to the thiolate form was discussed page 18. This tautomerisation is a means by which charge can be delocalised within the molecule, and it therefore renders the

hydrazinic proton the most acidic one in the structure. Deprotonation of the coordinated TSC results in a negative charge on the ligand, which is delocalised towards the metal centre to counteract the loss of the negatively charged monodentate ligand. The result is a mono-cationic complex of the general formula [(*p*-cymene)Ru(L-H)]$^+$.

2.4.3 X-ray Crystal Structures

Crystals of DTSC*NMe* (**2b**) for structure determination by X-ray diffraction grew in a saturated solution of the ligand in dmso-d_6, probably due to water uptake in DMSO over several days. Dmso is known to be hygroscopic,[25] and because the solubility of TSCs in aqueous systems is much lower than in DMSO, crystallisation is facilitated by the increasing water content in the sample.

In the structure presented in Section 2.3.4, ligand **2b** shows *E*-configuration. This is expected, as this configuration is the lowest energetic form for the TSC structure due to intramolecular H-bonding interactions between the amide NH and the imino nitrogen. H-bonding is a common structural feature in thiosemicarbazones,[4, 26] and both crystallographic and structural parameters were in good agreement with a previous report for this structure.[4, 11]

However, the opposite configuration is required for N,S-chelate formation. The five-membered chelate ring can only form when the azomethine nitrogen (HC=N1) and the sulfur atom are *cis*-configured, i.e. both are facing the metal. The PTSC*NMe*$_2$ ligand (**1c**) demonstrates this in the structure of [(*p*-cymene)Ru(**1c**)Cl]PF_6 [**10**]. The thiosemicarbazone adopts *Z*-configuration as it coordinates as an N/S chelating ligand to the ruthenium, forming a five membered chelate ring. The same conformation

was found in three different mercury complexes of the same ligand,[8] while the free ligand, which is reported in the same study, crystallised with *E*-configuration.

Mononuclear Complex [(*p*-cymene)Ru(1c)Cl]PF_6 [10]

Complex [**10**] appears to be the first example of an arene-ruthenium(II)-TSC complex that has been crystallised with a terminally *N*-dimethylated thiosemicarbazone. It crystallised from a concentrated methanolic solution, in a diffusion crystallisation experiment with diethylether.[27] The effect diffusing ether into the sample is a gradual saturation of the methanol solution with diethylether, causing the polarity (dielectric constant) of the solvent mixture to change slowly. As a result, the solubility of [**10**] in the mixture decreased, so that over a period of four days at 278 K, red block-shaped crystals formed. In addition to the single crystal structure which was presented in Section 2.3.4, this experiment also indicates that the compound is stable under these conditions, i.e. dissolved in methanol, for at least four days. However, the solution was kept in a closed atmosphere which contained only the vial headspace volume of air. The limit of oxygen supply to the sample appears to be a beneficial factor for the crystallisation of those Ru TSC complexes.

Crystallographic data for complex [**10**] are consistent with structures reported in the literature for similar Ru half-sandwich complexes that contain other TSC ligands.[14, 16, 18, 28] In particular, the space groups are mostly monoclinic $P2_1/C$[28–30] and all significant distances in the coordination sphere are similar to reported values. For this reason it is assumed that the structures within this series of ruthenium complexes that is presented in this thesis are of the expected piano-stool geometry, and that the thiosemicar-

bazone ligands bind as neutral chelators to a Ru^{2+} core. This assumption is also consistent with CHN elemental analyses for solids of the compounds, which confirmed the presence of two halide atoms per molecule.

Comparison to the Dinuclear Structure of [30]

The dinuclear complex **[30]** was obtained as a result of mixing the mononuclear chlorido complex [(*p*-cymene)Ru(DTSC*IPh*)Cl]Cl (**[21]**) of TSC ligand **2d** with NH_4PF_6 in methanol, to exchange the chloride counter ion for hexafluorophosphate. Introducing this bulky, non-coordinating anion can aid crystallisation of metal complexes by forming better ion pairs. Unexpectedly, in the case of complex **[21]**, the exchange of Cl^- for $PF_6{}^-$ did not yield the analogue [(*p*-cymene)Ru(DTSC*IPh*)Cl]$PFPF_6$. Instead, the dinuclear complex [(*p*-cymene)Ru(DTSC*IPh*)]$_2$[PF_6]$_2$ (**[30]**) crystallised during the slow evaporation of dichloromethane from the mixture.

The main feature of this dimeric structure is a rectangular Ru_2S_2 cluster which forms between the two metal centres and the sulfur atoms of the TSC ligands. Each TSC binds to two metal centres via its sulfur donor, while the imino nitrogen coordinates to only one ruthenium atom. Due to this particular binding mode, the two TSCs are arranged such that the dinuclear complex exhibits C_2 symmetry, making the TSC ligands equivalent by a 180° rotation around the long axis (Figure **??**).

A similar dimeric structure of a *p*-cymene-Ru(II) complex has recently been reported in the literature.[29] Comparable to complex **[30]** the structure contained two TSC ligands that bridge the two metal centres, forming a Ru_2S_2 rectangle, and the TSC is deprotonated at N^2, with and elongated C–S bond as a result.

In addition to the deprotonation, there are other structural changes in-

volved in the reaction of [**21**] with itself and NH_4PF_6, such as the E/Z isomerisation of the imine bond, and the formation of a second Ru-S bond which connects the two monomers. One aim of this thesis is to study this dimerisation in more detail, to gain an understanding of the processes that constitute this reaction. The results of the spectroscopic investigations presented in the following sections were undertaken to achieve this.

2.4.4 Natural-Abundance ^{1}H,^{15}N NMR Spectroscopy

Nitrogen NMR is a useful tool in both organic and inorganic chemistry.[19, 31–33] While the two nitrogen isotopes ^{14}N and ^{15}N both have NMR active nuclei, ^{15}N NMR is by far the more widely used technique, because ^{15}N has a nuclear spin of $\frac{1}{2}$.[34]

However, direct NMR detection of nitrogen-15 signals is difficult. The heavier isotope has a natural abundance of only 0.37%, ^{14}N, in contrast, accounts for 99.63% of the naturally occurring nitrogen.[35] Furthermore, the gyromagnetic ratio for ^{15}N ($\gamma^{15}N/\gamma^{1}H$) is -0.101. Combined with the low natural abundance of ^{15}N, the result is a relative signal intensity of 0.1% for nitrogen nuclei compared to an equal number of protons in the sample.

Before the use of indirect detection methods in two-dimensional quantum coherence NMR experiments,[19, 36, 37] one of two solutions led to a reasonable ^{15}N NMR spectrum. Either long measurement times (i.e. a large number of consecutive sweeps, followed by data averaging) or isotopic enrichment of the sample with ^{15}N. In other words, the acquisition of such a spectrum was expensive.

With the introduction of Fourier Transform (FT) methods in NMR spectroscopy, nitrogen-15 NMR experiments became much more practical, and the availability of stronger magnetic fields has since enhanced the sensit-

ivity and reduced the need for expensive ^{15}N labelling even further. The method has, for example, been applied to the study of protein motions in solution, by observing variations in the amide-nitrogen ^{15}N NMR chemical shift.[38] Today, the ^{1}H^{15}N-HMBC experiment is used routinely for structure elucidation of small and even large organic (bio)molecules.

Although ^{1}H^{15}N-HMBC is still the most insensitive[39] and time-consuming among the common two-dimensional NMR experiments used in small-molecule characterisation,[32, 33] it allows the use of naturally abundant ^{15}N for the detection of their ^{15}N NMR chemical shift.

^{1}H^{15}N-HMBC-NMR and chemical shifts of TSCs

The ^{1}H^{15}N HMBC experiment is a 2D heteronuclear spin correlation technique by which through-bond couplings between the two nuclei ^{1}H and ^{15}N can be detected. While the pulse program in this particular experiment was optimised for correlations through two and three bonds, the direct $^{1}J_{H,N}$ couplings were also observable, because no decoupling was applied during signal acquisition. Hence, the one-bond NH correlations are visible as double cross-peaks in the 2D spectra.

All ^{15}N chemical shifts that were determined in Section 2.3.6 are consistent with literature values for nitrogen atoms in similar structures.[19] The imino nitrogen can be compared with the shift of the pyridine nitrogen. The ^{15}N chemical shift of py-N is 317 ppm, which was used for relative shift referencing.[40] Figure 2.25 illustrates the influence of different substituents on δ_{N^1}, the ^{15}N chemical shift of the imino nitrogen. For each TSC ligand (see ligand number on x-axis), the graph shows the value for δ_{N^1} (Table 2.12 in the y-dimension.

The effect of phenyl substituents $\mathbf{R}^1$ is highlighted by the red and blue

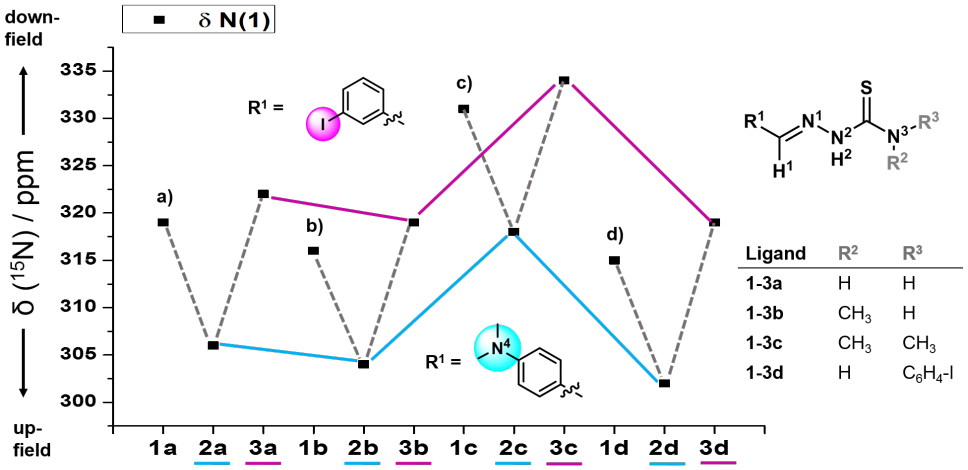

Figure 2.25: Influence of functional groups on the ^{15}N NMR chemical shift of the imino nitrogen, δ^1_N (data taken from Table 2.12). The phenyl substituent within the aldehyde residue $\mathbf{R}^1$ and thioamide substituents $\mathbf{R}^2/\mathbf{R}^3$ affect the resonance signal. While R^1 = 3-iodophenyl shifts the signal furthest downfiled, δ^1_N for dimethylamino TSCs **2a-d** is up-field shifted by 20 ppm compared to **3a-d**.

lines. The red line connects the values for series **3**, and the blue line represents the shifts for series **2** ligands. This representation highlights that the shift values for series **2** ligands are approx. 12 ppm smaller in all four groups **a - d**, which demonstrates the electron-donating ability and conjugation of the π-electron system in these ligands.

The *meta*-iodo substituent in series **3** ligands, however, does not affect the electron distribution in the TSC by as much: The purple line is shifted ca 5 ppm downfield compared to unsubstituted PTSCs (series **1**.

In contrast to the imino nitrogen N^1, the ^{15}N signal of N^3 is unaffected by methylation. The *p*-iodophenyl substituent in series **d**, however, has the biggest influence on the chemical shift of N^3. It de-shields the nitrogen and shifts the signal downfield by approx. 20 ppm compared to the other ligands.

The amide protons inter convert slowly on the NMR time scale due to

hindered rotation around the thioamide C-N bond, which has partial double-bond character.[41] The descriptors *cis* and *trans* refer to the orientation of the nitrogen-bonded proton relative to the thione sulfur (S3). *Trans* describes the proton lying *anti*, i.e. opposite (*E*; H3) to the sulfur, while and the *cis* proton (*Z*; H3') is the one *syn*, or adjacent, to the sulfur. For this reason, the chemical environment of the two most likely conformations, *cis* and *trans* to the sulfur atom, are different and their ^{1}H NMR chemical shifts are inequivalent as a result.[41]

One-bond NH couplings have the largest magnitude of all ^{15}N couplings.[19, 20] They can represent the s-character of the hybrid bonding orbital on the nitrogen,[42] which allows distinction between amino and imino NHs. Values for one-bond couplings are characteristic of the geometry at the specific nitrogen as follows: 75, 90, 135 Hz for pyramidal, trigonal, or linear bonding to nitrogen.[19] Values of ca. 96 Hz can represent either enamine or imino N(H) fuctionalities, with imino being C=N(+)H). Furthermore, amide geometry (cis-trans H / O) can result in both larger and smaller values from there (cis = 97.6 Hz , trans = 101.6 Hz).

2.4.5 NMR Spectroscopy with Ruthenium TSC Complexes

Table 2.13 on page 90 summarised characteristic ^{1}H NMR data for the 21 TSC complexes presented in this thesis. The results are in good agreement with NMR data for other piano-stool ruthenium complexes of the same or a similar type.[30] In particular, the ^{1}H NMR signals of the p-cymene aromatic protons show the expected coupling pattern due to the metal-centred chirality of the molecule.

The reason for this phenomenon is given by the chelating ligand, which introduces asymmetry to the structure. Because no symmetry operation achieves degeneracy between the aromatic ring protons, they become magnetically inequivalent. As a result, they appear as four signals in the NMR spectrum, each split into a doublet by a coupling of 6 Hz, consistent with the expected three-bond coupling to its neighbouring proton.

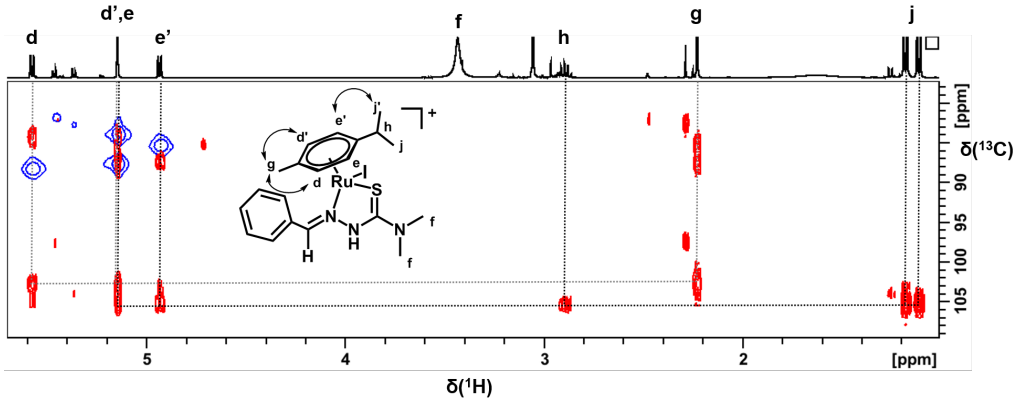

Figure 2.26: Section of ^{1}H,^{13}C-HSQC (blue) / HMBC (red) NMR spectra of [**20**] in $CDCl_3$, showing correlations between the aromatic and aliphatic *p*-cymene protons that were used to assign the four doublets **d**, **d'**, **e**, and **e'**.

The interpretation of 2D NMR spectra led to the full assignment of the ^{1}H NMR signals of the aromatic *p*-cymene protons. In Figure 2.26, the ^{1}H/^{13}C correlations are highlighted, showing the connection between **d/d'** and the methyl group **h** on the one hand, and between **e/e'** and the *iso*-propyl substituent **g,j** on the other.

The region for the *p*-cymene proton signals correlates well with literature reports for Ru *p*-cymene semicarbazone and thiosemicarbazone complexes. Zhou et al. report a *p*-cymene ruthenium complex of benzaldehydesemicarbazone *bzsc*, in which the half-sandwich complex crystallises in the same structure that is reported here. The four aromatic *p*-cymene protons show the same ^{1}H NMR chemical shifts and $^{3}J_{H,H}$ coupling constants for the

AA ´ BB ´ -spin system (four doublets at 5.53 - 4.59 ppm with $^3J_{H,H}$ = 5.7 Hz), and the ESI-MS results showed the same signal for $[(M^+)\text{-HCl}]^+$, as was discussed above.

One ^{1}H NMR signal stands out in Table 2.13, the one for the hydrazinic NH proton. For most of the complexes, the resonance of this exchangeable proton is shifted as far downfield as 12-14 ppm. It is notable that these shifts for N^{2}H are higher for the chlorido complexes than for the iodido complexes. This extreme downfield shift can be explained by hydrogen bonding of the NH with the chlorido ligand of another molecule in solution.

It is known that hydrogen bonding causes downfield shifts in ^{1}H NMR spectra of NH-containing molecules,[43] and the H-bond contacts which were found in the crystal structure of complex [10] indicate that connections between these groups are likely. In a non-polar solvent such as chloroform, solvation of the chloride is less likely, therefore the interaction with a hydrogen-bond donor becomes favourable.

The collection of ^{1}H NMR chemical shifts in Table 2.13 gives an overview of the electronic influence the variety of TSC substituents can have on the complex.

NMR spectra of the dinuclear TSC complex [30]

The aromatic protons of the *p*-cymene ring shift differently in the two structures. The arene protons are more de-shielded in the dimer, in which the ligand is deprotonated. They are found around 6 ppm (5.5 - 6.3 ppm), while for the monomeric, chloride containing complexes they are shifted closer to 5ppm (5.5-4.5 ppm). The difference between the chemical shifts is remarkable, compared to the data presented earlier in this chapter. It is assumed that the electronic structure of the deprotonated TSC influences the elec-

tronics at the metal and that this effect is transferred to the arene, leading to this de-shielding that is observed in the ^{1}H NMR spectrum.

Confirmation of Ru-N coordination by ^{1}H^{15}N-HMBC-NMR

^{15}N NMR is widely used in biological NMR, for structure elucidation of proteins or smaller peptides, and ^{1}H^{15}N coupling constants and residual dipolar couplings (RDC) provide a wealth of structural information, if recorded and interpreted carefully.[44] However, this technique is not used much for the analysis of metal complexes in solution, because it is mainly a phenomenon in large molecules that tumble slowly on the NMR timescale.

Table 2.15: ^{15}N NMR chemical shifts for Ru-TSC complexes, recorded in solution (50 μM in dmso-d_6), at 61.8 MHz and 298 K.

[C]		δ^{1}_{H}	δ_{N^1} (L)	δ_{N^1} [C]	$\Delta\delta_{N^1}$ [ppm]	δ_{N^2} (L)	δ_{N^2} [C]	$\Delta\delta_{N^2}$ [ppm]
12	**[Ru(1c)I]**	9.17	331	271	- 60	171	292	+ 121
19	**[Ru(2c)Cl]**	8.18	318	247	- 71	170	292	+ 122
29	**[Ru(3c)]I**	9.10	334	272	- 62	171	293	+ 122
30	**[Ru$_2$(2d-H)$_2$**	8.36	302	250	- 52	174	296	+ 122

Here, the ^{15}N NMR chemical shifts of thiosemicarbazones have been determined by ^{1}H^{15}N-HMBC-NMR in solutions, using natural abundance of ^{15}N. The same technique and experiment was applied to study selected ruthenium TSC complexes by ^{1}H^{15}N-HMBC-NMR in DMSO solution.

Table 2.15 presents the shift results for two ^{15}N NMR signals of each complex: of the nitrogen atom that binds to the metal (imino N) and its hydrazinic neighbour. Both signals show distinct and intense coordination shifts. The shift difference for the hydrazinic nitrogen signal, $\Delta\ \delta_{\ N^2}$ is particularly large – the signal is shifted 122 ppm downfield, which suggests a significant change in its electronic environment.

One report in the literature mentions the measurement of nitrogen-15 chemical shifts for a Ga^{3+} bis-TSC complex, and reports the imino N signals to be shifted to 277/288 ppm, respectively.[45] However, the data are not mentioned in the text of the article, and no details are given for a comparison to the free ligand, or which reference scale has been used. Therefore it is impossible to say without further data or an experiment, which nitrogen moiety in the gallium TSC complex the signals originate from.

Delp an coworkers published ^{15}N NMR chemical shift values for a series of amido and amino ligands, which were studied in combination with several metal ions or coordination compounds.[46] With the aim to build a data base for ^{15}N NMR chemical shifts of nitrogen-bound ligands in metal complexes.[46]

Their report presents one example in which the ^{15}N NMR chemical shift of an anilino nitrogen (Ph-NH$_2$) shifts by -62 ppm upfield upon its reaction with a [(Tp)Ru^{2+}(PMe$_3$)] complex (with Tp = trispyrazolylborate). However, the same ^{15}N NMR signal shifts in the opposite direction, 59 ppm downfield, when this amino group looses one proton and, as a result, binds to the metal as anilido ligand.

Therefore, the large shift that was observed for N2 in the ^{15}N NMR spectra of their TSC complexes could indicate that the TSC is deprotonated at N2 in the respective solutions.

Combined with the results from ESI-MS experiments presented above, and the knowledge that the hydrazinic nitrogen N2 is indeed deprotonated in the solid state structure of the dinuclear complex **[30]**, the conclusion from the comparison of ^{15}N-NMR chemical shifts between complexes of the ligands **1c**, **2c**, and **3c** with the dimer **[30]**, is that p-cymene ruthenium complexes with thiosemicarbazone chelating ligands are deprotonated in

polar solvents and subsequently tautomerise to their monocationic form [(*p*-cymene)Ru(TSC-H)]$^+$ by means of loosing the monodentate ligand.

2.5 Summary

This chapter presented the synthesis and NMR spectroscopic characterisation of arene ruthenium thiosemicarbazone complexes. Twelve TSCs were prepared and their ^{15}N NMR chemical shifts fully assigned to the corresponding nitrogen atoms in the structure and proved to be consistent with literature data. In total, 25 ruthenium complexes were prepared and their structures were characterised by spectroscopic methods. Two solid state structures of ruthenium complexes were obtained, one for complex [**10**] which confirmed the coordination mode of the TSC ligand in the arene ruthenium complexes as the neutral N,S(thione) form. The second structure presents a dinuclear Ru-TSC complex, at the heart of which is a Ru_2S_2 rectangle. This dimer formed in a solution of complex [**21**] with PF_6, and more work will be presented in Chapter 3 to investigate this conversion.

The reactivity of ruthenium TSC complexes was demonstrated by ^{1}H NMR spectra of several complexes that showed conversion into a second species in DMSO or methanol solution. ESI-MS spectra confirmed a mononuclear, monocationic ruthenium TSC species, after loss of both halides, to be the most stable form of the structure under the experimental conditions. The result of the ESI MS study highlights that a conversion takes places in which both the chlorido and iodido complex form the same mono-cationic species. The most stable species contains only the central ruthenium atom and the TSC ligand, but no monodentate ligand.

The relation of ^{15}N NMR chemical shifts determined for the TSCs to

their corresponding ruthenium complexes showed an up-field coordination shift for the imino nitrogen atom which confirmed binding of the ligand to the metal via this position. The dramatic downfield shift of the signal for N^2 suggests deprotonation of the TSC, which is consistent with the crystal structure of the dinuclear complex **30** and the ESI-MS data discussed above. Therefore, this deprotonation is likely part of the mechanism of the formation of dinuclear Ru-TSC complexes, which will be investigated further as part of Chapter 3.

References

[1] F. A. French and E. J. Blanz, *J. Med. Chem.*, 1966, **9**(4).

[2] F. A. French, E. J. Blanz, J. R. DoAmaral, and D. A. French, *J. Med. Chem.*, 1970, **13**(6), 1117–1124.

[3] M. D. Hall, N. K. Salam, J. L. Hellawell, H. M. Fales, C. B. Kensler, J. A. Ludwig, G. Szaka, D. E. Hibbs, and M. M. Gottesman, *J. Med. Chem.*, 2009, **52**(10), 3191–3204.

[4] M. D. Hall, K. R. Brimacombe, M. S. Varonka, K. M. Pluchino, J. K. Monda, J. Li, M. J. Walsh, M. B. Boxer, T. H. Warren, H. M. Fales, and M. M. Gottesman, *J. Med. Chem.*, 2011, **54**(16), 5878–5889.

[5] D. C. Reis, M. C. Pinto, E. M. Souza-Fagundes, S. M. Wardell, J. L. Wardell, and H. Beraldo, *Eur. J. Med. Chem.*, 2010, **45**(9), 3904–3910.

[6] X. Du, C. Guo, E. Hansell, P. S. Doyle, C. R. Caffrey, T. P. Holler, J. H. McKerrow, and F. E. Cohen, *J. Med. Chem.*, 2002, **45**, 2695–2707.

[7] S. Cunha and T. L. da Silva, *Tetrahedron Lett.*, 2009, **50**, 2090–2093.

[8] E. López-Torres and M. Mendiola, *Inorg. Chim. Acta*, 2010, **363**, 1275–1283.

[9] P. Ren, T. Liu, J. Qin, and C. Chen, *J. Coord. Chem.*, 2003, **56**(2), 125–132.

[10] Y. Sun, S. Fu, J. Zhang, X. Wang, and D. Wang, *Acta Crystallogr. Sect. E*, 2009, **65**, o237.

[11] Y.-F. Li and F.-F. Jian, *Acta Crystallogr. Sect. E*, 2010, **66**, o1397.

[12] M. Bennett and A. Smith, *J. Chem. Soc. Dalton Trans.*, 1974, (2), 233–241.

[13] S. J. Dougan, A. Habtemariam, S. E. McHale, S. Parsons, and P. J. Sadler, *Proc. Natl. Anal. Sci.*, 2008, **105**(33), 11628–11633.

[14] F. A. Beckford, G. Leblanc, J. Thessing, M. S. Jr., B. J. Frost, L. Li, and N. P. Seeram, *Inorg. Chem. Commun.*, 2009, **12**, 1094–1098.

[15] F. Beckford, J. Thessing, J. Woods, J. Didion, N. Gerasimchuk, A. Gonzalez-Sarrias, and N. P. Seeram, *Metallomics*, 2011, **3**, 491–502.

[16] F. Beckford, D. Dourth, M. S. Jr., J. Didion, J. Thessing, J. Woods, V. Crowell, N. Gerasimchuk, A. Gonzalez-Sarras, and N. P. Seeram, *J. Inorg. Biochem.*, 2011, **105**(8), 1019–1029.

[17] G. Sheldrick, *Acta Crystallogr. Sect. A*, 2008, **64**, 112–122.

[18] T. Stringer, B. Therrien, D. T. Hendricks, H. Guzgay, and G. S. Smith, *Inorg. Chem. Commun.*, 2011, **14**(6), 956–960.

[19] G. C. Levy and R. L. Lichter (Eds.) *Nitrogen-15 Nuclear Magnetic Resonance Spectroscopy*, John Wiley & sons, New York, 1979.

[20] E. de Alba and N. Tjandra, *J. Magn. Reson.*, 2006, **183**(1), 160–165.

[21] M. Pongratz, P. Schluga, M. A. Jakupec, V. B. Arion, C. G. Hartinger, G. Allmaier, and B. K. Keppler, *J. Anal. At. Spectrom.*, 2004, **19**, 46–51.

[22] N. Stoll, E. Schmidt, and K. Thurow, *J. Am. Soc. Mass Spectrom.*, 2006, **17**(12), 1692–1699.

[23] J. H. Gross, in *Mass Spectrometry*, Springer Berlin Heidelberg, 2010, 67–116.

[24] W. Su, Q. Zhou, Y. Huang, Q. Huang, L. Huo, Q. Xiao, S. Huang, C. Huang, R. Chen, Q. Qian, L. Liu, and P. Li, *Appl. Organomet. Chem.*, 2013, **27**(5), 307–312.

[25] R. G. LeBel and D. A. I. Goring, *J. Chem. Eng. Data*, 1962, **7**(1), 100–101.

[26] A. Matesanz and P. Souza, *Mini-Rev. Med. Chem.*, 2009, **9**, 1389–1396.

[27] B. Spingler, S. Schnidrig, T. Todorova, and F. Wild, *Cryst. Eng. Comm.*, 2012, **14**, 751–757.

[28] M. Adams, Y. Li, H. Khot, C. De Kock, P. J. Smith, K. Land, K. Chibale, and G. S. Smith, *Dalton Trans.*, 2013, **42**, 4677–4685.

[29] B. Demoro, C. Sarniguet, R. Sanchez-Delgado, M. Rossi, D. Liebowitz, F. Caruso, C. Olea-Azar, V. Moreno, A. Medeiros, M. A. Comini, L. Otero, and D. Gambino, *Dalton Trans.*, 2012, **41**, 1534–1543.

[30] Q. Zhou, P. Li, R. Lu, Q. Qian, X. Lei, Q. Xiao, S. Huang, L. Liu, C. Huang, and W. Su, *Z. Anorg. Allg. Chem.*, 2013, **639**(6), 943946.

[31] R. Marek, in *Encyclopedia of Spectroscopy and Spectrometry (Second Edition)* (Ed. E. in Chief: John Lindon), 2 ed., Academic Press, Oxford, 2010, 1892–1898.

[32] J. Furrer, *Chem. Commun.*, 2010, **46**, 3396–3398.

[33] J. Furrer, *Concepts Magn. Reson. A*, 2012, **40A**(3), 101–127.

[34] H. Friebolin, *Basic One and Two Dimensional NMR Spectroscopy*, VCH Verlaggesellschaft, Weinheim, New York, 1991.

[35] K. Rosman and P. Taylor, *Pure Appl. Chem.*, 1998, **70**(1), 217–235.

[36] G. Bodenhausen and D. J. Ruben, *Chem. Phys. Lett.*, 1980, **69**(1), 185–189.

[37] A. Bax, R. H. Griffey, and B. L. Hawkins, *J. Magn. Reson.*, 1983, **55**(2), 301–315.

[38] P. Schanda and B. Brutscher, *J. Am. Chem. Soc.*, 2005, **127**(22), 8014–8015.

[39] W. Aue, P. Bachmann, A. Wokaun, and R. R. Ernst, *J. Magn. Reson.*, 1978, **29**(3), 523–533.

[40] R. Harris, *Pure Appl. Chem.*, 2001, **73**(1), 1795–1818.

[41] A. G. Redfield and S. Waelder, *J. Am. Chem. Soc.*, 1979, **101**(21), 61516162.

[42] E. Breitmaier (Ed.) *Structure Elucidation by NMR in Organic Chemistry*, John Wiley & Sons Ltd., Chichester, 1993.

[43] G. Bergamaschi, M. Boiocchi, E. Monzani, and V. Amendola, *Org. Biomol. Chem.*, 2011, **9**, 8276–8283.

[44] J. H. Prestegard, C. M. Bougault, and A. I. Kishore, *Chemical Reviews*, 2004, **104**(8), 3519–3540.

[45] V. B. Arion, M. A. Jakupec, M. Galanski, P. Unfried, and B. K. Keppler, *J. Inorg. Biochem.*, 2002, **91**, 298–305.

[46] S. A. Delp, C. Munro-Leighton, C. Khosla, J. L. Templeton, N. M. Alsop, T. B. Gunnoe, and T. R. Cundari, *J. Organomet. Chem.*, 2009, **694**(9–10), 1549–1556.

Chapter 3

Synchrotron X-ray Absorption Spectroscopy of Arene Ruthenium TSC Complexes

This chapter is concerned with the solid and solution-state characterisation of ruthenium arene TSC complexes by XAS. It presents the results of experiments that were performed within 24 h of experiment time at beamline B18 at Diamond Light Source, UK.

In particular, complexes **10**, **13**, **14**, **21, 22** and **30** were studied by XAS in order to qualify the status of ligand-to-metal binding. EXAFS fitting will be presented, using the X-ray crystallographic data of **10** and **30**. The results of the fitting will be applied in a linear combination analysis to solution-state XAS data of the reaction mixture of **21** to observe the formation of the dinuclear ruthenium complex **30**.

3.1 Introduction

X-ray absorption spectroscopy is an important tool in the structural characterisation of non-crystalline materials.[1] In the analysis of metal complexes, EXAFS can be used to identify the types and distances of atoms in their coordination sphere without the need for the same long-range order as, for example, in single-crystal X-ray crystallography.

Information about molecular structure can be gathered from samples that are powders, amorphous materials, mixtures, or solutions. This is a great benefit for coordination chemistry, opening up a range of experiments which can help to observe changes within this coordination sphere, for example as a result of a different sample environment, substitution reactions or degradation.

The availability of structure elucidation techniques that are element specific but do not depend on long range order in the sample is one of the reasons why bioinorganic chemists increasingly utilise XAS in the research of metal-based drugs.[2–4]

3.2 Experimental Section

The following sections describe the details of the XAS experimental set-up and procedure as well as the data processing steps.

3.2.1 Materials

For the experiments described in this chapter, solids of complexes **10**, **13**, **14**, **21**, and **22** were used, the synthesis and characterisation of which were described in Section 2.2.3 (p. 47ff) in the previous chapter. In addition, the dinuclear complex **30** and its Os(II) analogue were synthesised as detailed below. $[(p\text{-cymene})OsCl_2]_2$ was prepared using a microwave method described in the literature.[5]

[30] $\mathbf{[(p\text{-cymene})Ru(2d)]_2[PF_6]_2}$ $[(p\text{-cymene})RuCl_2]_2$ (100 mg, 0.16 mmol) and *N,N*-dimethylaminobenzaldehyde-4-(4-iodophenyl)-3-thiosemicarbazone (ligand **2d**, 137 mg, 0.32 mmol) were placed in a Schlenk-tube and mixed in dichloromethane (10 mL). The red solution was stirred at room temperature and NH_4PF_6 (250 mg, 1.48 mmol) was added. A red solid precipitated while storing the solution at 278 K overnight. It was isolated by filtration and dried under vacuum (135 mg, 0.84 mmol, 50 %). Crystals suitable for X-ray diffraction were obtained by slow evaporation of methanol from a solution of the compound in methanol. ^{1}**H-NMR** (400 MHz, dmso-d_6) 0.86 (3H, d, J=6.7 Hz), 0.92 (3H, d, J=7.3 Hz), 2.37 (4H, m), 3.01 (6H, s), 5.93 (1H, d, J=6.1 Hz), 6.00 (1H, d, J=7.2 Hz), 6.02 (1H, d, J=6.9 Hz), 6.22 (2H, d, J=8.8 Hz), 6.27 (1H, d, J=6.6 Hz), 7.02 (2H, d, J=8.8 Hz), 7.25 (2H, d, J=8.5 Hz), 7.44 (2H, d, J=9.2 Hz), 8.18 (1H, s), 9.37 (1H, s).

^{13}C-NMR (100 MHz, dmso-d_6) 18.6 (CH_3), 21.7 (CH_3), 23.0 (CH_3), 40.3 (NMe_2), 83.3 (CH), 83.5 (CH), 90.4 (CH), 93.1 (CH), 110.5 (2CH), 119.8 (Cq), 122.3 (2CH) 134.8 (2CH) 137.1 (2CH), 165.0 (N=CH) **CHN** (calc. for $C_{52}H_{60}N_8I_2S_2Ru2P_2F_{12}$) 38.70 (38.86) %C, 3.69 (3.76) %H, 6.88 (6.97) %N.

[31] [(*p*-cymene)Os(2d)]$_2$[PF$_6$]$_2$ [(*p*-cymene)$OsCl_2$]$_2$ (50 mg, 0.063 mmol) was dissolved in methanol (10 mL) at 293 K which gave a clear yellow solution. *N,N*-dimethylaminobenzaldehyde-4-(4-iodophenyl)-3-thiosemicarbazone (**2d**, 53 mg, 0.13 mmol) was added and dissolved to give an orange solution. The mixture was stirred at 293 K overnight. To the orange solution NH_4PF_6 (100 mg, 0.60 mmol) was added, and an orange solid precipitated which was subsequently filtered and dried in air (56 mg, 70 %). **^{1}H NMR** (400 MHz, methanol-d_4) 1.04 (3H, d, J=7.0 Hz), 1.10 (3H, d, J=7.3 Hz), 2.48 (1H, m[7], J=7.8 Hz), 2.59 (3H, s), 3.19 (6H, s), 6.01 (2H, d, J=6.6 Hz), 6.01 (2H, d, J=8.9 Hz), 6.18 (1H, d, J=5.6 Hz), 6.28 (1H, d, J=5.6 Hz), 6.39 (2H, d, J=9.0 Hz), 7.14 (2H, d, J=8.9 Hz), 7.34 (2H, d, J=9.0 Hz), 7.64 (2H, d, J=9.3 Hz), 8.21 (1H, s). **^{1}H NMR** (400 MHz, $CDCl_3$) 0.90 (3H, d, J=7.0 Hz), 1.04 (3H, d, J=6.7 Hz), 2.30 (1, m, J=6.8 Hz), 2.62 (3H, s), 3.13 (6H, s), 5.68 (1H, d, J=5.8 Hz), 5.73 (1H, d, J=5.6 Hz), 5.82 (1H, d, J=5.7 Hz), 6.27 (2H, d, J=9.1 Hz), 6.49 (1H, d, J=6.4 Hz), 7.20 (2H, d, J=9.1 Hz), 7.27 (2H, d, J=9.2 Hz), 7.69 (2H, d, J=9.1 Hz), 8.30 (1H, s). **ESI-MS** (MeOH) m/z (rel. int.) = 749 (100) $[(M^+)\text{-HCl}]^+$ **CHN** (calc. for $C_{52}H_{60}N_8I_2S_2Os2P_2F_{12}$) %C 34.71 (34.98), %H 3.26 (3.39), %N 6.18 (6.28).

3.2.2 Solid-State X-ray Absorption Spectroscopy

X-ray Absorption Spectroscopy at the Ru K-edge and Os L_3-edge was carried out at beamline B18 at Diamond Light Source, Didcot, UK. Samples for XAS measurements were prepared at the synchrotron, in the chemistry lab located at the beamline, either on the day of the experiment or one day before. Solid-state samples were stored at ambient temperature in air.

Solid-state Sample Preparation

Samples for X-ray transmission measurements were prepared as homogeneous ultra-finely ground powders. Approx. 50 mg of each complex were ground in a marble mortar and mixed with cellulose powder as binding material to achieve a total sample weight of 100 mg. The two powders were ground together in the mortar until the colour of the mixture appeared homogenous. Each mixture was then compressed with a 5 Ton hydraulic press into a thin disc of 13 mm diameter. The ruthenium content in those pellets varied between 7% - 15%. Figure 3.3 shows the sample pellets assembled in the sample stage which was used during the transmission experiment, to move each sample into the X-ray beam consecutively.

Transmission-XAS Set-up

The sample pellets were mounted onto a holder (Figure 3.3) which was placed in the path of the X-ray beam. Motors on the sample stage allowed its vertical position to be adjusted remotely. Much beamtime was saved by remotely controlling the vertical movement of the sample stage, so that each pellet was brought into the beam consecutively without the need to enter the experimental hutch for a sample change.

With the sample stage in place, XAS data was acquired in transmission

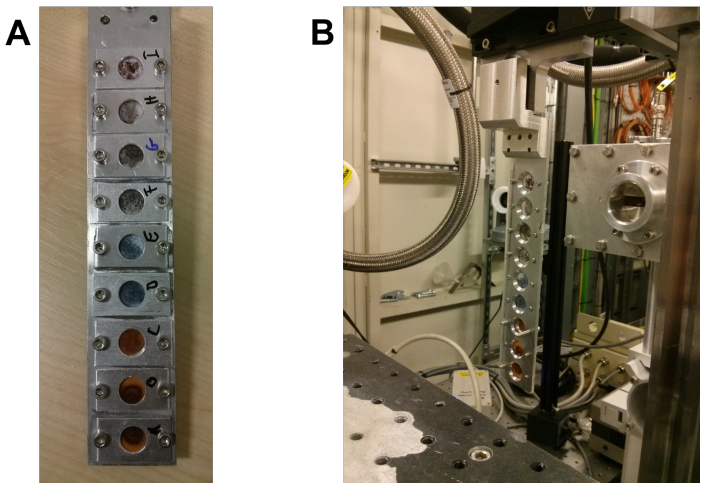

Figure 3.1: A) Sample holder filled with 9 pellets prepared form powders of ruthenium complexes mixed with cellulose. **B)** Sample stage located in the beam path at beamline B18 (X-ray beam coming from the right in this view).

mode at ambient temperature as illustrated in Figure 3.2. Three argon-filled ionisation chambers, I_0, I_t, and I_{ref} are positioned in the beam path: One before and one after the sample and the third one after a reference sample of Ru^0 powder. This set-up was aligned such that the incident beam passes through the first chamber (I_0), then through the sample pellet and subsequently through the second chamber (I_t). It then passes through the reference material followed by the third ion chamber (I_{ref}). Signal intensity is collected in each of the chambers, and the X-ray transmission is calculated as the difference between the readings in two consecutive chambers.

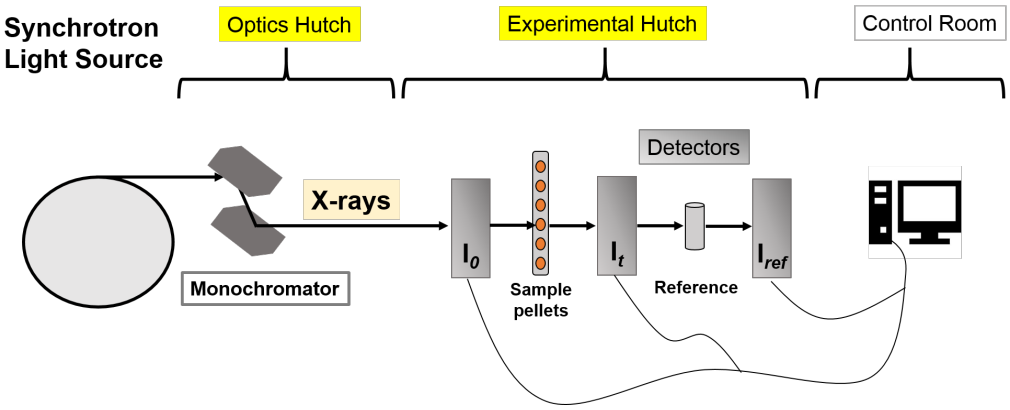

Figure 3.2: This scheme illustrates the experimental set-up of the solid-state XAS experiment in transmission mode. X-rays, produced in the synchrotron, are filtered by a double-crystal monochromator to select the required energies. Signal is acquired in each of the three ionisation chambers I_0, I_t, and I_{ref} which flank the sample holder and the reference sample. The intensity difference between the two detector chambers I_0 and I_t represents the absorbance of X-ray energy by the sample.

3.2.3 Solution-State X-ray Absorption Spectroscopy

Complex **21** (40 mg, 0.05 mmol) was dissolved in chloroform (400 μL) and immediately diluted with 3.8 mL of a saturated solution of NH_4PF_6 in methanol. Aliquots of this reaction mixture (0.5 mL) were taken with a micro syringe and transferred into sample-cells (Figure 3.3 B, C) after 0.5 min, 1.5 min, 3 min, 6 min, 10 min, and 15 min. These aliquots were immediately frozen by submerging the sample-cells in liquid nitrogen, and the frozen samples were then stored at -77 K until further use.

Due to the high concentration of complex **21** in the solution, the reaction proceeded fast and crystallisation of the product in the reaction vessel started 15 min after the reactants were first mixed. A second solution was prepared by dissolving 5 mg of complex **21** in 0.05 mL of chloroform and diluting with 0.4 mL methanol. This solution was stored at room temperature in a closed glass vial for 30 h.

Solution-state XAS measurements were carried out in fluorescence mode.

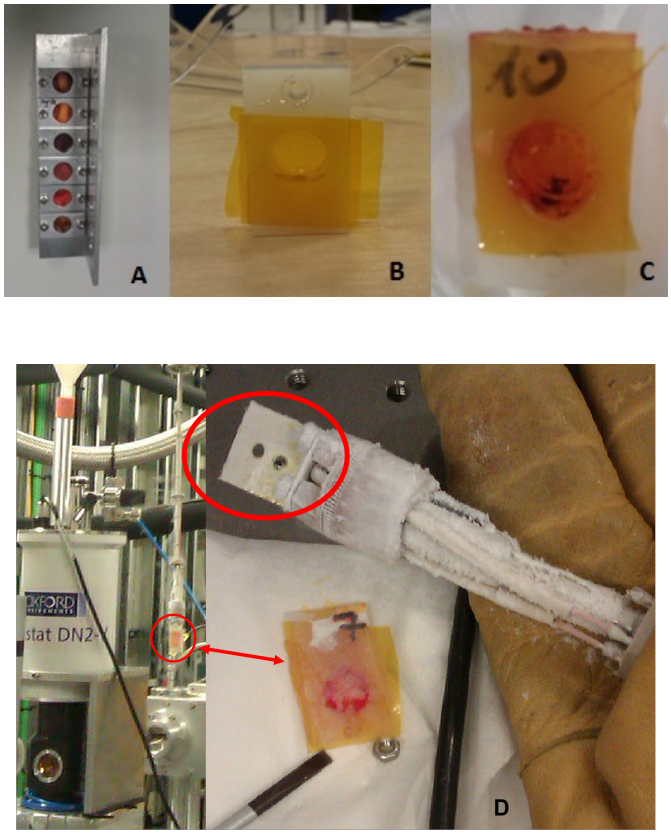

Figure 3.3: Experimental equipment for XAS data collection at Beamline B18, Diamond Light Source, UK. **A** - Sample stage holding pellets of powders; **B** - Liquid sample cell; **C** - Sample cell containing liquid sample; D - Stick for insertion of sample into cryostat: red circle shows metal plate for attaching the sample cell.

The frozen samples were transferred from the storage dewar into a liquid nitrogen cryostat individually before the XAS measurement. Figure 3.3 (**D**) shows the cryostat on the left and the respective sample holder on the right. The red circle marks the position at which the sample cell is attached to the holder before insertion into the cryostat.

X-ray fluorescence of the Ru K_α line was detected using a 9-element Ge detector[?] which was placed at at 90° to the incident beam. The sample cell was oriented at a 45° angle to the incident beam. The counts in each detector element were examined for artefacts prior to summing over all

elements.

3.2.4 Solid-State XAS Data Collection

Ru K-edge and Os L_3-edge XAS data were collected at the core-EXAFS bending magnet beamline (B18) at Diamond Light Source, Didcot, UK. The synchrotron provides a 3.0 GeV electron beam, which is operated in top-up mode with injections from the booster synchrotron every 10 minutes. On the day of the Ru XAS experiments, an average beam current of 150 mA was maintained. The beamline optics at B18 consist of an Al 200 μm white-beam filter, Pt-coated collimating and focussing mirrors, and a double-crystal monochromator which allows tuning of the incident beam energy to the required edges.

Ru K-edge XAS

Si(311) monochromator crystals were used to tune the X-ray energy in the region of the Ru K-edge (22117 eV). In this energy range, a resolution of $3{\cdot}10^{-5}$ eV is achieved, with a beam size of 200 x 250 μm on the sample. The X-ray energy was increased step-wise from 21917.0 eV to 23765.0 eV (Ru K-edge) with a step size of 10 eV before the edge (21917 - 22087 eV, 0.5 eV through the edge (22087 - 22127 eV) and 0.05 $Å^{-1}$ after the edge (22127 - 23765 eV) to account for the increasing attenuation of oscillations in higher k-space. EXAFS signal was recorded up to k = 20 $Å^{-1}$. A reference spectrum (Ru foil) was collected with each scan to allow for energy calibration and data alignment.

Os L_3-edge XAS

Osmium L_3-edge XAS was acquired as part of a second visit to beamline B18. The general set-up of the transmission XAS experiment was the same as for ruthenium, except for the following parameters: the beam current in the storage ring was 300 mA; Si(111) monochromator crystals were used to obtain X-ray energies in the Os L_3-edge region; and the incident beam energy was varied from 10660 eV to 11670 eV in steps of 0.5 eV. The energy resolution with this set-up was $1.4 \cdot 10^{-4}$ eV^{-1}.

3.2.5 XAS Data Processing

Data processing and analysis was performed using the Demeter software package,[6] version 0.9.12 under windows 7 and version 9.20 with Mac OS X 10.9.5, respectively. Within Demeter, ATHENA is used for processing raw XAS data, XANES analysis and extraction of the EXAFS, while ARTEMIS is used for EXAFS analysis. Fitting of the optimised, Fourier-filtered experimental EXAFS data to theoretical scattering amplitudes and phases was performed in Artemis with the IFEFFIT program (FEFF6).[7]

Calibration and Alignment of XAS Data

For each sample, the individual data sets (scans) were imported into Athena, including the data that was collected in the reference channel I_{ref}. The μ(E) spectrum of the reference channel was used for energy calibration. The energy at which the first derivative of the reference spectrum has the first maximum was assigned to the tabulated literature value (22117 eV for Ru foil, 11136 eV for Ta foil).

All useful scans for each sample were aligned to the reference channel.

Calibrated μ(E) data of the individual scans were then averaged to reduce the signal-to-noise ratio. The edge position E_0 was determined as the maximum of the first derivative of the averaged μ(E) spectrum for each sample.

EXAFS Extraction and Fourier Filtering

Fourier filtering is the application of window functions to the χ(k) data to reduce the data in R-space to a meaningful range that is used for EXAFS fitting. Normalisation to a unit edge-step and background removal were performed on the averaged μ(E) data sets. The 'Autobk' function in Athena was used to apply spline functions in a normalisation range from −150 to −60 eV before and from +150 eV to 1150 after E_0.

After extracting the EXAFS in this way, the k-space plots were examined to determine the noise-free range (k_{min} - k_{max}) to be used for the Fourier transformation (FT). Next, Fourier-transformed data (R-space) were evaluated by backwards Fourier transforming the physically meaningful region of the R-space plot (R_{min} - R_{max}). Hanning window functions were applied in both FT processes to filter, i.e. truncate the data. Comparison between extracted k-space and the backward FT was used in addition to optimising the height of the first-shell peak in R-space.

3.2.6 UV-visible Spectroscopy

UV-vis spectra were measured on a Varian Cary 300 spectrometer using quartz micro-cuvettes of 0.1 dm path length and 0.9 mL volume. The instrument was equipped with a PTP1 Peltier temperature control unit, which was used to regulate the temperature of the sample holding block.

Sample Preparation

A stock solution of complex **21** (1.9 mg, 2.6 μmol) in dichloromethane (500 μL, c(**21**) 5.2 mM) was split into aliquots of 10 μL (0.052 μmol) which were dried with compressed air. Each aliquot was re-dissolved in 50 μL dmso or methanol immediately before dilution in the cuvette.

Aqueous Solution Stability

Seven solutions of different concentrations of sodium chloride were prepared between 154 mM and 4 mM were achieved by sequential dilution of 0.9% saline solution (c(NaCl) = 154 mM). Aliquots of **21** as prepared above were dissolved in 50 μL dmso and diluted by adding 20 μL of the dmso solution to a cuvette filled with 980 μL of the respective sodium chloride solutions. The solutions were mixed inside the cuvette and the spectra collected immediately. Spectra were recorded at 298 K for 5 - 20 min, using a scan rate of 600 nm/min between 630 nm and 230 nm and a cycling rate of one spectrum per minute.

3.3 Results

XAS data is presented here for eight arene ruthenium complexes and one osmium analogue. Comparison of the transmission XAS data, collected on Ru K-edge or Os L3-edge, to the X-ray crystallographic results presented in Chapter 2

3.3.1 X-ray Absorption Near-Edge Spectroscopy

The results of pre-processing and Fourier filtering are summarised in Table 3.1. Table 3.1 presents the average edge-position E_0 for each sample. All samples

Table 3.1: Results of processing and Fourier filtering Ru K-edge XAS data. Edge position $\mathbf{E}_0$, upper and lower limits of meaningful EXAFS, degrees of freedom $\mathbf{N}_{ind}$ for EXAFS fit, and resolvable absorber-scatterer distances $\boldsymbol{\delta}$ **R**.

No	**1st shell** (η^6-$C_{10}H_{14}$) + A, B, X	$\mathbf{E}_0$ [eV]	$\mathbf{k}_{min}$ [Å^{-1}]	$\mathbf{k}_{max}$ [Å^{-1}]	$\mathbf{R}_{min}$ [Å]	$\mathbf{R}_{max}$ [Å]	$\mathbf{N}_{ind}$	$\boldsymbol{\delta}$**R** [Å]
4	Cl, Cl, Cl	22123.25	2.68	16.97	1.1	2.38	11.64	0.11
5	I, I, I	22122.23	2.94	14.03	1.2	2.78	11.15	0.14
10	N, S, Cl	22123.00	2.60	13.55	1.1	2.35	8.71	0.14
13	N, S, Cl	22123.70	2.60	12.20	1.1	2.35	7.64	0.16
21	N, S, Cl	22123.09	2.68	12.90	1.2	2.30	7.73	0.16
14	N, S, I	22122.58	2.70	15.30	1.1	2.72	12.99	0.12
22	N, S, I	22122.62	2.66	15.35	1.1	2.75	13.33	0.12
30	N, S1, S2	22122.73	2.64	14.72	1.1	4.00	22.30	0.13
31	N, S1, S2	10879.45	3.00	10.00	1.3	3.80	10.45	0.13

showed absorption edges in the region of 22122 to 22127 eV. Comparison between E_0 for the TSC complexes and the starting materials (dimers **4** and **5**) shows that both are shifted from 22117 eV, the value for Ru(0), in the same order of approx. + 5 eV. The results for complexes that differ in structure by only one atom in their first coordination shell (Z = Cl vs I) shows that iodido complexes **14** and **22** have a slightly lower edge energy than their corresponding chlorido analogues **13** and **21**.

The change within the TSC chelating ligand from a phenyl substituent in TSC*IPh* (**1d**) in complex **13** to the dimethylanilino moiety in DMTSC*IPh* (**2d**) within complex **21** does not influence the XANES region. The first coordination sphere is identical in both compounds, and so is the oxidation state of the Ru centre.

The molecular structures of the dinuclear ruthenium precursor complexes **4** and **5** are depicted in Figure 3.4. The molecules contain two (η^6-$C_{10}H_{14}$)RuX_3 units (X = Cl, I) which are connected by a bridge of two of the X ligands. Compound **4** has three chloride ions in its first shell (X=Cl) while **5**, with X = I, bears three iodide ions.

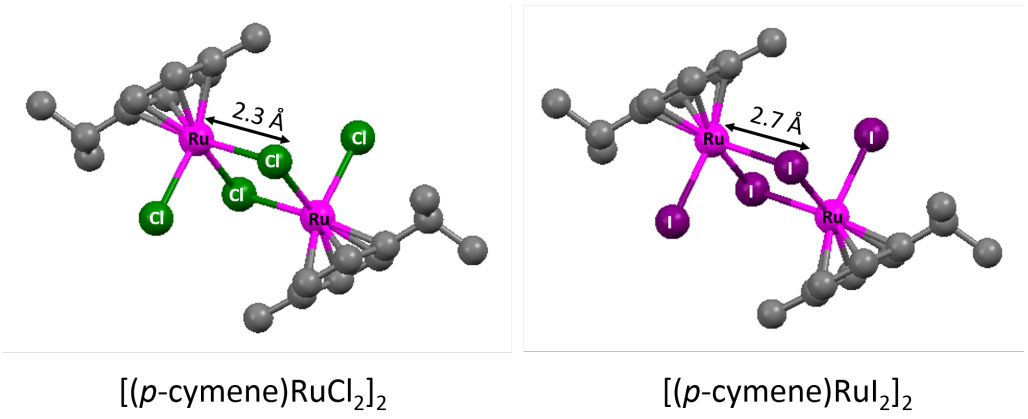

Figure 3.4: Comparison of two crystal structures for dinuclear Ru starting materials. The distance between the central metal Ru and the halogenide half-shell varies between 2.4 Å for Ru-Cl in [(***p*-cymene)RuCl**$_2$]$_2$ and 2.7 Å for Ru-I bonds in [(***p*-cymene)RuI**$_2$]$_2$.

The Fourier transformed signal, shown in Figure 3.5 III, reflects the absorber - scatterer distances R. The graphs are visibly different between the two starting materials. The radial distribution plot for the iodido dimer **5** (red) shows a second peak at $\sim$ 2.7 Å which corresponds to the ruthenium-iodide distance (R_{eff} = 2.72 Å).

Figure 3.6 compares the EXAFS signal and FT for monomer **21** and

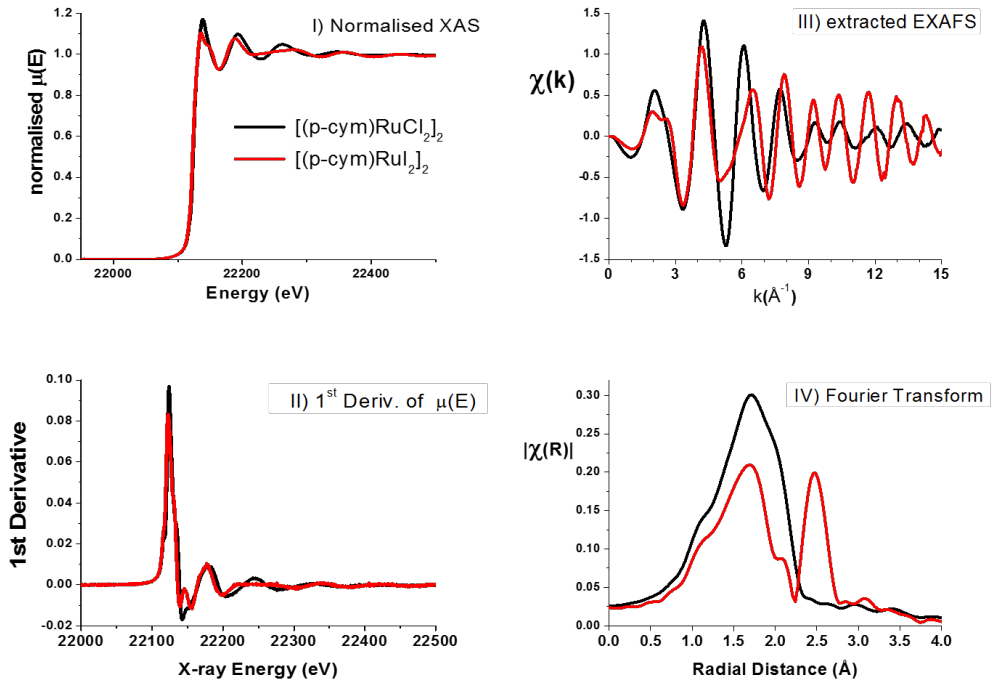

Figure 3.5: I) Normalised XAS spectra, II) First derivative, III) extracted EXAFS, and IV) Fourier Transform of XAS data for **[(*p*-cymene)RuCl$_2$]$_2$** and **[(*p*-cymene)RuI$_2$]$_2$** .

the dimer **30**. The k-space data (III) suggest that the EXAFS signal of the dimer **30** is similar compared to monomer **21**.

3.3.2 EXAFS Fitting

The least-squares EXAFS fit was produced in all three k-weights. Parameters that were varied during the fit were the edge-shift ΔE_0, the amplitude reduction factor S_0^2, and the mean-square relative displacement of the scattering path-length, σ^2, (also referred to as the 'Debye-Waller factor' of XAFS), presented in Table 3.2.

Inter-atomic distances in the first coordination sphere were fitted to crystallographic data, and are summarised in Table 3.3.

For chlorido complexes **4**, **10**, **13** and **21** the main peak in R-space in

Table 3.2: Results of the first-shell fits of Ru K-edge EXAFS data. Least-squares fit of edge-shift ΔE_0, amplitude reduction factor S_0^2, expansion factor $\boldsymbol{\alpha}$, and the mean-square relative displacement parameter σ^2. Goodness of fit given by χ^2_{red} R-factor.

Sample	χ^2	χ^2_{red}	**R-factor**	$\boldsymbol{\Delta E_0}$ **(eV)**	$\mathbf{S_0^2}$	$\boldsymbol{\alpha}$ $\cdot 10^{-2}$	σ^2 $\cdot 10^{-2}$ **Å**^{2}
Ru^0	-	-	-	-	-		
4	104724	32369	0.019	2.8 ± 1.7	0.8 ± 0.13	n.a.[a]	0.3 ± 0.1
5	41188	3831	0.033	3.4 ± 0.7	0.7 ± 0.07	0.2 ± 0.2	0.5 ± 0.08
10	71554	17715	0.014	3.7 ± 1.4	0.8 ± 0.05	n.a.[a]	0.07 [b]
13	44728	17691	0.016	3.3 ± 1.7	0.8 ± 0.06	n.a.[a]	0.08 [b]
21	81317	12406	0.019	3.2 ± 1.7	0.8 ± 0.05	1.7 ± 0.8	0.4 ± 0.6
14	31495	4492	0.027	3.9 ± 1.0	0.8 ± 0.09	1.4 ± 0.4	0.17 ± 0.08
22	47533	5756	0.027	3.9 ± 1.4	0.8 ± 0.10	n.a.[a]	0.15 ± 0.08
30	65909	3173	0.037	4.0 ± 0.9	1.1 ± 0.08	0.8 ± 0.1	0.3 ± 0.09
31	12622	1956	0.010	7.9 ± 1.0	0.9 ± 0.08	0.1 ± 0.3	0.5 ± 0.1
30$*$	43364	5851	0.019	3.2 ± 1.1	0.8 ± 0.08	-0.4 ± 0.4	0.01 ± 0.1

[a] not applicable, R_S was fitted as $R_X + \Delta R$. [b] fixed value.

$*$fitted to X-ray crystallographic data of [**10**]. χ^2 is the goodness-of-fit parameter, scaled to the estimated uncertainty. χ^2_{red} is χ^2 divided by the number of free fit-parameters. R-factor describes the deviation between the fitted and the experimental curve.

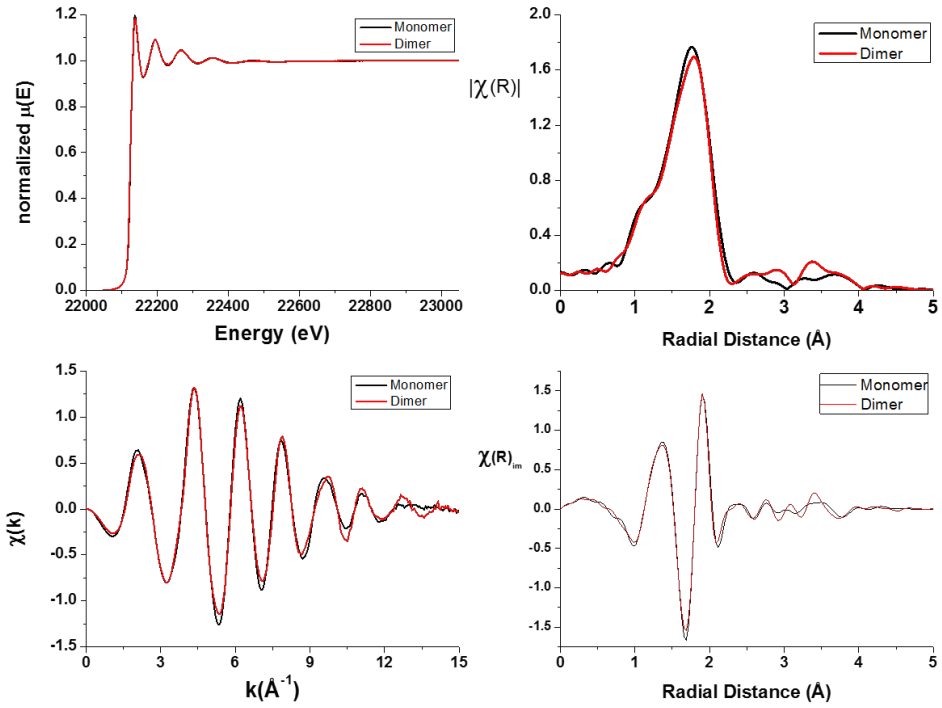

Figure 3.6: XAS data for complexes **21** and **30**. I) Normalised XAS spectra, II) extracted EXAFS ('k-space'), III) Fourier Transform ('R-space'), IV) real part of FT.

the range of Δ R = $R_{max} - R_{min}$ (Table 3.1) was used for the fit. The iodido complexes **5**, **14** and **22** showed a significant second-shell peak in the FT which was included into the fitting range after successfully fitting the first-shell peak.

Table 3.3 compares the calculated absorber-scatterer distances (R_S) to the crystallographically determined inter atomic distances (R_X). The comparison between the crystallographic data that were presented in Chapter 2 (Section 2.3.4, p. 72) and the Ru K-edge XAS data obtained here aims to answer the question whether the TSCs are sulfur bound in the solid state.

The data in Table 3.3 show that the bond distances calculated by the EXAFS fit are within $\pm$ 0.05 Å of each other and also match the range of the crystallographically determined distances. In particular, the Ru-S distance

Table 3.3: Fit result for interatomic distances (Å), fitted as separate distances (Å)

No.	X, Y, Z	d Ru-N	d Ru-S1	d Ru-Cl/I/S2	δ(S1/Cl)
$\mathbf{R}_X$	N, S, Cl	2.13	2.36	2.43	0.08
10	N, S, Cl	2.08	2.32	2.41	0.09
13	N, S, Cl	2.12	2.35	2.42	0.07
21	N, S, Cl	2.11	2.35	2.41	0.05
14	N, S, I	2.12	2.36	2.73	0.37
22	N, S, I	2.12	2.36	2.73	0.37
30	N, S1, S2	2.11	2.33	2.42	0.09
		(R_X = 2.1027)	(R_X = 2.31)	(R_X = 2.39)	-0.08
30*	N, S1, S2	2.12	2.33	2.41	0.08

*fitted to X-ray crystallographic data of **10**.

is very similar between all mononuclear complexes. The theoretical values are close to the crystallographic standard of 2.3519 Å, except for monomer **21**. For **21**, the fit result of 2.3214 Å is closer to the Ru-S distance in the dimer **30** (2.3113 Å). The Ru-I distances in complexes **14** and **22** were fitted via an arbitrary single scattering path of 2.7 Å length with a result of 2.7284 Å for **14** and 2.7249 Å for **22**. The last column in Table 3.3 presents the difference between the fitted distance between the Ru-S bond and the Ru-Cl bond.

The EXAFS data of **30** were also fitted to the X-ray crystal structure of mononuclear complex **10** to show that the geometry is different and the fit result worse than when the correct structure of the dimer is used to build the model. The results show that this is the case. Although a fit with a reasonable R-factor was obtained (see Table 3.2), and the main parameters are refinable to sensible values, the half path-length for the single scattering paths in the first shell differ from the monomer model to a greater extent than from the correct structure.

It is therefore concluded that the bulk material of **30** is of dimeric nature, because it fits better to the X-ray crystal structure of **30** than that of monomer **10**.

Os L3-edge EXAFS of complex [31]

The Os L_3-edge XAS data were treated in the same way as the Ru K-edge data. EXAFS fitting to the crystallographic data for complex **30** was achieved by exchanging the central absorber in the model for Os prior to the prediction of scattering paths with iffeffit.

Figure 3.8 shows the fit result in k-space and R-space, including the fitting window. The optimised parameters of the fit are included in Table 3.2.

Table 3.4: Fit-results of first-shell EXAFS fit of Os L_3-edge XAS of complex **31**

Path	**N**	$\mathbf{S_0^2}$	σ^2 $\cdot 10^{-3}$	$\Delta\ E_0$ (eV)	$\Delta\ R$ $\cdot 10^{-3}$ Å	R_{eff} Å	R Å
N1.1	1	0.913	5.34±1.0	7.9±1.0	2.49±	2.10270	2.10520
C57.1	2	0.913	5.34±1.0	7.9±1.0	2.60±	2.18930	2.19190
C25.1	2	0.913	5.34±1.0	7.9±1.0	2.66±	2.24370	2.24636
C48.1	2	0.913	5.34±1.0	7.9±1.0	2.72±	2.29180	2.29452
S3.1	1	0.913	5.34±1.0	7.9±1.0	2.74±	2.31130	2.31404
S3.2	2	0.913	5.34±1.0	7.9±1.0	2.84±	2.39220	2.39504
C15.2	1	0.913	5.34±1.0	7.9±1.0	3.03±	2.55490	2.55793
C14.1	1	0.913	5.34±1.0	7.9±1.0	3.49±	2.94250	2.94599
C23.1 C25.1	1	0.913	5.34±1.0	7.9±1.0	3.51±	2.96210	2.96562
N2.1	1	0.913	5.34±1.0	7.9±1.0	3.67±	3.09320	3.09687
C56.2	1	0.913	5.34±1.0	7.9±1.0	4.07±	3.42770	3.43177
Os3.1	1	0.913	5.34±1.0	7.9±1.0	4.15±	3.49560	3.49975

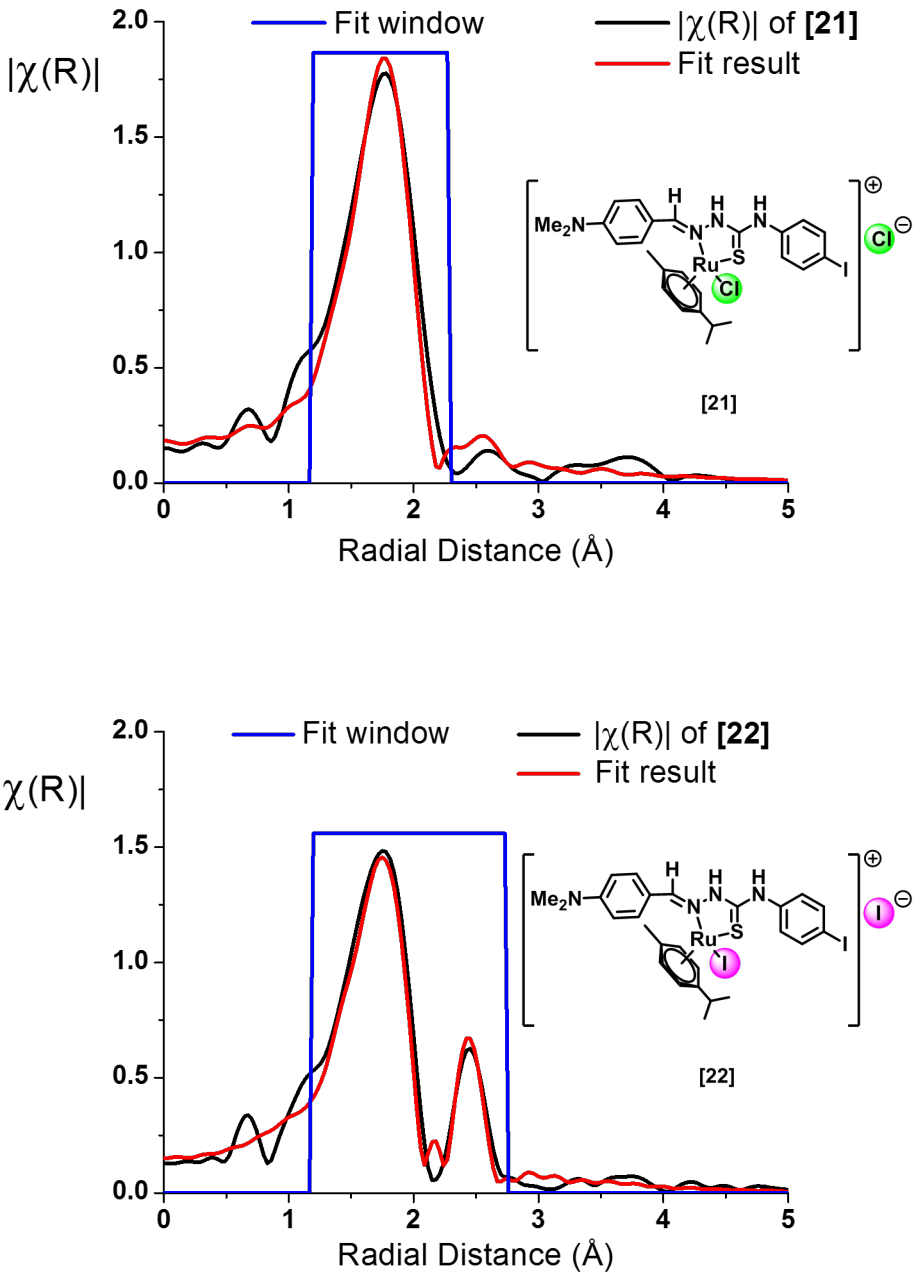

Figure 3.7: First-shell EXAFS fit results shown in R-space to compare chloride complex [**21**] to its iodido analogue [**22**]. Theoretical model for the fit was produced from X-ray crystallographic data of complex [**10**].

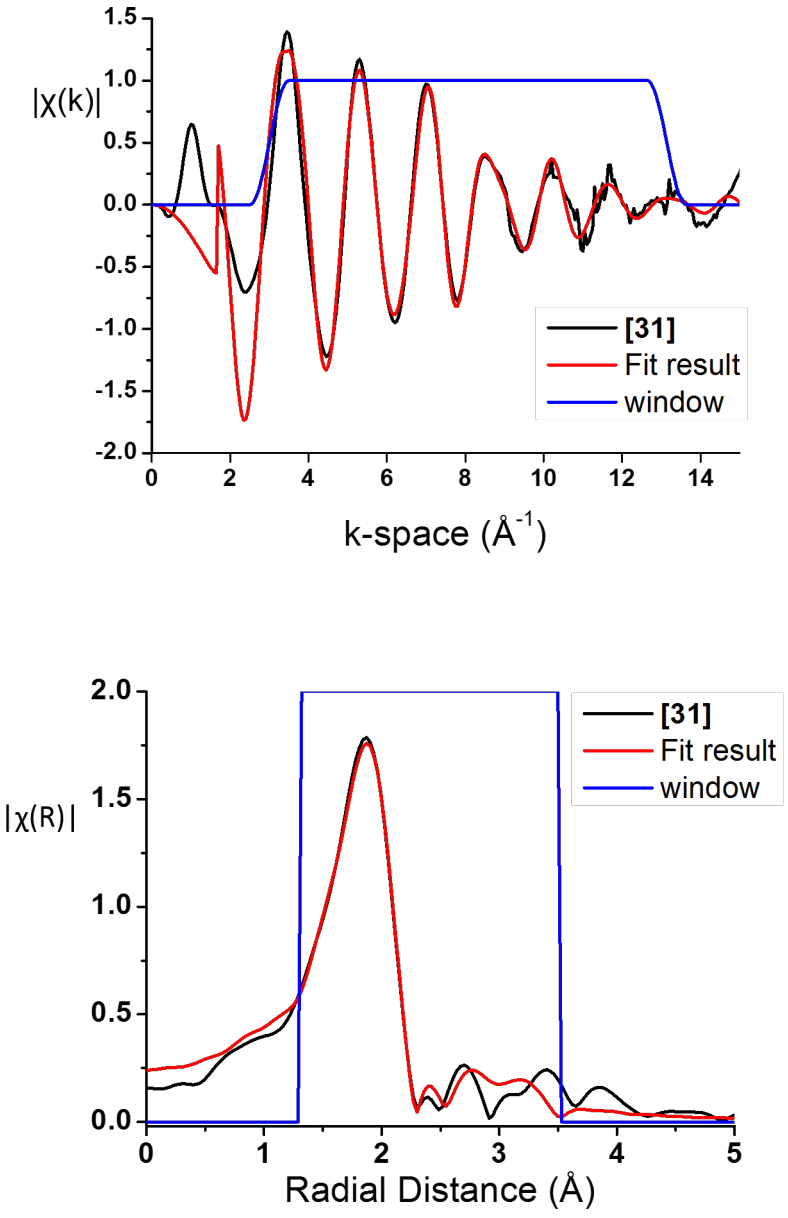

Figure 3.8: Plots demonstrating the fitting result for Os L_3-edge data recorded for Os(II) complex **31**. Fit result is shown in k2-weighted k-space, and in R-spacce. Theoretical model for the fit was produced from X-ray crystallographic data of complex

3.3.3 Solution-state Ru K-edge XAFS

In this experiment, the reaction of complex **21** with 10 eq. NH_4PF_6 in methanol was repeated and observed by XAFS on freeze-quenched aliquots of the reaction mixture. Because of the high concentration of complex **21** in the solution, crystallisation in the reaction vessel started after 15 min of reaction time. For this reason, samples were collected at only four time points.

For data analysis, a linear combination analysis (LCA) approach was taken. In this method, the XAS data of individual reaction time steps were analysed with respect to a linear combination of several components that might be present in the mixture.

In order for this approach to succeed, four different samples were measured as standards: The solid-state samples of complex **21** and complex **30**, a concentrated frozen solution of **21** in methanol and a concentrated frozen solution of complex **30** in acetonitrile (due to the low solubility of **30** in methanol).

Linear Combination Fitting

After data alignment and background subtraction, the groups of individual scans for each standard, as well as for each reaction time-step, were averaged in μ(E) as described above.

The LCF tool in the Demeter software package (Athena) was used to fit the spectra of the reaction steps to the two standards. First, a combinatorial fit was executed to choose the best two endpoint standards for the fit of the reaction data. Table 3.5 shows the results of this fit that used the solution of the monomer (**21LS1**), the solution of the dimer (**30LS2**) and both solid scans.

Table 3.5: Cominatorial fit result for the relative contribution of standards **A** - **D** to the Ru K-edge XANES of the reaction mixture of mononuclear complex **21** with NH_4PF_6.

Standard		weight
A	**21**	-0.002±0.081
B	**21LS1**	0.497±0.055
C	**30**	0.475±0.053
D	**30LS2**	0.030±0.025

The result of the combinatorial fit shows that the solution of the monomer (**B**) and the solid-state data for the dimer (**C**) give the best combination of standards. This combination showed the lowest R-factor ($3.64 \cdot 10^{-5}$) and reduced χ^2 ($7.3 \cdot 10^{-6}$).

Second, LCF was performed using the two standards A and C only, forcing the sum of both to be equal to one for each time step. The fitting procedure used flattened μ(E) data in the range from 22103.77 to 22153.77 eV, which is from 20 eV below the edge energy E_0 to 30 eV above the edge. The result is summarised in Table 3.6.

Table 3.6: Relative content of monomer (**21**) and dimer (**21**) in the reaction mixture, determined by LCF of the two endpoint standards (**21L**) and **30S**) forcing their sum to be equal to 1.

time **min**	**E_0** [eV]	**weight** (monomer)	**weight** (dimer)	**R** $\cdot 10^{-3}$	χ $\cdot 10^{-5}$	χ^2 $\cdot 10^{-3}$
1.5	22123.33	0.77 ± 0.04	0.23 ± 0.06	0.04	0.87	0.99
3	22123.77	0.66 ± 0.09	0.34 ± 0.10	0.20	3.87	4.42
6	22123.77	0.52 ± 0.04	0.48 ± 0.06	0.04	0.73	0.83
10	22123.33	0.42 ± 0.11	0.58 ± 0.12	0.32	6.45	7.35
30 h	22123.33	0.12 ± 0.07	0.88 ± 0.08	0.12	2.43	2.77

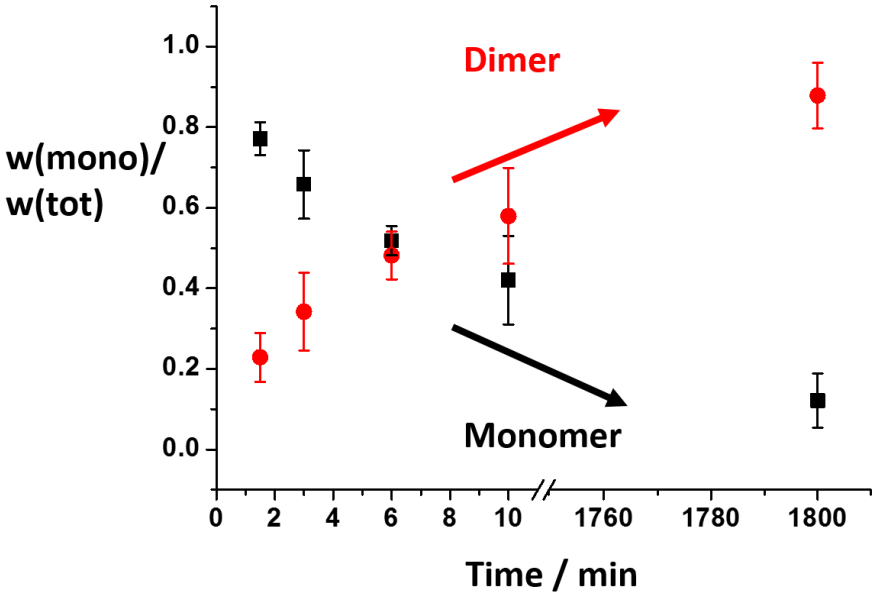

Figure 3.9: Graph showing the decrease of monomer proportion compared to the increasing dimer concentration over time, Reaction of a 40 mM solution of **21** in methanol, containing 5 % chloroform (T = 298 K) and 10 mol eq. NH_4PF_6. Ru K-edge XANES data for each time point was collected on a frozen (freeze quenched) aliquot of the reaction mixture. The monomer : dimer ratios are the result of linear combination fitting (LCF) of the time-dependent Ru K-edge XANES, fitted as flattened μ(E) from 22103.77 to 22153.77 eV.

The graph in Figure 3.9 shows the relative concentration of monomer **21** compared to dimer **30** that were present in the mixture at the time at which the aliquot was removed from the reaction mixture. The last data point (30 h) was obtained by measuring Ru K-edge XANES on a second sample of the reaction mixture which was prepared with the exact same monomer concentration, but without the addition of PF_6, to avoid crystallisation of the sample from the concentrated reaction mixture.

3.3.4 UV-vis Spectroscopy

UV/vis spectroscopy was carried out in order to test solution stability of complex **21**. For 1 hour, a solution of complex **21** in water (containing

5% methanol) was monitored in the region between 200 to 600 nm and Figure 3.10 shows a superimposed plot of the accumulated spectra.

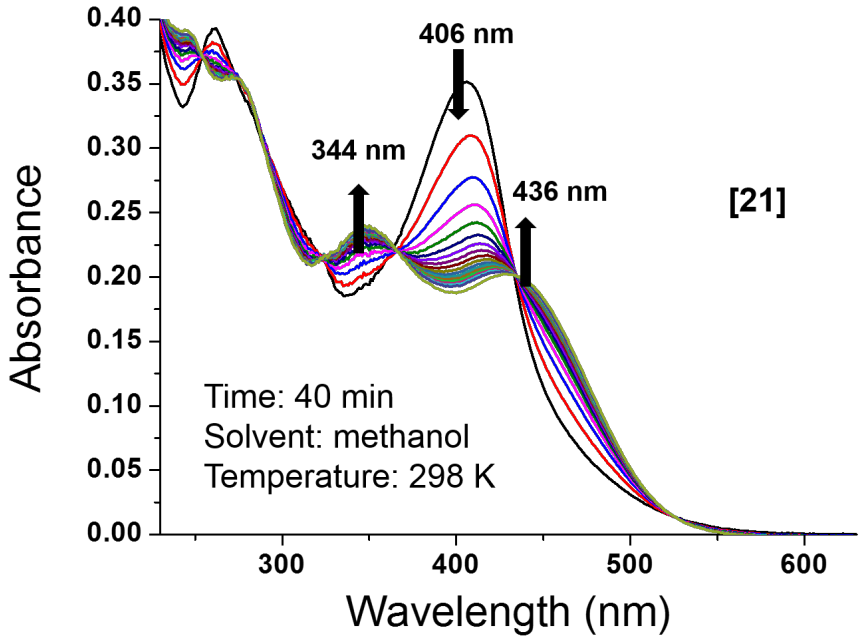

Figure 3.10: Graphic shows the dynamic changes in UV-vis absorbance spectra of complex dissolved in methanol.

Several changes were observed during this period, which are highlighted by arrows to indicate the increase or decrease of band intensities over time. The ESI-MS of the solution both 10 min and 21 h after dilution showed the same signal, corresponding to the deprotonated complex that has lost both chloride ions. This suggests that not only the arene, but also the TSC ligand stay connected to the ruthenium centre over 21 h.

The species which appears to form in solution from arene Ru TSC complexes has been described by the formula $[(p\text{-cymene})\text{Ru(L)}]^+$ in Chapter 2, which is the same as one of the two halves of a Ru-TSC dimer such as **[30]**.

Suppression of Hydrolysis by Sodium Chloride

The concentration of sodium chloride in the solution is directly related to the rate of hydrolysis, as was observed by UV/vis. Figure 3.11 compares the spectra of an aqueous solution of complex **21** in the presence of varying chloride concentrations.

Each plot presents spectra of a separate experiment in which complex **21** was added to a sodium chloride solution. Each plot therefore represents one concentration of Cl^-. In each experiment, five spectra were recorded over a period of 5 min, and the first one marks 1 min after after the initial mixing.

The first two graphs in Figure 3.11, for high Cl^- concentrations of 154 μM and 51 μM, show no change of the spectra over the 5 min. With decreasing chloride content, however, the dynamics in the spectra recur. At 15 μM and below, the changes in absorbance are clearly visible after the first few minutes.

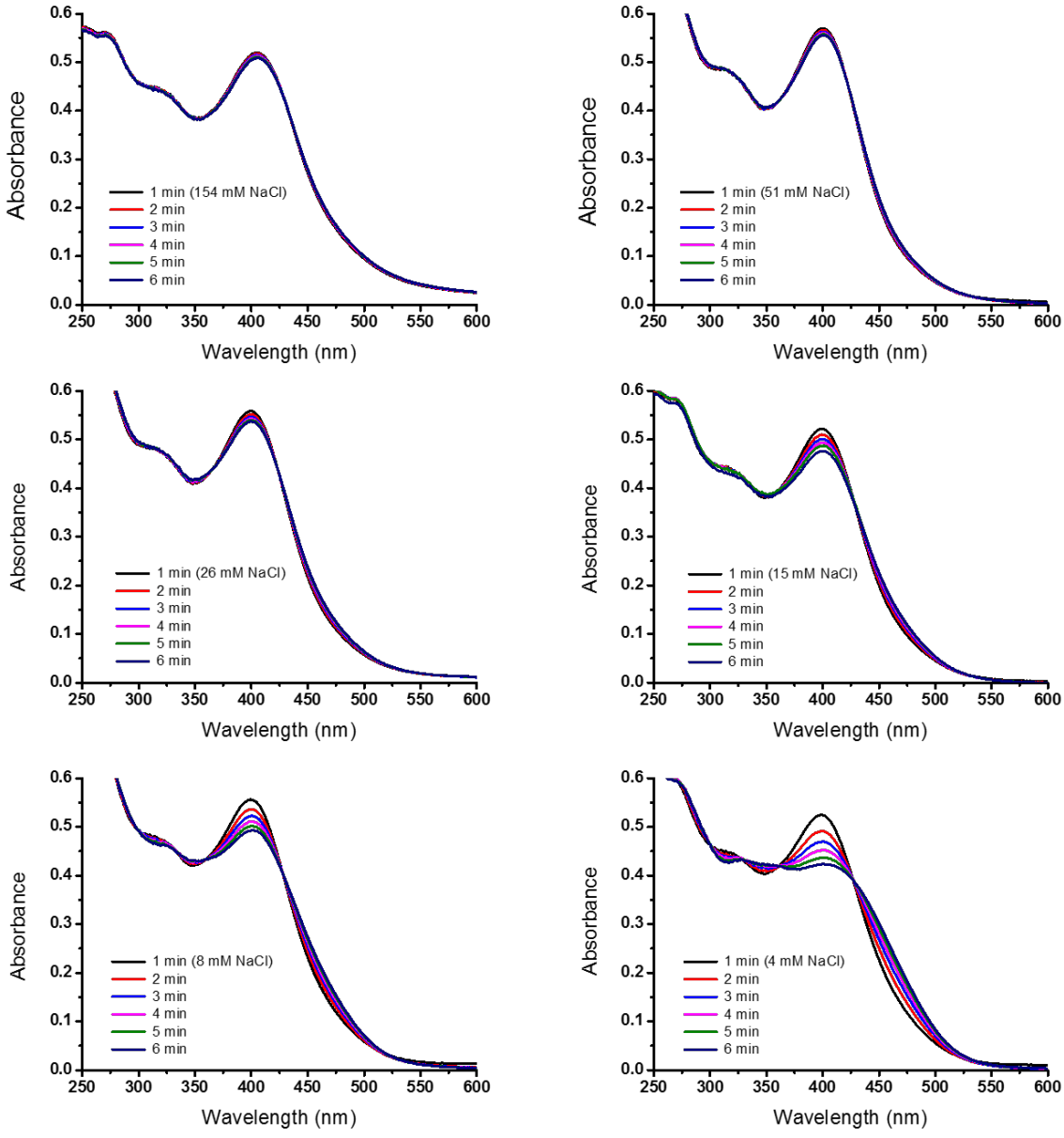

Figure 3.11: The graphs show that dynamic changes in UV/vis absorbance spectra of complex **21** are suppressed at higher Cl^- concentrations (154 μM - 26 μM), are slow at concentrations of 15 and 8 μM, and fast at 4 μM NaCl.

3.4 Discussion

XAS is a powerful spectroscopic technique for structure elucidation. Ru K-edge XAS data was collected for six arene ruthenium complexes that have been presented in the previous Chapter. Four structures are shown in Figure 3.12. Additionally, the two dinuclear starting materials [(*p*-cymene)$RuCl_2$]$_2$ **[4]** and [(*p*-cymene)$RuCl_2$]$_2$ **[5]** were studied as reference materials for the Ru(II) oxidation state in arene complexes as well as for the EXAFS fitting of Ru-X bond distances in half-sandwich motifs.

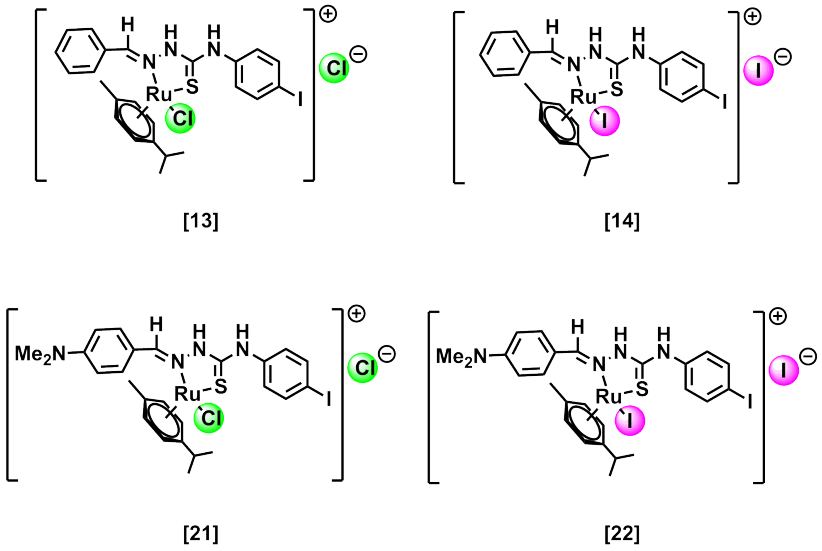

Figure 3.12: Structures of four Ru TSC complexes **[13]**/**[14]** and **[21]**/**[22]**

The four mononuclear Ru TSC complexes of *p*-iodophenyl substituted TSCs **1d** and **2d** were used to confirm their structure for both the chlorido and iodido analogues (Figure 3.12), and the mononuclear TSC complex [(*p*-cymene)Ru(PTSCNMe_2)Cl]PF_6 **[10]** was used as the crystallographic reference. EXAFS fitting to its crystal structure data was achieved for all TSC complexes. Finally, the two dinuclear complexes were studied, the Ru TSC dimer [(*p*-cymene)Ru(**2d-H**)]$_2$[PF_6]$_2$ and its osmium analogue [(*p*-

cymene)Os(**2d-H**)]$_2$[PF_6]$_2$ which was prepared especially to confirm that its structure matches the one for the Ru dimer.

3.4.1 X-ray Absorption Near-Edge Structure

For metal K-edge XANES, the most important spectroscopic processes are the electronic transitions of the excited core-electron (1s) into higher atomic or molecular orbitals. Both metal-centred d-orbitals, either empty or partially filled, and metal-ligand molecular orbitals are accessible by the excited core electron. XANES data is in most cases analysed by comparison of the edge energy E_0 with reference spectra, as these provide information about the oxidation state of the absorber.

The edge energies that were determined for the eight structures were all within ± 2 eV of each other, and the TSC complexes have similar edge energies as the two p-cymene dimers [**4**] and [**5**]. This confirms their Ru(II) oxidation state and indicates a similar geometry.[8, 9]

3.4.2 Extended X-ray Absorption Fine Structure

Before EXAFS data can be analysed in a useful way, it is important to understand the phenomenon which causes the oscillations in the X-ray absorption spectra beyond the rising edge. The next sections will therefore briefly outline the theoretical background to the technique.

The EXAFS phenomenon can be explained by electron scattering theory. With the continuous increase in incident beam energy above the absorption edge, the photoelectric effect causes photoelectrons to be emitted from the absorbing atom into the continuum.[i] Their kinetic energy increases linearly

[i] 'If a beam of light or of X-rays falls on a piece of matter, the latter will emit rapidly moving electrons.'[10]

with the frequency of the incident X-rays, and their movement away from the central atom (the *absorber*) can be described as a plane wave of electrons.

With increasing incident energy, the energy of the emitted photoelectron wave increases as well.[10] X-ray absorbance, however, varies non-linearly due to interference that occurs when the photoelectrons are scattered by surrounding atoms within the coordination sphere of the central absorber. Constructive interference of the outgoing wave with the back-scattered wave leads to higher transmitted energy, resulting in a local minimum in X-ray absorbance, while destructive interference results in the opposite effect - the total absorbance increases and the measured transmitted X-ray intensity is lower. In summary, the back-scattering of the photoelectron wave leads to a modulation of the total absorption intensity which is characteristic for the nature and position of the neighbouring atoms (*scatterers*).[11, 12]

EXAFS Theory

EXAFS can be described as the difference between the observed absorption coefficient μ(E) and the free-atom absorption coefficient μ_0(E), normalised by the free-atom contribution.[13] This modulation of the absorbance that is caused by scattering effects is mathematically expressed by the χ function (Eq. 3.1).

$$\chi\,(E) = \frac{(\mu(E) - \mu(E_0))}{\mu(E_0)} \tag{3.1}$$

The transformation of χ (E) into the χ (k) ('k-space'), aids the visualisation of the absorbance modulation.[13] χ (k) is the wave-vector dependent form of Eq. 3.1, it captures the oscillatory portion of the absorption coefficient which is used for the fit. Figure 3.6 II gives an example of a χ (k)

plot.

The theoretical approximation of the oscillations is summarised in the EXAFS Equation (Equation 3.2), first suggested by Stern in 1974.[14] It describes χ (k) as the sum over all single scattering paths of the photoelectron wave.

$$\chi_i(k) = \sum_j \frac{N_j B_j(k)}{r_j^2} e^{\frac{-2r_j}{\lambda(k)}} e^{-2k^2\sigma_j^2} sin(2kr_j + \delta_j(k)) \qquad (3.2)$$

Assuming plane-wave character, k represents the wave vector of the scattered photoelectron, i.e. its direction. The vector lengths, then, represents one leg of a scattering path or, the absorber-scatterer distance.

EXAFS fitting is the process of theoretically modelling the oscillations that are extracted as k-space data, by use of the EXAFS equation. Several parameters are required to obtain a reasonable fit of theoretical amplitudes and phases to experimantal χ (k) data. Most important is the starting point model for the structure. The next section therefore details the structural model for ruthenium arene TSC complexes for EXAFS analysis, followed by the discussion of the fitting procedure in the context of the results presented above.

3.4.3 Structural Models for EXAFS of Ruthenium Arene Complexes

In EXAFS analysis, a 'shell' of scatterers describes the number N_i of atoms of one particular element and at one particular distance R_i from the absorber. In highly ordered structures, such as rock salt which contains of two types of scatterers A and B in alternating shells, or similarly simple lattice types in which the atoms of type A are surrounded by atoms of type

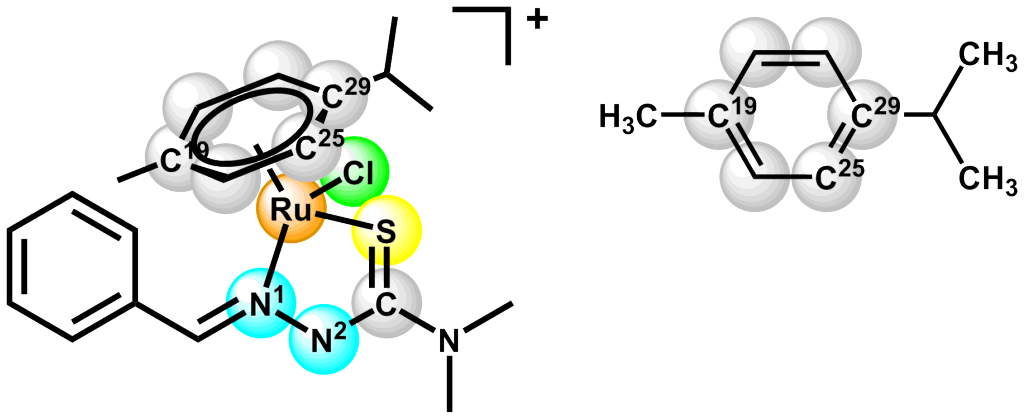

Figure 3.13: Illustration of the atoms in the first coordination sphere of the ruthenium centre in complex **10** [(*p*-cymene)Ru(DMTSCNMe_2)Cl]PF_6. The three carbon atoms C19, C25, and C29 are the main relevant scatterers in the EXAFS fitting model used in this chapter.

B, followed by a second shell of type A, each such shell is reflected by one peak in the Fourier-transformed EXAFS (R-space).

Because of this correlation, the magnitude of the R-space plot can be seen as a zero-order approximation for a radial distribution function.[15] Often, a material that comprises of shells that fit this description are of a regular, salt-like structure.

The first coordination sphere of an octahedral metal complex is defined as the six atoms which are closest in space to the metal, and which are located in positions that allow the best interactions between populated ligand s- or p- orbitals and empty or partially empty metal d-orbitals while minimising repulsive interactions between each other.

Arene ruthenium complexes are pseudo-octahedral by the above definition. The arene ligand effectively occupies three of the six positions in an octahedral ligand field, and the remaining three nearest-neighbour positions define the scope for the coordination of other ligands.

Figure 3.13 illustrates the first coordination sphere of the piano stool Ru TSC complex **10** as determined by single-crystal X-ray crystallography.

Table 3.7: Bond distances (Å) in the mononuclear complex [(*p*-cymene)Ru(1c)Cl]PF_6 **[10]** and dinuclear complex [(*p*-cymene)Ru(2d)]$_2$[PF_6]$_2$ **[10]**.

Bond	**[10]**	**[30]**
Ru-N(5)	2.1364(14)	2.0835(16)
Ru-S(12)	2.3589(4)	2.3511(5)
Ru-Cl(1)	2.4319(4)	-/-
Ru-S(12)	-/-	2.4249(5)
Ru-C(19)	2.260(2)	2.239(2)
Ru-C(25)	2.177(2)	2.207(2)
Ru-C(29)	2.222(2)	2.217(2)
Ru-C_6 centroid	1.700	1.709
Ru(1)...Ru(1)	-/-	3.5042(3)

Here, the three 'legs' are the N and the S donor atoms of the TSC, and the chlorido ligand. This structure was used to build the theoretical model for the calculation of XAS scattering amplitudes, and Table 3.7 provides the distances from the central Ru atom to the atoms in the first coordination sphere of two complexes that were presented in the previous chapter.

Fitting of the EXAFS data for the two dinuclear starting materials was achieved using X-ray crystallographic data which is available from the CCDC. For **4**, CCDC 618603 was used, and **5** was fitted against its Os(II) analogue, [(η^6 *p*-cymene)OsI_2]$_2$ (CCDC 776272).[16]

3.4.4 EXAFS Fitting

Fitting of experimental EXAFS data to theoretical χ(k) amplitudes and phases which are approximated by varying parameters of the EXAFS equation is limited by the number of independent data points (N_{ind}) that are available within a data set. This number can be calculated from the upper

and lower limits of the data (Eq. 3.3).

$$N_{ind} = \frac{(2\Delta k \Delta R)}{\pi} \tag{3.3}$$

The number of independent data points describes the degrees of freedom within a fit as a correlation of the noise-free EXAFS range $\Delta\ k$ in which the data are analysed, and the region of the Fourier transformed spectrum $\Delta\ R$ in which the data have a physically relevant meaning.[17]

The fitting regions were decided upon during the process of Fourier filtering of the normalised XAS data as described in Section 3.2.5. They were presented alongside the results of XAS data processing and are summarised in Table 3.1. The maximum k-range was from 3 to 12 - 16 $Å^{-1}$ for the Ru samples, which resulted in a number of independent points N_{ind} of $7 \leq N_{ind} \leq 16$. With $N_{ind} = 7$, a minimum number of four parameters can be varied simultaneously during an EXAFS fit. The four parameters that built the starting point in the EXAFS analysis of the Ru TSC complexes are summarised in Table 3.2.

The absorber-scatterer distances R were refined as half path-length of each single-scattering path in the fitting range Δ R. These were optimised in one of two ways: Either by using independent parameters $delr(S)$ (with S denoting the scatterer) as variables for the differences between the real distance R and the half path-length R_{eff} as

$$R = R_{eff} + delr(S) \tag{3.4}$$

or by using an expansion/contraction factor α which is multiplied with R_{eff}:

$$R \; = \; a \; \cdot \; R_{eff} \tag{3.5}$$

Using the expansion/contraction factor α with each of the crystallographic inter-atomic distances as $\alpha \; \cdot \; R_eff$ has the advantage that it is only one parameter in the fit and so allows to keep more degrees of freedom (Eq. 3.3), while accounting for the individual differences in scattering path length due to the atomic radius of the scatterers.

The resolution of two peaks in the radial dimension (R-space) is given, for two identical scatterers, by

$$\delta R = \frac{\pi}{(2\Delta k)} \tag{3.6}$$

which is dependent on the quality of the data as represented by the maximal k; the achieved resolutions (δR) are given in Table 3.2.5.

The critical evaluation of the fit results and the structural parameters obtained in the theoretical fitting procedure shows that the difference in bond length between Ru-Cl and Ru-S cannot be resolved for the data obtained on the ruthenium chlorido complexes.[17] Therefore, the data in Table 3.3 only gives an estimate of the structure, and needs to be used in combination with data provided by other spectroscopic or analytical techniques when referring to the atom type at distances that are not technically resolvable. Here, both NMR and MS have already strongly suggested that the presented ruthenium complexes have similar structures, as for example the ^{1}H NMR chemical shifts for the *p*-cymene aromatic protons show (Table 2.13).

The Ru-Ru distance in the crystal structure of dinuclear complex **30** was determined to be 3.49 Å. The corresponding scattering path was included in the EXAFS fit, but the contribution of this path to the EXAFS is so

small that it does not justify the width of the fitting range. One principle in EXAFS fitting is that the fit range in R-space should only be as wide as it contains useful information. In the plot in Figure 3.6 it can be seen that beyond the first-shell peak, no significant peaks occur in the FT. In comparison to the R-space plot in Figure 3.7, which compares the chlorido and iodido monomers of the N,N-dimethylamino-TSC ligand **2d**.

3.4.5 The Dimerisation of an Arene Ruthenium TSC Complex

Chapter 2 presented the X-ray crystal structure of a dinuclear arene ruthenium(II) TSC complex [(*p*-cymene)Ru(*IPh*)]$_2$[PF$_6$]$_2$ which appeared to have formed in a reaction between molecules of the mononuclear complex [(*p*-cymene)Ru (DTSC(*IPh*)Cl]Cl (**21**) and ammoniumhexafluorophosphate, both dissolved in the polar solvent methanol. The reaction scheme in Figure 3.14 illustrates the structures of the monomer and the dimer.

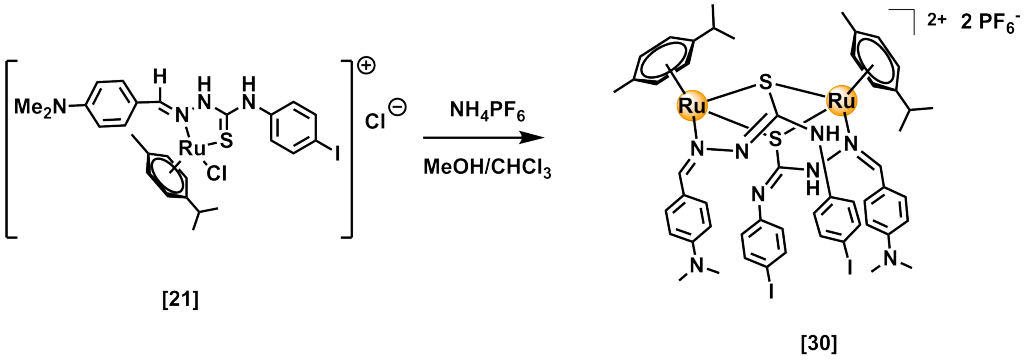

Figure 3.14: Reaction scheme of the formation of dinuclear arene Ru TSC complex **30**.

This section aims to elucidate the process of the dimerisation in more detail. The results presented here summarise spectroscopic information about the molecular structures of the two complexes **21** and **30**, and, in partic-

ular, about the process of the conversion of **21** as gathered by different spectroscopic techniques:

^{1}H-NMR, UV-vis and ESI-MS showed that hydrolysis of the Ru-Cl bond, deprotonation of a TSC NH, and E/Z-isomerisation of the imino bond are part of the reaction mechanism. Solution-state XAS adds the perspective of the metal itself to the investigation, and should reveal the time frame in which the changes to the first coordination sphere of the two ruthenium centres occur.

The suppression of UV-vis spectral dynamics in aqueous solutions of complex **21** allows the conclusion that the observed process is the hydrolysis of the Ru-Cl bond and that this process is part of the reaction mechanism for the dimerisation of **21** to **30**.

Furthermore, it supports the hypothesis that two different processes were observed with two different techniques, one being hydrolysis by UV-vis and the other being the E/Z isomerisation of the deprotonated TSC which occurs as part of the crystallisation of the dimer **30**.

Meier et al. have reported on the dimeristaion of Ru complexes with 2-pyridinecarbothioamide ligands.[18] In their study, a Ru_2S_2 rectangular structure is assumed as an intermediate before the reaction with a nucleophile breaks the dimeric arrangement.

The crystal structure of the dimer showed π-stacked aromatic rings. Aromatic π-stacking as well as the dimethylamino substituent appear to play a role in the reaction mechanism.

Qualitatively, a dependence of the reaction rate on the presence of a non-coordinating, scaffolding anion such as hexafluorophosphate (PF_6) was noticed, but was not followed-up. During the XAFS experiment, the reaction was repeated without PF_6, and no crystallisation occurred during 30

hours at highest concentration, which allowed the XAS measurement and yielded the last data point in the LCF graph. From this, the conclusion is that the reaction is driven towards completion by the crystallisation of the product and resultant removal from the equilibrium.

However, to solve the mechanism, more studies are required to obtain information about the rates of the individual processes it constitutes of. For the aim of this work, it was important to investigate the solution structures of arene ruthenium TSC complexes by EXAFS to establish a fitting protocol and gain confidence in the results both experimentally and theoretically. Next, the same technique should be applied to aqueous systems and to biological environments such as cell-culture media and cell samples.

3.5 Summary

The experiments presented in this chapter aimed to elucidate the first coordination sphere of ruthenium arene TSC complexes and confirm whether these are identical to the X-ray crystal structure data obtained for complex [**10**].

Ru-K-edge XAS data was collected on solid samples (powders) of eight ruthenium complexes, and the EXAFS region of the spectra was successfully fitted to these crystallographic data, which represents the first example of a detailed EXAFS analysis for ruthenium arene TSC complexes.

In the solution state experiment, freeze quenched aliquots of a dimerisation reaction mixture were measured in fluorescence XAS and the spectra were fitted in a linear combination analysis to XAS spectra of the reaction endpoint standards.

This is the first time that such a reaction of a ruthenium TSC complex has been studied by XAFS. The result of linear combination fitting showed that the subtle changes to the first coordination sphere between the monomer and the dimer are sufficient to affect their Ru K-edge XANES.

References

[1] P. J. Riggs-Gelasco, R. Mei, C. F. Yocum, and J. E. Penner-Hahn, *J. Am. Chem. Soc.*, 1996, **118**(10), 2387–2399.

[2] A. A. Hummer and A. Rompel, *Metallomics*, 2013, **5**, 597–614.

[3] A. A. Hummer, P. Heffeter, W. Berger, M. Filipits, D. Batchelor, G. E. Büchel, M. A. Jakupec, B. K. Keppler, and A. Rompel, *J. Med. Chem.*, 2013, **56**(3), 1182–1196.

[4] A. Levina, J. Aitken, Y. Gwee, Z. Lim, M. Liu, A. Singharay, P. Wong, and P. Lay, *Chem. Eur. J.*, 2013, **19**(11), 3609–3619.

[5] J. Tönnemann, J. Risse, Z. Grote, R. Scopelliti, and K. Severin, *Eur. J. Inorg. Chem.*, 2013, **2013**(26), 4558–4562.

[6] B. Ravel and M. Newville, *J. Synchrotron Rad.*, 2005, **12**(4), 537–541.

[7] M. Newville, *J. Synchrotron Rad.*, 2001, **8**, 322–324.

[8] T. Sriskandakumar, H. Petzold, P. C. A. Bruijnincx, A. Habtemariam, P. J. Sadler, and P. Kennepohl, *J. Am. Chem. Soc.*, 2009, **131**(37), 13355–13361.

[9] A. A. Hummer, C. Bartel, V. B. Arion, M. A. Jakupec, W. Meyer-Klaucke, T. Geraki, P. D. Quinn, A. Mijovilovich, B. K. Keppler, , and A. Rompel, *J. Med. Chem.*, 2012, **55**, 5601–5613.

[10] L. D. Broglie, *Noble Lecture*, 1929, **12th Dec**.

[11] J. E. Penner-Hahn, *Encyclopedia of Life Sciences - www.els.net*, 2004, 1–4.

[12] G. Bunker, *Introduction to XAFS: A Practical Guide to X-ray Absorption Fine Structure Spectroscopy*, Cambridge University Press, 2010.

[13] J. Yano and V. K. Yachandra, *Photosynth. Res.*, 2009, **102**(2-3), 241–254.

[14] E. A. Stern, *Phys. Rev. B*, 1974, **10**, 3027–3037.

[15] S. Calvin, *XAFS for Everyone*, 1 ed., CRC Press, Florida, US, 2013.

[16] Y. Fu, A. Habtemariam, A. M. Pizarro, S. H. van Rijt, D. J. Healey, P. A. Cooper, S. D. Shnyder, G. J. Clarkson, and P. J. Sadler, *J. Med. Chem.*, 2010, **53**(22), 8192–8196.

[17] K. Clark-Baldwin, D. L. Tierney, N. Govindaswamy, E. S. Gruff, C. Kim, J. Berg, S. A. Koch, and J. E. Penner-Hahn, *J. Am. Chem. Soc.*, 1998, **120**(33), 8401–8409.

[18] S. M. Meier, M. Hanif, Z. Adhireksan, V. Pichler, M. Novak, E. Jirkovsky, M. A. Jakupec, V. B. Arion, C. A. Davey, B. K. Keppler, and C. G. Hartinger, *Chem. Sci.*, 2013, **4**, 1837–1846.

Chapter 4

Biological Investigations and Iodine Tracing

This chapter combines studies of the anticancer properties of iodine-labelled TSC ruthenium half-sandwich complexes with the quantification of both their metal centre and chelating ligand inside cancer cells by ICP-MS.

4.1 Introduction

Drug speciation is one of the main challenges in medicinal inorganic chemistry. As such, one important question that arises during the investigations of piano-stool anticancer complexes is whether their general structure, $[(\eta^6\text{-arene})\text{M(XY)(Z)}]^{n+}$, remains intact after the molecule has entered the cell. It was discussed in Chapter 1 that some piano-stool complexes can undergo substitution reactions of the monodentate ligand Z for a water molecule, while the assumption for the chelating ligand XY is that it stays attached to the metal, due to the chelate effect.[1] The experiments presented in this chapter aim to test this hypothesis for the TSC chelating ligands in the presented complexes.

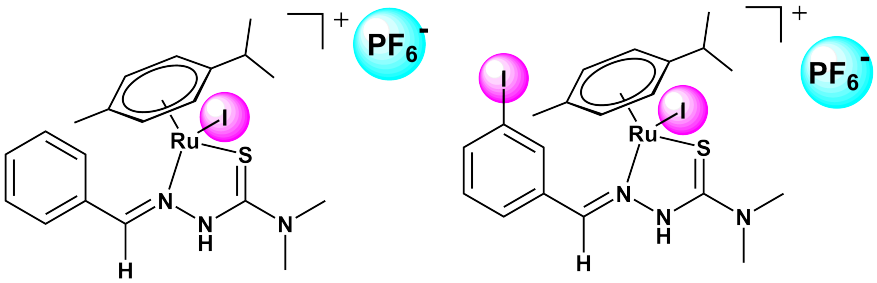

[(*p*-cym)Ru(1c)I]$^+$ **12**

[(*p*-cym)Ru(3c)I]$^+$ **29**

Figure 4.1: The two TSC ruthenium complexes **12** and **29** differ only by one iodine substituent at the TSC. This Chapter investigates the effect of this substituent on the compound's anticancer properties.

In particular, the anticancer activity and mode of action of complex **29** (Figure 4.1) of the iodine-labelled thiosemicarbazone ligand 3-iodobenzaldehyde-4-dimethyl-3-thiosemicarbazone (**3c**) will be compared with its non-labelled congener **12** of ligand **1c**. The influence of the iodine substituent within the TSC **3c**, highlighted in Figure 4.1, on the cytotoxicity, cellular accumulation, and the mode of action of its Ru complexes is discussed.

4.2 Experimental Section

This section describes the experiments which were carried out to study the iodinated TSC ruthenium complexes as anticancer agents. Details of the cell-culture experiments are included here as well as the procedures of metal quantification, colorimetric, and flow-cytometric assays which were used to analyse treated cells.

4.2.1 Materials

The synthesis and analytical data of the complexes presented in this chapter have been described in Sections 2.2.3 and 2.3 in Chapter 2. Table 4.1 lists the materials which were obtained from commercial and other sources.

Table 4.1: Materials which were used to carry out the work presented in this chapter.

Material (**Quality**)	**Source**
ICP-MS Element Standards:	
Ruthenium (1.003 ± 0.5 μg/mL in 10% HCl)	Inorganic Ventures, Inc.
Iodide (1.001 ± 3 μg/mL in 1% TEA)	Inorganic Ventures, Inc.
Biological media:	
Phosphate-Buffered Saline (PBS)	Biological Sciences, University of Warwick
Foetal Bovine Serum	Invitrogen
Roswell Park Memorial Institute cell-culture medium (RPMI-1640)	PAA-GE healthcare[b)]
Dulbecco's Modified Eagle Medium (DMEM)	PAA-GE healthcare
L-Glutamine	PAA-GE healthcare
Penicillin/Streptomycin mixture	PAA-GE healthcare
Trypsin & Trypsin/EDTA	PAA-GE healthcare

[b)] (formerly PAA Laboratories)

4.2.2 Inductively Coupled Plasma Mass Spectrometry

Inductively coupled plasma mass spectrometry (ICP-MS) was performed on an Agilent technologies 7500cx ICP-MS instrument in the Mass Spectrometry Facility of Warwick University. The solvent for all ICP-MS experiments was doubly deionised water (dd-H_2O) with 3.5 % HNO_3. ICP-MS was also used for quantification of ruthenium and iodine in human ovarian cancer cells which were treated with the complexes presented in this chapter.

Standard solutions for the external calibration of the instrument were freshly prepared in dd-H_2O for each experiment. Commercially available standard solutions of ruthenium and iodide (see Table 4.1) were diluted sequentially, using water for iodide and 3.5 % HNO_3 for ruthenium, up to a concentration of 1 ppm. The two solutions were then mixed in the following dilution to achieve a mixed standard that contained 200 ppb of both element ions. From this solution, the calibration standards of the following concentrations were prepared by sequential dilution with 3.5 % HNO_3: 0, 5, 10, 15, 20, 25, 30 ppb.

The isotopes ^{101}Ru and ^{127}I were detected and quantified simultaneously in helium collision mode, along with ^{166}Er as internal standard to validate the reading. The method details are summarised in Table 4.2. It was important to inject a blank of 3.5 % HNO_3 in dd-H_2O after each sample injection to allow for noise reduction in the iodine readings, which were used without correction or background subtraction. Triplicates of three independent readings were averaged for each sample and are reported with their standard deviations (SD), as mean±SD.

Detection of defined Ru:I ratios and their identity after nitric-acid digestion were tested, and the method was validated by a standard-addition

Table 4.2: Details of method for simultaneous detection of ^{101}Ru and ^{127}I by ICP-MS

	Parameter	
Flow rates	Plasma	15 L·min^{-1}
	Auxiliary	
	Nebulizer	
	Cooling water	1.5 L·min^{-1}
Sample Introduction	Peristaltic pump	0.3 rps
	Sample uptake rate	
	Nebulizer	
Acquisition parameters	Initial stabilisation time	30 s
	Acqu. mode	Spectrum (multitune)
	Sweep time	0.1 s per point 0.3 s per mass
	Isotopes	^{101}Ru, ^{127}I, ^{166}Er$^{a)}$
	Replicates per mass	3
	No of sweeps	3
	Stabilisation times between sweeps	15 s
	Total acqu. time	80 s
	Total wash/rinse time	90 s
	Total run time	200 s
Detection limits	^{127}I	2.50±0.05 ppb
	^{101}Ru	0.05 ppb

$^{a)}$^{166}Er was used as the internal standard to validate each reading.

experiment: A known quantity of iodide standard solution was added to a sample of unknown iodine concentration. Readings of iodine in this sample were taken prior to and after addition of the spike volume and the data showed the expected increase in detected iodine, without background interference. The results presented in this chapter for the simultaneous detection of the two elements ruthenium and iodine were obtained with an iodine detection limit of 2.00±0.05 ppb.

4.2.3 High Performance Liquid Chromatography

Complexes **10**, **12**, **27**, and **28** were dissolved in DMSO and immediately diluted 1:20 into dd-H_2O, 0.9% NaCl in dd-H_2O, or 0.9% KI in dd-H_2O to achieve a final concentration of 0.1 mM and 5% dmso (v/v). The resulting solutions were filtered through a 0.2 μm syringe filter prior to injection of 50 μL into the HPLC system. Samples were injected manually within 10 min after the initial preparation, and again after 24 h of equilibration at 298 K.

Reverse-phase HPLC was carried out using an Agilent 1100 instrument with a photo-DAD detector (λ= 320 nm, reference channel 360 nm) and a *ZORBAX Eclipse Plus* C18 column (250 x 4.6 mm, 5 μm pore size). The mobile phase system was H_2O containing 0.1% trifluoroacetic acid (TFA) [**A**] and acetonitrile (ACN) containing 0.1% TFA [**B**]. With a flow rate of 1 mL $\cdot$ min^{-1}, the following gradient was applied: 30% [**B**] to 80% [**B**] in 30 min, decrease to 30% [**B**] in 1 min, hold for 7 min.

4.2.4 Cell-Culture Experiments

Cell-culture experiments, except for the digestion of cell pellets for metal quantification, was carried out in the facilities of the School of Life Sciences, University of Warwick. The following experiments were performed in collaboration with Dr. I. Romero-Canelón from the same research group. Details of the respective experimental procedures are summarised following this overview.

- Determination of antiproliferative activity of ruthenium TSC complexes by growth inhibition of human ovarian cancer cells A2780 *in vitro*, measured with the Sulforhodamine B (SRB) colorimetric assay.

- Accumulation of ruthenium and iodine in A2780 cells after incubation with solutions of ruthenium TSC complexes, quantified by ICP-MS of cell-digests.
- Determination of sub-cellular Ru/I distribution by fractioning of treated cells and Ru/I quantification by ICP-MS.
- Analysis of cell-cycle populations after drug exposure for 24, 48, and 72 h, with quantification of cells by flow cytometry.
- Detection of apoptotic populations in treated A2780 cells at the same three time points, measured by flow cytometry.

Cell Culture

A2780 human ovarian carcinoma cells were cultured as adherent monolayers[2, 3] in RPMI-1640 cell-culture medium supplemented with fetal calf serum (10 %), L-glutamine (1 %), and penicillin/streptomycin (1 %). The cells were incubated at 310 K in a humidified atmosphere containing 5 % CO_2 until they reached 80-90 % confluency. The medium was removed and the cells were washed with phosphate-buffered saline (PBS) before addition of trypsin-EDTA (25%). A single-cell suspension was obtained by mixing with fresh RPMI-1640 medium and the concentration of cells in a 10 μL aliquot was determined with a hemocytometer.

Preparation of Drug Solutions for Cell-based Assays

For all *in vitro* assays, solutions of complexes were prepared as follows: **10**, **12**, **27**, and **28** were dissolved in dmso at room temperature and diluted so that the concentration of the stock solutions was 50 μM in a 50/50 mix (v/v) of RPMI-1640 and saline, containing 2% of dmso. From the stock,

all test concentrations were achieved by sequential dilution into RPMI-1640 medium (fully supplemented with 10% fetal calf serum, 1% L-glutamine, and 1% penicillin/streptomycin). Absolute concentrations of ruthenium in the stock solutions were determined by ICP-MS, and those results were used for the calculation of IC_{50} values.

In vitro growth-inhibition assay

The growth-inhibition assay was carried out using 24-well micro titre plates seeded with 10^5 cells per well. The cells were pre-incubated at 310 K in drug-free cell-culture medium for 24 hours before addition of the drug solutions. The medium was removed with suction and replaced with solutions of the complexes (prepared as described above) in triplicates of six concentrations between 50 μM and 0.1 μM. After incubation with these solutions for 24 h, the supernatant solutions were removed and the cells were washed with PBS. No recovery time in drug-free media was allowed. For time-dependent studies, the experiment was repeated in the same way, using 24, 48, and 72 h exposure times without recovery time. For the quantification of viable cells, the SRB assay was used as detailed below.

Sulforhodamine B Colorimetric Assay

Cell viability was determined as percent of cell-survival compared to untreated control cells using the SRB colorimetric assay.[4–6]

Briefly, trichloroacetic acid (TCA, 50 % in H_2O, 150 μL/well) was added to each well, and the plate was left to incubate for 1 h at 277 K to fix the cells. After removal of the TCA the plate was rinsed with tap water and dried in air. SRB dye (dissolved at 0.4 % in 1 % acetic acid) was added (150 μL/well) and the plate was kept at 298 K for 30 min, followed

by removal of excess dye and washing of the plate with 1% acetic acid. Addition of 10 mM Tris-base solution (200 μL, pH 10.5) was followed by incubation at room temperature for 1 h to dissolve the dye. Absorbance readings were taken at 570 nm, using a BioRad iMark microplate reader.

Percent cell-survival was plotted against the $\log_{10}$(c) of the complex solutions (with c in mM) and the half-maximal inhibitory concentration (IC_{50}) of each complex was determined as the inflection point of the fitted sigmoidal curves. Origin software (v.8.5) was used for curve fitting of the experimental data. The results are reported as the mean ± SD of duplicates of triplicates of two independent experiments.

Cellular Accumulation Studies

Accumulation of the two elements ruthenium and iodine in A2780 cells was determined after exposure to complexes **10**, **12**, **27**, and **28** for 24 h. The experiment was carried out in triplicates for each complex. A2780 cells were cultured as described above, and three petri dishes of 145 mm width were seeded with $5x10^6$ cells each.

These were pre-incubated in drug-free RPMI-1640 medium for 24 h. The medium was removed from the cells and replaced with 10 mL of drug solution at IC_{50} concentration (2 μM). Cells were exposed to the drugs for 24 h before the supernatant solutions were removed, the cells were washed with PBS and detached from the plates using trypsin solution (25%). The detached cells were suspended in 5 mL fresh RPMI medium, counted and pelleted by centrifugation at 1000 rpm for 5 min.

The cell pellets were digested in 73% nitric acid (0.6 mL) at 353 K overnight, diluted 1:10 with dd-H_2O and the ruthenium and iodine content were quantified by ICP-MS and compared to un-treated control cells.

Determination of Sub-cellular Ru/I Distribution

In order to quantify the amount of ruthenium and iodine in four different sub-cellular fractions, the cell-accumulation experiment was repeated in the same way as described above, but with twice as many cells. This increase was necessary to assure a sufficiently high reading of ruthenium and iodine in the ICP-MS measurement after the pellet is divided into the four fractions.

Three large petri dishes (145 mm width) were seeded with 10^7cells which were exposed to 45 mL of a 2 μM solution of complex **29** for 24 h without recovery time. After collecting and counting the cells, the following steps were carried out consecutively, using the buffers provided in the BioVision FractionPREP kit according to the supplier's instructions to obtain the following fractions.

1. The **cytosolic fraction** was extracted first, by re-suspending the cell pellet in the provided cytosol extraction buffer (CEB) and keeping the suspension on ice for 20 min. After centrifuging for the following 10 min at 2000 rpm and 277 K, the supernatants were collected.

2. For extraction of the **membrane fraction**, the cells were re-suspended in a mix of membrane extraction buffer A (MEA) and membrane extraction buffer B (MEB) by vortexing for 1 min, centrifuging for 5 min at 3400 rpm and 277 K, and collection of the supernatants.

3. Next, the **nuclear fraction** was obtained. The cell pellet was suspended in nuclear extraction buffer (NEB) and the suspension was incubated on ice for 40 min. Subsequently, after centrifuging for 10 min at 12000 rpm and 277 K the supernatants were collected.

4. The remaining pellet represents the **cytoskeletal fraction**.

Samples of each fraction were obtained in triplicates and digested overnight in 73% nitric acid (300 μL). The amount of ruthenium and iodine in each sample was quantified by ICP-MS after dilution into 2700 μL dd-H_2O as described earlier. To compare iodine levels to ruthenium levels in each fraction, data were normalised to nmol $\cdot 10^{-6}$ (nmol per million) cells.

Cell-Cycle Analysis

For analysis of cell-cycle populations, A2780 cells were seeded in 6-well plates at 10^6 cells per well. After 24 h of pre-incubation, the media was replaced with solutions of complexes **12** and **29** of 2 μM, except in the wells of the control, which remained unchanged. The cells were exposed to the drug for 24 h in the first experiment, and for 24, 48, and 72 h in the time-dependence experiment. After the exposure time, the supernatants were collected and centrifuged. Viable cells were detached from the plate using trypsin solution, removed with added RPMI 1640 medium and combined with the cells that were harvested from the supernatant. After washing the combined cells with PBS, the pellets were incubated in 1 mL ethanol at 253 K prior to analysis by flow cytometry.

To prepare for flow cytometry, the ethanol was removed and the cells were washed with PBS before staining them with a mixture of propidium iodide (PI) solution and RNAse in PBS for 30 min. The following removal of the stain and re-suspending in fresh PBS was necessary to minimise background readings of dye in solution. Fluorescence emission of the intercalated dye (excitation of DNA-bound PI at 536 nm) was read at 617 nm using a *Becton Dickinson FACScan* flow cytometer.

Detection of Apoptotic Populations

For the apoptosis detection assay, A2780 cells were seeded in 6-well plates at $1 \cdot 10^6$ cells per well. After 24 h of pre-incubation, a solution of complexes **12** and **29** of 2 μM was added. The cells were exposed to the drug for 24, 48, and 72 h. The population of apoptotic cells after the respective incubation time was determined by flow cytometry on cells that were stained using the Annexin V-FITC Apoptosis-detection kit (BioVision) according to the supplier's instructions. Intensity of fluorescence emissions was read using a *Becton Dickinson FACScan* flow-cytometer.

Flow Cytometry

Flow cytometry was carried out using a *Becton Dickinson FACScan Flow Cytometer* (courtesy of Prof. David Scanlen, School of Life Sciences, University of Warwick).

Single-cell suspensions were obtained by mixing the previously harvested cells in the appropriate buffer, including any stains or reactants as detailed in the respective experimental procedures. These suspensions were transferred into flow-cytometry sample-tubes immediately before the measurement.

Flow-cytometry data were analysed using the Flowjo software package (version 10.0.6). After plotting the total forward-scatter against total side-scatter (FSC vs. SSC), the entire cell population was gated to exclude debris from useful data, thus reducing noise to achieve a population of cells to be analysed. The data were normalised to the gated population and standard deviations were calculated.

Cell-cycle data were further normalised against the results for the neg-

ative control in each experiment (see Section 4.3.5) and the standard deviations of the resulting data were calculated using the error propagation formula given in equation 4.1.

$$\frac{\sigma_y}{y} = \sqrt{\left(\frac{\sigma_a}{a}\right)^2 + \left(\frac{\sigma_b}{b}\right)^2} \tag{4.1}$$

For apoptosis detection, data recorded in the two channels FL2-H (PI fluorescence, red) and FL1-H (FITC fluorescence, green) were plotted against each other, and in each quadrant of the plot the number of cells was counted, representing the relative population in each of the four different viability stages.

4.2.5 Significance Tests

To determine statistical significance of the experimental results, *p*-values were calculated using a two-sample, two-tailed Student's T-test[7, 8] as implemented in MS excel.

Table 4.3: Significance of test results as represented by the *p*-value (adapted from Coolican.[9]

Significance level	***p*-value**
significant	$0.01 < p < 0.05$
highly significant	$0.001 < p < 0.01$
very highly significant	$p < 0.001$

Statistically relevant differences between the experimental results obtained in this chapter and negative controls are reported as either "significant" or "highly significant", based on the probability levels described in Table 4.3 as adapted from Coolican.[9]

4.3 Results

Two groups of arene ruthenium complexes were synthesised and fully characterised as described in Section 2.2.3 in Chapter 2. Their general structure is presented in Table 4.4, which gives an overview of the systematic structural variations that were chosen for the comparative studies described below.

Table 4.4: Systematic iodine labelling in arene ruthenium TSC complexes.

Complex		R	X	Y
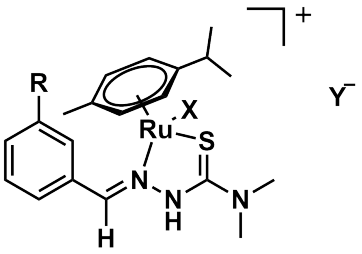	**10**	H	Cl	PF_6
	11	H	I	I
	12	H	I	PF_6
	27	I	Cl	Cl
	28	I	I	I
	29	I	I	PF_6

Four complexes in Table 4.4 have iodide as their monodentate ligand (**11**, **12**, **28**, **29**). Complexes **12** and **11** both bear the non-labelled benzaldehyde-4-dimethyl-3-thiosemicarbazone ligand **1c** and only vary in their counter ion, in the same way as complexes **28** and **29** of the iodinated TSC ligand 3-iodobenzaldehyde-4-dimethyl-3-thiosemicarbazone (**3c**).

As a result of this systematic labelling with iodine in three different positions of the structure, i.e. the chelating TSC ligand, the monodentate ligand, and the counter ion, the ratio of I : Ru increases as follows. The I : Ru ratio is 1:1 in complex **12**, it increases to 2:1 in complexes **11** and **29**, and complex **28**, with iodine in three positions, shows an I : Ru ratio of 3:1.

In the following, the anticancer activity of these four compounds against human ovarian cancer cells (A2780) will be described, followed by studies of their cellular accumulation in those cells. The distribution of ruthenium

and iodine in A2780 cells was investigated for complex **29**. The two chlorido complexes **10** and **27** were used in HPLC experiments in order to compare the aqueous solution stability between the chlorido and iodido analogues in the presence and absence of sodium chloride.

4.3.1 Antiproliferative Activity

The antiproliferative activity of complexes **11**, **12**, **28**, **29** as well as **19** and **15** was determined in human ovarian carcinoma cells (A2780), using the sulforhodamine B (SRB) colorimetric assay[4–6] with Cisplatin (CDDP) as positive control.

The assay relies on the binding of SRB to alkaline residues of proteins in fixed cells at low pH. At high pH levels, the SRB dye is released quantitatively, and a linear correlation between free dye and the amount of proteins is observed. For quantification of viable cells compared to un-treated control cells, the relative absorbance of SRB at 570 nm is used. The half-maximal inhibitory concentrations (IC_{50}) were determined as the inflection point of the cell-viability vs. log(c) plot and are compared in Figure 4.2.

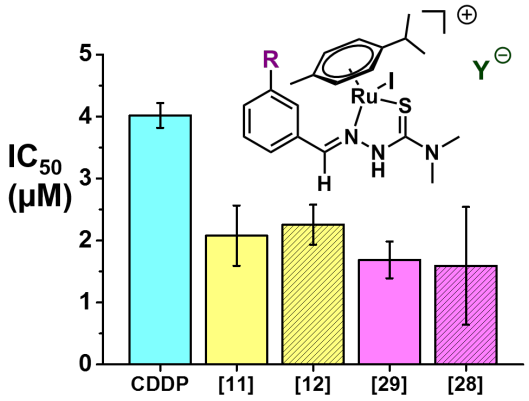

	R	Y⁻	IC_{50} / µM
11	H	PF_6	2.1 ± 0.5
12	H	I	2.3 ± 0.3
29	I	PF_6	1.6 ± 0.9
28	I	I	1.7 ± 0.3
CDDP			4.0 ± 0.2

Figure 4.2: Antiproliferative activity (IC_{50}) of complexes **11**, **12**, **28**, and **29** against human ovarian carcinoma cells (A2780) after 24 h of exposure without cell-recovery in drug-free medium. Cisplatin (CDDP) was used as a positive control.

All four complexes exhibit similar activity, with IC_{50} values in the range of 1.6 - 2.1 μM (Table 4.6). Evaluating these results using Student's T-Test[7] to a significance level of $p = 0.05$ suggests that there is no statistically significant difference ($p > 0.05$) between the activities of the complexes in this series.[8] The activities of the four ruthenium TSC complexes are also comparable to the IC_{50} of Cisplatin, which was determined to 4.0 μM under the same conditions.

Table 4.5: Time dependent antiproliferative activities (IC_{50}) of complexes **12** and **29** against A2780 cells.

Compound		Exposure Time	IC_{50} [μM]
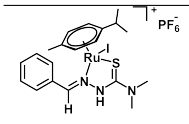	**12**	**24 h**	3.9 ± 0.2
		48 h	2.6 ± 0.1
		72 h	3.3 ± 0.5
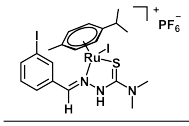	**29**	**24 h**	3.6 ± 0.1
		48 h	2.5 ± 0.1
		72 h	3.4 ± 0.2

The experiment was repeated using only complexes **12** and **29** at three different lengths of exposure, to determine whether the duration of drug exposure had an influence on the activities of the two compounds. The results in Table 4.5 show that the IC_{50} values are similar to the results that were obtained in the assay which only used 24 h of exposure (Table 4.6). IC_{50} values were in the range of 2.45 ± 0.1 to 3.9 ± 0.2 μM. A p-value of 0.814 was determined between the results for the two complexes. It can be concluded that the activities of **12** and **29** are identical within error. Moreover, they also do not vary significantly between the three recorded time points of 24, 48, and 72 h of exposure.

4.3.2 Total Cellular Ru/I Accumulation

In this experiment, the total amount of ruthenium and iodine was determined that was accumulated by A2780 cells within 24 h of exposure to the four complexes. Four ruthenium TSC complexes were compared, and the results are tabulated below (Table 4.6). The drug concentration to which the cells were exposed was 2 μM of complex **11**, **12**, **28**, or **29**; representing the average IC_{50} value which was determined in the previous experiment. No recovery time was allowed prior to collecting the cells for the digestion in nitric acid and subsequent Ru/I quantification by ICP-MS.

The bar chart in Figure 4.3 summarises the results of the quantification of the two elements ^{101}Ru and iodine ^{127}I in the digested cell pellets. For each complex, the orange (left) bar represents the ruthenium quantity, while the purple bar represents the amount of iodine that was detected, in units of pico mole per one million cells (pmol/10^6cells). This unit is a result of normalising the initial ICP-MS data, detected in ppb (μg/L), by the atomic mass of the respective element, the sample volume, and by the number of

Table 4.6: Accumulation of ruthenium (^{101}Ru) and iodine (^{127}I) in A2780 (in pmol per 10^6 cells) after 24 h of exposure to 2 μM solutions without subsequent recovery time.

Compound	**pmol Ru** / 10^6 **cells**	***p*-value**	**pmol I** / 10^6 **cells**	***p*-value**
12	34 ± 4	0.0218	<2	-
11	35 ± 1	0.0005	<2	-
28	60 ± 14	0.0184	19 ± 4	0.0182
29	62 ± 6	0.0034	22 ± 2	0.0041

cells in each sample. This normalised value represents the average number of ruthenium or iodine atoms accumulated by one million cells, which allows comparison of the results not only between replicates of cell samples but also between different elements.

For the two complexes [(*p*-cymene)Ru(PTSCNMe_2I)]I (**11**) and [(*p*-cymene)Ru(PTSCNMe_2I)]PF_6 (**12**) that do not have an iodine substituent as part of the TSC ligand (Table 4.4 R = H), 34 ± 4 and 35 ± 1 pmol ruthenium were detected per one million cells, while no iodine was detected in these cell samples. For complexes [(*p*-cymene)Ru(ITSCNMe_2I)]I **28** and [(*p*-cymene)Ru(ITSCNMe_2I)]PF_6 **29** with R = I in the TSC, Ru accumulation was twice as high (60 and 62 pmol per million cells) as for **12** and **11**, and 19 ± 4 and 20 ± 2 pmol iodine were detected. These iodine quantities represent 1/3 of the ruthenium that was accumulated by the same cells.

In summary, the data presented in Figure 4.3 highlight that the four complexes enter A2780 cells within 24 h of drug exposure. All quantities were statistically significant compared to untreated control cells as shown by *p*-values below 0.05 or 0.01 (Table 4.6).

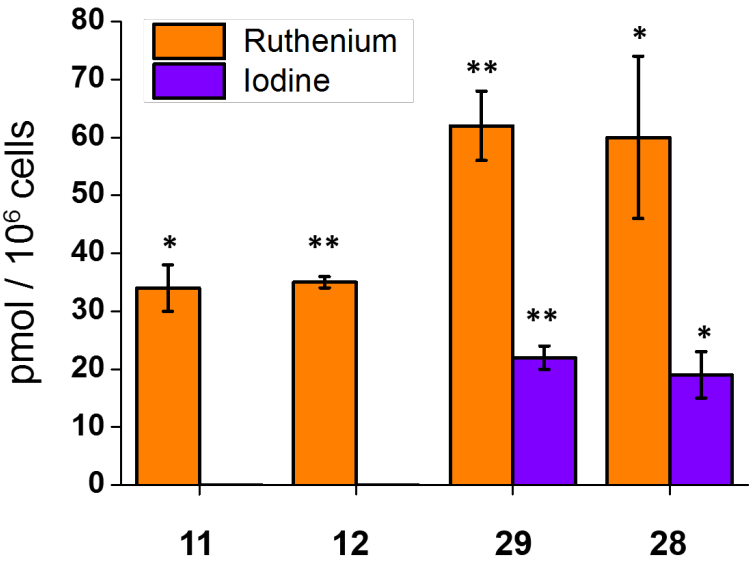

Figure 4.3: Bar chart shows statistically significant accumulation of ruthenium (^{101}Ru) in A2780 cells from all four complexes, and of (^{127}I) from complexes **28** and **29**. Quantities were determined by ICP-MS after 24 h of exposure to equimolar/equipotent solutions (2 μM) without subsequent cell-recovery. The results show significant difference compared to un-treated controls (** $p < 0.01$, * $p < 0.05$).

4.3.3 Sub-cellular Ru/I Distribution

An experiment was performed to assess structural integrity of the complex inside cells on the one hand, and to narrow down possible target sites on the other. This assay quantifies the amount of ruthenium and iodine in four different sub-cellular fractions of A2780 cells after treatment with the iodine labelled complex **29**. It aims to elucidate in which parts of the cell the metal and the halide accumulate.

A2780 cells were exposed to complex **29** at its IC_{50} concentration of 2 μM for 24 h. After this, the cells were collected, and four cell-fractions were obtained that contained the sub-cellular compartments detailed below.

Results are presented in Figure 4.4, with orange bars for ruthenium

Table 4.7: Quantities of ^{101}Ru and ^{127}I (in pmol/10^6 cells) in four fractions of A2780 cells after 24 h of exposure to [(*p*-cym)Ru(**3c**)I]PF_6 (**29**, 2 μM) without recovery time.

	pmol $\cdot 10^{-6}$ cells			
	Ru	**I**	**Ru : I**	***p*-value**[†]
Cytoskeleton	10 ± 1	8 ± 2	1	0.10
Membrane/Particulate	33 ± 2	8 ± 1	4	0.02
Nuclear Fraction	7.5 ± 0.5	4 ± 1	2	0.10
Cytosol	1.5 ± 0.1	1.0 ± 0.2	1	0.31
Σ	52	21	2.6	-

[†] T-Test compares between the results obtained for the two elements per fraction, $p < 0.05$ is treated as a statistically significant difference between the levels of Ru and I.

Cytosole:	Soluble proteins from the cytoplasm
Membrane:	Membrane proteins, cellular organelles & their membranes
Nucleus:	Soluble nuclear proteins, nuclear-membrane proteins
Cytoskeleton:	Insoluble cellular proteins, genomic DNA

quantities and purple bars for iodine, and Table 4.7 provides an overview of the ruthenium and iodine contents in each fraction.

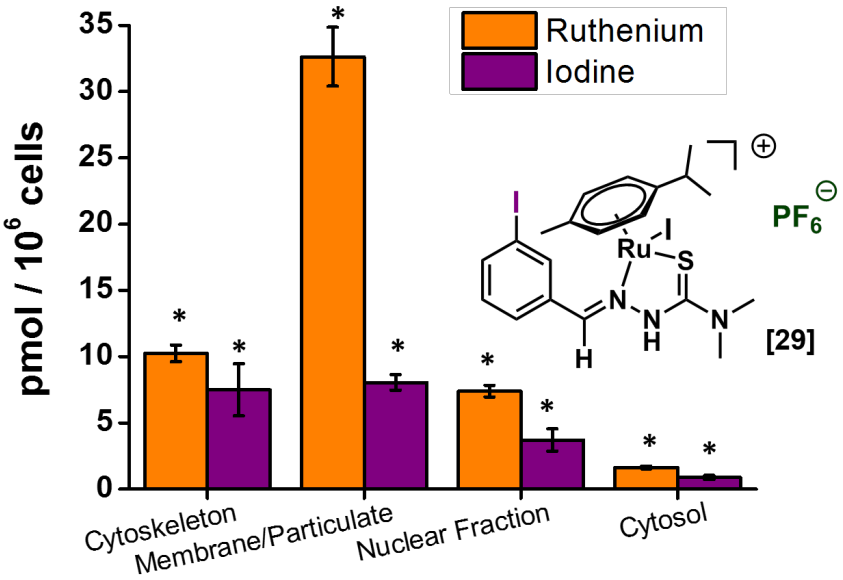

Figure 4.4: Compartmentalisation of ^{101}Ru and ^{127}I in A2780 cells, determined after 24 h of exposure to **[(*p*-cym)Ru(3c)I]PF$_6$** (**29**, 2 μM) without recovery time. **Cytoskeleton:** insoluble cellular proteins, genomic DNA; **Cytosole:** Soluble proteins from the cytoplasm; **Membrane:** membrane proteins, cellular organelles and organelle membranes; **Nucleus:** soluble nuclear proteins, nuclear-membrane proteins. * All detected quantities were statistically significant compared to the control ($p < 0.05$). The result for Ru in the membrane fraction was significantly different from the iodine level in the same fraction ($p < 0.05$).

All quantities reported in Figure 4.4 were statistically significant compared to un-treated control cells ($p < 0.05$). The membrane fraction contained the largest part (63%) of the total accumulated metal in this experiment, with 33 pmol ruthenium per one million cells. Of the other three fractions, cytoskeletal and nuclear fraction both accumulated one third of the total Ru each, with 10 pmol/10^6 cells and 7.5 pmol/10^6 cells, respectively. In the cytosolic fraction, 1.5 pmol/10^6 cells ruthenium was detected.

Iodine distribution differed compared to the metal. In the membrane fraction, 8 pmol iodine per one million cells were detected, and the same quantity was found in the cytoskeletal fraction. 1.8 pmol/10^6 cells iodine

were detected in the cytosol, which equals the amount that was found in the nuclear fraction.

Comparing the two bars for each fraction against each other (Figure 4.4), there is a 4:1 ratio of ruthenium over iodine in the membrane which stands out from the rest of the data. A low *p*-value confirms the significant difference between the quantities of the two elements. In contrast to this finding, both cytoskeletal and cytosolic fraction show a Ru:I ratio closer to 1. The nuclear fraction showed an elevated ruthenium content over iodine, with approx. twice as much metal as halide.

HPLC experiments were used to assess the aqueous solution speciation of the compounds in the presence and absence of chloride ions. These aim to explain the lack of iodine in cells treated with complexes **12** and **11**.

4.3.4 HPLC of iodido and chlorido complexes

This study was designed to elucidate the speciation of the four complexes **12** (R = H, X = I), **28** (R = H, X = I), **10** (R = H, X = Cl), and **27** in aqueous solution, using high performance liquid chromatography (HPLC).

The test was carried out by comparing four complexes, two X = Cl/I pairs and two pairs with R = H/I (Figure 4.5), in both doubly-deionised water and in physiological saline solution (0.9% NaCl, 154 mM). This chloride concentration (154 mM) compares well with the concentration of chloride in RPMI-1640 medium (140 mM). This way, the comparison between chromatograms in the presence and absence of Cl^- should show whether there is an exchange of the monodentate halido ligand, by appearance of more than one signal in the chromatogramm.

Figure 4.5 shows the chromatograms that were recorded 10 min after each of the respective samples was dissolved and diluted into dd-H_2O, com-

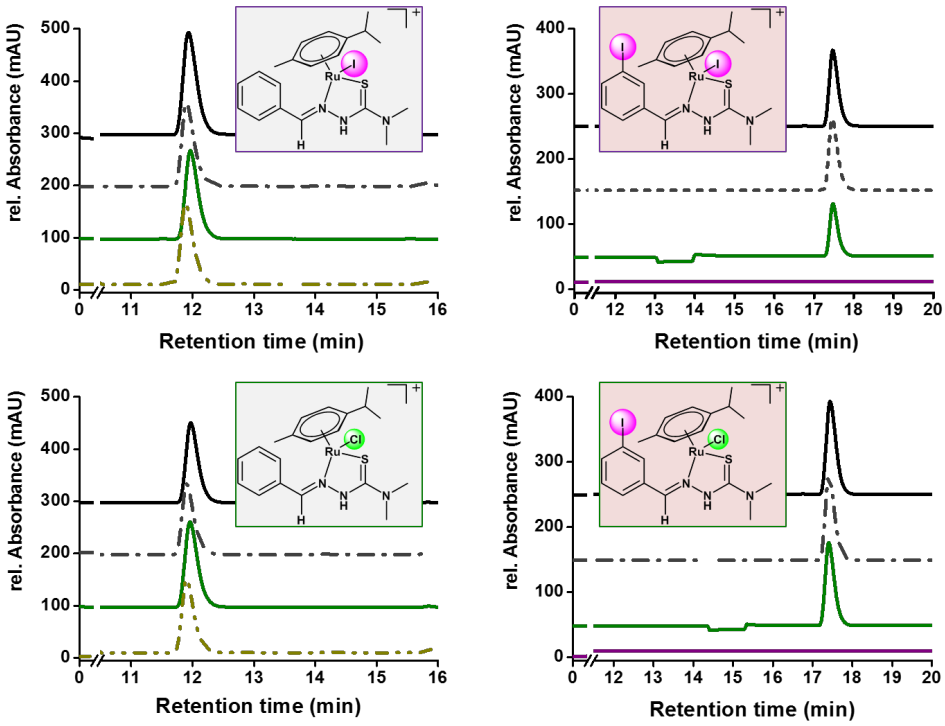

Figure 4.5: Reverse-phase HPLC chromatograms show a 5 min difference in retention times between complex **12** (R = H, X = I) and **28** (R = I, X = I) as well as between **10** (R = H, X = Cl) and **27** (R = I, X = Cl). Injections 10 min and 24 h of after dissolving the compounds at 0.1 mM in H_2O or 0.9% Saline (both 5% dmso) at 298 K.

pared to the chromatograms of the same solutions after 24 h equilibration at ambient temperature. The graphic shows the 5 min difference in retention times (t_R) between the complexes of the iodine-labelled TSC ligand **3c** and their non-labelled analogues. Complexes **12** and **10** have a retention time (t_R) of 12 min, while complexes **28** and **27** have a retention time of 17.5 min.

The retention times do not change within 24 h of equilibration at 298 K, and no additional peaks appear in the chromatogram. The comparison between water and saline solution after 10 min and 24 h shows no difference or change in the retention time. An attempt to dilute the complexes into 0.9% KI solution as a comparison resulted in precipitation of an orange-red

solid which was removed using the syringe filter. The chromatograms of the filtrate did not show any signals (pink graph in Figure 4.5).

Table 4.8: pH-values in HPLC sample solutions at 298 K, measured 24 h after the complexes had been dissolved in dmso and diluted into either water or saline.

Complex	pH in H_2O	pH in 0.9% saline
12	4.2	4.2
28	4.3	4.3
10	4.5	4.2
27	4.3	4.3

At the end of the experiment, the pH of the sample solutions was measured in order to detect any differences compared to the solvent (Table 4.8). The pH had decreased to values between 4.2 and 4.5 (**10** in saline or water), but there was no difference between the pH of the solutions in water or saline.

4.3.5 Cell-Cycle Analysis by Flow Cytometry

The cell replication cycle can be divided into the four phases: G1, S, G2, and M. DNA duplication occurs in S-Phase, and the separation of the two new cells (mitosis) occurs during M-phase.[10] The flow-cytometric analysis of these different cell-cycle phases relies on the quantification of double stranded DNA (stained with the intercalator propidium iodide) that is present in each phase of the cell-cycle. It is therefore important to understand the different phases and their relation to DNA quantities. The two gap phases G1 and G2 are preparatory and precede the two functional phases S and M, respectively. The transition from a preparatory to a functional phase is controlled rigorously by checkpoints, and only cells with undamaged DNA can progress to the next stage. When, due to DNA damage,

such a checkpoint is not passed by the cell, the cell-cycle is arrested in the previous phase. This experiment aims to detect the effect that complexes [(*p*-cymene)Ru(PTSCNMe_2I)]PF_6 **12** and [(*p*-cymene)Ru(ITSCNMe_2I)]PF_6 **29** have on the cell-cycle of A2780 cells during an exposure time of 24, 48, and 72 h at IC_{50} concentration (2 μM).

- **G1 phase:** During the first gap phase, a single copy of double-stranded DNA is present. Propidium iodide (PI) can intercalate into those strands to quantify them.

- **S-phase:** During DNA replication, between one and two copies of DNA are present in the cell, and some of it is already single-stranded. Although PI cannot bind to single strands, all present double strands are quantified in this phase.

- **G2-M phase:** After successful DNA duplication, two complete copies of double stranded DNA are present.

Table 4.9 summarises the populations of cells in three different cell-cycle stages (G1, S, G2/M) at three different time points: In columns for 24 h, 48 h, and 72 h of exposure, cell populations are listed for the untreated cells (**-ve**, top rows), and for cells after treatment with complexes **12** (middle) and **29** (bottom rows) at IC_{50} level. Each result was compared with the negative control (**-ve**) using Student's T-Test, to determine whether the detected effects were statistically significant (p-value < 0.05).

The distribution of untreated cells over the three stages was 51.2±1.9% in G1 : 27.7 ± 1.5% in S : 21.1±0.6% in G2/M after 24 h. Both complex **12** and **29** significantly alter this distribution. Cells treated with **12** showed an increase in the G1 population by more than 20% (65.7±1.4 %), while

Table 4.9: % population of A2780 cells in cell-cycle phases **G1**, **S**, and **G2/M** after incubation with complexes **12** and **29** for 24, 48, and 72 hours, without recovery in drug-free media.

Compound		Cell-cycle phase	% Population after 24 h	48 h	72 h
	-ve	**G1**	51.2 ± 1.9	51.8 ± 0.6	74.4 ± 0.3
		S	27.7 ± 1.5	23.6 ± 1.1	16.4 ± 1.6
		G2 / M	21.1 ± 0.6	24.6 ± 0.6	9.2 ± 1.9
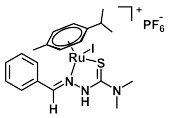	**[12]**	**G1**	65.7 ± 1.4	69.5 ± 4.5	74.2 ± 4.6
		S	21.4 ± 1.1	15.5 ± 2.3	15.4 ± 3.2
		G2 / M	12.9 ± 1.3	15.0 ± 3.7	10.4 ± 1.4
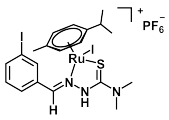	**[29]**	**G1**	67.5 ± 2.1	66.8 ± 0.9	72.0 ± 2.4
		S	19.5 ± 1.1	16.0 ± 2.7	17.5 ± 1.5
		G2 / M	13.0 ± 2.3	17.2 ± 2.2	10.5 ± 1.0

populations in G2/M significantly decreased by almost 50% to 12.9±1.3. These results are similar for cells treated with complex **29**, which showed 67.5±2.1% G1 population and 13.0±2.3% of cells in G2/M phase. Differences in G1 and G2/M populations compared to the control were statistically significant to $p < 0.01$. Changes in S-phase populations were less pronounced, but with 21.4±1.1 and 19.5±1.1% compared to 27.7±1.5 ($p < 0.05$) still significantly different from the control.

After 48 h of exposure, the distribution is similar to that after 24 h, but with differences only significant to a $p < 0.05$ level for most populations. The largest change compared to 24 h occurred in S-phase, where the population of cells decreased further to 15.5% and 16.0% compared to 23.6% in the control.

To better visualise the differences between samples and controls, and to assess whether a change in the populations as a result of an effect by the complexes was positive (i.e. the population in this phase after the treatment is larger compared to the control) or negative (the population has decreased

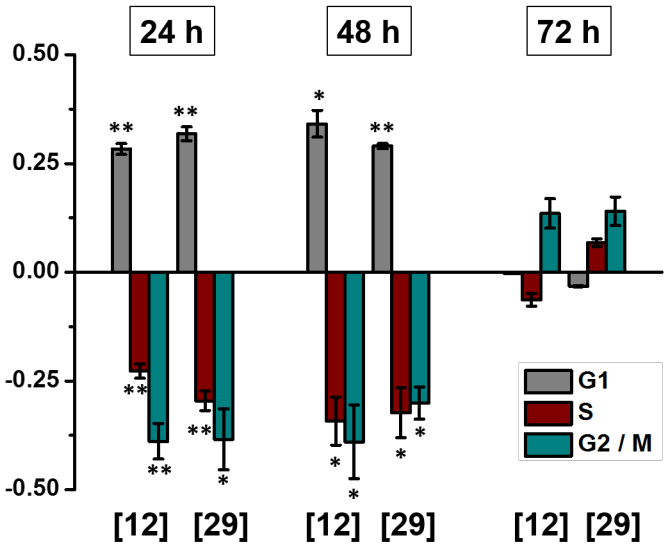

Figure 4.6: Relative population differences of A2780 cells in cell-cycle phases G1, S, and G2/M compared to untreated control cells (** $p < 0.01$, * $p < 0.05$). The time dependent cell-cycle analysis experiment used equipotent and equimolar solutions of complexes **12** and **29** (2 μM) at 24, 48, and 72 h of exposure.

as a result of treatment), data was normalised by the control populations at each time point.

This normalisation was achieved by dividing data for the samples that were treated with complexes **12** and **29** by the respective value for the control, and subtracting 1 from the result.

The graph in Figure 4.6 presents these relative population differences and clearly highlights the significant increase in G1 populations (grey, upward facing bars) after treatment with the complexes ($p < 0.01$) for 24 h and 48 h, respectively. Due to larger errors at the 48 h time point than at 24 h, the significance level here is only $p < 0.05$, but it can still be concluded that both complexes arrest A2780 cells in G1-phase during 24 and 48 h of exposure.

4.3.6 Detection of Apoptotic Cell-Populations

This experiment aims to determine the extent of apoptosis in A2780 cells that is caused by exposure to complexes **12** and **29**. The assay quantifies the loss of both membrane asymmetry and membrane integrity, which occur as a result of programmed cell-death (PCD). Membrane asymmetry is assessed by Annexin-V-FITC fluorescence. Annexin-V binds to phosphatidyl serin (PS) that is located on the inside of the membrane bilayer.[11] Membrane integrity-loss is detected by intercalation of propidium iodide (PI) into double stranded nuclear DNA and RNA. The flow-cytometer measures fluorescence intensity of the two dyes: PI emits red fluorescence, which is measured in channel FL-1, while Annexin-V-FITC emits green fluorescence, read in channel FL-2. With this double-staining technique, four viability levels can be differentiated in a cell sample:

- When the cells are **viable**, the outer cell-membrane is intact. This means that neither PI nor Annexin-V can bind to their respective targets. As a result, the fluorescence reading in both channels (FL-1 and FL-2) of the flow cytometer is low.

- In **early apoptotic** stages, the asymmetry of the cell membrane is spoilt, and the inner side of the lipophilic bilayer turns to the outside. This allows the Annexin-V stain to bind to PS which is now outward facing. This loss of membrane asymmetry, however, does not affect the integrity of the cell wall, and as such, PI still cannot reach its target. Thus, only green fluorescence (FL-2) is high in early apoptotic cells. The earlier in the apoptotic pathway, the lower is the intensity in FL-2.

- At a **late apoptotic** stage, both the outer and the nuclear membrane

are disrupted, which allows the PI stain to enter the nucleus and intercalate into DNA. This leads to both high red and high green fluorescence readings.

- **Non-viable** cells are those which did not follow apoptotic pathways. The membrane integrity of those cells is compromised, so that PI reaches nuclear DNA, but PS receptors are not accessible for the Annexin-V to bind. Therefore, non-viable cells show high red, but no green fluorescence.

Table 4.10: Percentages of apoptotic cells as determined by flow cytometry using Annexin V-FITC / PI staining immediately after A2780 cells were exposed to complexes **12** and **29** for 24, 48, and 72 hours without recovery time.

Time [h]		**% Viable**	**% Early - Apoptotic**	**% Late-Apoptotic**	**% Non-Viable**
	-ve	97.6 ± 0	0.9 ± 0.03	0.5 ± 0.05	0.99 ± 0.04
24	**12**	91.1 ± 0.6	3.24 ± 0.09	4.2 ± 0.4	1.5 ± 0.1
	29	92.4 ± 0.4	3.10 ± 0.06	3.1 ± 0.3	1.5 ± 0.2
	-ve	92.2 ± 0.3	2.22 ± 0.08	3.5 ± 0.1	2.0 ± 0.3
48	**12**	81.5 ± 1.6	7.8 ± 1.0	7.8 ± 0.6	2.9 ± 0.4
	29	86.5 ± 0.4	5.7 ± 0.7	5.8 ± 0.3	2.0 ± 0.3
	-ve	93.0 ± 0.3	1.5 ± 0.2	2.5 ± 0.2	3.1 ± 0.6
72	**12**	91.5 ± 0.5	2.1 ± 0.3	3.1± 0.3	3.4 ± 0.5
	29	93.9 ± 3.8	1.6 ± 1.3	2.1 ± 1.4	2.4 ± 1.2

Data were gathered for A2780 cells after 24, 48, and 72 hours of exposure to complexes **12** and **29** (see Table 4.10). The bar chart in Figure 4.7 compares the cell-counts per viability stage at each of the three time points.

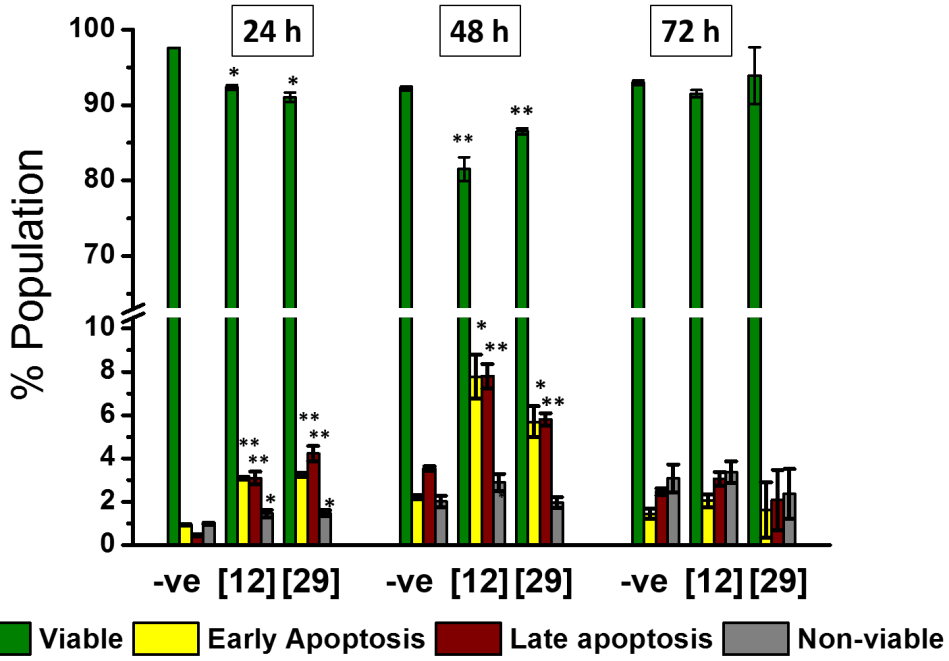

Figure 4.7: Time dependent detection of apoptotic cell-populations using complexes **12** and **29**. Height of the bars represents relative cell populations in four viability stages after exposure to complexes **12** and **29** for 24, 48, and 72 h.

After 24 h, 6 - 7% of apoptotic cells were detected. These populations were significantly higher than in the untreated control (**-ve**, 1.4%). Late-stage apoptotic populations were ten times larger than in the control cells, and early apoptotic populations were three times larger, while the number of viable cells had decreased from 98% to 92%.

An increase in the induction of apoptosis is visible after 48 h of exposure. Even more cells were found in both the early and late apoptotic stages, with sums being twice as high as after 24 h (15.6% for **12** and 11.5% for **29**). Viable cells were diminished compared to the control, while non-viable populations were comparable (2-3%).

The trend of increased number of apoptotic cells after longer exposure times did not continue at 72 h. All results were similar to the untreated control at this time point (Table 4.10, bottom). Variations are as small as

0.1% for early apoptotic cells to 1.0% for viable cell populations. These differences were negligible, with p-values $>> 0.05$.

In summary, cells treated with complexes **12** or **29** show a statistically significant population of early and late-stage apoptotic cells after 24 h and 48 h of exposure.

4.4 Discussion

Six arene ruthenium TSC complexes were studied in this chapter, and four of those were tested in a range of *in vitro* assays to investigate their anticancer properties. All complexes are of the piano-stool geometry. The X-ray crystal structure of **10** and all spectroscopic data for the compounds listed in Table 4.4 was discussed in Chapter 2, and was shown to be consistent with the presented structure. The systematic structural variations within this series of four Ru TSC complexes are presented in Figure 4.8.

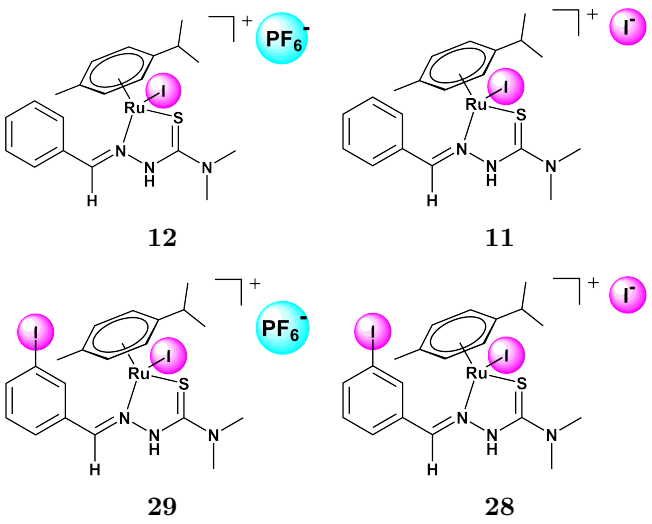

Figure 4.8: p-cymene ruthenium (II) complexes discussed in this chapter.

Complex **12** on the top left in Figure 4.8 compares to **11** (top right) by changing the counter ion from PF_6 to I^-, and the same change relates **29** (bottom left) to **28** (bottom right). The two pairs **12** / **29** (left) and **11** / **28** (right) differ only in their TSC phenyl substituent (H vs I). Their anticancer activity against human ovarian cancer cells (A2780) was determined, followed by studies of cellular ruthenium accumulation and a measurement of the distribution of accumulated ruthenium and iodine in the same cell line.

Table 4.11: Overview of the results obtained for complexes **12** and **29**.

Compound	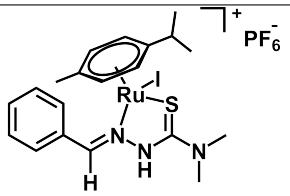 **12**	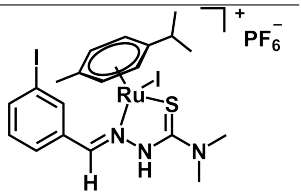 **29**
$\mathbf{t_R}$**(C18)**	12.0 min	17.5 min
	24 h	**24 h**
IC$_{50}$ (μ**M**)	2.6 ± 0.1	2.5 ± 0.1
Cell-uptake (pmol/10^6 cells)		
^{101}Ru	34 ± 4	62 ± 6
^{127}I	<2	22 ± 2
Cell-cycle Arrest	G1	G1
Apoptosis Induction	15%	12%

Furthermore, the mode of action of two complexes was investigated, to directly compare the iodine-labelled complex **29** to **12**. Their effect on the cell-cycle of A2780 cells was measured and related to their capacity to induce apoptosis. Table 4.11 provides a summary of the results that where gathered for the two compounds.

4.4.1 Antiproliferative Activity

The four TSC ruthenium iodido complexes **12**, **11**, **28**, and **29** can be regarded as highly active against the human ovarian carcinoma cell-line A2780, with IC_{50} values in the range of 2 μM for all four compounds. Interestingly, there was no significant difference between the activities determined at three different time points. In contrast to this finding, ruthenium piperonal-TSC chlorido half-sandwich complexes reported by Beckford et al. that exhibit low-to-moderate activities against HCT-116 (colon carcinoma)

and Caco-2 (epithelial colorectal adenocarcinoma) cell-lines,[12] were 1.3 and 2 times more active during 72 h than during 24 h of exposure.

However, this difference is of lesser impact, when the activities are compared directly by the reported IC_{50} values. For the compound [(η^6-*p*-cymene)Ru(Et-pTSC)Cl]Cl (with Et-pTSC = piperonal-4-ethyl-thiosemicarbazone), IC_{50} values in the HTC-116 cell-line are between 77 μM after 24 h, and 50 μM after 72 h, which is one order of magnitude higher than the iodinated TSC complexes **28**, and **29** of this thesis in A2780 cells. While it is not strictly possible to compare IC_{50} values between different cell lines, the comparison to Cisplatin as a reference is accepted practice. Compared to the above mentioned piperonal-TSC complex, CDDP was slightly more active in the same cell-line (41 μM after 72 h in HTC-116). Therefore, the complexes reported by Beckford are of similar potency to CDDP, which is consistent with the conclusion for the iodo-TSC compounds presented in this Chapter. Overall, the literature comparison highlights that arene-ruthenium TSC complexes show consistent cytotoxicity against cancerous cell-lines which is sufficient to warrant further research of their use as anti-cancer agents.

4.4.2 Accumulation and Distribution of Ruthenium and Iodine in Cancer Cells

The high antiproliferative activity of Ru TSC complexes is congruent with their cellular accumulation. Statistically significant ruthenium quantities were found in A2780 cells after 24 h of exposure to the four iodido complexes **12** - **29**, showing that during this time their uptake rates are higher than their efflux rates. As a result, it is reasonable to assume that the cytotoxicity

of the complexes is related to their action inside the cancer cells, and further studies are required to elucidate the mode(s) of action for this particular class of compounds.

The molecular structure of the four coordination compounds seems to change either before or during internalisation into the cell. The accumulation of iodine from the complexes was almost two thirds lower than of ruthenium, which is a first indicator that not all ligands remain bound to the metal centre during the experiment time. Interestingly, no iodine was accumulated in cells exposed to **12** and **11**, although both complexes have either one (**12**) or two (**11**) iodide ions in their structure (Figure 4.8).

A similar result was recently obtained with osmium arene azopyridine complexes. MCF7 (breast cancer) cells exposed to those complexes did not accumulate iodine from radio-labelled iodido monodentate ligands.[13] Both of these independent findings suggest that the monodentate ligand X is lost from the structure.

The fact that the detected quantity of iodine in cells treated with **29** and **28** was the same for both compounds, while the latter has one additional iodide per molecule further supports the hypothesis. Thus, all iodine which accumulates in A2780 cells from complexes **29** and **28** originates from the chelating thiosemicarbazone ligand ITSCNMe_2 (**3c**), i.e. its iodide substituent R = I.

Sub-cellular Distribution of Ruthenium and Iodine

Having confirmed in the previous experiment that it is possible to detect both elements simultaneously in the digested cell-samples by ICP-MS, the next questions follow naturally from this result:

1. In which sub-cellular compartments of human ovarian cancer cells

(A2780) do the metal and the halogen accumulate?

2. Do the two elements ruthenium and iodine accumulate in the same compartments and in the same quantities?

The results of the cell fractoning experiment (described in Section 4.3.3) can answer those question to a good approximation.

The disadvantage of this method is that the cell-fractioning procedure only differentiates between four different sub-groups: In the membrane fraction, the plasma membrane is contained together with organelle membranes, including the nuclear membrane. The proteins of the nuclear membrane, however, and all other soluble nuclear proteins, are contained in the nuclear fraction. Genomic DNA is found together with all insoluble proteins in the cytoskeletal fraction. This must be taken into account when the quantities in the four fractions are compared.

Interestingly, iodine accumulation was distributed differently compared to the metal. Most of the ruthenium from complex **29** was found in the membrane fraction (63%), which showed a high Ru:I ratio of 4:1, while this ratio was closer to 1 in the cytosole. This suggests that the species in the cytosole is a $[(p\text{-cymene})\text{Ru}(\text{ITSC}NMe_2)]^{n+}$ complex in which the TSC ligand is still chelating the metal, and n is either 1 or 2, depending on the protonation state of the TSC.

The reason for higher quantities of metal than iodine in the membrane fractions of compartmentalised A2780 cells can be interpreted as an interaction between the complex and membrane proteins. Most likely, the deactivation already occurs on the outside of the cell-wall, so that the ligand does not enter the cell.

Ruthenium iodido complexes of similar general structure have shown to mainly accumulate in the membrane,[14] with 88-91% being even higher than the 63% found for complex **29** here. The same report highlights that the corresponding chlorido complexes distribute differently inside A2780 cells, with only 73-84% metal accumulation in cellular membranes and membrane proteins.[14] Interestingly, more of the complexes presented in this chapter is entering the nuclear fraction than is reported for Ru-impy complexes, suggesting that thiosemicarbazone complexes, especially those of higher lipophilicity, have a higher probability of reaching nuclear DNA as a target site. Osmium anticancer complexes were found to exhibit greater extend of DNA binding depending on their lipophilicity.[15]

ICP-MS dual detection of Ruthenium and Iodine

The cellular accumulation studies in this chapter relied on the accurate determination of trace amounts of both ruthenium and iodine in cell samples. A reliable technique to quantify both elements is by their mass, using the high sensitivity of modern mass spectrometers, for example in inductively coupled plasma mass spectrometry.[16] While metal distribution in cancer cells can also be assessed with fluorescence[17] or X-ray imaging techniques,[18] the advantage of ICP-MS is that it allows the element(s) of interest to be quantified accurately. One aim of the work presented in this chapter was the simultaneous detection of iodine and ruthenium by ICP-MS.

A method which can be applied to cell or tissue samples to detect both elements at the same time and ideally in the same solution/cell-digest is particularly useful for the quantitative study of metallodrugs in biological tissues such as cell-culture samples.

However, simultaneous detection of iodine and metal ions by ICP-MS

appears to not be straight forward, the reason for which is the sample environment. Because of the high sensitivity of the equipment towards particles, all biological material such as cell samples must be completely dissolved in concentrated nitric acid prior to sample introduction. Therefore, the standard sample environment for metal quantification by ICP-MS is in acidic solutions.

Problems related to the quantification of iodine in acidic sample environments include the following. Iodine can be oxidised to volatile iodine, which might cause errors to the measurement in two different ways. On the one hand due to loss of evaporating iodine from acidic sample solutions, and on the other hand due to gaseous iodine that can persist in the spray chamber of the instrument and cause memory effects that lead to elevated readings. Those two factors need to be considered as possible sources of systematic errors to the iodine measurement by ICP-MS of acidic solutions.

While iodine quantification by ICP-MS normally uses alkaline solutions,[16] research shows that acidic detection of iodine is possible,[19] and that acidic digestion might be preferable over alkaline variations.[20, 21] Couto et al. state that iodide ions are not readily oxidised by nitrate ions in nitric acid solutions.[22]

In the cellular accumulation experiments, 60 pmol ruthenium and 20 pmol iodine per one million cells were detected from both complexes **29** and **28**, which represents a ratio of Ru : I of 3 : 1 total accumulation. In the fractioning experiment with complex **29**, the total amount of ruthenium that was accumulated by the cells was 52 pmol/10^6 cells, while total iodine was 21 pmol/10^6 cells. The ratio of Ru : I is 2.6 : 1, which is comparable to the first experiment. These results suggest that the simultaneous determination of ruthenium and iodide by ICP-MS after nitric acid cell di-

gestion is a reliable technique to quantify cellular accumulation of iodinated metal complexes. This opens up perspectives for the study of speciation of other ruthenium arenes, such as the iminopyridine complexes mentioned previously.[14]

4.4.3 HPLC of Iodido and Chlorido Complexes

One reason why no iodine was accumulated in cells from either the monodentate ligand or the counter ion might be that both are lost from the complex before it enters the cell. However, no conversion of iodido to chlorido complexes could be shown by HPLC methods.

The retention time on the RP-HPLC column did not vary between the chlorido and the iodido complex in each of the two pairs. Moreover, it remained the same even between water and saline solutions, and no significant additional signals appeared. These findings suggest both identity and stability of the complexes during 24 h in solution.

Two scenarios can be ruled out to explain this result: Firstly, the detected species is not formed by loss of the chelating TSC ligand, because if this was the case, the four chromatograms should show a peak at the retention time of the remaining species, identical between all four complexes. No peak with this property is detected in this study.

Secondly, the species formed from Cl/I pairs cannot be the chlorido complex, because the retention times of Cl and I complexes is identical even for solutions in which no chloride is present: The iodido complexes were dissolved in dmso and diluted into doubly deionised water, which has a chloride concentration lower than 1 μM.[23]

However, a number of explanations are reasonable for the observation of identical retention times. In case the X ligand exchanges for water, both

complexes in a pair become identical, which is also the case when a different substitution reaction takes place in X position. Figure 4.9 suggests a third mechanism by which the Cl/I pairs can form an identical species, which is deprotonation of the TSC ligand, followed by loss of the monodentate ligand X. Deprotonation of the ligand at the NH results in a negative charge which, after electron rearrangement, is localised at the sulfur atom. The complex then bears an overall charge of +1 and is consequently a mono-cationic complex [(*p*-cymene)Ru(L-H)]$^+$.

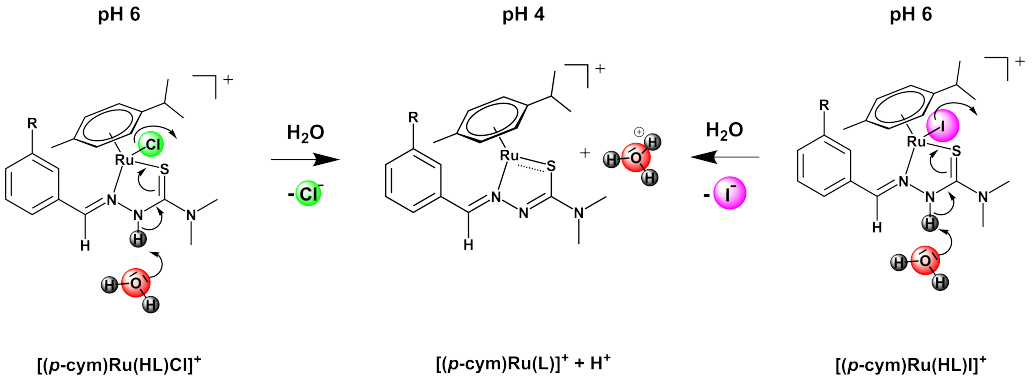

Figure 4.9: Deprotonation of the chelating TSC ligand, which can explain the pH decrease in aqueous solution from pH 6 to pH 4. Subsequent electron rearrangement towards the Ru^{2+} facilitates the loss of the monodentate ligand X, by which both the chlorido complex **[(*p*-cymene)Ru(HL)Cl]**$^+$(left) and the iodido complex **[(*p*-cymene)Ru(HL)I]**$^+$ (right) react to the same complex **[(*p*-cymene)Ru(L)]**$^+$ (middle).

The low pH after 24 h supports this mechanism, as the deprotonation of the TSC ligands leads to acidification of the solution. Furthermore, mass-spectrometric results were discussed in Section 2.4.2 (page 101), also strongly support this hypothesis. ESI-MS spectra show the same species that is formed by loss of the monodentate ligand in conjunction with deprotonation. It is therefore concluded that this mono-cationic complex is the most stable species in aqueous solution, even in the presence of high concentrations of chloride.

4.4.4 Structure-Activity Relations

Previous examples from the Sadler group have shown that a change of the metal (Ru vs Os),[24] a change of Cl for I[25] can affect the antiproliferative activity of a piano-stool complex, while only some SAR have been formulated for changes in chelator-substitution. The donor atom within the chelating ligand itself (N vs C) is another interesting switch.[26]

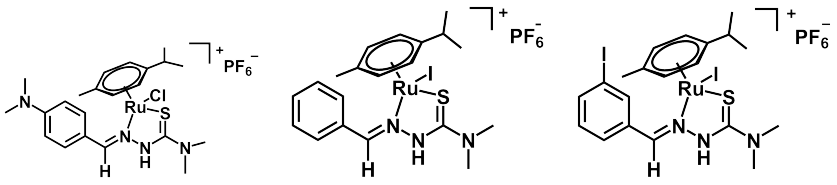

19 **12** **29**

Figure 4.10: Comparison of substituents in the structures of complexes **19** (Chapter 2), **12**, and **29**.

In the studies presented here, the systematic structural variations that were outlined above seem to not not directly affect the antiproliferative activity of the Ru TSC iodido complexes. However, under the same experimental conditions and in the same cell line, assays with complexes **15** and **19** of the two *N*-dimethylated TSCs DTSC (**2a**) and DTSCNMe_2 (**2c**) showed no antiproliferative activity.

The comparison between the three complexes of ligands **1c**, **2c**, and **3c** (Figure 4.10) shows that the dimethylamino substituent in complex **19** leads to loss of activity compared to **12**. Between [(*p*-cymene)Ru(**1c**)Cl]PF_6 (**12**) with an IC_{50} of 2 μM and [(*p*-cymene)Ru(**2c**)I]PF_6 **19** which is inactive at the highest test concentration of 50 μM. Both complexes are accumulated in A2780 at 33 pmol$\cdot$ 10^{-6} cells. Under the assumption that the monodentate ligand is not taken up by the cells, the only difference is the NMe_2 substituent in the TSC ligand in complex **19**.

The electronic effects of the aromatic substituents can play an important role in the activation or deactivation of the metal centre for substitution reactions. Dimethylamino substituents in *para*-position have a strong mesomeric (+M) effect on the π electronic system. In complex **19**, the aromatic π-electrons are in conjugation with the TSC moiety and are easily delocalised towards the ruthenium centre. This conjugation of a *para*-NMe_2 group to the metal had proven to enhance the cytotoxicity of arene Os azopyridine complexes,[27] which was one reason for incorporating the same group in the presented Ru TSC complexes. The difference between the two observations is yet another example for the tune-ability of piano-stool anticancer complexes.

In contrast to the *para*-NMe_2, the iodine substituent in ligand **3c** does not deactivate the Ru TSC complex. Compared to complex **12** with an un-substituted phenyl-TSC moiety (**1c**), iodinated complex **29** of *meta*-iodo-TSC **3c** shows the same anticancer activity. This is consistent with the hypothesis that delocalised electrons might deactivate the metal centre. Iodine in *meta*-position has only a weak inductive effect on the π-electrons of the aromatic ring, which is also pulling those electrons rather than pushing them towards the metal. In other words, electron density is delocalised away from the ring and from the metal. This basic scheme can explain why there is no difference between the anticancer activity of complexes **12** and **29**, while complex **19** is inactive at a similar level of cellular accumulation.

When the total ruthenium uptake is compared between the four TSC complexes, it is notable that twice as much metal is accumulated from complexes **29** and **28** as from analogues **12** and **11**. This finding suggests that the iodine substituent of ITSCNMe_2 (**3c**) in complexes **29** and **28** appears to facilitate the uptake. A literature report supports this hypothesis,

as Antony et al. found that iodinated indazole ligands remain attached to ruthenium(III) in analogues of the metallo-drug KP1019,[28] and suggest that iodination of the organic ligand increases the lipophilicity of the complex, which could facilitate cellular uptake by passive diffusion pathways.

Lipophilicity of a molecule can be related to its retention time on a chromatography column.[29] The stronger the interactions with the hydrophobic stationary phase are, the longer the molecule is retained on the column.

The HPLC experiments described above (Section 4.3.4) have shown that the retention time of complexes **28** and **27** on the reversed-phase column is approximately 15% longer (17.5 min) than for the non-labelled complexes **12** and **10**. This finding supports the hypothesis that an iodine substituent within the TSC ligand enhances the lipophilicity of the metal complex, and that consequently the higher cellular accumulation of the iodinated complexes is correlated to this increase in lipophilicity. Previous research has shown a correlation between the hydrophobicity, cytotoxicity, cellular uptake and distribution of arene Os(II) anticancer complexes.[15]

4.4.5 Cell-Cycle Analysis

Proliferating, healthy cells use the cell-cycle to control tissue homeostasis (maintenance of living cell populations). To avoid uncontrolled growth (over-proliferation), cells initiate apoptosis, a form of programmed cell-death which is characterised by unique features such as membrane blebbing and cell shrinkage.[30, 31] These morphological features are important signals for the clearance of dead cells from the tissue. Cancer cells fail to regulate the balance of dead and living cells, and these faulty processes are what results in over-proliferation and the formation of tumours.[32]

Within the cell cycle, several checkpoints control the healthy progression

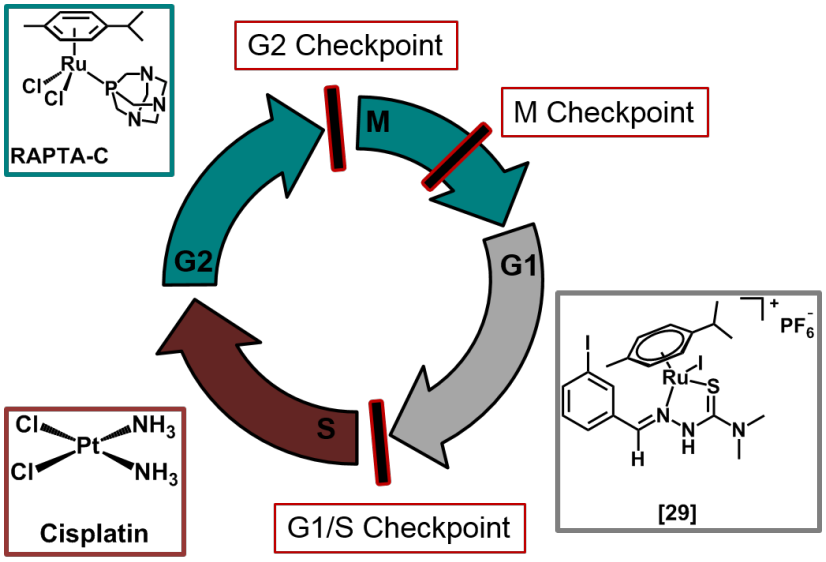

Figure 4.11: Schematic of the Cell Proliferation Cycle with indicated location of checkpoints that control cell-cycle progression. Three stages are detectable by DNA staining of fixed cells with propidium iodide: G1 (grey), S-phase (red), and G2/M (green). Each of the three metal complexes **29**, Cisplatin, and RAPTA-C induce cell-cycle arrest in a different phase.

of cell-division, three of which are depicted schematically in Figure 4.11. These controls are in place to validate external growth conditions as well as detect (possible) DNA damage, which can occur in any of the cell-cycle phases.[10, 32, 33] During G1 phase, the cells grow to twice their size while synthesising mRNA and proteins that are necessary for DNA replication, for which they require a healthy environment and sufficient nutrition. When the G1/S checkpoint indicates DNA damage, the cell-cycle can be arrested at this stage in order to halt DNA replication.

Complexes **12** and **29** both caused significant increase in A2780 cell-populations in G1-phase after 24 h and 48 h of exposure, and one explanation for this effect is interaction of the drug with DNA. Given that high quantities of complex **29** were detected in the nuclear fraction of these cells, it is likely that DNA is one of its target molecules. However, while DNA damage is the cause for most cell-cycle arrests, G1 arrest can also be caused

by other factors that lead to insufficient conditions for the cell to proceed with proliferation.[34, 35] More information is therefore required to confirm that the G1 arrest caused by ruthenium TSC complexes is due to direct DNA interaction.

After the first gap phase, when cells have successfully passed the G1/S checkpoint, DNA is replicated during the next phase of the cell-cycle, S-phase. Here, all steps that are required to reproduce DNA are carried out. When DNA damage is detected during this phase, the reproduction of DNA is slowed down to allow time for its repair. The more DNA molecules are affected, the slower the repair and, consequently, the cell-cycle.[35]

Therefore, S-phase arrest can indicate direct DNA-drug-interactions. In the case of Cisplatin (Figure 4.11), S-phase arrest is caused due to the distortion of DNA double strands by covalent Pt-DNA interactions. Those 'kinks' in the DNA prevent its correct translation.[36–38] Conclusively, S-phase arrest is in accordance with the established mechanism of action of the platinum drug.[39]

The two ruthenium complexes **12** and **29** do not arrest A2780 cells in S-phase, and might therefore not directly target DNA. Although examples of piano-stool Ru TSC complexes reported by Beckford appear to be weak multi-mode DNA binders,[40] their effect on the cell-cycle has not been studied so far. In contrast, G1 arrest caused by **12** and **29** shows that for these complexes the mode of action is different from Cisplatin.

The G2/M checkpoint tests whether DNA has been replicated completely. If this is the case, the G2 checkpoint passes the cell on to the second preparatory growth phase, otherwise, S-phase arrest is detected. If cells sense DNA damage while in G2 phase, before entering mitosis (M-phase), a G2/M cell-cycle arrest will occur.

The ruthenium piano-stool complex RAPTA-C has been found to cause G2/M cell-cycle arrest.[41] Comparing the structures of TSC complex **29**, Cisplatin, and RAPTA-C (Figure 4.11), it is notable that these three molecules arrest the cell-cycle in three different stages. All three structures include labile halido ligands that can potentially be replaced by water and, subsequently, by DNA bases. However, only in the case of Cisplatin has this mechanism been confirmed.[42] For the purpose of this research project and in the context of the aim to find metal complexes that exhibit anticancer activity with novel modes of action, i.e that differ in their behaviour from the established platinum drug, the finding that the arene ruthenium TSC complexes arrest the cell-cycle in a different stage compared to Cisplatin is a step in the right direction.

When investigating the effects of a molecule on the cell cycle, it is useful to also screen for apoptosis induction under the same treatment conditions. Because apoptosis is a response to DNA damage,[35] it makes sense to relate the results of the cell-cycle analysis with detection of apoptotic cell populations.

4.4.6 Apoptosis Detection

When the concept of apoptosis was first discussed by Kerr and co-workers,[30] little was known about the pathways involved in those morphological changes in cells they had investigated mostly by light microscopy. However, what already appeared as a strictly controlled mechanism had obvious implications for the study of health and disease. Since these early findings, much therapeutic potential has been seen in the ability to interfere with the regulation of cell-death,[43] and research into the processes involved in apoptosis[31] has moved forward fast. Today, many proteins which are key regulators of

programmed cell-death (PCD) have been identified, while most of their molecular mechanisms of action still remains to be elucidated.[31]

In apoptotic cells, the stages of PCD can be characterised by the state of the plasma membrane and the nuclear membrane. Annexin-V staining[11] was used to obtain the results presented in Section 4.3.6. It relies on relocation of Annexin-V receptors to the outside of the membrane during apoptosis.

The asymmetrical, but non-random distribution of lipids in eucariotic cell-membranes is a consequence of multiple factors,[44, 45] such as spontaneous "flipping" of polar head-groups through the hydrophobic membrane. Disruption of phospholipid asymmetry during apoptosis is caused by lipid scrambling enzymes, so-called "scramblases".[46] PLSCR3, for example, is a mammalian, Ca^{2+}-dependent phospholipid scramblase.[47] An important functional consequence of this scrambling is the controlled externalization of phosphatidyl serine (PS), the receptor for Annexin-V binding. It is because of this affinity that the relocation of PS allows characterisation of apoptotic cells.[11]

Compared to un-treated control cells, complexes **12** and **29** induce statistically significant populations of both early and late-stage apoptosis. The two complexes did not exhibit statistically significant differences in their respective capacity to induce apoptosis, but the incidence of both early and late stage apoptosis doubled between 24 h and 48 h of exposure. Arene ruthenium iminopyridine complexes, which have been studied in this research group previously,[14] also cause high incidences of apoptosis in 24 h of exposure. This suggests that the two classes of ruthenium half-sandwich complexes might share some mechanisms of anticancer activity.

There are two main ways of apoptosis induction: via death receptors on the cell surface (extrinsic) on the one hand, and a mitochondria mediated

(intrinsic) pathway. Tumour cells often have faulty apoptotic pathways, which can result not only in over-proliferation and increased tumour mass, but also in resistance to therapy.[48]

The intrinsic, mitochondrial pathway, characterised by loss of mitochondrial membrane potential (MMP), activation of caspase-9, and the release of cytochrome c,[10, 31] is the main apoptosis mechanism described for ruthenium complexes such as RAPTA-C,[41] ruthenium(II) carboranes,[49] and ruthenium(II) polypyridyl complexes.[50–52] These reports encourage the thought that complexes **12** and **29** also follow the intrinsic apoptotic pathway, but more work is required to support this conclusion.

Ruthenium(II) polypyridyl complexes can induce apoptosis through ROS-mediated mitochondrial pathways,[51, 52] which is a mechanism proposed for iridium half-sandwich complexes.[53] The relation of mitochondrial ROS production to DNA damage and effects on the cell-cycle could explain the early cell-cycle arrest (G1) by ruthenium TSC complexes **12** and **29**. If ROS are produced, which cause DNA damage, these are sensed by the cell earlier than the faulty DNA itself, thus leading to G1 arrest rather than S-phase arrest.[54–56]

After 72 h of exposure to complexes **12** or **29**, no effect of the drugs on the cells could be detected compared to untreated controls, neither in the cell-cycle analysis nor for detection of apoptosis. A plausible explanation for this is extrinsic induction of apoptosis *via* death receptors, due to insufficient growth conditions.[31, 48, 57] In the experiment described in Section 4.2.4 (Page 171), the cells were seeded on day one, and drugs were added as solutions in fresh cell-culture medium on day two. In wells containing controls, however, the medium was not replaced. During the following 72 h of continuous incubation, the untreated control cells are assumed to prolif-

erate normally, until the conditions become unfavourable for proliferation, either because no further nutrients and/or space are available, or because the presence of non-viable cells has contaminated the medium. Lacking survival signals in this way, proliferating cells induce apoptosis, after G1 arrest, as a mechanism of self-defence.[58]

4.5 Summary

Four arene ruthenium TSC complexes were tested for their antiproliferative activity in human ovarian cancer cells. The complexes have IC_{50} values in the low micromolar range which makes them promising candidates for further investigations into their mechanism of action.

Through coherent, systematic labelling of four complexes with iodine atoms, and by use of a new method for simultaneous detection of ruthenium and iodine by ICP-MS, it was possible to quantify both the transition metal and the chelating organic ligand of a piano-stool anticancer Ru-TSC complex inside cancer cells.

It was conclusive from cell-accumulation experiments that neither the monodentate ligand X nor the counter ion Y were accumulated in ovarian A2780 cancer cells, but that instead the entire detected iodine stems from the iodinated thiosemicarbazone ligand **3c**. The presence or absence of the lipophilic iodine substituent in the TSC ligand did only affect the total accumulation of the complex but not its anticancer activity.

HPLC studies support the conclusion that the complexes lose their monodentate halido ligand within seconds in dmso/water solutions, where they form a stable mono-cationic species. This new species is taken up by human ovarian cancer cells and, even though most of the metal is retained

in the membrane, approx. 30% of the complex pass this barrier and remains intact in the cytoplasm as well as in the nucleus, with a Ru : I ratio of close to 1 which suggests that the ligand is still bound to the metal centre.

The detailed comparison of two complexes showed that the iodine substituent in the organic TSC ligand 3-iodobenzaldehyde-4-dimethyl-3-thiosemicarbazone (**3c**) does not influence the activity of the ruthenium complex **29** compared to its non-iodinated analogue **12**. Their antiproliferative activities after three different exposure times were identical within error, and both complexes arrest the cell-cycle of ovarian carcinoma cells in G1 phase, coinciding with the induction of apoptotic pathways and increased cell-death. IC_{50} values do not improve significantly with extended drug exposure, and the best result is found after an exposure time of 48 hours.

In conclusion, the findings of this chapter add to the ongoing research of metallo-drug speciation inside cancer cells and can contribute to the elucidation of the mechanism of action of Ru-TSC anticancer complexes.

References

[1] D. F. Shriver, P. W. Atkins, T. L. Overton, J. P. Rourke, M. T. Weller, and F. A. Armstrong, *Inorganic Chemistry*, 4th ed., Oxford University Press, Oxford, UK, 2006.

[2] K. Maramorosch and H. Hirumi (Eds.) *Practical tissue culture applications*, New York Academic Press, 1979.

[3] J. Davis (Ed.) *Basic cell culture : a practical approach*, Oxford University Press, Oxford, 2002.

[4] V. Vichai and K. Kirtikara, *Nat. Protoc.*, 2006, **1**, 1112–1116.

[5] K. T. Papazisis, G. D. Geromichalos, K. Dimitriadis, and H. Kortsaris, *J. Immunol. Methods*, 1997, **208**, 151–158.

[6] P. Skehan, R. Storeng, D. Scudiero, A. Monks, J. McMahon, D. Vistica, J. Warren, H. Bokesch, S. Kenney, and M. R. Boyd, *J. Nat. Cancer Inst.*, 1990, **82**, 1107–1112.

[7] J. Miller, *Statistics and Chemometrics for Analytical Chemistry*, Harlow : Prentice Hall, 2010.

[8] T. J. Cleophas, A. H. Zwinderman, T. F. Cleophas, and E. P. Cleophas, *Statistics Applied to Clinical Trials*, Springer, 2008.

[9] H. Coolican, *Research Maethods and Statistics in Psychology*, 5 ed., Routlege - Taylor & Francis Group, London, New York, 2013.

[10] R. C. Bast, D. W. Kufe, R. E. Pollock, R. R. Weichselbaum, J. F. Holland, E. F. III, and T. S. Gansler (Eds.), *Cell Proliferation, Differentiation, and Apoptosis*, chap. 2, 5 ed., BC Decker Inc., Ontario, 2000.

[11] I. Vermes, C. Haanen, H. Steffens-Nakken, and C. Reutelingsperger, *J. Immunol. Methods*, 1995, **184**(1), 39–51.

[12] F. Beckford, D. Dourth, M. S. Jr., J. Didion, J. Thessing, J. Woods, V. Crowell, N. Gerasimchuk, A. Gonzalez-Sarras, and N. P. Seeram, *J. Inorg. Biochem.*, 2011, **105**(8), 1019–1029.

[13] R. Needham, in preparation, 2014.

[14] I. Romero-Canelón, L. Salassa, and P. J. Sadler, *J. Med. Chem.*, 2013, **56**(3), 1291–1300.

[15] S. H. van Rijt, A. Mukherjee, A. M. Pizarro, and P. J. Sadler, *J. Med. Chem.*, 2010, **53**(2), 840–849.

[16] A. A. Oliveira, L. T. Trevizan, and J. A. Nóbrega, *Appl. Spectrosc. Rev.*, 2010, **45**, 447–473.

[17] A. R. Cowley, J. Davis, J. R. Dilworth, P. S. Donnelly, R. Dobson, A. Nightingale, J. M. Peach, B. Shore, D. Kerr, and L. Seymour, *Chem. Commun.*, 2005, (7), 845–847.

[18] R. Ortega, G. Devès, and A. Carmona, *J. R. Soc. Interface*, 2009, **6**(5), S649–S658.

[19] A. V. Izmer, S. F. Boulyga, and J. S. Becker, *J. Anal. At. Spectrom.*, 2003, **18**(11), 1339–1345.

[20] G. Raedlinger and K. G. Heumann, *Anal. Chem.*, 1998, **70**, 2221–2224.

[21] A. L. H. Muller, P. A. Mello, M. F. Mesko, F. A. Duarte, V. L. Dressler, E. I. Muller, and E. M. M. Flores, *J. Anal. At. Spectrom.*, 2012, **27**, 1889–1894.

[22] A. B. Couto, D. C. de Souza, E. R. Sartori, P. Jacob, D. Klockow, and E. A. N. (in memoriam), *Analytical Letters*, 2006, **39**(15), 2763–2774.

[23] T. S. Light, S. Licht, A. C. Bevilacqua, and K. R. Morash, *Electrochem. Solid-State Lett.*, 2005, **8**(1), E16–E19.

[24] A. Bergamo, A. Masi, A. F. Peacock, A. Habtemariam, P. J. Sadler, and G. Sava, *J. Inorg. Biochem.*, 2010, **104**, 79–86.

[25] I. Romero-Canelón, A. Pizarro, A. Habtemariam, and P. Sadler, *Metallomics*, 2012, **4**, 1271–1279.

[26] Z. Liu, A. Habtemariam, A. M. Pizarro, S. A. Fletcher, A. Kisova, O. Vrana, L. Salassa, P. C. Bruijnincx, G. J. Clarkson, V. Brabec, and P. J. Sadler, *J. Med. Chem.*, 2011, **54**, 30113026.

[27] Y. Fu, M. J. Romero, A. Habtemariam, M. E. Snowden, L. Song, G. J. Clarkson, B. Qamar, A. M. Pizarro, P. R. Unwin, and P. J. Sadler, *Chem. Sci.*, 2012, **3**, 2485–2494.

[28] S. Antony, J. B. Aitken, S. Vogt, B. Lai, T. Brown, L. Spiccia, and H. H. Harris, *J. Biol. Inorg. Chem.*, 2013, **18**, 845–853.

[29] A. M. Pizarro, R. J. McQuitty, F. S. Mackay, Y. Zhao, J. A. Woods, and P. J. Sadler, *ChemMedChem*, 2014, **9**(6), 1169–1175.

[30] J. Kerr, A. Wyllie, and A. Currie, *Br. J. Cancer*, 1972, **26**(4), 239–257.

[31] S. Elmore, *Toxicol. Pathol.*, 2007, **35**(4), 495–516.

[32] Z. H. Siddik (Ed.) *Checkpoint Controls and Targets in Cancer Therapy*, Cancer Drug Discovery and Development Series, Humana Press, Springer, Dordrecht Heidelberg London New York, 2010.

[33] B. Rollins, T. Golub, K. Polyak, and et a, *Molecular Biology*, 5 ed., BC Decker Inc., Ontario, 2000.

[34] K. K. Dijkstra, C. Blanchetot, and J. Boonstra, in *Checkpoint Controls and Targets in Cancer Therapy*, Humana Press, Springer, Dordrecht Heidelberg London New York, 2010, 3–26.

[35] J. O. Funk, T. Samuel, and H. O. Weber, *DNA Damage, Cell Cycle Control and Cancer*, Eurekah.com, 2001, 65–78.

[36] W. D.E., C. Ng, and G. Raaphorst, *Cancer Chemother. Pharmacol.*, 1997, **40**(2), 159–66.

[37] H. Zheng, W. Hu, D. Yu, D.-Y. Shen, S. Fu, J. J. Kavanagh, I.-C. Wei, and D. J. Yang, *Pharm. Res.*, 2008, **25**(10), 2272–2282.

[38] I. Romero-Canelón, *Design and mechanism of action of organometallic anticancer complexes*, The University of Warwick, 2012.

[39] J. Reedijk, *Eur. J. Inorg. Chem.*, 2009, (10), 1303–1312.

[40] F. Beckford, J. Thessing, J. Woods, J. Didion, N. Gerasimchuk, A. Gonzalez-Sarrias, and N. P. Seeram, *Metallomics*, 2011, **3**, 491–502.

[41] S. Chatterjee, S. Kundu, A. Bhattacharyya, C. G. Hartinger, and P. J. Dyson, *J. Biol. Inorg. Chem.*, 2008, **13**(7), 1149–1155.

[42] S. Sherman, D. Gibson, A. Wang, and S. Lippard, *Science*, 1985, **230**(4724), 412–417.

[43] U. Fischer and K. Schulze-Osthoff, *Cell Death Differ.*, 2005, **12**(S1), 942–961.

[44] G. van Meer, D. R. Voelker, and G. W. Feigenson, *Nat. Rev. Mol. Cell Biol.*, 2008, **9**, 112–124.

[45] B. Fadeel and D. Xue, *Crit. Rev. Biochem. Mol. Biol.*, 2009, **44**(5), 264–277.

[46] P. Williamson, A. Christie, T. Kohlin, R. A. Schlegel, P. Comfurius, M. Harmsma, R. F. A. Zwaal, and E. M. Bevers, *Biochemistry*, 2001, **40**(27), 8065–8072.

[47] T. Wiedmer, Q. Zhou, D. Y. Kwoh, and P. J. Sims, *BBA-Biomembranes*, 2000, **1467**(1), 244–253.

[48] F. H. Igney and P. H. Krammer, *Nat. Rev. Cancer*, 2002, **2**(4), 277–288.

[49] G. Zhang, C. Wu, H. Ye, H. Yan, and X. Wang, *J. Nanobiotechnology*, 2011, **9**(1), 1–8.

[50] Y. Chen, M.-Y. Qin, L. Wang, H. Chao, L.-N. Ji, and A.-L. Xu, *Biochimie*, 2013, **95**(11), 2050–2059.

[51] C. Qian, J.-Q. Wang, C.-L. Song, L.-L. Wang, L.-N. Ji, and H. Chao, *Metallomics*, 2013, **5**, 844–854.

[52] G. B. Jiang, J. H. Yao, J. Wang, W. Li, B. J. Han, Y. Y. Xie, G. J. Lin, H. L. Huang, and Y. J. Liu, *New J. Chem.*, 2014, *accepted manuscript.*

[53] J. M. Hearn, I. Romero-Canelón, B. Qamar, Z. Liu, I. Hands-Portman, and P. J. Sadler, *ACS Chem. Biol.*, 2013, **8**(6), 1335–1343.

[54] X. Deng, F. Gao, and J. W. Stratford May, *Blood*, 2003, **102**(9), 3179–3185.

[55] J. An, K. Shi, W. Wei, F. Hua, Y. Ci, Q. Jiang, F. Li, P. Wu, K. Hui, Y. Yang, and C. Xu, *Cell Death Dis.*, 2013, **4**, e973.

[56] A. Banafa, S. Roshan, Y.-y. Liu, H.-j. Chen, M.-j. Chen, G.-x. Yang, and G.-y. He, *J. Huazhong University of Science and Technology*, 2013, **33**(5), 717–724.

[57] J. C. Rathmell, M. G. Heiden, M. H. Harris, K. A. Frauwirth, and C. B. Thompson, *Mol. Cell*, 2000, **6**(3), 683–692.

[58] M. C. Raff, *Nature*, 1992, **356**, 397–400.

Chapter 5

Conclusions and Future Work

Ruthenium complexes have been investigated as alternatives to cisplatin and its analogues, and with the Ru(III) compounds NAMI-A and NKP1339 two promising candidates are currently undergoing clinical trials. The former is an antimetastatic agent, and the latter is cytotoxic against solid cancers.

Arene ruthenium and osmium complexes show an interesting profile of anticancer activity that ranges from antimetastatic activity to cytotoxicity. The challenge in the research for metal-based drugs, therefore, is to find a combination of ligands for a metal ion that will provide the required reactivity, i.e. bind strongly enough to provide stability of the complex, but retain reactivity towards target site(s) inside the cancer cell or -tissue. The fact that the two compounds NAMI-A and KP1019 (see Chapter 2, Figure 1.4, p. 7) show different activity profiles even though their molecular structures are highly related to one another, highlights the importance to confirm the mode(s) of drug-action (MOA) for new therapeutic metal complexes.

In this research project, novel thiosemicarbazones have been designed and incorporated into ruthenium arene complexes. Their design was guided, one the one hand, by previous research that had shown NMe_2 substituents

to enhance anticancer activity in ruthenium and osmium arene azopyridine complexes,[1] and on the other hand with the objective to trace the chelating ligand alongside the metal in cancer-cell accumulation studies.

Iodine was chosen for this purpose because it is detectable by ICP-MS, which is a common technique for the quantification of trace metal ions, not exclusively in cell samples. Furthermore, with the right properties, a stable and soluble iodinated compound might have the potential to be developed into a radioactive iodine tracer, which use the synthetic isotope ^{131}I.

Thiosemicarbazones have widely been studied as imaging agents,[2–4] and have also been used for radio-labelling experiments, although only in their capacity as ligands for radioactive gallium (^{67}Ga)[4] or copper (^{64}Cu),[3] and not for iodine. One TSC with a 3-iodophenyl substituent has been reported in the literature, but the study does not highlight any impact of the iodine substituent on the activity of the TSC.[5, 6]

5.1 Structure and Spectroscopy of Arene Ruthenium TSC Complexes

Chapter 2 presented the design, preparation and characterisation of twelve TSC ligands and the confirmation of their structure by X-ray crystallography and NMR spectroscopic methods, followed by the reaction to the corresponding ruthenium arene complexes.

The synthesis resulted in Ru complexes with a neutral TSC, coordinated through the imino N1 and a thione sulfur. The crystal structure of the chlorido complex [**10**] shows that the coordination mode and the bond distances around the metal centre are consistent with data for other TSC-Ru complexes that have been reported in the literature.

The chapter also introduces natural-abundance ^{15}N NMR spectroscopy (^{1}H^{15}N-HMBC) as a characterisation technique and presents the results in form of a chemical-shift database with detailed description of the assignment procedure. TSCs in complexes were characterised by their nitrogen chemical shift, which has not been used before to characterise TSC complexes, or Ru piano-stool complexes in general. The ^{15}N NMR chemical shifts of the TSC nitrogen atoms showed an up-field coordination shift for the imino nitrogen atom N^2 in ther corresponding ruthenium complexes. A dramatic downfield shift of the signal for N^2 of -122 ppm suggests deprotonation of the TSC at the hydrazinic nitrogen, which is consistent with the crystal structure of the dinuclear complex **30** and ESI-MS results that show the signal for a deprotonated monocationic complex.

XAS experiments were presented in Chapter 3 which achieved solid and solution state characterisation of the first co-ordiantion sphere of several Ru TSC complexes. Ru K-edge XAS data was collected in a 24 h experiment at the EXAFS beamline B18 at the Diamond Light Source Synchrotron Facility in Didcot, UK. The XANES confirmed the oxidation state of the TSC complexes to be the expected Ru(II) state. The edge energies E_0 compare well between the Ru precursor complexes and the TSC complexes, and are shifted by 5-6 eV to higher energies compared to Ru(0)-foil.

It was the aim of Chapter 3 to collect and analyse EXAFS data for ruthenium TSC complexes that did not crystallise. With a total of 24 complexes but only two X-ray crystal structures, which showed two entirely different compounds, the use of EXAFS for the solid-state characterisation was reasonable. EXAFS fitting of the data collected for eight different complexes was achieved by comparison to the crystallographic data, and the fit results showed high levels of consistency with the single crystal structure

of the mononuclear complex **10**.

Moreover, EXAFS was used successfully for the reaction monitoring of the dimerisation of complex **21** to the dinuclear complex **30**. Solution-state X-ray absorption spectroscopy was carried out to detect and analyse changes in the XANES region, using linear combination fitting. Time-dependent EXAFS studies of freeze-quenched reaction mixtures represent the ability to follow the reaction *in situ* and to confirm with a second technique that the dimerisation takes place on a timescale of minutes. Remarkably, the reaction time of only 15 min was sufficient to obtain a curve that showed the increasing content of the dimer in solution.

5.2 Anticancer Activity and Mode of Action of Arene Ruthenium TSC complexes

Complex **12** and complex **29** were compared in a number of cell-culture assays using the A2780 cell-line to investigate their anticancer activity. Both complexes have good antiproliferative activities, with stable IC_{50} values of 2-4 μM that do not significantly change with extended drug exposure. However, 48 hours gave the best results for antiproliferative activities, high populations of cell in G1 cell-cycle arrest and the largest population of early and late stage apoptotic cells.

From the presented results, the following points can be inferred as SAR for arene ruthenium TSC complexes:

- Terminal dimethylation in TSC ligands of series **1c-3c** is important for the stability of the corresponding complex, but does not influence antiproliferative activity.

- Iodination of the TSC ligand does not alter anticancer activity.
- A lipophilic iodine substituent increases cellular accumulation of the Ru TSC complex.

The results of Chapter 4 suggested that complexes **12** and **29** follow an intrinsic apoptotic pathway. However, more work is required to support this hypothesis. Mitochondrial involvement in PCD can be tested, for example by measuring the effect of the complexes on the mitochondrial membrane potential. Disruption of the mitochondrial membrane potential is a sign for redox processes and ROS. This is important, as DNA damage which was discussed in correlation to the detected G1 cell-cycle arrest, can be secondary, i.e. caused by ROS rather than by the complex directly. More information is needed to confirm the cause of G1 arrest induced by ruthenium TSC complexes in ovarian cancer cells A2780, and confirm or dismiss a relation to direct DNA interaction of the complexes.

5.2.1 Iodine Labelling

Chapter 4 also presented the systematic labelling of four complexes with iodine atoms, which was used in conjunction with a dual detection method for ruthenium and iodide by ICP-MS. Those studies allowed to detect and quantify both the transition metal and its chelating, organic component of a piano-stool anticancer complex inside cells, which was a main aim of this research project. However, this method is only one step in the process towards understanding of metallo-drug speciation inside cancer cells, and improvements to the detection of metal and ligand in cells are necessary.

For example, another method for ruthenium and iodine detection is X-ray fluorescence spectroscopy. To elucidate the cellular fate of arene

ruthenium and osmium anticancer drugs, X-ray fluorescence mapping can be used. This is particularly interesting for biological samples because it is a non-invasive technique.

The advantage of XAS or XRF based imaging techniques is that they can directly observe the compound of interest, without changing its structure or adding dyes to the sample which might obstruct information.

Examples in the literature already report the use of synchrotron X-ray methods for the study of metal-based drugs inside cancer cells. For example, platinum complexes have been studied by XAS on cells, and it was shown that the intracellular reduction of platinum(IV) pro-drugs to active platinum(II) species could be determined from XANES measurements as a ratio of the two oxidation states.[7, 8]

XRF imaging of gallium and ruthenium complexes has been successfully performed by Hummer and others.[9–11] Results from Diamond Light Source's microXRF beamline I18[9, 12] and the investigation of tissue samples from *in vivo* studies with the drug candidates NAMI-A and KP1019 by Aitken et al. (Australian Light Source)[11] highlight the advantages of XRF for the research of metal-based anticancer drugs.

The aim to detect the metal and the chelating ligand of a piano-stool anticancer complex in cells by means of XRF mapping is a logical next step from the presented results, and the examples by other researchers in the field who report similar approaches support this suggestion.

References

[1] Y. Fu, M. J. Romero, A. Habtemariam, M. E. Snowden, L. Song, G. J. Clarkson, B. Qamar, A. M. Pizarro, P. R. Unwin, and P. J. Sadler, *Chem. Sci.*, 2012, **3**, 2485–2494.

[2] J. R. Dilworth and R. Hueting, *Inorg. Chim. Acta*, 2012, **389**, 3–15.

[3] J. L. Hickey, S. Lim, D. J. Hayne, B. M. Paterson, J. M. White, V. L. Villemagne, P. Roselt, D. Binns, C. Cullinane, C. M. Jeffery, R. I. Price, K. J. Barnham, and P. S. Donnelly, *J. Am. Chem. Soc.*, 2013, **135**(43), 16120–16132.

[4] T. Ismail, D. D. Rossouw, P. Beukes, J. P. Slabbert, and G. S. Smith, *Inorg. Chem. Commun.*, 2013, **33**, 154157.

[5] H. Pervez, M. Yaqub, M. Ramzan, and M. N. Tahir, *Acta Cryst. Sect. E*, 2010, **66**, o1629.

[6] H. Pervez, M. Iqbal, M. Tahir, F. Nasim, M. Choudhary, and K. Khan, *J. Enzyme Inhib. Med. Chem.*, 2008, **23**(6), 848–854.

[7] M. Hall, C. Dillon, M. Zhang, P. Beale, Z. Cai, B. Lai, A. Stampfl, and T. Hambley, *J. Biol. Inorg. Chem.*, 2003, **8**(7), 726–732.

[8] M. D. Hall, G. J. Foran, M. Zhang, P. J. Beale, and T. W. Hambley, *J. Am. Chem. Soc.*, 2003, **125**(25), 7524–7525.

[9] A. A. Hummer, C. Bartel, V. B. Arion, M. A. Jakupec, W. Meyer-Klaucke, T. Geraki, P. D. Quinn, A. Mijovilovich, B. K. Keppler, , and A. Rompel, *J. Med. Chem.*, 2012, **55**, 5601–5613.

[10] A. A. Hummer, P. Heffeter, W. Berger, M. Filipits, D. Batchelor, G. E. Büchel, M. A. Jakupec, B. K. Keppler, and A. Rompel, *J. Med. Chem.*, 2013, **56**(3), 1182–1196.

[11] J. B. Aitken, S. Antony, C. M. Weekley, B. Lai, L. Spiccia, and H. H. Harris, *Metallomics*, 2012, **4**, 1051–1056.

[12] I18, *http://www.diamond.ac.uk/Beamlines/Spectroscopy/I18.html*.

Appendix

X-ray Crystallographic Parameters

Table 5.1: Crystallographic data for the structure of TSC ligand **2b** and ruthenium chlorido complex **[10]Cl**

	DTSC*NMe* **(2b)**	[(*p*-cymene)Ru(PTSCNMe_2)Cl]Cl **[10]Cl**
Empirical formula	$C_{11}H_{16}N_4S$	$C_{21}H_{31}Cl_2N_3ORuS$
Formula Weight	236.34	M = 545.52
Crystal system	Monoclinic	Monoclinic
Space group	P2(1)/c	P2(1)/c
Unit cell dimensions		
a, Å	10.3583(14)	8.80659(12)
b, Å	12.9262(9)	10.79573(14)
c, Å	10.6254(14)	24.5286(3)
β, °	118.784(17)	96.0639(12)
Cell volume	1246.9(2)	2318.97(5)
Z, D(cal)	4, 1.259 Mg/m^3	4, 1.563 Mg/m^3
F(000)	504	1120
Crystal size, mm	0.30 x 0.20 x 0.20	0.24 x 0.22 x 0.06
Crystal colour, shape	colourless, block	orange, block
Temperature, θ_{max} (K, °)	100 , 31.33	100, 70.67
Index range, hkl	$-13 \leq h \leq 14$	$-8 \leq h \leq 10$
	$-17 \leq k \leq 18$	$-13 \leq k \leq 9$
	$-13 \leq l \leq 14$	$-29 \leq l \leq 29$
Absorption correction	Semi-empirical from equivalents	
Max. and min. transm.	0.72 and 1.00	0.37 and 1.00
Goodness-of-fit on F2	1.052	1.128
Reflections collected / unique (Rint)	6933 / 3646 (0.0794)	13208 / 4426 (0.0252)
Data / restraints / parameters	3646/ 0/ 154	4426/ 0/ 269
R1	0.0449	0.0315
wR2	0.1251	0.082
Largest peak and hole, $eÅ^{-3}$	0.557 and -0.362	1.400 and -0.845

Table 5.2: Crystallographic data for complexes [*p*-cymene)Ru(**1c**)Cl]PF_6 **[10]** and [*p*-cymene)Ru(**2d-H**)]$_2$[PF_6]$_2$ **[30]**.

	[*p*-cymene)Ru(**1c**)Cl]PF_6 **[10]**	[*p*-cymene)Ru(**2d-H**)]$_2$[PF_6]$_2$ **[30]**
Empirical formula	$C_{20}H_{27}ClF_6N_3PRuS$	$C_{52.5}H_{62}F_{12}I_2N_8P_2Ru_2S_2$
Formula Weight	623.00	1623.10
Crystal system	Monoclinic	Monoclinic
Space group	P2(1)/n	P2/n
Unit cell dimensions		
a, Å	9.37387(12)	12.67920(16)
b, Å	12.56956(16)	16.80130(18)
c, Å	20.8979(3)	14.8296(2)
β, °	102.2374(14)	102.7363(13)
Cell volume	2406.35(5)	3081.38(7)
Z, D(cal)	4, 1.720 Mg/m^3	2, 1.749 Mg/m^3
F(000)	1156	1602
Crystal size, mm	0.20 x 0.18 x 0.16	0.24 x 0.10 x 0.08
Crystal colour, shape	orange, block	orange, block
Temperature, θ_{max} (K, °)	150, 30.64	150, 30.69
Index range, hkl	$-13 \leq h \leq 13$ $-17 \leq k \leq 17$ $-29 \leq l \leq 29$	$-17 \leq h \leq 17$ $-23 \leq k \leq 23$ $-21 \leq l \leq 21$
Absorption correction		
Max. and min. transm.	0.95 and 1.00	0.91 and 1.00
Goodness-of-fit on F2	1.076	1.054
R1	0.0275	0.0274
wR2	0.0585	0.0654
Largest peak and hole, eÅ^{-3}	0.447 and -0.427	1.152 and -0.490

Conference Proceedings and Scientific Training

Conference Proceedings

- "Monomer-dimer Equilibrium of a Thiosemicarbazone Ru(II)-arene complex studied via XANES and EXAFS", 16th International Conference of Biological Inorganic Chemistry (ICBIC 16), Grenoble, France, July 2013. Poster presentation.

- "Using Synchrotron Radiation to study Ru(II) anticancer complexes", University of Warwick Postgraduate Research Symposium, Coventry, UK, May 2013. Oral presentation.

- "Double up! Dinuclear Ru(II) and Os(II) arene complexes circumvent cisplatin resistance", COST WG#4 meeting "Metallodrugs II", Palacky University Olomouc, Czech Republic, March 2013. Oral presentation

- "XAS, NMR and DFT Studies of Arene Ruthenium(II) and Osmium(II) Anticancer Complexes", Diamond Light Source Annual Synchrotron User Meeting, Didcot, UK, September 2012. Poster presentation.

- "Novel Chelators for Ruthenium(II)-Arene Anticancer Complexes?" Dalton Young Researcher Symposium, University of Warwick, UK, September 2011. Poster presentation.

- "Organometallic Ruthenium-Arene Complexes of Functionalized S,N-ligands", 15^{th} International Conference of Biological Inorganic Chemistry (ICBIC 15), University of British Columbia, Vancouver, Canada, August 2011. Poster presentation.

- "Bioinspired Catalysts with Bifunctional Ligands in Alkyne Hydration", 5^{th} International Symposium of Bio-organometallic Chemistry (ISBOMC), Ruhr- Universitat Bochum, Germany, July 2010. Poster presentation.

- "Bifunctional (Cyclopentadienyl)Ruthenium Catalysts with Imidazole-based Phosphane Ligands", 8^{th} Ferrocene Colloquium, February 2010, Ruhr-Universität Bochum, Germany. Oral presentation.

Publications

"Designing organometallic compounds for catalysis and therapy", **A. L. Noffke**, A. Habtemariam, A. M. Pizarro and P. J. Sadler, *Chem. Commun.* 2012, **48**, 5219–5246.

Scientific Training

- Circular Dichroism Winter School, Warwick Centre for Analytical Science, December 2010

- Bruker Avance TopSpin Training Course, Bruker UK, Coventry, June 2011

- Bruker Avance *Advanced* TopSpin Training Course, Bruker UK, Coventry, August 2012

- Synchrotron Radiation Summer School, Diamond Light Source, Didcot, September 2012

- XAS Analysis course, Diamond Light Source, Didcot, November 2012